

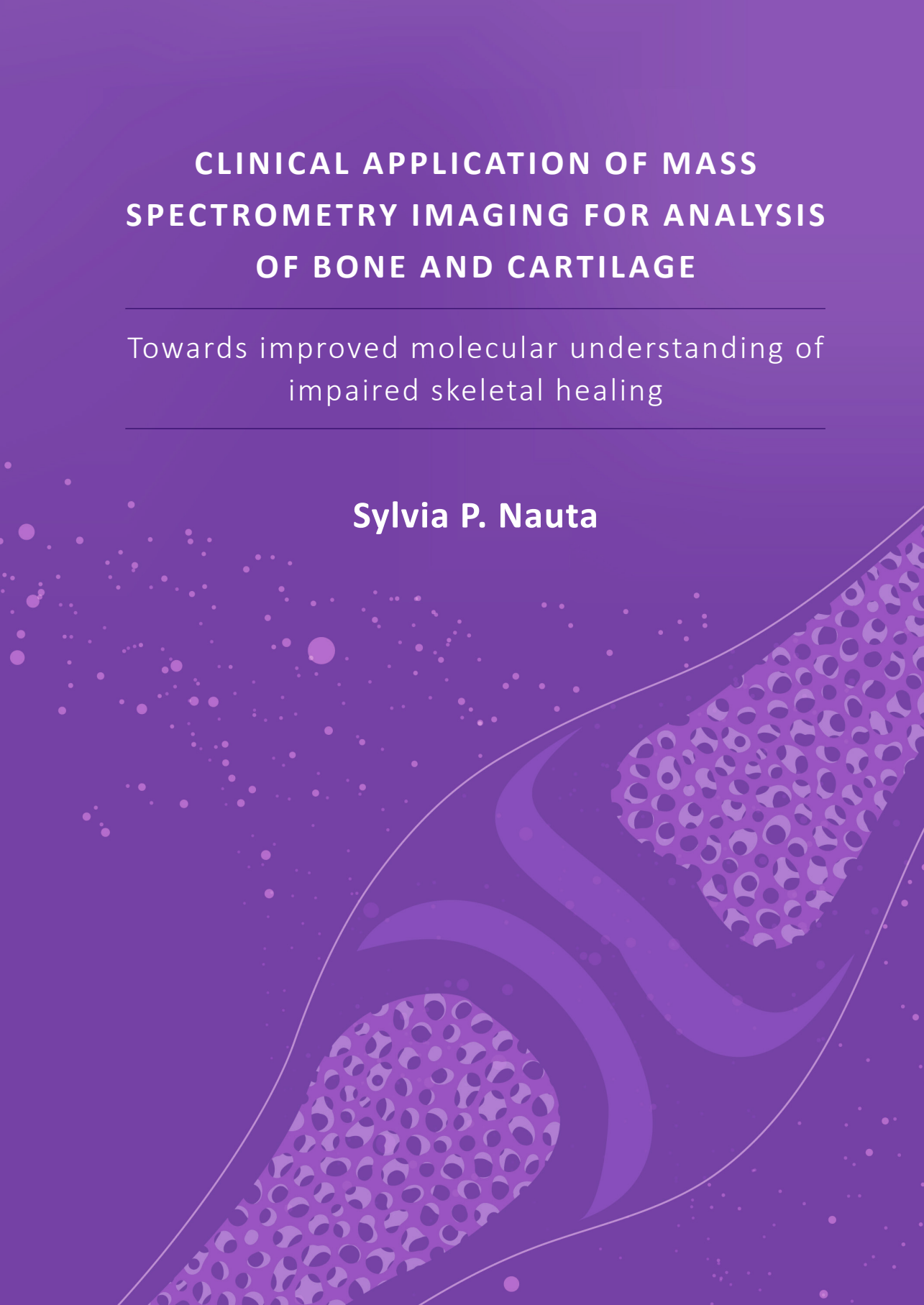
# CLINICAL APPLICATION OF MASS SPECTROMETRY IMAGING FOR ANALYSIS OF BONE AND CARTILAGE

---

Towards improved molecular understanding of  
impaired skeletal healing

---

**Sylvia P. Nauta**





# Clinical application of mass spectrometry imaging for analysis of bone and cartilage

Towards improved molecular understanding of impaired skeletal healing

Sylvia P. Nauta

The research reported in this dissertation was carried out at Maastricht MultiModal Molecular imaging (M4i) institute, division of imaging mass spectrometry, Universiteitssingel 50, 6229ER, Maastricht, the Netherlands.

© **Sylvia P. Nauta**, Maastricht, the Netherlands, 2023

All rights served. No parts of this thesis may be reproduced, distributed, or transmitted in any form or by any means, electronic, mechanical, photocopying, recording, or otherwise, without prior written permission of the author or the publishers of the published chapters.

Lay-out: Sylvia Nauta

Cover design: Harma Makken

Printed by: Ridderprint

ISBN: 978-94-6458-933-7

# Clinical application of mass spectrometry imaging for analysis of bone and cartilage

Towards improved molecular understanding of impaired skeletal healing

PROEFSCHRIFT

ter verkrijging van de graad van doctor aan de Universiteit Maastricht,

op gezag van de Rector Magnificus, Prof. dr. Pamela Habibović

volgens het besluit van het College van Decanen,

in het openbaar te verdedigen

op maandag 6 maart 2023 om 13.00 uur

door

**Ir. Sylvia Paulien Nauta**

Geboren op 31 augustus 1993 te Almere

## **Promotores**

Prof. dr. Ron M.A. Heeren

Prof. dr. Martijn Poeze

## **Copromotores**

Dr. Tiffany Porta Siegel

Dr. Eva Cuypers

## **Beoordelingscommissie**

Prof. dr. Daisy Jonkers (chair)

Prof. dr. Kristine Glunde (The Johns Hopkins University School of Medicine, USA)

Dr. Nina Ogrinc (University of Lille, France)

Prof. dr. Steven Olde Damink

Prof. dr. Tim Welting

This research was part of the M4i research program that is financially supported by the province of Limburg (the Netherlands) via the LINK program.

This research was also part of the collaboration between MUMC+ and M4i via the MUMC+ institutional grant for clinical collaborative research.





# Table of contents

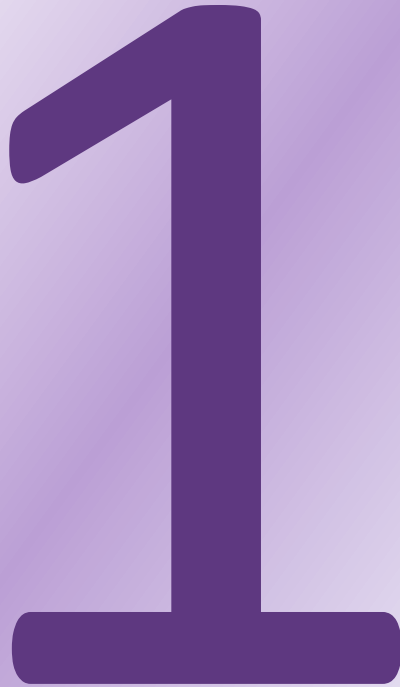
<b>Chapter 1: General introduction and outline</b>	<b>11</b>
1.1 Bone fractures	14
1.2 Articular cartilage damage	18
1.3 Mass spectrometry (imaging)	22
1.4 Thesis outline	29
<b>Chapter 2: Clinical use of mass spectrometry (imaging) for hard tissue analysis in abnormal fracture healing</b>	<b>31</b>
2.1 Abstract	33
2.2 Introduction	33
2.3 Delayed healing and non-union	35
2.4 Post-traumatic osteoarthritis	42
2.5 Mass spectrometry imaging	45
2.6 Ambient ionization mass spectrometry and the potential toward <i>in vivo</i> tissue evaluation	52
2.7 Conclusions and outlook	63
<b>Chapter 3: Sample preparation of bone tissue for MALDI-MSI for forensic and (pre)clinical applications</b>	<b>67</b>
3.1 Abstract	69
3.2 Introduction	69
3.3 Materials and methods	75
3.4 Results	79
3.5 Discussion	97
3.6 Conclusion	102
<b>Chapter 4: Lipid analysis of fracture hematoma with MALDI-MSI - Specific lipids are associated to bone fracture healing over time</b>	<b>105</b>
4.1 Abstract	107
4.2 Introduction	107

4.3	Materials and methods	110
4.4	Results	115
4.5	Discussion	128
4.6	Conclusion	131
<b>Chapter 5: Effect of citrulline supplement on lipid and protein profiles during bone fracture healing in a rat model</b>		<b>133</b>
5.1	Abstract	135
5.2	Introduction	135
5.3	Materials and methods	138
5.4	Results	145
5.5	Discussion	170
5.6	Conclusion	187
<b>Chapter 6: Automated 3D sampling and imaging of uneven sample surfaces with LA-REIMS</b>		<b>191</b>
6.1	Abstract	193
6.2	Introduction	193
6.3	Materials and methods	196
6.4	Results	204
6.5	Discussion	217
6.6	Conclusion	226
<b>Chapter 7: General discussion and outlook</b>		<b>229</b>
7.1	Application of MALDI-MSI for bone tissue and fracture hematoma	231
7.2	3D imaging with LA-REIMS	242
7.3	Translation to a (pre)clinical application	245
7.4	Conclusion and outlook	254
<b>Chapter 8: Impact paragraph</b>		<b>257</b>
8.1	Scientific impact	259
8.2	Social impact	261

8.3	Economic impact	264
<b>Chapter 9: Summaries</b>		<b>267</b>
9.1	English summary	269
9.2	Nederlandse samenvatting	273
<b>Chapter 10: References</b>		<b>279</b>
<b>Chapter 11: Appendices</b>		<b>301</b>
11.1	List of abbreviations	303
11.2	List of publications	308
11.3	Acknowledgements	310
11.4	Curriculum Vitae	317



## Chapter 1: General introduction and outline



## Chapter 1

The skeletal system is composed of a wide variety of different bones and different types of connective tissue, including cartilage, tendons, and ligaments. The bones of the skeleton are held together by ligaments and muscles. Most bones in the limbs are long bones, which consist of cancellous/trabecular/spongy and cortical/compact bone and of which the medullary cavity is filled with bone marrow. The joints between bones allow for movement and are lined with articular cartilage. This articular cartilage allows for smooth movement and acts as a shock absorber. The skeletal system provides different functions, including a framework for support of the body, movement, protection of vital organs, and blood cell production in the bone marrow.

Common, injury-related traumas to the skeletal system are bone fractures and articular cartilage damage. Both bone and cartilage tissue can be affected in intra-articular cartilage fractures. Bone fractures heal via a complex fracture healing process, which results in bone restoration in the majority of cases. In case of cartilage damage, a regeneration process arises, but the healing capabilities of articular cartilage are extremely limited. The healing process following a bone fracture or articular cartilage damage can be dramatically impaired by various circumstances. This results in delayed healing or non-union development for bone fractures. Injury-related articular cartilage damage can result in post-traumatic osteoarthritis (PTOA). Both non-unions and PTOA are long-lasting problems that affect the quality of life of the patients and result in a significant social and economic burden. Molecular understanding of the different healing and impaired healing processes is limited, despite the large amount of research performed. Different molecular classes and key molecules have been identified for both bone healing and articular cartilage repair, which will be addressed in detail in Chapter 2. The exact contribution of different molecules and their role in the different healing and repair processes are still largely unknown, due to the complexity of these processes and the constantly changing molecular and cellular environment. In addition, it is expected that impaired healing is not the result of the up- or downregulation of one molecule or pathway, but is in fact related to a larger molecular disturbance. The lack of molecular knowledge contributes to the clinical challenges related to abnormal fracture healing. One of the biggest challenges is the early outcome prediction following bone fracture and articular cartilage damage. Improved molecular understanding can contribute to early detection and determination of prediction markers of impaired healing. This can advance the treatment of bone fractures and articular cartilage damage.

The use of mass spectrometry (MS) to improve molecular understanding of the different healing and impaired healing processes is explored in this thesis. MS is an analytical technique that allows for the unlabeled analysis of a wide range of molecular classes. This technique has been used in a wide variety of clinical applications and biomedical tissue studies. The use of MS on bone, cartilage, and other tissues related to the healing processes is very limited. Therefore, methodological developments are still needed and this thesis aims to contribute to this development and provide further insight into healing processes in the skeletal system. A general introduction to MS will be provided, including more detailed information on the different techniques applied and developed in this thesis. However, bone fracture, bone fracture healing, and non-union will be introduced first. In addition, articular cartilage damage, cartilage repair, and PTOA development will be introduced before the MS introduction.

### 1.1 Bone fractures

Bone fractures are the first type of trauma to the skeletal system introduced in this thesis. Around 200 000 bone fractures occur yearly in the Netherlands, of which more than 70 000 patients are annually admitted to a hospital (see Table 1.1).<sup>1,2</sup> The epidemiology of bone fractures is constantly changing and is area-dependent.<sup>3</sup> Overall, the incidence of bone fractures is increasing, also due to a growing and aging population.<sup>1</sup> The fracture location and incidence change with age and is gender dependent.<sup>1,3</sup> Bone fractures are a major health issue, especially when occurring in osteoporotic bone.<sup>1,3</sup> The treatment of these bone fractures became more complicated and expensive, also as a result of the aging population.<sup>3</sup>

A bone fracture is a complete or incomplete break of the anatomical continuation of the bone resulting in mechanical instability.<sup>4</sup> Bone fracture occurs when the bone absorbs too much energy/force and structurally fails.<sup>4,5</sup> Contributing factors to bone fractures are weakening of the bone due to specific bone diseases, such as osteoporosis, and accumulation of micro-fractures in healthy bone due to continuous loading.<sup>5</sup> A common classification is open versus closed fractures, which is based on the nature of the fracture.<sup>5</sup> Bone fractures, especially open fractures, are commonly related to damage to the surrounding soft tissue, vascularity, and bone marrow, which results in a higher rate of abnormal healing.<sup>6</sup>

#### 1.1.1 Bone fracture healing

Normal bone fracture healing is a highly complex process that involves many different cell types and molecular pathways.<sup>2,4-10</sup> The process is a cascade of a well-

**Table 1.1:** Number of fractures per year based on the hospital admissions in the Netherlands. Data obtained from CBS Open data StatLine<sup>11</sup>.

Fracture location	2013	2014	2015	2016	2017	2018	2019
Skull/facial bone	4710	4300	4225	4210	4265	4290	4205
Neck	830	955	1025	1065	1080	1130	1045
Rib/sternal/thoracic spine	3690	3915	4155	4125	3910	4085	4010
Lumbar spine/pelvis	4095	4290	4525	4510	4425	4235	4180
Spine, not specified	40	10	15	35	10	20	15
Shoulder/upper arm	8820	9120	9735	9410	8900	9230	8990
Elbow/forearm	10785	10275	10815	11160	11125	11615	11645
Wrist/hand	4905	4565	4800	5135	4965	5050	5220
Upper extremities, not specified	5	0	5	5	0	0	0
Femur	21190	21840	22830	22595	22890	23260	23620
Lower leg/ankle	11955	11845	12620	12600	12760	12305	12750
Foot	1540	1520	1630	1705	1540	1600	1610
Lower extremities, not specified	25	5	5	10	0	5	0
Multiple body regions	800	920	895	1055	975	945	855
Total	73390	73560	77280	77620	76845	77770	78145

defined series of biological phases and corresponding mechanical requirements.<sup>2,4-8,10,12,13</sup> There is a great amount of overlap in these phases, despite the well-defined successive series of events.<sup>2,6,12</sup> The result is a continuously changing cellular and molecular environment during bone fracture healing.<sup>7,8,10</sup> Different cells (e.g. bone and cartilage forming cells) and regulatory factors (e.g. cytokines, and growth and differentiation factors) are recruited from the tissues around the fracture site (e.g. cortex, periosteum, bone marrow, and surrounding soft tissues) as well as circulation.<sup>7,10</sup> The contribution of these tissues depends on conditions at the bone fracture site in terms of the molecular and mechanical environment and the type

## Chapter 1

of fracture healing.<sup>7,10,13</sup> The exact contribution of the different cellular and molecular mechanisms involved in bone fracture healing is not fully understood, due to the complexity of the process.<sup>2,5,10,12,13</sup> The objective of bone fracture healing is to achieve complete structural and functional restoration of the affected bone without any scar formation.<sup>2,4,5,7,8,12,14</sup> Complete restoration can be achieved via direct (primary) or indirect (secondary) fracture healing, of which indirect fracture healing occurs for most bone fractures.<sup>4,5,7,8,10,12-14</sup>

Direct fracture healing can only take place if the different fracture fragments are secured closely to each other with a rigid internal fixation method to achieve absolute stability and reduce inter-fragmentary strain.<sup>4,5,7,8,10,12-14</sup> The maximum distance between fracture fragments that can be bridged with direct fracture healing is between 200 and 500  $\mu\text{m}$ .<sup>13</sup> A direct effort is made to restore mechanical continuity during direct fracture healing.<sup>5,7,8,10,12</sup> This is achieved by the formation of discrete remodeling units, named 'cutting cones', formed from the cortex, which attempts to bridge the gap and recreate the Haversian systems of the bone.<sup>5,7,10,13,14</sup> The direct bridging allows the osteoclasts in the cutting cones to form cavities that are filled with bone produced by the osteoblasts.<sup>5,12-14</sup> The absence of callus formation is one of the characteristics of direct fracture healing.<sup>5,7,10</sup>

Indirect fracture healing is a well-defined process of four phases: inflammation and hematoma formation, soft callus formation, hard callus formation, and bone union and remodeling (see Figure 1.1).<sup>2,5,6,9</sup> Indirect fracture healing is a combination of intramembranous (direct bone formation) and endochondral ossification (formation of cartilage that is calcified and replaced by bone).<sup>2,4,5,7,8,10,12,14</sup> Endochondral ossification occurs at the parts of the fracture that are mechanically unstable and dominates in the majority of fractures.<sup>4,6,7,10</sup> Indirect fracture healing is enhanced by a certain amount of motion between the fracture fragments as well as by weight-bearing.<sup>5,7,14</sup> Indirect fracture healing starts after a bone fracture and surrounding tissue damage via the activation of different inflammation pathways.<sup>4-6,12,14</sup> A fracture hematoma is formed within the fracture site due to the accumulation of blood.<sup>4-6,12,14</sup> The initial inflammatory reaction and the formation of the fracture hematoma are critical to the fracture healing process.<sup>2,12</sup> Different types of inflammatory cells infiltrate the hematoma to fight potential infection and secrete cytokines and growth factors.<sup>4,6</sup> Mesenchymal stem cells are recruited by the cytokines and growth factors from various origins and differentiate into osteogenic cells.<sup>4-6,12,14</sup> The hematoma is replaced by granulation tissue with blood capillary ingrowth.<sup>4-6</sup> The granulation tissue is replaced by cartilage to form a

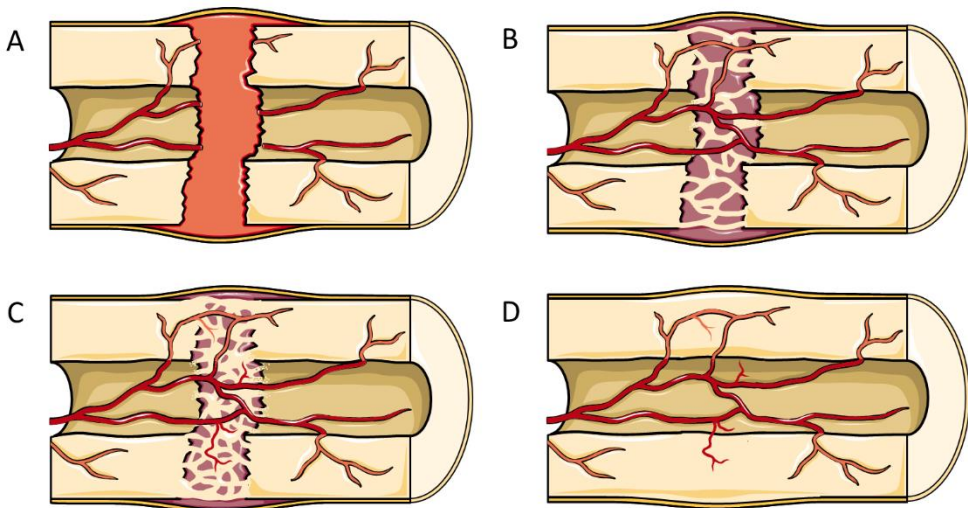


**Figure 1.1:** The different phases during indirect bone fracture healing, namely **A** inflammation and hematoma formation, **B** soft callus formation, **C** hard callus formation, and **D** bone union and remodeling.

fibrocartilaginous bridge between the fracture fragments.<sup>4-6,12,14</sup> This soft callus is formed to provide mechanical support and is the scaffold for bone formation.<sup>4-6,12,14</sup> The soft callus undergoes mineralization and is subsequently replaced with woven bone.<sup>4-6,12,14</sup> Mineralized bone is formed in areas that are stabilized due to the soft callus formation.<sup>6,14</sup> This newly formed bone is usually irregular and is named the hard callus.<sup>4,6,12,14</sup> This hard callus provides additional stability, but has reduced strength and stiffness compared to the initial bone structure.<sup>4,5,12,14</sup> The vascular ingrowth into the woven bone is crucial for the hard callus formation.<sup>6,14</sup> In the final phase, the woven bone of the hard callus is remodeled into the initial cortical and trabecular bone structure.<sup>4-6,14</sup> Orderly bone resorption by osteoclasts and formation by osteoblasts of lamellar bone is critical in this remodeling phase.<sup>2,4-6,14</sup> The bone structure after bone remodeling will respond to the mechanical demands on the bone.<sup>2,4,5</sup> The bone remodeling can take years to regenerate the initial bone structure.<sup>2,5,14</sup>

### 1.1.2 Non-union development

Complete fracture healing can only be achieved when inflammatory and osteogenic cells, osteoconductive scaffolds, growth factors, and mechanical stability are present, which are combined in the diamond concept.<sup>4,8,12,13</sup> In addition, adequate blood flow to the fracture side is essential.<sup>4,5,10,12,14</sup> Bone fracture healing is affected by numerous physiological and pharmacological factors, including the location and

extent of injury to the bone and surrounding soft tissue, amount of vascularization, mechanical stability, infection, general bone health, and underlying diseases or genetic conditions.<sup>2,4,6,9,13,15</sup> The fracture healing time and chances of functional repair are affected by these factors, which complicates the prediction of the outcome of fracture healing.<sup>9</sup> For example, the location of the fracture is directly related to the blood supply, which can affect the fracture healing process in cases of low blood supply.<sup>2</sup> Any variation in the molecular expression or imbalance between growth factors and their inhibitors at any point in the complex fracture healing process can result in complications and impaired healing.<sup>8,10</sup> In addition, a balance between anabolic (cartilage and bone formation) and catabolic (cartilage and bone resorption) processes is essential.<sup>6</sup> Any failure in timely tissue resorption or formation can result in impaired healing of the fracture.<sup>6</sup> Other factors that could impair the fracture healing process are a lack of osteogenic cells due to extensive tissue damage and/or low blood supply.<sup>4</sup> The gap between the fracture fragments is too large to bridge in case of a critical defect, which can impair healing due to a lack of osteoconductive scaffold.<sup>4</sup> All these complications during the fracture healing can result in delayed healing or non-union development and prolong the time until returning to complete functioning.<sup>4,13</sup> The initial treatment of a bone fracture can be a contributing factor to the incidence of non-unions.<sup>9,15</sup>

A non-union occurs when there is a termination in the fracture healing process without reaching a bone union, while the fracture healing process takes longer and the outcome is uncertain in delayed healing.<sup>4,12</sup> The distinction between delayed union and non-union can be challenging in practice.<sup>2</sup> Impaired healing can have many causes and the viability for eventual fracture healing varies between different types of non-unions.<sup>2,9,13</sup> Delayed healing or non-union occurs in 5-10% of the fractures, but non-union rates depend on the anatomical location and treatment.<sup>2,4,9,13,15</sup> The annual number of cases of impaired fracture healing is thousands of patients in the Netherlands.<sup>2</sup> Delayed healing and non-unions are a major burden for both the patient and society.<sup>12,13,16</sup> Besides, non-unions are associated with high treatment costs due to the complexity and length of the treatment and economic costs due to productivity loss.<sup>9,12,13,16</sup> The exact costs of a non-union depend among others on the fracture location and treatment.<sup>16</sup>

### **1.2 Articular cartilage damage**

Next to bone fractures, articular cartilage damage is another common trauma to the skeletal system, especially in intra-articular fractures, that will be introduced further. Estimation of the incidence of articular cartilage damage is difficult due to the difficulty in early diagnosis and limited awareness.<sup>17-19</sup> The relationship of initial

articular cartilage damage to the development of joint degeneration later on is unclear.<sup>18,20</sup> The lack of symptoms up to a certain amount of damage is a contributing factor to this.<sup>21</sup> In addition, the understanding of the mechanisms, frequency, and history of articular cartilage damage is poor.<sup>18</sup> It is likely that at least some amount of articular cartilage damage will occur in a large amount of the population, especially in the older generation.<sup>17,18</sup> In addition, articular cartilage damage due to injuries occurs frequently in athletes.<sup>17,19</sup> The risks for and the type of articular cartilage damage are highly age-dependent, which might be related to the changes in the mechanical properties of the cartilage with age.<sup>17,21</sup>

Articular cartilage damage can occur due to direct trauma, repetitive impact loadings, indirect impact loading, or torsional loading of the joint, which can affect the calcified cartilage-subchondral bone region with any effect on the surrounding soft tissue.<sup>17,18,20</sup> The extent of articular cartilage damage depends on the magnitude of the applied force, the orientation relative to the articular surface, and the rate/frequency of loading.<sup>20,22</sup> Damage to articular cartilage can be divided into small defects in otherwise normal cartilage and degenerative defects that affect the whole surface.<sup>21</sup> The pathogenesis, extent of involvement of the articular surface, and location within the joints differ between the different types of cartilage damage.<sup>21</sup> Some mechanical types of injury leave the articular cartilage surface intact while damaging the calcified cartilage zone and/or the subchondral bone.<sup>17,18,20</sup> The small mechanical defect group is commonly injury-related and can be divided into 1) chondral damage without visible tissue disruption, 2) chondral damage with disruption to the articular cartilage, or 3) osteochondral damage with disruption of the articular cartilage as well as the subchondral bone.<sup>17,18,20,21,23</sup> For example, high intensity traumas or ligament injuries can result in intra-articular fractures that extend from the cartilage into the subchondral bone.<sup>17,24</sup> In contrast, degenerative defects start as small regions of softening and superficial fraying and fibrillation of the articular cartilage surface.<sup>21,24</sup> These regions will extend over the articular surface and progress into deeper layers of the cartilage, although this process can be slow.<sup>21,24</sup> Articular cartilage damage also affects other joint tissues, like menisci, ligaments, and synovium.<sup>17,18,23,25,26</sup>

### 1.2.1 Cartilage repair

In case of the articular cartilage damage and/or loss, the body tries to repair the tissue.<sup>21</sup> Often, articular cartilage damage is not or only partly repaired, due to the extremely limited healing capacity of cartilage.<sup>17,19,21,24</sup> The type of and potential for healing depends highly on the kind, location, and size of the articular cartilage damage.<sup>17,18,20</sup> Articular cartilage damage initiates a chronic remodeling process

that eventually results in cartilage degeneration in most cases.<sup>27</sup> The ability of articular cartilage to repair itself decreases with age, due to structural, molecular, cellular, and mechanical changes.<sup>17,18,20,21</sup> In addition, these changes result in decreased tensile strength of the articular cartilage, which contributes to a higher vulnerability to injury and degenerative defect development.<sup>18,21</sup>

In case of chondral damage without tissue disruption, the articular cartilage matrix is altered.<sup>17,18</sup> The chondrocytes will respond to these changes by synthesizing new molecules to repair the damage.<sup>17,18</sup> The point of irreversible damage is unclear and progressive loss of articular cartilage occurs after this point.<sup>17,18,20</sup> In case of chondral damage with tissue disruption, the chondrocyte will try to repair the injury by proliferation and synthesis of matrix molecules near the injury.<sup>17,18</sup> This does not result in a repair of the damage, as the tissue defect cannot be filled due to a local lack of cells.<sup>17,18</sup> Additionally, the increased synthesis and proliferation stop quickly after the initial injury.<sup>17,18</sup>

Osteochondral damage causes the formation of a hematoma in the bone injury site, which is replaced by a fibrin clot.<sup>17,18,20,24</sup> This fibrin clot extends into the cartilage defect.<sup>17,18,20</sup> Over time, the fibrin clot is replaced by immature bone, fibrous tissue, and hyaline-like cartilage in the subchondral bone part and a repair tissue between hyaline cartilage and fibrocartilage in the articular cartilage part (see Figure 1.2).<sup>17,18,20,24</sup> The repair tissue in the chondral part does not replicate the properties of the articular cartilage.<sup>17,18,20,24</sup> The repair tissue will disintegrate over time resulting in the exposure of the subchondral bone due to the different mechanical and structural properties, despite initially filling the osteochondral defect.<sup>17,18,20,24</sup>

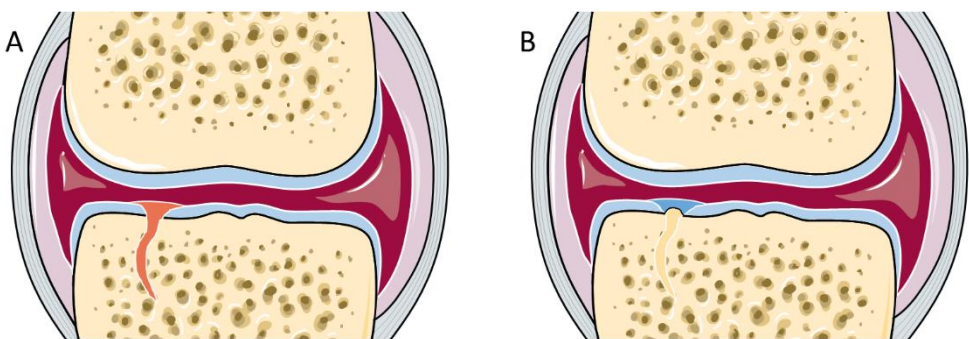


**Figure 1.2:** The two phases of the healing response after osteochondral cartilage damage, namely **A** fibrin clot formation extending from the subchondral bone into the cartilage defect, and **B** immature bone, fibrous tissue, and hyaline-like cartilage formation in the subchondral part and hyaline cartilage and fibrocartilage formation in the chondral part.

In the case of degenerative defects, cartilage repair involves remodeling and sclerosis of the subchondral bone along with the formation of subchondral bone cysts and marginal osteophytes.<sup>17,21</sup> This results in structural changes in the joint, which affect joint movement and often causes pain.<sup>17,21</sup> The effort of the articular cartilage to repair itself often results in the development of osteoarthritis (OA).<sup>17,21</sup> The structural changes occurring with osteoarthritis also affect other joint tissues, including the subchondral bone and synovium.<sup>21</sup>

### 1.2.2 Posttraumatic osteoarthritis

The healing potential of articular cartilage after a fracture is extremely limited.<sup>17,19,21</sup> Large gaps or step-offs in the articular cartilage have only very little or no repair potential.<sup>20</sup> Irregularities of the joint surface especially when combined with joint instability will affect the articular cartilage repair process.<sup>20,22,25,28,29</sup> These areas of elevated joint contact stress can result in cartilage thinning.<sup>22</sup> Additionally, the structure, composition, and mechanical properties of the repair tissue are not the same as the initial articular cartilage.<sup>17-20,24</sup>

Viable chondrocytes are required for any type of repair that requires the chondrocytes to proliferate and synthesize new matrix.<sup>17,20,28</sup> The chondrocyte can restore the cartilage matrix as long as the damage is not bigger than what the chondrocytes can produce rapidly.<sup>20,28</sup> Herein, the balance between catabolic and anabolic processes in the cartilage is of importance.<sup>19,23</sup> High impact loadings and intra-articular fractures can result in chondrocyte death, reduced chondrocyte viability, and affects the matrix composition.<sup>20,23,25,27-30</sup> The lack of repair by chondrocytes results in a decrease in the cartilage stiffness and causes increased loading and stress on the remaining cartilage matrix and chondrocytes.<sup>20,27,28</sup> These alterations enhance the vulnerability of the articular cartilage and eventually can result in cartilage degeneration.<sup>20,27,28</sup> A similar process takes place in the case of osteochondral cartilage damage. Failure of the initial repair tissue results in altered loadings on the surrounding matrix and progressive structural damage over time.<sup>20</sup> The structure and function of the subchondral bone are of great importance for the health and repair capacity of articular cartilage.<sup>25,28</sup> Overall, the exact relation between the injury severity and the risk for progressive cartilage degeneration is unclear.<sup>17,18,20,22</sup>

Direct, indirect, or repetitive impact loading, torsional joint loading, joint dislocation, and joint instability after trauma can damage articular cartilage.<sup>18,20,23,25,26,28,31</sup> All joint tissues are affected by this joint trauma, but the irreversible cartilage damage seems to be the most critical.<sup>27</sup> The resulted injury-

related articular cartilage damage increases the risk for progressive cartilage degeneration, which is called posttraumatic osteoarthritis (PTOA).<sup>18,20,22,25,26,28,29</sup> Especially, intra-articular fractures frequently progress into cartilage degeneration and, thus, PTOA, although the degree of displacement and fracture size affect the outcome.<sup>20,22,26,28,30</sup> Nevertheless, it is not only the magnitude and the type of injury that will determine whether or not cartilage damage will progress into PTOA, although it is of great importance.<sup>19,20,22,29,30</sup> Chronic abnormal joint loading and contact stress can also contribute to the development of PTOA.<sup>19,20,22,25,29,31</sup> Trauma-related cartilage damage and the development of PTOA are often related to participation in sports and affect a younger and more active population.<sup>18-20,25,27,28,30</sup> The risk for and rate of PTOA development varies between joints, joint regions, and age.<sup>19,20,23,25,27-29</sup> The complexity of the cartilage interaction with surrounding joint tissues and response to external factors is a strong contributor that determines patient outcome.<sup>19,23,25,28</sup> Approximately 12% of the symptomatic OA cases can be attributed to PTOA.<sup>22,23,25-29,31</sup> Injury-related cartilage damage will result in PTOA in 10-75% of the cases depending on the involved joint and the time since injury.<sup>22,23,26,28-31</sup> Exact incidence numbers are difficult to obtain due to the lack of large population-based studies.<sup>23,31</sup> PTOA development is a major burden for the patient and society due to its progressive nature and disabling effect on patients.<sup>23,31</sup> Prevention and treatment options are very limited for PTOA and often do not provide the desired long-term results, especially in younger patients.<sup>23,28,30</sup> These treatments are related to high costs and are accompanied by high costs related to productivity loss.<sup>26,31</sup>

### 1.3 Mass spectrometry (imaging)

Mass spectrometry (MS) is the analytical technique applied in this thesis and its possibilities to improve molecular understanding of bone fracture healing, articular cartilage repair, and impaired skeletal healing are explored. MS is a sensitive analytical technique that allows for the rapid and simultaneous detection and identification of a wide range of molecules without prior knowledge or labeling.<sup>32-34</sup> Molecular classes that can be analyzed with MS include metabolites, lipids, peptides, and proteins.<sup>32,33,35</sup> Mass spectrometry imaging (MSI) can be used to study local molecular distributions in tissue sections.<sup>32,33,35-37</sup> In addition, different near real-time techniques using MS have been developed during the past decade for the analysis of native tissue and these have the potential to be used intra-operatively. MS(I) has been used in an increasing number of clinical applications for, for example, biomarker discovery, diagnosis, and prediction of treatment outcome. One of the main clinical application fields is tumor research, although many other diseases have been studied as well.<sup>35</sup>

A mass spectrometer consists of different parts, of which the ionization source, mass analyzer, and ion detector are probably the most important elements.<sup>33,34</sup> The ionization source is responsible for the transformation of the different biomolecules from the sample into gas phase ions.<sup>34</sup> Numerous sampling and ionization techniques have been developed, including hard and soft ionization sources. Hard ionization sources cause extensive molecular fragmentation, due to the high amount of energy delivered to molecules. This is not the case for soft ionization techniques, which allow the ionization and analysis of larger biological molecules without fragmentation. Secondary ion mass spectrometry (SIMS) is an example of a hard ionization technique, while matrix-assisted laser desorption/ionization (MALDI) and electrospray ionization (ESI) are examples of soft ionization techniques.<sup>32,33,36</sup> MALDI is one of the ionization methods that is commonly used in MSI. Referred to as MALDI-MSI, it is applied to different tissue types for biomedical and clinical research.<sup>32</sup> The possibility to explore the use of MS for *in vivo* tissue analysis was accelerated by the development of different ambient ionization techniques. One of these techniques is rapid evaporative ionization MS (REIMS) coupled to, for example, a CO<sub>2</sub> laser, which is referred to as laser-assisted (LA-)REIMS.<sup>38,39</sup> MALDI-MSI and LA-REIMS are the two techniques that were mainly applied in this thesis and those techniques will be explained in more detail below.

The mass analyzer separates the ionized molecules (generated in the ionization source) based on their mass-to-charge ( $m/z$ ) ratio. Ion signals are acquired by the detection system and converted into electrical signals, which results in the generation of a mass spectrum. Mass spectra display the signal intensity of different detected molecular ions as  $m/z$  peaks in the acquired mass range. There are different types of mass analyzers, including a time-of-flight (TOF), Fourier transform ion cyclotron resonance (FT-ICR), and Orbitrap. In a TOF system, an electrical field accelerates the ions towards the ion detector and the ions are separated based on the time required to reach this detector.<sup>33,34,40,41</sup> The reflectron TOF in combination with a quadrupole is the geometry predominantly used in this thesis. A reflectron is an electrostatic mirror that reflects the ions at the end of the flight tube towards the detector.<sup>33,34,40,41</sup> The penetration depth in the reflectron depends on the kinetic energy of the ions and the time spent in the reflectron differs.<sup>40,41</sup> This effect compensates for the initial time and velocity differences between ions with the same  $m/z$  value with proper adjustment of the reflectron.<sup>34,40,41</sup> This compensation in combination with a longer flight distance improves the mass resolving power of the TOF system.<sup>33,34,41</sup> The addition of a quadrupole in front of the TOF mass analyzer allows for tandem mass spectrometry, also called MS/MS or MS<sup>2</sup>.<sup>33,34</sup> MS/MS experiments are used to obtain further structural information for the

identification of the ionized molecule of interest, the so-called precursor ion.<sup>32-34</sup> The precursor ion is isolated by the quadrupole and is subsequently fragmented into pieces, i.e. the product ions, by, for example, collision-induced dissociation (CID) in a collision cell before analysis in the TOF.<sup>33,34</sup> An FT-ICR traps the ions in an ICR cell after which the ion cyclotron motion is made spatially coherent and detectable following excitation by the application of an oscillating electric field.<sup>33,42</sup> The ion cyclotron motion's frequency is dependent on the magnetic field strength in which the ICR is positioned and the  $m/z$  ratio of the ion.<sup>42</sup> An Orbitrap traps the ions in a static electrical field in which they oscillate in a stable trajectory along an axial center electrode.<sup>43</sup> These axial oscillation frequencies are related to the  $m/z$  value of the ions and the detected current can be transformed into a mass spectrum using Fourier transformation.<sup>43</sup> The oscillation frequencies of the ions are detected with increasing mass resolving power with increasing measurement time for both the FT-ICR and Orbitrap.<sup>33,42,43</sup> Orbitraps and FT-ICRs can be combined with quadrupoles and/or ion traps to enable tandem mass spectrometry.<sup>33</sup> FT-ICRs can also be used for tandem mass spectrometry inside the ICR cell.<sup>42</sup>

### 1.3.1 MALDI-MSI

MALDI allows for the generation of intact gas-phase ions that are usually single-charged, i.e. molecules that have one positive or negative charge.<sup>33,34</sup> MALDI is a two-step ionization process involving small organic molecules named the matrix, which provide desorption and ionization of a wide range of molecules (see Figure 1.3).<sup>32,33,37</sup> The matrix molecules are dissolved in a solvent and this solution is applied onto the sample via, for example, spotting or spraying.<sup>33,36,37,44</sup> A homogeneous matrix coverage can be achieved by automated spraying a matrix solution on the sample.<sup>33,36,37,44</sup> The solvents evaporate into the air after application.<sup>33</sup> Another method of matrix application is sublimation, in which the matrix molecules are brought into the gas phase by heating and condense on the sample by rapid cooling under vacuum conditions.<sup>37,45</sup> The different application methods result in the formation of a thin layer on the sample that consists of matrix and analyte molecules that co-crystallize.<sup>32-34</sup> The sample plate is placed into the mass spectrometer for the second step of the ionization process. In this step, a focused laser irradiates the matrix-analyte crystals.<sup>33</sup> The focused laser is usually an UV laser, but this depends on the spectral absorption properties of the used matrix.<sup>32,33</sup> The desorption and ionization of the matrix and analyte molecules occur due to local the accumulation of large amounts of energy from the laser that excites the matrix molecules.<sup>33</sup> The matrix absorbs the majority of the laser energy and makes the energy transfer to the analyte more efficient, which results in less

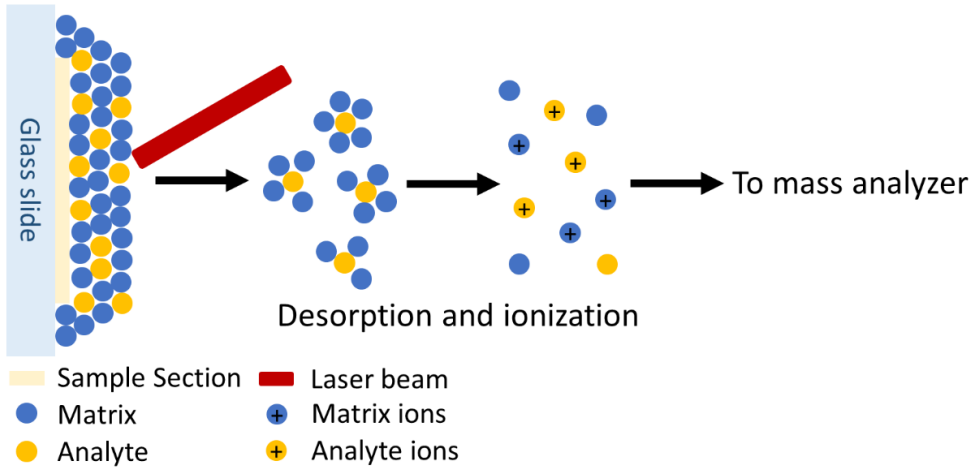


**Figure 1.3:** Simplified MALDI process for positive ionization mode. A thin sample section is placed on a glass slide and covered with a matrix. Matrix and analyte molecules from the sample section co-crystallize and form a layer on the glass slide. These crystals are irradiated with a laser resulting in their sublimation. Expansion and charge transfer take place in the gas phase resulting in ion formation of the matrix and analyte. The ions are transferred to the mass analyzer.

damage, for example, fragmentation, to the analyte.<sup>32,33,37</sup> The presence of protons from the matrix or added acids support positive ionization, while the matrix acts as a proton acceptor from analytes for negative ionization.<sup>32,33</sup> Analytes generated with MALDI are often single charged, but the exact ionization mechanism is still under debate and not fully understood.<sup>34</sup> The resulting ions are transferred to the mass analyzer for separation and detected by the ion detector. MALDI is often combined with TOF mass analyzers due to the pulsed nature of the lasers, but can also be combined with other mass analyzers.<sup>32,35</sup>

MALDI is often used for MSI, as it allows for spatial MS profiling directly from a surface of endogenous molecules, like lipids and peptides, as well as exogenous compounds, like drugs and their metabolites.<sup>32,33</sup> MSI allows for the visualization of molecular distributions in a sample by acquiring a single mass spectrum for each defined pixel on the sample surface.<sup>32,33,36,37</sup> Commonly the sample plate moves from position to position while the laser focus remains at a fixed position in MALDI-MSI to acquire the mass spectra in the defined region of interest.<sup>33,35</sup> The intensity of a single (or multiple)  $m/z$  values are displayed in molecular distribution images, which can be obtained by combining the information from the single pixel mass spectra with their spatial location.<sup>35</sup> These distributions can be associated with

histological features in a tissue section, for example, by overlaying the molecular distributions with an H&E staining.<sup>32,33</sup>

The MALDI-MSI workflow is highly dependent on the sample type and molecular class of interest. The basic MALDI-MSI workflow consists of sample collection, sample sectioning, sample preparation, including matrix application, spatial ionization, MS analysis and acquisition of single pixel mass spectra, and data analysis, which results in the construction of the molecular distribution images (see Figure 1.4). Sample collection is the critical first step within the workflow, as sample integrity should be preserved, and degradation and delocalization of biomolecules should be limited.<sup>33,36,37,44</sup> Fresh-frozen samples, which are stored at -80 °C until use, are preferred for MALDI-MSI, because of the wide variety of biomolecules that can be analyzed.<sup>33,36,44</sup> However, proteins and peptides can still be examined in formalin-fixed and paraffin-embedded (FFPE) samples.<sup>33,36</sup> The samples need to be sectioned before they can be analyzed, as thin and flat sections are required for

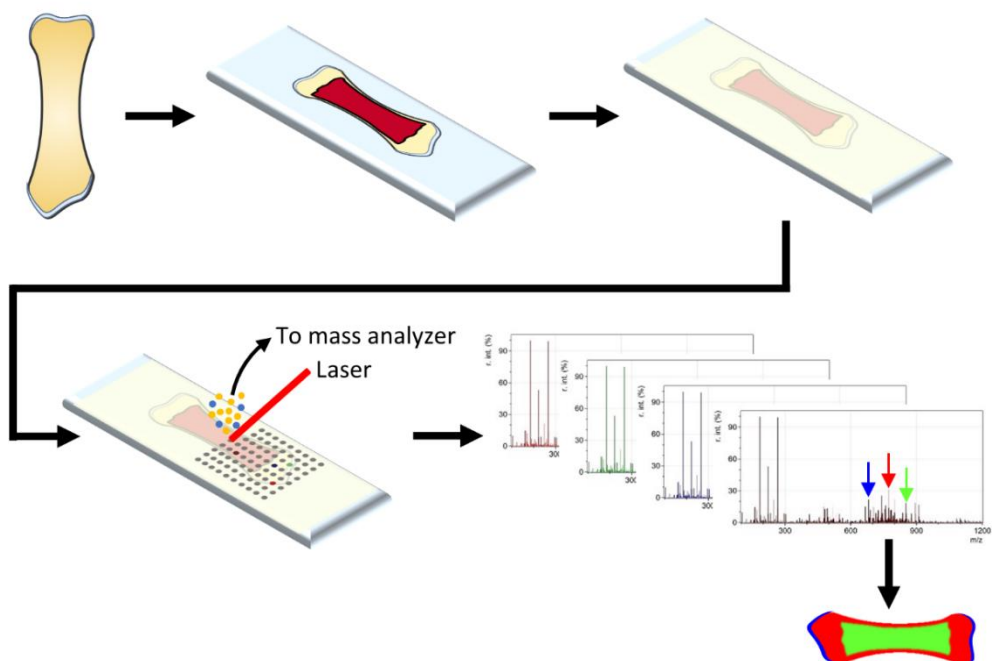


**Figure 1.4:** General MALDI-MSI workflow consisting of sample collection, sample sectioning and mounting, matrix application, MSI analysis and data acquisition for each pixel, and data analysis and visualization resulting in molecular distribution images.

most MALDI-MSI approaches.<sup>37,44</sup> Samples are sectioned in a cryotome in slices with a thickness usually between 10 and 20  $\mu\text{m}$  for fresh frozen samples.<sup>33,36,37,44</sup> The sections are commonly thaw-mounted on microscopic or indium tin oxide coated (ITO) glass slides.<sup>33,36,37</sup> Certain types of samples require embedding before sectioning and/or transferring with tape support to maintain spatial integrity.<sup>33,36,37</sup> The next step is sample preparation of the section, which is highly dependent on the molecular class of interest as well as the type of sample. It usually consists of specific washing steps to remove unwanted molecules that affect the ionization efficiency, and/or digestion or derivatization steps to render the molecules of interest amenable to desorption and ionization.<sup>33,36,37</sup> Sample preparation is continued with matrix application, which will enhance desorption and ionization of the analytes of interest. The matrix crystal size and amount of delocalization will depend on the application method and the matrix choice.<sup>35,37,44,45</sup> In addition, the matrix choice will depend on the molecular class of interest and the sample type.<sup>33,35,36,44</sup> Different matrix application methods can be used, of which spraying and sublimation are commonly used in MALDI-MSI.<sup>35,36,44,45</sup> The matrix-coated sample is subsequently introduced into the MALDI-source of the mass spectrometer and the data acquisition of the region of interest is performed. During this data acquisition, a mass spectrum per pixel is acquired. Lastly, data analysis is performed to create, among others, molecular images of molecules of interest. Common steps in data analysis are normalization, baseline correction, peak picking, visualization, and often molecular identification.<sup>32</sup> The results of a MALDI-MSI acquisition are highly dependent on the different steps in the workflow from sample treatment to matrix application.<sup>33,35,36,44</sup> Therefore, optimization and standardization of the sample preparation protocol and matrix selection are crucial steps in method development, especially for tissue types that have not been analyzed extensively yet.

### 1.3.2 LA-REIMS

REIMS is an ambient ionization technique that allows the analysis of native tissue and requires minimal sample preparation.<sup>46,47</sup> The possibility to analyze native tissue opens up the possibility to use MS for *in vivo* tissue classification, as with REIMS near real-time evaluation of the sample is possible.<sup>46</sup> The mass spectra created with REIMS depict molecular profiles that are specific to tissue type.<sup>38,39,46-48</sup> In the future, this can instantly provide a surgeon with tissue classification information during surgery using the complex molecular information and could contribute to improved surgical decision-making. Currently, REIMS in combination with different handpieces is predominantly employed *ex vivo* for the analysis of

tissues. One of the options explored in this thesis is the combination of REIMS with a surgical CO<sub>2</sub> laser resulting in LA-REIMS.<sup>38,39</sup>

In LA-REIMS (see Figure 1.5), a CO<sub>2</sub> (or another type of) laser is used to thermally ablate and aerosolize part of a biological tissue resulting in the generation of a smoke rich in molecular information from the tissue.<sup>38,39,46,47</sup> The smoke is transported via a tube to the front part of the mass spectrometer, the Venturi pump, and the flow is supported by an additional aspiration pump.<sup>46-48</sup> The molecular-rich smoke is mixed with a solvent matrix in the Venturi, as this solvent matrix improves ionization and signal intensity.<sup>47</sup> The molecules in the aerosol rich smoke are evaporated and ionized by collision with the heated impactor.<sup>46-48</sup> Thereafter, the resulting ions are transferred to the mass analyzer for  $m/z$  separation and subsequent detection by the ion detector. REIMS is commonly coupled to a qTOF analyzer. Metabolites and lipids are the molecular classes that are mainly detected with REIMS.<sup>38,39,46-48</sup> Lipid fragments and/or lipids clusters can also be observed with LA-REIMS.<sup>38</sup>

LA-REIMS is an invasive technique, as part of the biological tissue is ablated for MS analysis. The amount of damage to the tissue depends on many factors, including

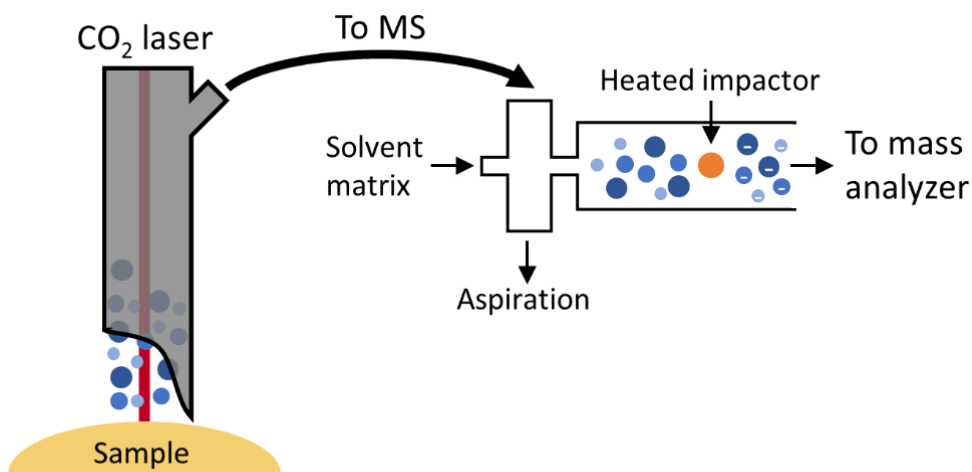


**Figure 1.5:** Simplified LA-REIMS overview for negative ionization mode. A smoke rich with molecules is ablated from a sample using a CO<sub>2</sub> laser. This smoke is aspirated into the mass spectrometer and mixed with a solvent matrix. The molecules are ionized by collision with a heated impactor. The resulting ions are transferred to the mass analyzer.

the type of laser, the laser power, the laser pulse duration, and the laser repetition rate, but also the tissue type.<sup>39,49-51</sup> The damage to the tissue can be separated into two classes: the ablation crater from which the tissue is removed and a zone of heat damage to the surrounding tissue.<sup>49,52,53</sup> In addition, some laser types, including a CO<sub>2</sub> laser, result in the formation of a carbonized layer in the ablation crater.<sup>49,52,53</sup>

## 1.4 Thesis outline

The aim of this thesis is to explore the application of different MS techniques for the analysis of skeletal tissue with a focus on MSI of these tissues. This thesis concentrates on the methodological developments necessary to achieve MSI analyses on skeletal tissue as well as their application in different aspects of skeletal research. The thesis will start with a more extensive explanation of the clinical importance of non-union and PTOA development in Chapter 2, which includes the currently known risk factors and key molecules involved in both fracture healing and cartilage repair, and the main challenges with the prediction of outcome after injury. In addition, Chapter 2 will address the opportunities for MS to contribute to extending the molecular understanding of normal and impaired healing by discussing the current knowledge and challenges of analysis of bone and cartilage tissue using MSI and ambient MS techniques. The optimization of the sample preparation protocol of undecalcified bone tissue for MALDI-MSI will be discussed and this protocol will be used in targeted forensic (methadone and EDDP detection) and untargeted clinical (matrix selection for detection of unknown lipids) applications in Chapter 3. The methodological development for lipid analysis in fracture hematoma with MALDI-MSI and the specific lipid patterns related to different time points after bone fracture will be addressed in Chapter 4. The protocol developed in Chapter 3 will be applied in Chapter 5 for the analysis of lipids using MALDI-MSI in a citrulline supplement study during fracture healing in rats. Furthermore, the analysis of the proteome with LC-MS/MS of these samples will be addressed in Chapter 5. Chapter 6 describes the development and functioning of an automated device for the sampling of a 3D sample surface with LA-REIMS and its application in the creation of 3D molecular distribution images of different types of samples. Chapter 7 is the general discussion, including considerations for the implementation and development into patient care. The impact paragraph (Chapter 8), and English and Dutch summaries (Chapter 9) finalize this thesis.



## Chapter 2: Clinical use of mass spectrometry (imaging) for hard tissue analysis in abnormal fracture healing

# 2

Sylvia P. Nauta

Martijn Poeze

Ron M.A. Heeren

Tiffany Porta Siegel

Clinical Chemistry and Laboratory Medicine (CCLM)

2020; 58(6): 897-913



## 2.1 Abstract

Common traumas to the skeletal system are bone fractures and injury-related articular cartilage damage. The healing process can be impaired resulting in non-unions in 5–10% of the bone fractures and in posttraumatic osteoarthritis (PTOA) in up to 75% of the cases of cartilage damage. Despite the amount of research performed in the areas of fracture healing and cartilage repair as well as non-unions and PTOA, still, the outcome of a bone fracture or articular cartilage damage cannot be predicted. Here, we discuss known risk factors and key molecules involved in the repair process, together with the main challenges associated with the prediction of outcome of these injuries. Furthermore, we review and discuss the opportunities for mass spectrometry (MS) – an analytical tool capable of detecting a wide variety of molecules in tissues – to contribute to extending molecular understanding of impaired healing and the discovery of predictive biomarkers. Therefore, the current knowledge and challenges concerning MS imaging of bone and cartilage tissue as well as *in vivo* MS are discussed. Finally, we explore the possibilities of *in situ*, real-time MS for the prediction of outcome during surgery of bone fractures and injury-related articular cartilage damage.

## 2.2 Introduction

Bone fractures and injury-related articular cartilage damage are common traumas to the skeletal system. A bone fracture is a complete or incomplete break of the anatomical continuation of the bone, resulting in its mechanical instability.<sup>4</sup> Normal fracture healing is a highly complex process involving a well-defined series of biological phases and mechanical requirements (see Figure 1.1).<sup>2,4,5,7,8,10,54</sup> Although these phases are successive, there is great overlap between them, resulting in a continuously changing environment in terms of cell populations and signaling processes.<sup>2</sup> Bone fracture healing normally results in completely functional and structural restoration of the involved bone.<sup>2,55</sup> Due to its complexity, fracture healing is not fully understood in detail, as the exact contribution of different molecules is largely unknown.<sup>2,5,8</sup>

With cartilage injuries, its structures and functions are damaged, which can result in reduced mobility.<sup>18,26,31</sup> Cartilage damage can have different causes, but for posttraumatic osteoarthritis (PTOA) a previous joint injury is the cause.<sup>20,26,29,31</sup> The repair capacity of articular cartilage is extremely limited and, therefore, small surface disruptions do not heal and even worsen over time.<sup>18,19,56</sup> Despite the extracellular matrix (ECM) deposition by chondrocytes, an injury to cartilage will often result in the loss of tissue and the formation of a defect.<sup>18,56</sup> If an increasing defect reaches the underlying bone, scar tissue will be formed in the defect from

the bone (see Figure 1.2).<sup>18,20,23</sup> It is unknown when cartilage damage becomes irreversible and results in progressive damage.<sup>18,56</sup> This is because of the complexity of cartilage interaction with surrounding joint tissues and response to external factors.<sup>19,20,23</sup>

Abnormal healing of the bone and/or articular cartilage can result in long-lasting problems for the patient, such as non-unions and PTOA. The bone fracture healing process is abnormal in 5–10% of fractures, resulting in delayed healing or non-union.<sup>2,4,13,54,57</sup> Nevertheless, the non-union rate differs per anatomical location and per treatment method.<sup>4,9,15</sup> Non-union rates have been published in the range of 3–48% of the bone fractures.<sup>15,58,59</sup> Injury-related cartilage damage can result in PTOA in 10–75% of the cases, depending on the involved joint.<sup>22,29,30</sup> Furthermore, approximately 12% of the osteoarthritis (OA) cases can be assigned to PTOA.<sup>23,26,29,31</sup> Non-unions and PTOA are difficult to predict, diagnose in an early phase, and treat, making them current challenges for surgeons and researchers.<sup>2,4,15,19,20,23,31</sup> Although some key molecules and risk factors associated with abnormal healing are known, these cannot predict the outcome of bone fractures or injury-related cartilage damages.<sup>19,23,25,60</sup> Establishing predictive markers could contribute to early detection (e.g. at the time of the initial surgery) and/or prediction of abnormal healing, which can contribute to earlier and/or new treatment options.

Despite the knowledge of some key molecules in the healing processes, the exact molecular contribution to and interactions with these processes and how these molecules are involved in non-union and PTOA development are still unknown. This lack of knowledge contributes to the clinical challenges related to abnormal fracture healing. Extending the knowledge of molecules involved in abnormal fracture healing can support the development of new prediction, diagnosis, and treatment options. Mass spectrometry (MS) is an analytical technique that is used for an increasing number of applications in clinical research, including cancer research and prediction of cancer treatment outcome.<sup>33,35,61</sup> This technique allows for unlabeled analysis of a wide range of molecules without the need for prior knowledge or labeling; these include metabolites, lipids, peptides, and proteins.<sup>33,35,62-64</sup> Mass spectrometry imaging (MSI) is particularly used in clinical applications to study the distribution of different molecules in tissue sections for, among others, biomarker discovery, diagnosis, and studying the intra-tumor heterogeneity, which has been used to a lesser extent for imaging molecular distributions in bone and cartilage.<sup>35,63,65</sup> Furthermore, intra-operative techniques using MS are being developed mainly for diagnostic purposes in oncology, with one

of the most important advantages being the real-time monitoring of the molecular profile of native tissues.<sup>66-69</sup> The main focus of studies using MSI or intra-operative MS has been on tumor research, showing the potential of MS. The work performed on hard tissues (bone and cartilage) and abnormal fracture healing using MS is limited. Extending this work will provide new molecular insights, which can contribute to a better understanding and prediction of abnormal healing.

This article provides an overview of the current knowledge of delayed fracture healing and non-union development as well as the development of PTOA with a focus on hard tissues (bone and cartilage). Herein, important molecules in the healing processes and diagnostic opportunities will be discussed, which show the current challenges in the prediction of outcome and resulting complications. Lastly, we will discuss the potential for MS to overcome these current clinical challenges, as this technique can contribute to discovery of novel biomarkers and involved processes for development of delayed healing/non-union and PTOA, while it can also be used as a prediction tool for these conditions and make a major leap in patient management.

### 2.3 Delayed healing and non-union

A fracture non-union can be defined as the termination of the fracture healing process without reaching a bone union, while in delayed healing the fracture healing time is longer than expected.<sup>57,59,70-72</sup> Impaired healing can be caused by disturbance of any of the phases in the fracture healing process.<sup>54,70</sup> A lack of consensus between surgeons exists about the definition of a non-union.<sup>2,4,15</sup> Non-union can be defined as no healing in 9 months and no progressive signs of healing in the last 3 months according to the United States Food and Drug Administration.<sup>2,4,57,59,71,72</sup> Nevertheless, there is a great variation in healing time based on different skeletal locations and amount of soft tissue damage.<sup>2,4,72,73</sup>

An often-used classification for non-unions is the differentiation between hypertrophic and atrophic nonunions.<sup>2,57,59,72,74</sup> In a hypertrophic non-union, there is formation of a large callus, but no bony bridging due to instability.<sup>2,57,59,71,74</sup> Hypertrophic non-unions are characterized by their biological potential and can further be divided into elephant foot, horsefoot, or oligotrophic non-union.<sup>4,57,59,71,74</sup> An atrophic non-union shows no to very little callus formation, because of a lack of biological regeneration.<sup>2,57,71,72,74</sup> Damage to the vascularization at the fracture site is often a contributing factor in the development of an atrophic non-union.<sup>2,59</sup>

The general goal of treatment is to achieve a union and return the affected bone to complete functioning.<sup>2,57,59,73</sup> Nevertheless, treatment of non-unions is complex and related to high costs.<sup>57,71-73</sup> The type and location of non-union in combination with the alignment will dictate the best treatment option.<sup>57,71-73</sup> The parameters necessary to achieve are based on the diamond concept: mechanical stability, osteogenic cells, osteoconductive scaffolds, and growth factors, which result in an adequate biological environment when adequate vascularity is present.<sup>4,8,13,57,59,72</sup> These requirements can be reached using different treatment methods or a combination thereof, which can be classified into biological, mechanical, and biophysical treatments.<sup>2,57</sup> Each patient will need an individualized treatment plan to achieve union, due to the unique nature of each non-union.<sup>57,59,73</sup>

Despite the large amount of research performed on fracture healing as well as impaired healing and improvement of treatment, understanding of the causes of non-unions is limited and there is still no accurate way to predict the outcome.<sup>9,15,55,73,75</sup> Nevertheless, there are some known risk factors and essential molecules for the bone fracture healing process. Furthermore, the current diagnostic options will be discussed.

### 2.3.1 Risk factors for non-union development

Although there is still no way to predict the outcome of the fracture healing process, there are some risk factors that can be related to non-union development.<sup>60</sup> One of the most important factors is inadequate vascularization, as disturbance of the blood supply can increase the risk of non-union development.<sup>2,57,60,70,73,74,76</sup> This can be caused by high-energy trauma resulting in extensive soft tissue damage, excessive displacement, and operative treatment at the fracture site.<sup>58,60,70,72,73,76</sup> In addition, the amount of vascularization can be related to the location of the fracture, which can influence its healing process, as delayed unions and non-unions occur mainly in diaphyseal parts of the bone.<sup>2,57,58,60,76</sup> Bones with lower blood supply (e.g. tibia and femoral neck) show higher non-union rates compared to, for example, humeral fractures, which receive higher blood supply.<sup>15,72,76</sup> High-energy trauma and open fractures can result in disruption of the biological environment and/or comminuted bone, which both are risk factors.<sup>4,60,76</sup> Another important factor is instability and/or movement between fracture fragments, as the natural fracture healing process is disturbed.<sup>2,57,58,70,72-74</sup> Other mechanical causes can be displacement and a fracture gap, in which the main fracture fragments are not in contact and the fracture gap is too large to bridge.<sup>2,57-60,70,73,74,76</sup> A contributing risk factor is the quality of the surgical treatment in terms of stabilization and reduction of the fracture gap.<sup>9,57,58,73</sup> In addition, the type of

fracture will also influence the fracture healing process, as unstable complex, comminuted, or segmental fractures have a higher risk of non-union development.<sup>9,55,60,76</sup> A (deep) infection resulting from contamination of an open fracture or as a complication of operation is a risk factor for non-union development.<sup>2,55,57-60,72,73,76</sup> Furthermore, there are some factors that increase the risk of non-union development, but are not the main reason for impaired healing.<sup>54,57,71</sup> These contributing factors include old age, osteoporosis, malnutrition, anemia, alcohol consumption, smoking, genetics, systematic disorders (like diabetes mellitus), multiple trauma or fractures, and certain medications (such as corticosteroids, anticoagulants, chemotherapeutic agents, nonsteroidal anti-inflammatory drugs (NSAIDs), and some antibiotics).<sup>2,9,54,55,57-60,72,73,76</sup> Because of the complexity and interaction between these risks factors, early detection and accurate prediction of the outcome of the healing process remain a challenge.<sup>9,55,60,77</sup> Nevertheless, risk factors and prediction models could allow for early identification and treatment initiation of non-unions.<sup>60</sup>

### 2.3.2 Key molecules involved in bone fracture healing

Multiple classes of molecules have been reported to play a role in the normal bone fracture healing process, and can be divided into three main classes: pro-inflammatory cytokines, growth factors, and metalloproteinases and angiogenic factors.<sup>4,7,10</sup> Several cell types interact in a coordinated way with these molecules in the fracture healing process, including immune cells, bone and cartilage forming primary cells, and muscle mesenchymal stem cells (MSCs).<sup>2,5,7,10,13</sup> Any alteration in local and systemic regulatory molecules can have an effect on the cellular response, which may result in impaired healing.<sup>4,5,8,13</sup> Table 2.1 gives an overview of the molecules that have been shown to be involved in the bone fracture healing process.

Despite the numerous molecules that have been discovered to contribute to the bone fracture healing process, there is still no complete understanding of which of these molecules are essential for the process.<sup>2,10,55</sup> No biomarkers for impaired healing have been used yet in a clinical setting for outcome prediction, as the consequences of the imbalance in the expression of different molecules are largely unknown.<sup>2,55,58,77</sup> Thus, these molecules fail to serve as predictors of non-union.<sup>55,77</sup>

### 2.3.3 Diagnosis and prediction of non-unions

For the diagnosis of non-unions and evaluation of fracture healing, clinicians use mainly clinical, radiographic, and laboratory examinations.<sup>2,55,72,73,77</sup> However, the

**Table 2.1:** Different molecules have been shown to contribute to the repair processes in bone and cartilage.

These molecules have been reported in animal models of bone healing, cartilage damage, or intra-articular fracture as well as knock-out animal models. In addition, some molecules have been shown to differ between healing and non-healing patients groups. For bone healing, the molecules are given that have been shown to have an important role in bone healing. For cartilage damage, the molecules are given that have been shown to contribute to cartilage loss and changing chondrocyte metabolism. Lastly, for intra-articular fractures, some molecules are given that have been shown to be involved in the healing response from the subchondral bone. Although, these molecules have been reported to have an important role in these processes, they are not used in the clinic for prediction of outcome. In addition, some molecules, especially for bone healing, are investigated for therapeutic applications.

<b>Molecules</b>	<b>Bone healing</b>	<b>Cartilage loss</b>	<b>Intra-articular fracture</b>
ADAM metalloproteinase with thrombospondin type 1 motif 4 and 5 (ADAMTS-4 and -5)	-	25,27,56,78,79	-
Angiopoietins 1 and 2	5,7,13	-	-
Bone morphogenetic proteins (BMPs) antagonists	7,13,60	-	-
Noggin	4,7,13,55,60		
Bone morphogenetic protein and activin membrane-bound inhibitor (BAMBI)	4,13,55		
Screlostin	13,55		
Cartilage oligomeric matrix protein	-	27,56,80	-
C-C chemokine receptors (CCRs) and ligands (CCLs), including	-		-
CCR-2		78	
CCR-5		78	
CCL-2		78,80	
CCL-4		78,80	

**Table 2.1 (continued):** Different molecules have been shown to contribute to the repair processes in bone and cartilage.

<b>Molecules</b>	<b>Bone healing</b>	<b>Cartilage loss</b>	<b>Intra-articular fracture</b>
Extracellular matrix molecules and their fragments, including Fibronectin Fibromodulin Collagens Proteoglycans	55 5,55 55 5,70 -	23,25,27,56 27,29,56 - 27,56,79,80 18,29,56,79,80	-
Fibroblast growth factors (FGFs), including FGF-1 FGF-2	2,4,5,7,8,55 7,13 5,7,9,13	18,27,56 - 23	-
Insulin-like growth factors (IGFs)	4,5,7,8,13,55	18,27,56	18,20
Interferon- $\gamma$ (IFN- $\gamma$ )	5	78,80	-
Interleukins (ILs), including IL-1 IL-6	5,8 4,5,7-9,13 4,5,7-9,13	19,25,29,78-80 19,23,25,27,29,78 23,27,78,79	-
Matrix metalloproteinases (MMPs)	5,7,13,55	19,23,25,27,29,56,78-80	-
Nitric oxide	5,55	23,80	-
Osteocalcin (OC)	55	-	-
Osteopontin (OPN)	-	56,80	-
Platelet-derived growth factor (PDGF)	2,4,5,7-9,13,55,60	-	18,20
Prostaglandin E2 (PGE2) and cyclooxygenase-2 (COX-2)	4,5,60,70	-	-
Tenascin-C (TnC)	5	56,78,80	-
Tissue inhibitors of matrix metalloproteinases (TIMPs)	5,13	25,56,79,80	-
Toll-like receptors (TLRs)	-	78	-

**Table 2.1 (continued):** Different molecules have been shown to contribute to the repair processes in bone and cartilage.

<b>Molecules</b>	<b>Bone healing</b>	<b>Cartilage loss</b>	<b>Intra-articular fracture</b>
Transforming growth factor- $\beta$ (TGF- $\beta$ ) superfamily, including Activins	8 2,5,7,13	-	-
Bone morphogenetic proteins (BMPs)	2,4,5,7,9,13,55,70	56	18,20
Growth differentiation factors (GDFs)	4,7,13,55	23,27,29	-
TGF- $\beta$	2,4,5,7,9,13	18,56	18,20
Tumor necrosis factor- $\alpha$ (TNF- $\alpha$ )	4,5,7-9,13,55	19,23,25,27,29,56,78-80	-
Vascular endothelial growth factor (VEGF)	4,5,7-9,13,55	-	-
Wnt signaling pathway	55	-	-

diagnosis of non-unions is often difficult.<sup>4,58,77</sup> Non-unions are diagnosed when they have already established.<sup>9,57,77</sup> Therefore, prediction of outcome and/or detection at the beginning of the fracture healing process would allow for earlier diagnosis, but this is lacking.

The clinical assessment contains documentation of the patient's history and the bone fracture history, as well as a physical examination.<sup>57-59,72,73</sup> The physiological assessment of a non-union can show, among others, pain and tenderness at the fracture site, persistent motion, the inability of complete weight-bearing, and reduced motion in adjacent joints.<sup>57-59,72,73,75</sup>

The radiographic appearance of the fracture is still the gold standard used to confirm the non-union, to determine its classification, and to check the integrity of implants.<sup>57,72,73,77</sup> General radiological signs of non-unions are the absence of bone bridging, persistent fracture lines, the presence of loose or broken implants, lack of progressive healing on serial radiographs, and hypertrophic or absent callus.<sup>9,58,59,75</sup> Furthermore, multiple additional imaging modalities can be helpful, for example, computed tomography (CT), magnetic resonance imaging (MRI), and bone scans.<sup>57-59,72,75,77</sup>

Laboratory evaluations are used to define whether an infection is present as well as to discover metabolic or endocrine abnormalities that can explain the non-union.<sup>57,58,73,75</sup> The laboratory evaluation should include a complete blood count (CBC), erythrocyte sedimentation rate (ESR), and C-reactive protein for the detection of infections as well as tests for the nutritional status when necessary.<sup>57-59,72,75</sup> Nevertheless, these tests have no direct linkage with the bone healing process. A few studies have been performed to analyze biological markers of fracture healing as predictors of impaired healing, for example, transforming growth factor- $\beta$  (TGF- $\beta$ ) and bone morphogenetic proteins (BMPs), but they have not been applied in general clinical practice and sufficient evidence is lacking.<sup>4,13,77</sup>

Despite the diagnostic options available, non-unions can only be diagnosed when they have already been established. Currently, it is not possible to predict the outcome of a bone fracture in the early phase, e.g. during the initial surgery. Early prediction would allow for adaption of treatment, if necessary, preventing non-union development and, thereby, avoiding additional surgeries and long burden for the patient.

## 2.4 Post-traumatic osteoarthritis

PTOA can be defined as the development of OA after a known joint injury causing cartilage degeneration, dysfunction, and pain.<sup>20,26,29,31</sup> In general, PTOA has an earlier onset than OA and, therefore, affects a younger and more active population.<sup>19,23,30</sup> PTOA-causing injuries can be an intra-articular fracture, acute ligament sprain, or instability of ligaments.<sup>25,26,29,30</sup> These injuries can be classified into three groups: (1) joint injury without visible mechanical disruption, but with articular cartilage and possibly subchondral bone damage; (2) joint injury with visible mechanical damage limited to the articular cartilage; and (3) joint injury with visible mechanical damage to the articular cartilage and the subchondral bone.<sup>18,20,23</sup>

In PTOA development, the subchondral bone is of great importance and influence, as its properties affect the articular cartilage and vice versa.<sup>25,81-85</sup> Nevertheless, the relation between bone changes and cartilage degeneration is not well understood.<sup>81-84</sup> It has been shown that cartilage degeneration is associated with increased bone resorption and trabecular bone thinning in the early phase.<sup>81,84,85</sup> On the contrary, in the later phase of OA development, increased bone formation and trabecular bone thickening have been shown.<sup>82-85</sup> Nevertheless, the mineralization of the formed bone reduces with the progression of OA.<sup>82,83,85</sup>

Treatment of cartilage damage should be focused on slowing or preventing the progressive tissue damage in the development of PTOA.<sup>18-20,23</sup> Orthopedic surgeons try to achieve this by restoring the alignment, stability, and congruity of the joint, which is currently the best possible treatment.<sup>22,25,29,30</sup> Nevertheless, joint restabilization does not reduce the risk of PTOA development.<sup>20,22,27,78,86</sup> The treatment should focus on facilitating cartilage repair and remodeling, which is currently clinically unavailable.<sup>18,20</sup> Surgeons can penetrate the subchondral bone to initiate a healing response resulting in fibrocartilage, which fails with time, however.<sup>18</sup> Cartilage repair may also be induced by periosteal or perichondrial grafts, cell transplants, scaffolds, and growth factors, but these methods have not been proven in clinical studies.<sup>18,27</sup> Furthermore, cartilage can be replaced by osteochondral auto- or allografts.<sup>18</sup>

Despite the amount of research performed for PTOA and OA, the reason for PTOA development after a joint injury is still poorly understood.<sup>22,26,29,86</sup> Some risk factors and molecules, which have been defined, will be discussed as well as the current diagnostic options.

### 2.4.1 Risk factors for PTOA development

Cartilage health depends on a combination of biological, mechanical, and structural factors.<sup>19,23,56</sup> Any disturbance in one of these factors, which cannot be compensated for by the other factors, will potentially result in the development of OA.<sup>19</sup>

PTOA cannot be predicted, but some risk factors are known. Certain injuries often result in development of PTOA, including joint impact loading; anterior cruciate ligament (ACL); meniscal, ligament, or joint capsule tears and injuries; joint dislocations; and recurrent joint instability.<sup>19,20,25,26,31,78</sup> One of the major risk factors for the development of PTOA is damage to the chondral surface during injury, which is related to the injury severity.<sup>25,26,29,30</sup> In intra-articular fractures, the underlying subchondral bone is also affected, which increases the risk of PTOA development.<sup>19,26,29,87</sup> The severity of the injury depends on the magnitude, orientation, and rate of the applied force and determines the absorbed energy and mechanical damage to cartilage and the surrounding structures.<sup>18,20,22,23,27</sup> The injury results in chondrocyte death and ECM damage, which contributes to cartilage loss.<sup>23,25,27,29</sup> Nevertheless, Zhang *et al.* suggested that chondrocyte catabolism instead of death results in cartilage degeneration, although the chondrocytes eventually will die.<sup>79</sup> Although mechanical trauma is a major risk factor, it is insufficient to explain all the changes in the cartilage in the unaffected areas.<sup>19,23</sup> Therefore, the severity of the injury is not the only factor that determines whether damaged cartilage will repair or undergo progressive degeneration.<sup>20</sup> After injury and/or surgery, the joint kinematics change, which results in abnormal mechanical loading and contact pressures at the articular cartilage.<sup>20,22,30,87</sup> Thus, chronic joint instability, incongruity, and malalignment contribute to the development of PTOA via abnormal distribution of joint loadings, which is worsened by surface gaps and step-offs.<sup>19,20,22,23,25,26,29,31,87</sup> It has been shown that these increased contact stresses can be related to cartilage thinning.<sup>22</sup> In addition, the biological response to the joint injury, for example, bleeding and inflammation, can lead to the development of PTOA.<sup>27,29,78</sup> Other risk factors of PTOA development are the involved joint, certain bone fracture types and related dislocation, time since injury, genetics, obesity and other co-morbidities, age, gender, muscle weakening, and joint disuse or overuse.<sup>18,19,23,25-27,29,78,88</sup> The relative contribution of each factor is poorly understood as PTOA is considered a multifactorial condition, which makes optimal treatment planning challenging.<sup>22,29,78,86</sup>

### 2.4.2 Key molecules relevant for cartilage health

The molecular pathways involved in the development of PTOA are still mostly unknown, which is mainly due to the complexity of cartilage interaction with surrounding joint tissues and response to external factors.<sup>19,20,23</sup> Inflammatory cytokines and chemokines are two major molecular classes involved in the development of PTOA and interact with chondrocytes and other joint tissue cell types.<sup>19,29,78,80</sup> PTOA development is affected by cytokines and chemokines in both positive and negative ways.<sup>78,80</sup> Cartilage loss is caused by progressive cartilage damage when the catabolic pathway is more active than the anabolic pathway and, therefore, the chondrocytes are unable to restore the damage.<sup>19,20,23,56,87</sup> Table 2.1 gives an overview of the molecules that have been shown to contribute to cartilage loss and to be involved in intra-articular fracture repair.

A number of metabolic changes after a joint injury have been shown, but relating these changes to healthy or pathological joint adaptations is challenging and using them as predictors of clinical outcome is extremely difficult.<sup>19,26,27,56,78,80</sup> Therefore, at the moment, no predictive biomarkers for PTOA are available.<sup>19,23,80</sup>

### 2.4.3 Diagnosis and prediction of PTOA

Early detection of OA-related changes to the cartilage would allow for early intervention, which might prevent the development of end-stage OA.<sup>19</sup> The detection of PTOA (or OA) is very difficult and limited by the lack of symptoms in the early phase.<sup>19,20,23</sup> The variability in the time between injury and the development of PTOA symptoms depending on the severity of the injury and differences between patients is adding to this challenge.<sup>19,23,25</sup> In addition, joint injuries that can cause PTOA are difficult to diagnose and often overlooked in cases of other joint tissue injuries.<sup>18</sup> Therefore, PTOA is often diagnosed after the onset of symptoms based on clinical and radiographic findings, when irreversible damage to the articular cartilage has already occurred.<sup>19,86</sup> This clearly illustrates the need for early detection and prediction before irreversible changes occur.

Radiography and CT scans are often used for the assessment of articular fracture reduction and diagnosis of OA.<sup>29,89</sup> With radiography, OA is diagnosed based on the bone (sclerosis and osteophytes) and cartilage changes as well as reduction of the joint space.<sup>19,80,81,83</sup> CT scans have a higher sensitivity than radiography for articular cartilage assessment, with improved detection of surface gaps, step-offs, and other surface disruptions allowing for estimation of the absorbed energy during injury.<sup>22,23,29,89</sup> Double-contrast CT can be used for the measurement of cartilage thickness to determine areas of cartilage thinning.<sup>22</sup> MRI can be used for the

measurement of, among others, cartilage thickness and the detection of cartilage and bone marrow lesions.<sup>22,25,26</sup> Nevertheless, there is currently no method to measure the extent of cell and matrix damage.<sup>18,20</sup> MRI has been proposed for studying the amount of damage for injuries without visible mechanical disruption.<sup>18</sup>

Biomarkers that can be measured in, for example, blood, urine, or synovial fluid could contribute to early detection of OA, but they are currently not used for diagnosis because of lack of specificity.<sup>19,80,86</sup> Different molecules have been investigated, for example, ECM molecules and inflammation markers, but they have not been applied in general clinical practice, as there is only limited consensus about their predictive value.<sup>19,23,80,86</sup>

PTOA can only be diagnosed when irreversible changes to the articular cartilage have occurred, despite the current diagnostic options. Currently, it is not possible to predict the outcome of injury-related cartilage damage in the early phase, e.g. during the initial surgery. Early prediction would allow for adaption of treatment, if necessary, delaying or even preventing PTOA development and, thereby, avoiding additional surgeries and long burden for the patient.

## 2.5 Mass spectrometry imaging

A method is required that provides detailed molecular and spatial information to understand the molecular and structural changes in bone and cartilage during impaired healing. The spatial information also provides insight into the interaction of these affected areas with surrounding tissues. MSI is a widely used technique for the analysis of a broad variety of molecules in tissue slices, including metabolites, drugs, lipids, peptides, and proteins while maintaining their spatial integrity.<sup>33,35,62-64</sup> The advantages over traditional histopathological methods, such as immunohistochemistry (IHC), are rapid simultaneous detection and identification of a wide variety of molecules in complex biological tissues without the use of targeted labels.<sup>33,35,63</sup> In clinical research, MSI has been employed for biomarker discovery, tissue classification, and prediction of outcome.<sup>35,63,65</sup>

The general workflow for MSI consists of sample preparation, MSI data acquisition, and data processing and visualization (see Figure 2.1).<sup>33,63</sup> Sample preparation depends partly on the ionization technique used, but for all of these techniques, tissue sections need to be cut and mounted on a flat support, such as glass slides, for analysis.<sup>63</sup> The glass slide is placed in a mass spectrometer and the molecules from the tissue are desorbed and ionized with an appropriate ionization technique during MSI data acquisition.<sup>33,35,63</sup> The ionized molecules are subsequently analyzed

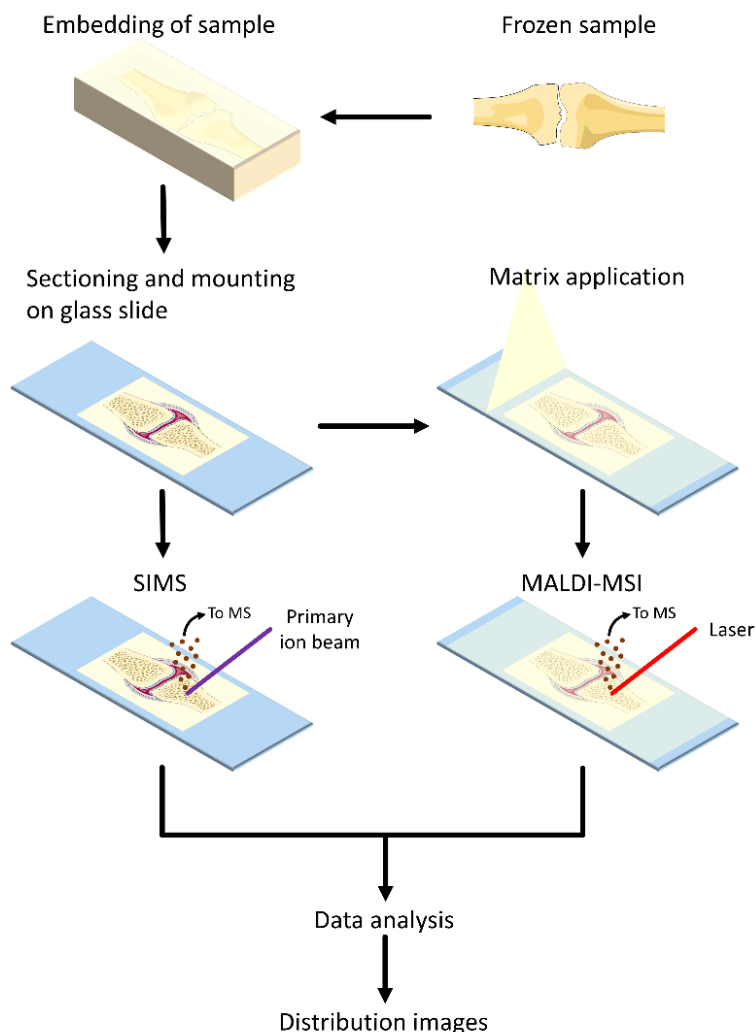


**Figure 2.1:** General mass spectrometry imaging workflow. The sample is collected and stored frozen until use. For hard tissue samples, the tissue is embedded in an embedding material, which supports sectioning. After embedding, the sample is sectioned and mounted on a glass slide. For secondary ion mass spectrometry (SIMS), a primary ion beam shoots at the sample and secondary ions are created from the sample, which are analyzed by the mass spectrometer (MS). For matrix-assisted laser desorption/ionization mass spectrometry imaging (MALDI-MSI), first, a matrix is applied on the sample to support ion generation. Afterward, a laser shoots at the sample and generates ions, which are analyzed by the MS. Per pixel in the image, a mass spectrum is created of the generated ions. After data processing and analysis, distribution images of mass-to-charge values ( $m/z$ ) can be created.

based on their mass-to-charge ratio ( $m/z$ ), which results in a complete mass spectrum per pixel.<sup>35</sup> Distribution images can be created for specific molecules based on the intensities of corresponding  $m/z$  values per pixel, often after data reduction and/or the removal of artifacts.<sup>35,62,63</sup>

Numerous surface sampling and ionization techniques exist, which have been reviewed elsewhere.<sup>33,35</sup> The techniques that have been specifically employed for MSI of hard tissue are matrix-assisted laser desorption/ionization (MALDI) and secondary ion mass spectrometry (SIMS) (see Table 2.2).<sup>90</sup> MALDI requires a matrix to be deposited on the tissue section during sample preparation to support the desorption and ionization of the molecules from the tissue after exposure to laser radiation.<sup>33,35,62,63</sup> SIMS utilizes the generation of secondary ions created and ejected from the tissue by sputtering its surface with a focused primary ion beam.<sup>33,35</sup> SIMS can be used for the analysis of the elemental and mineral distribution in tissue sections, as well as small ( $<m/z$  1000) inorganic and organic molecules, like lipids and peptides.<sup>35,91-96</sup> The sensitivity of this technique for the mass range above  $m/z$  1000 is reduced as most larger organic ions will fragment as a result of the energetic impact of the primary ion beam.<sup>33,93</sup> These fragments of larger molecules can, in selected cases, be informative on the surface composition nevertheless.<sup>33,93</sup> The analytical possibilities of MALDI are broader and range from the analysis of small molecules such as metabolites to larger (intact) proteins, including also lipids, peptides, and glycans.<sup>33,35,63</sup> The spatial resolution of SIMS is higher (down to 50 nm) than the current achievable spatial resolution with MALDI (commonly down to 10  $\mu\text{m}$ ).<sup>33,35,90,94,95</sup>

The application of MALDI-MSI to the analysis of hard tissues (e.g. bone and cartilage) is very limited so far, due to the complex sample preparation and the lack of appropriate protocols.<sup>65,97</sup> As bone consists of both hard and soft tissue parts (i.e. the calcified matrix and bone marrow, respectively), bone sectioning is very challenging.<sup>90</sup> Therefore, bone is often decalcified and/or dehydrated during the sample preparation to simplify the sectioning and to remove the interference of hydroxyapatite crystals in the determination of the molecular distributions in MALDI-MSI.<sup>90,97</sup> During sample preparation for SIMS and sometimes for MALDI, the necessary fixation and dehydration causes substantial chemical changes to the tissue, such as the removal of phospholipids.<sup>90,96</sup> However, decalcification and removal of interfering molecules are highly undesirable when the molecular distribution needs to be related to the *in vivo* situation, for example, for intra-operative applications. The importance of embedding a hard tissue sample to keep

**Table 2.2:** Comparison of different mass spectrometry techniques useable on hard tissue, namely secondary ion mass spectrometry (SIMS), matrix-assisted laser desorption/ionization mass spectrometry imaging (MALDI-MSI), and rapid evaporative ionization mass spectrometry (REIMS).

Mass spectrometry technique	Useable for analysis of hard tissue (bone, cartilage)	Spatial resolution	Molecular classes	Strengths	Limitations
SIMS	Yes	Down to 50 nm	Elementals, minerals, metabolites, lipids	<ul style="list-style-type: none"> <li>- High spatial resolution</li> <li>- Detection of minerals</li> </ul>	<ul style="list-style-type: none"> <li>- Limited molecular range</li> <li>- Long measurement times</li> </ul>
<i>Ex vivo</i> MALDI-MSI	Yes, only recently applied	Down to 10 µm	Metabolites, lipids, peptides, proteins, glycans	<ul style="list-style-type: none"> <li>- Broad molecular range</li> <li>- Simultaneous detection of wide variety of molecules</li> </ul>	<ul style="list-style-type: none"> <li>- Not widely applied on hard tissues</li> <li>- Possible interference of salts and minerals</li> </ul>
<i>In vivo</i> REIMS	Only for a laser coupled to REIMS	Depending on sampling tool, typically in mm range	Mainly lipids and lipid fragments	<ul style="list-style-type: none"> <li>- Near real-time feedback to the surgeon</li> <li>- No sample preparation</li> </ul>	<ul style="list-style-type: none"> <li>- Invasive technique</li> <li>- Limited molecular range</li> </ul>

the structural composition has been shown, especially when soft tissue surrounds the bone or cartilage, or for diseased bone.<sup>33,63,90,93,98</sup> While sectioning, applying adhesive tape to the sample can contribute to maintaining the structural composition and spatial integrity of the hard tissue.<sup>33,90,98</sup> Despite the challenges in sample preparation of native hard tissue, analysis of these tissue types is essential for the understanding of impaired healing.

### 2.5.1 Mass spectrometry imaging of bone

Most of the research performed with MSI on bone has been performed with time-of-flight (ToF) SIMS, but more recent literature reports the application of MALDI-MSI. The limited number of studies applying MS proteomics methods on bone did not use MSI, as they were either applied to cell cultures and ECM, or blood products.<sup>99</sup> One of these studies was focused on bone fracture healing, in which Grgurevic *et al.* showed that the detected proteins were involved in cell growth and proliferation, transport, and coagulation using liquid chromatography-MS.<sup>100</sup>

#### 2.5.1.1 ToF-SIMS imaging of bone

One of the application fields of ToF-SIMS is to study bone mineralization in relation to, among others, fracture healing, bone-implant interaction, and disturbances of minerals (see Figure 2.2A).<sup>101</sup> This is mainly due to the high sensitivity of SIMS for elements and elemental and molecular distributions of, for example, Ca, P, PO<sub>2</sub>, and PO<sub>3</sub>. In addition, different fragments of hydroxyapatite and collagen have been reported.<sup>91,92,95,101,102</sup>

Different studies have used ToF-SIMS on bone tissue to study its elemental and molecular composition. In osteoporotic animal models, ToF-SIMS was used to show decreasing trabecular number and thickness, and declining cortical bone based on calcium and collagen distribution.<sup>91,95</sup> For quantification of the calcium content, calcium hydroxyapatite scaffolds have been used in a rat model with encouraging results, although quantification was affected by the surface properties of the standards.<sup>92</sup> Furthermore, the bone-titanium implant interaction has been studied with ToF-SIMS, showing higher mineralization around the implant after a longer time period and specific molecules for bone tissue, the implant, and the interface.<sup>96,102</sup> Multiple studies have researched the effect of a strontium-enriched calcium phosphate cement on fracture healing on healthy and osteoporotic bone.<sup>94,103-105</sup> It was shown that this implant improved bone formation and strontium could be found in the newly formed bone as well as pre-existing tissue as strontium diffused up to 6 mm from the implant.<sup>94,103-105</sup>

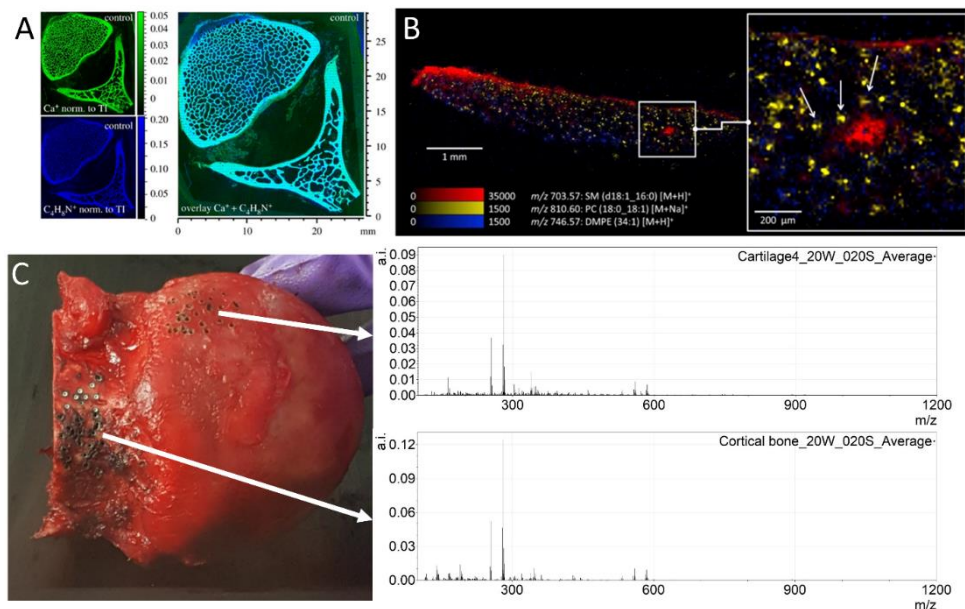


**Figure 2.2:** Examples of application of mass spectrometry for the direct analysis of hard tissues, namely ToF-SIMS on bone, MALDI-MSI on cartilage, and  $\text{CO}_2$  laser coupled to REIMS on bone and cartilage. **A** ToF-SIMS image of healthy sheep vertebra showing  $\text{Ca}^+$  (inorganic compound),  $\text{C}_4\text{H}_8\text{N}^+$  (organic compound), and overlay of the selected  $m/z$  values. ToF-SIMS measurement was performed with a  $\text{Bi}^{3+}$ -primary ion beam and a lateral resolution of 10  $\mu\text{m}$ . Reprinted with permission from Müller *et al.*<sup>95</sup> **B** MALDI-MSI image of osteoarthritic cartilage showing an overlay image of SM ( $d18:1\_16:0$ ) in the damaged superficial part of the tissue, PC ( $18:0\_18:1$ ) specific for chondrocytes, and DMPE ( $34:1$ ) in the matrix of the tissue. The arrows point at chondrocyte pellets. MALDI-MSI image was taken at a spatial resolution of 15  $\mu\text{m}$ . Reprinted with permission from Barré *et al.*<sup>106</sup> **C** Mass spectra for the mass range  $m/z$  500–1200 obtained from a human femoral head with a  $\text{CO}_2$  laser (continuous wave with a laser power of 20 W with a pulse duration of 0.20 s) coupled to REIMS from cartilage (top) and cortical bone (bottom).

### 2.5.1.2 MALDI-MSI of bone

A few studies have shown the opportunity of using MALDI-MSI on bone tissue. Chughtai *et al.* studied lipids, peptides, proteins in bone, muscle, and skin from a limb of a mouse model with rheumatoid arthritis (RA) using both ToF-SIMS and MALDI-MSI.<sup>65</sup> With this multimodal approach, they showed the localization of proteins involved in inflammation in different regions related to the effect of RA on the tissues.<sup>65</sup> Fujino *et al.* compared different fixation and decalcification methods for the preparation of bone samples for MALDI and concluded that sections from trichloroacetic acid-treated samples were the most suitable.<sup>97</sup> Nevertheless, no

## Clinical use of mass spectrometry (imaging) in abnormal fracture healing

significant differences between the obtained mass spectra were observed between bones that were decalcified, fixed, or both.<sup>97</sup> Svirkova *et al.* showed the combination of MALDI-MSI and micro X-ray fluorescence ( $\mu$ XRF) to study the lipid (focus on sphingomyelins and phosphatidylcholines) as well as the elemental composition of bone and surrounding soft tissue without tissue decalcification.<sup>98</sup> They were able to combine the elemental distribution obtained from the undecalcified tissue ( $\mu$ XRF) with the lipid distribution of the surrounding soft tissue (MALDI-MSI).<sup>98</sup> Atmospheric-pressure scanning microprobe MALDI (APS-MALDI) and ToF-SIMS have been applied on undecalcified human bone sections by Schaepe *et al.*<sup>90</sup> They showed the lateral localization of different major lipid classes, including glycerolipids, glycerolphospholipids, and sphingolipids.<sup>90</sup> Signals specific for the hard part of the bone as well as the bone marrow were found with ToF-SIMS.<sup>90</sup> With APS-MALDI, a hydroxyapatite fragment could be found in the mineralized tissues as well as different triacylglycerols in the bone marrow.<sup>90</sup>

The recent developments in the usage of MALDI-MSI on bone tissue show the opportunities of this technique for the application in the impaired healing research on bone, allowing for the discovery of a wide range of molecules that could be linked to impaired molecular pathways.

### 2.5.2 Mass spectrometry imaging of cartilage

Several MSI studies have been performed on cartilage, but most studies use electrospray ionization or liquid chromatography-MS/MS. These methods have been used to study mainly proteins, peptides, and lipids in cartilage, other joint tissues, serum, and synovial fluid. The MSI studies mainly employed ToF-SIMS and MALDI for the analysis of cartilage and other joint tissues.<sup>63</sup>

#### 2.5.2.1 ToF-SIMS imaging of cartilage

With ToF-SIMS, osteoarthritic and healthy human cartilage were studied and showed that these two types of cartilage could be distinguished by specific peaks.<sup>107</sup> Furthermore, colocalization of cholesterol and other lipids in lipid droplets was seen in the superficial area of the cartilage, with a similar localization of fatty acids in osteoarthritic cartilage.<sup>107</sup> Calcium and phosphate ions were observed in the areas surrounding chondrocytes in osteoarthritic cartilage.<sup>107</sup>

#### 2.5.2.2 MALDI-MSI of cartilage

In a study on peptides and proteins in human healthy and osteoarthritic cartilage using MALDI-MSI, osteoarthritic-specific peptides and proteins were found with a higher intensity in the deep cartilage.<sup>62</sup> Distinctive peptides for OA included fibronectin, cartilage oligomeric matrix protein, and fibromodulin.<sup>62</sup> The peptides

of young, old, and osteoarthritic equine cartilage showed different profiles between the groups using MALDI-MSI.<sup>108</sup> Increased intensities of fibronectin peptides and decreased intensities of fibromodulin peptides were seen in osteoarthritic cartilage, while collectin-43 and cartilage oligomeric matrix protein were age-specific.<sup>108</sup> Recently, in a MALDI-MSI study about the lipid distribution in human osteoarthritic cartilage, the superficial layer and the cartilage layer could be distinguished by specific molecules, but more interestingly a phosphatidylcholine was found to be specific for chondrocyte cluster cells (see Figure 2.2B).<sup>106</sup> Furthermore, N-glycans have been studied in cartilage and bone marrow with MALDI-MSI, as the subchondral bone is affected by OA by bone marrow lesions.<sup>109</sup> Different N-glycans showed different distributions over the cartilage and bone marrow, with a high mannose N-glycan being prominent in osteoarthritic cartilage and a disialylated biantennary complex glycan was prominent in bone marrow of the patient with bone marrow lesion stage 1.<sup>109</sup> The distribution of triamcinolone acetonide (TAA) in cartilage was shown for sample submerged in TAA with MALDI-MSI using an essential derivatization step.<sup>110</sup>

MALDI-MSI has already been applied to cartilage to study a wide range of molecules, including lipids and peptides, although most research is applied on late osteoarthritic tissue. Applying this technique to impaired healing research on cartilage could contribute to a better understanding of, among others, the early phase of PTOA.

### **2.6 Ambient ionization mass spectrometry and the potential toward *in vivo* tissue evaluation**

The development of ambient ionization techniques opened up the possibility to employ MS for *in vivo* tissue analysis, evaluating metabolic and lipid composition and changes.<sup>66-68,111</sup> An advantage of the *in vivo* application of MS is the near real-time evaluation of the tissue with minimal sample preparation.<sup>66-68,111,112</sup> The instant availability of complex molecular information allows for improved decision-making by surgeons.<sup>68,112</sup> The ideal *in vivo* technology should have a high clinical sensitivity and specificity and low invasiveness. Therefore, these *in vivo* techniques have the potential to be employed for the early prediction of non-unions and PTOA during the initial surgery. Existing or new surgical handpieces are connected to a mass spectrometer for the evaluation of the molecular profile of the tissue for future *in vivo* intra-operative MS-based diagnostic techniques. The development of these *in vivo* techniques focuses on the ablation and ionization of minimal amounts of molecules from the tissue that are analyzed by a mass spectrometer.<sup>68</sup> This ionization method allows for the analysis of living tissue in its native environment

while creating tissue-specific mass spectra, which is considered its major advantage.<sup>48</sup> These techniques currently result in mass spectra that predominantly contain lipids and their fragments.<sup>66,111,112</sup> Different techniques have been coupled to MS systems, including the electrocautery, different laser-based techniques, and others. Table 2.3 gives an overview of the studies performed with these techniques, which are reviewed below.

### 2.6.1 Electrocautery

Electrocautery combined with rapid evaporative ionization MS (REIMS) for rapid, *in situ* profiling has been mainly used for cancer research and tumor margin assessment (see Table 2.3).<sup>64,68,111,113</sup> The coupling of electrocautery with REIMS is often referred to as the intelligent Knife (iKnife).<sup>64,68,111,113</sup> With this approach, electrocautery is used for cauterizing and cutting of the tissue resulting in aerosol-rich smoke containing aerosolized molecules, which is transported to the mass spectrometer via a tube using a Venturi pump.<sup>46,61,64,113-115</sup> The basis for this technique is rapid thermal evaporation of biological tissue by, for example, electrocautery resulting in the formation of gaseous ions.<sup>35,46,48,64,111,113,115</sup> Several research groups have shown that different tissues show different and characteristic mass spectra of specific lipid patterns allowing for differentiation between healthy and cancer tissue, different tumor grades, and tumor necrosis.<sup>46,48,64,113-115</sup> In general, these studies show high accuracy (range 74.7–97%), sensitivity (range 78.6–97.7%), and specificity (range 89.7–100%) (see Table 2.3).<sup>46,64,113-116</sup> Although most of the research is currently performed *ex vivo*, the usage of the electrocautery-REIMS has also been tested *in vivo*.<sup>46,64,114,115</sup>

In a similar manner, Balog *et al.* used electrosurgical dissection via an endoscopic polypectomy snare connected to REIMS for the classification of gastrointestinal tract tissue.<sup>116</sup> This technique was able to differentiate between healthy intestinal wall tissue, colorectal cancer, and adenomatous polyps.<sup>116</sup>

### 2.6.2 Laser-based methods

Laser ablation of tissues has shown to result in characteristic ion patterns and combined with MS could be used for the near real-time *in vivo* identification of tissues.<sup>39,112</sup> For this, both ultraviolet and infrared lasers have been used, whereby the CO<sub>2</sub> laser is the most common employed infrared laser in surgical procedures.<sup>39,68,111,112</sup>

Schäfer *et al.* used laser desorption/ionization mass spectrometry (LDI-MS) for the *ex vivo* analyses of biological tissues comparing different ultraviolet and infrared

**Table 2.3:** Overview of studies performed with mass spectrometry (MS) techniques that have the potential to be used *in vivo* during operation.

The samples used in the studies all are fresh and/or fresh frozen tissue. Only the on-tissue studies are listed and per study the most important *ex vivo* results are given. If *in vivo* experiments with the technique were performed, this information is provided as well. The results are predominately based on measurement of the molecules in the lipid mass range. For the different *in vivo* MS techniques, databases are built up based on which validation or prediction models are generated. For these models, the accuracy, sensitivity, and specificity of classification into the different groups are provided if reported.

Author (year)	Sampling tool	Samples	Ex vivo results	In vivo experiments
Balog, <i>et al.</i> (2010) <sup>46</sup>	Electrocautery CO <sub>2</sub> -laser	Porcine organs, rat model, canine, and human samples.	<ul style="list-style-type: none"> <li>- Tissue classification rates were higher than 97% for organ identification.</li> <li>- Mass spectra obtained with infrared laser ablation and electrocautery showed high similarity.</li> </ul>	<i>In vivo</i> analysis of rat model showed that the mass spectra of various tissues were independent of nutritional fatty acid intake.
Schäfer, <i>et al.</i> (2011) <sup>117</sup>	Cavitron ultrasonic surgical aspirator (CUSA)	Porcine organs, human brain samples (also with tumors), and liver cancer tissue.	<ul style="list-style-type: none"> <li>- Mass spectra from gray and white matter showed characteristic differences.</li> <li>- Good separation was shown between healthy and cancer tissues as well as between different brain tumor types.</li> <li>- <i>Ex vivo</i> validation resulted in correct classification rate of 100% for glioblastoma multiform and healthy brain tissue, partly because of the small sample size</li> </ul>	Not performed.

**Table 2.3 (continued):** Overview of studies performed with MS techniques that have the potential to be used *in vivo* during operation.

<b>Author (year)</b>	<b>Sampling tool</b>	<b>Samples</b>	<b>Ex vivo results</b>	<b>In vivo experiments</b>
Schäfer, <i>et al.</i> (2011) <sup>39</sup>	Ultraviolet and infrared lasers	Porcine human carcinoma, and canine tissue.	<ul style="list-style-type: none"> <li>- The reproducibility of the spectra obtained with the CO<sub>2</sub>-laser was higher than those obtained with the ultraviolet (Nd:YAG) laser, with correct classification rates of 82-95% and 55-70%, respectively.</li> <li>- The obtained spectra showed high similarity with spectra obtained with electrocautery.</li> <li>- Tissue identification of various tissues using the CO<sub>2</sub>-laser resulted in 96-99% accuracy.</li> </ul>	<i>In vivo</i> analysis of canine tissue showed high similarity between <i>ex vivo</i> and <i>in vivo</i> data, with the main difference caused by the presence of blood.
Balog, <i>et al.</i> (2013) <sup>115</sup>	Electrocautery	Human cancer and healthy tissue of different regions; stomach, colon, liver, lung, breast, brain, and others.	<ul style="list-style-type: none"> <li>- <i>Ex vivo</i> analysis of solid tumors showed complete separation between different tumor types.</li> <li>- The origin of metastatic tumors could be identified <i>ex vivo</i> as well as <i>in vivo</i>.</li> </ul>	Electrocautery was used during 81 resections, resulting in an accuracy of 96.2% with a sensitivity of 97.7% and specificity of 96.5% for different cancer types.
Balog, <i>et al.</i> (2015) <sup>116</sup>	Electrocautery via an endoscopic polypectomy snare	Human colonic adenocarcinoma, healthy colonic mucosa, and adenomatous polyps.	<ul style="list-style-type: none"> <li>- Differentiation was possible between healthy intestinal wall tissue, colorectal cancer, and adenomatous polyps.</li> </ul>	The method was tested in three patients and was used for diagnosis.

**Table 2.3 (continued):** Overview of studies performed with MS techniques that have the potential to be used *in vivo* during operation.

<b>Author (year)</b>	<b>Sampling tool</b>	<b>Samples</b>	<b>Ex vivo results</b>	<b>In vivo experiments</b>
Fatou, <i>et al.</i> (2016) <sup>61</sup>	SpiderMass	Bovine liver, human normal and cancer ovarian tissue, and human skin.	- Different mass spectra were obtained from healthy and normal ovarian tissue.	<i>In vivo</i> analysis was done on human skin and showed different lipid profiles between men and women and for treatment with hand cream.
Alexander, <i>et al.</i> (2017) <sup>114</sup>	Electrocautery	Human colorectal cancer and colonic adenomas.	- Cross-validation of the classification model for cancer vs. adenomas resulted in an overall accuracy of 94.4% with a sensitivity of 78.6% and specificity of 97.3% for the adenomas. - Classification based on tumor histological subtype, tumor stage, and lymphatic involvement resulted in overall accuracies of 90.0%, 74.7%, and 83.5%, respectively.	Electrocautery was used in 5 patients and showed that the lipids identified with <i>ex vivo</i> analysis could be captured in near real-time.
St John, <i>et al.</i> (2017) <sup>64</sup>	Electrocautery	Human breast cancer and healthy tissue.	- Cross-validation of <i>ex vivo</i> classification model resulted in an overall accuracy of 94.4% with a sensitivity of 93.4% and specificity of 94.9%. - <i>Ex vivo</i> validation of the classification model resulted in an overall model accuracy of 95.8% with a sensitivity of 90.9% and specificity of 98.8%.	Electrocautery was used in 6 case studies, resulting in an interpretation of 99.27% of the obtained spectra during surgery.

**Table 2.3 (continued):** Overview of studies performed with MS techniques that have the potential to be used *in vivo* during operation.

<b>Author (year)</b>	<b>Sampling tool</b>	<b>Samples</b>	<b>Ex vivo results</b>	<b>In vivo experiments</b>
Woolman, <i>et al.</i> (2017) <sup>118</sup>	Picosecond InfraRed (PIRL)	Mouse breast cancer model and other mouse tissue.	<ul style="list-style-type: none"> <li>- High reproducibility of the mass spectra between animals.</li> <li>- Good separation of different tissue types.</li> <li>- The presence of different necrosis and cancer markers in metastatic breast tumors was shown.</li> </ul>	Not performed.
Woolman, <i>et al.</i> (2017) <sup>119</sup>	PIRL	Murine xenografts of two medulloblastoma subtypes.	<ul style="list-style-type: none"> <li>- The medulloblastoma subgroups showed significantly different mass spectra.</li> <li>- A subgroup determination success rate of 98% was achieved.</li> <li>- Cross-validation of the classification model resulted in a correct prediction rate of 94%, with no misclassification.</li> </ul>	Not performed.

**Table 2.3 (continued):** Overview of studies performed with MS techniques that have the potential to be used *in vivo* during operation.

<b>Author (year)</b>	<b>Sampling tool</b>	<b>Samples</b>	<b>Ex vivo results</b>	<b>In vivo experiments</b>
Zhang, <i>et al.</i> (2017) <sup>120</sup>	MasSpec Pen	Human normal and cancer (breast, lung, thyroid, and ovary) tissues, and mouse normal and cancer tissue.	<ul style="list-style-type: none"> <li>- Ex vivo analysis resulted in an overall accuracy of 96.3% with a sensitivity of 96.4% and specificity of 96.2% for the four cancer types.</li> <li>- Different subtypes of lung and thyroid cancer could be separated with accuracies of 93.8%, 92.2%, 94.7%, and 97.8% for squamous cell carcinoma (lung), adenocarcinoma (lung), follicular thyroid adenoma, and papillary thyroid carcinoma, respectively.</li> </ul>	<i>In vivo</i> analysis was performed on a mouse model and showed no macroscopic or microscopic observable tissue harm. Cancer tissue showed a distinctive profile from the normal soft tissue.
Phelps, <i>et al.</i> (2018) <sup>113</sup>	Electrocautery	Human normal, ovarian cancer, and borderline ovarian tumor.	<ul style="list-style-type: none"> <li>- Cross-validation of a classification model for normal vs. ovarian cancer resulted in an accuracy of 97.6% with a sensitivity of 97.4% and specificity of 100%.</li> <li>- Cross-validation of a classification model for ovarian cancer vs. borderline ovarian tumors resulted in accuracies ranging from 90.0 to 93.5% with a sensitivity of 90.5% and specificity of 89.7%.</li> <li>- Validation with fresh tissue resulted in an overall accuracy of 99.1%.</li> </ul>	Electrocautery was used on 45 tissue samples of 6 patients and provided high-quality mass spectra.

**Table 2.3 (continued):** Overview of studies performed with MS techniques that have the potential to be used *in vivo* during operation.

Author (year)	Sampling tool	Samples	Ex vivo results	In vivo experiments
Saudemont, et al. (2018) <sup>121</sup>	SpiderMass	Canine soft tissue sarcomas, and normal tissue.	<ul style="list-style-type: none"> <li>- Cross-validation of the classification model for normal and cancer resulted in a correct classification rate of 99.94% for positive mode and 97.63% for negative mode.</li> <li>- Cross-validation of the classification model for normal, cancer, and necrosis resulted in a correct classification rate of 99.06% for positive mode.</li> <li>- <i>Ex vivo</i> validation did not show classification failures and class similarity values above 91%.</li> <li>- Different tumor grades and subtypes could be differentiated.</li> </ul>	The instrument was used <i>in vivo</i> on dog patients to confirm the low invasiveness.
Genangeli, et al. (2019) <sup>38</sup>	Electrocautery CO <sub>2</sub> -laser	Bone, bone marrow, cartilage, fat, liver, muscle, skin of different animals.	<ul style="list-style-type: none"> <li>- Compared to electrocautery, the CO<sub>2</sub>-laser resulted in less tissue damage, higher reproducibility, and improved quality in mass spectra.</li> <li>- Tissue classification models based on mass peaks that are tissue-specific and common between electrocautery and CO<sub>2</sub>-laser improved the correct classification rate.</li> <li>- The CO<sub>2</sub>-laser was used on hard tissues (bone, bone marrow, cartilage) resulting in lipid-rich signals.</li> </ul>	Not performed.

**Table 2.3 (continued):** Overview of studies performed with MS techniques that have the potential to be used *in vivo* during operation.

<b>Author (year)</b>	<b>Sampling tool</b>	<b>Samples</b>	<b>Ex vivo results</b>	<b>In vivo experiments</b>
Sans, <i>et al.</i> (2019) <sup>122</sup>	MasSpec Pen	Human ovarian, fallopian tube, and peritoneum tissue sample, including cancerous tissue.	<ul style="list-style-type: none"> <li>- The classification model for serous carcinomas (high- and low-grade) and normal tissue showed an accuracy of 92.3% with a sensitivity of 91.7% and specificity of 92.9%.</li> <li>- The classification model for high-grade serous carcinomas, low-grade serous carcinomas, and normal tissue showed an overall accuracy of 97.7%.</li> <li>- Ovarian cancer could be distinguished from healthy fallopian tube and peritoneum.</li> <li>- The obtained mass spectra where highly comparable between mass spectrometers with different resolving powers.</li> </ul>	Not performed.
Woolman, <i>et al.</i> (2019) <sup>123</sup>	PIRL	Human medulloblastoma of four different subgroups.	<ul style="list-style-type: none"> <li>- The medulloblastoma subgroups could clearly be separated.</li> <li>- Cross-validation of the classification model resulted in a misclassification rate of 4.2% and 5.8% of the data was unclassifiable.</li> <li>- <i>Ex vivo</i> validation resulted in a correct classification rate of 98.9%, in which failed classifications were explained by high amounts of stroma and sample damage.</li> </ul>	Not performed.

lasers.<sup>39</sup> The reproducibility of the spectra obtained with the CO<sub>2</sub> laser was higher than of those obtained with the ultraviolet (Nd:YAG) laser, resulting in high accuracies for tissue identification with the CO<sub>2</sub> laser (see Table 2.3).<sup>39</sup> The mass spectra generated with the CO<sub>2</sub> laser differed considerably between the two modes of the laser (continuous wave and pulsed mode) and was associated with the different laser powers.<sup>39</sup> This indicates that laser-tissue interaction differs per mode and, therefore, should be optimized per tissue type and clinical application. The obtained spectra showed high similarity with spectra obtained with electrocautery, suggesting similar ion formation mechanisms, which was confirmed by Balog *et al.*<sup>39,46</sup> Genangeli *et al.* showed that the quality and reproducibility of the mass spectra obtained with the CO<sub>2</sub> laser coupled to REIMS were higher compared to electrocautery.<sup>38</sup> In addition, the CO<sub>2</sub> laser enabled to generate a lipid-rich signal from hard tissues, i.e. bone, bone marrow, and cartilage.<sup>38</sup> An example of the mass spectra obtained from hard tissues is provided in Figure 2.2C. The use of the CO<sub>2</sub> laser has been tested *in vivo*.<sup>39</sup>

Fatou *et al.* developed an *in vivo* near real-time analysis technique, named the SpiderMass, which uses resonant infrared laser ablation (RIR-LA) for the production of mainly lipid ions.<sup>35,61,121</sup> Different signals could be obtained for normal, cancer, and necrotic tissue and high correct classification rates have been shown (see Table 2.3).<sup>61,121</sup> The minimal invasiveness of this technique was shown *in vivo* on human skin and canine tissue, although the technique can result in local dehydration of the tissue.<sup>61,121</sup>

Woolman *et al.* developed a handheld sampling probe using picosecond infrared laser (PIRL) ablation MS for the sampling of tissue with minimal thermal damage and tissue removal.<sup>118</sup> In different studies,  $m/z$  values in the signal were identified, which belonged to fatty acids, ceramides, and (fragments of) phospholipids, including phosphatidic acids, phosphatidylethanolamines, and phosphatidylcholines.<sup>118,119,123</sup> *Ex vivo* studies using PIRL showed good separation of tissue types and medulloblastoma subgroups with high classification rates (see Table 2.3).<sup>118,119,123</sup> PIRL combined to MS has not been used *in vivo* yet.

### 2.6.3 Other techniques

Schäfer *et al.* combined a cavitron ultrasonic surgical aspirator (CUSA), which uses ultrasound for the disintegration of tissue, to sonic-spray ionization MS.<sup>112,117</sup> A clear differentiation could be made between different tissues and tumor types (see Table 2.3).<sup>117</sup> With this technique, besides lipid-related ions, the spectra also contained ions of metabolic constituents, carbohydrates, and peptides.<sup>117</sup> The

combination of CUSA with MS has not been used *in vivo* yet, but is expected to give similar results.<sup>117</sup>

The MasSpec Pen extracts molecules (metabolites, lipids, and proteins) from the tissue via a water droplet, which is analyzed in a mass spectrometer.<sup>120,122</sup> This device allows for the rapid and nondestructive analysis of tissue, independently of the tissue shape and rigidity.<sup>120</sup> The MasSpec Pen has been shown to be able to differentiate between different tissue types and cancer and normal tissue with high accuracy, sensitivity, and specificity (see Table 2.3).<sup>120,122</sup> No visible tissue damage was observed in the *in vivo* testing of the MasSpec Pen.<sup>120</sup>

### 2.6.4 Implementation and limitations

Although each potential *in vivo* MS technique has its own application field, only a CO<sub>2</sub> laser coupled to REIMS has recently been used on bone and cartilage (see Table 2.2).<sup>38</sup> The implementation and limitations of the different techniques will be discussed to explore which technique could be used for the prediction of non-unions and PTOA.

The main advantages of these ambient techniques are the possibility to analyze intact samples *in vivo* in their native environment with the near real-time feedback.<sup>46,66,111,118,124</sup> Furthermore, multiple techniques, including electrocautery and the CO<sub>2</sub> laser, use surgically approved handpieces for the ablation and ionization of tissue, which allows for easier implementation in the operating room.<sup>38,46,111,112</sup> In contrast, other techniques, like the SpiderMass and the MasSpec Pen, are not medically approved, which will extend the implementation process in the operating room in the near future.

The amount of unwanted tissue damage generated by these *in vivo* techniques varies depending on the approach used. The main disadvantage of the electrocautery is the thermal and mechanical damage to healthy surrounding tissue, which is unavoidable during surgery but additional damage is an unwanted side effect.<sup>61,66,68,120,121</sup> Consequently, the spatial resolution of this method is low and defined by the size of the blade used.<sup>66,125</sup> Furthermore, this tissue damage complicates the use on healthy tissues and the histopathological validation of tissues sampled with electrocautery.<sup>64,66,113,119</sup> Other methods prevent extensive tissue damage, with limited damage for different ablation-based methods (infrared and ultraviolet lasers, CUSA, and PIRL) and almost no damage for other techniques (SpiderMass and MasSpec Pen).<sup>38,61,66,117-124</sup> For CO<sub>2</sub> laser and PIRL-based techniques, another advantage compared to electrocautery is the minimal thermal spread as well as the fact that these probes interact mostly with the top tissue

Clinical use of mass spectrometry (imaging) in abnormal fracture healing surface.<sup>111,112,118,119,123</sup> Compared to the electrocautery, CO<sub>2</sub> laser-based techniques allow for the more precise sampling of the tissue with less tissue damage.<sup>38,39</sup> The higher reproducibility of the CO<sub>2</sub> laser compared to other lasers allows for more frequent sampling during surgical interventions to improve the efficiency of analysis and decrease the invasiveness of intentional sampling.<sup>39</sup>

In addition, different techniques have their own disadvantages. As already mentioned, electrocautery results in extensive tissue damage.<sup>61,66,68,120,121</sup> The possible contamination with tissue debris limits the usage of the SpiderMass, which is the result of the close contact of the device and the tissue.<sup>121</sup> In the PIRL-based technique, a separate plume collection tube is used for the transfer of the molecules to the mass spectrometer.<sup>118,119,123</sup> The need for this additional tube might limit the translation to the operating room because of practical reasons. For the MasSpec Pen, the disposable tip can be cleaned by automated flushing of the system or needs to be replaced.<sup>120</sup> Due to the contact of the tip with the tissue, contamination can occur when the tip is only flushed while replacing the tip every time is clinically unpractical.<sup>66</sup>

Until now, implementation of *in vivo* methods in the clinic has been limited, which can partly be explained by the lack of multicenter and validation studies performed in the operating room.<sup>112</sup> In addition, the implementation is constrained by the need for the development of large data sets (which can take years) to improve the accuracy of the built tissue classification models as well as the need for validated and quick data processing workflows.<sup>69,111,112</sup> These databases are generated based on *ex vivo* measurements of patient material and associated clinical information. The potential for intra-operative MS techniques in the improvement of patient care is foreseen as revolutionary, especially for those techniques using existing surgical handpieces. For the prediction of non-unions and PTOA, we propose the usage of a CO<sub>2</sub> laser coupled to REIMS, as it can be used on hard tissues, employs an existing surgical handpiece, and has low invasiveness. This *in vivo* MS technique can be used intra-operatively in patients for the prediction of outcome of fracture healing by sampling the bone and/or cartilage without tissue removal.

## 2.7 Conclusions and outlook

Non-unions and PTOA can only be diagnosed in a later phase and, therefore, early prediction of outcome of the healing process is required. Nevertheless, currently, outcome prediction is not possible, despite the known risk factors and limited knowledge of involved molecules. More detailed molecular information about the bone fracture healing and cartilage repair processes is necessary, which can be

## Chapter 2

provided by MS, as this technique can be used for the analysis of bone, cartilage, and surrounding tissue. MSI has the potential to analyze the involved molecules in the repair processes in more detail, while *in vivo* MS can be used for the outcome prediction during the initial surgery.

MSI analysis of bone, cartilage, and surrounding tissue can contribute to the improvement of our knowledge and understanding of the key molecular processes involved in bone fracture healing and cartilage repair. As a broad range of molecules can be studied, in the upcoming years, this can result in defining key molecules and pathways, e.g. lipids and proteins, as well as their distribution. This information can be used for the development of new treatment options for earlier intervention.

Only recently a potential *in vivo* MS technique using CO<sub>2</sub> laser coupled to REIMS has been shown to allow for the analysis of bone and cartilage. Therefore, this technique has to be tested further for optimization of analysis of these tissues and to assess the predictive value for outcome of bone fractures and injury-related cartilage damage. Nevertheless, we expect that the CO<sub>2</sub> laser coupled to REIMS can already be used as an *in vivo* MS technique in the operating room in the upcoming years for the first analyses and, later on, for prediction of outcome.

Improved patient management will be possible by earlier intervention and more treatment options based on both the improvement of the understanding of key molecular pathways in the repair processes as well as the outcome prediction of bone fracture and injury-related cartilage damage.





# Chapter 3: Sample preparation of bone tissue for MALDI-MSI for forensic and (pre)clinical applications



Michiel Vandenbosch\*

Sylvia P. Nauta\*

Anastasiya Svirikova

Martijn Poeze

Ron M.A. Heeren

Tiffany Porta Siegel

Eva Cuypers

Martina Marchetti-Deschmann

\*Shared first authorship

Analytical and Bioanalytical Chemistry

2021; 413: 2683-2694



### 3.1 Abstract

In the past decades, matrix-assisted laser desorption/ionization mass spectrometry imaging (MALDI-MSI) has been applied to a broad range of biological samples, e.g., forensics and preclinical samples. The use of MALDI-MSI for the analysis of bone tissue has been limited due to the insulating properties of the material, but more importantly the absence of a proper sample preparation protocol for undecalcified bone tissue. Undecalcified sections are preferred to retain sample integrity as much as possible or to study the tissue-bone bio interface in particular. Here, we optimized the sample preparation protocol of undecalcified bone samples, aimed at both targeted and untargeted applications for forensic and preclinical applications, respectively. Different concentrations of gelatin and carboxymethyl cellulose (CMC) were tested as embedding materials. The composition of 20% gelatin and 7.5% CMC showed to support the tissue best while sectioning. Bone tissue has to be sectioned with a tungsten carbide knife in a longitudinal fashion, while the sections need to be supported with double-sided tapes to maintain the morphology of the tissue. The developed sectioning method was shown to be applicable on rat and mouse as well as human bone samples. Targeted (methadone and EDDP) as well as untargeted (unknown lipids) detection was demonstrated. DHB proved to be the most suitable matrix for the detection of methadone and EDDP in positive ion mode. The limit of detection (LOD) was estimated to approximately 50 pg/spot on bone tissue. The protocol was successfully applied to detect the presence of methadone and EDDP in a dosed rat femur and a dosed human clavicle. The best matrices for the untargeted detection of unknown lipids in mouse hind legs in positive ion mode were CHCA and DHB based on the number of tissue-specific peaks and signal-to-noise ratios. The developed and optimized sample preparation method, applicable on animal and human bones, opens the door for future forensic and (pre)clinical investigations.

### 3.2 Introduction

The range of applications of mass spectrometry imaging (MSI) has grown exponentially over the last decades.<sup>65,126</sup> A main advantage of MSI is the possibility to detect a wide range of molecules and visualize their distributions without the need for targeted labels while maintaining sample integrity.<sup>126</sup> The development of matrix-assisted laser desorption/ionization (MALDI)-MSI has contributed to a broader application field for MSI, due to the soft ionization of molecules and the broader molecular weight range than previous ionization techniques, for example, secondary ionization mass spectrometry (SIMS).<sup>126</sup> MSI can be applied to a wide variety of sample types, including tissue samples. As a consequence, MSI has been

used more and more in (pre)clinical research, including tissue classification, studying treatment efficacy, and biomarker discovery.<sup>35</sup> Next to this, MALDI-MSI is used to study *in situ* drug, metabolite, and lipid distributions.<sup>35,127</sup> The sample preparation workflow for MALDI-MSI is highly critical for the quality and reliability of the MSI measurements. On one side, the measurements depend on the analytes of interest. Small molecules can be masked by endogenous molecules or signals from the selected matrix.<sup>128</sup> On the other side, the quality and reliability depend on the complexity of the tissue of interest. The sample preparation will affect, among others, sample integrity, the ionization efficiency of molecules, and local ion suppression due to salts and endogenous compounds in the tissue.

For calcified tissues, like bone, decalcification is often performed to allow for easier sectioning and to reduce insulating properties of the sample, but more over to remove the unwanted background signal in MALDI-MSI caused by the mineral structure of these tissues.<sup>129</sup> These procedures, however, pose a high risk of contamination and analyte delocalization.<sup>90</sup> Despite the wide range of tissues that have been studied using MALDI-MSI, there are only a few studies that apply this technique on skeletal tissue.<sup>90,97,98,130,131</sup> This can be explained by the absence of proper section preparation protocols for undecalcified bone tissue. Undecalcified bone tissue is preferred to avoid solvent-induced analyte delocalization, which better preserves the *in vivo* distribution. The lack of existing sample preparation protocols can be explained by the complex morphology of bone tissue.<sup>90,97,130</sup> The combination of hard (bone), stiff (cartilage, tendons, skeletal muscle), and rather soft tissue (bone marrow, surrounding periosteum, smooth muscle) in the skeletal tissue makes sectioning a challenge.<sup>90,130</sup> Bone sections have the tendency to curl or fall apart.<sup>130</sup> Another difficulty lies in the creation of homogenous tissue sections with MALDI-MSI-compatible techniques.<sup>126</sup> Previous methods for sectioning skeletal tissue have been shown to be successful in preparing bone sections.<sup>131</sup> However, they often involve decalcification and/or dehydration methods, which consist of washing steps using an acid.<sup>130</sup> In 2014, Hirano *et al.* reported an application of MALDI-MSI on tooth cryosections, which were prepared using adhesive film without any pretreatment of the tissue.<sup>129</sup> Nevertheless, teeth have a different texture than bone tissue. In 2018, Svirkova *et al.* adapted Hirano's method to make cross-sectional sections of chicken digits, which only contain small and thin bone pieces.<sup>98</sup> These and the different studies provided in Table 3.1 show that it is possible to cut samples containing bone and surrounding soft tissue, although each of the methods is different. Here, we aim to optimize the sample preparation and analytical workflow of undecalcified longitudinal bone sections for

**Table 3.1:** Overview of MALDI-MSI and similar techniques studies performed on bone tissue. Information is provided about the sample, sample preparation (pretreatment, embedding material, sectioning specifications, and washing), MSI specification, and results.

Abbreviations: APS-MALDI-MSI = atmospheric pressure scanning microprobe matrix-assisted laser desorption/ionization mass spectrometry imaging, CMC = carboxymethyl cellulose, IR-MALDESI-MSI = infrared matrix-assisted laser desorption electrospray ionization mass spectrometry imaging, MALDI-MSI = matrix-assisted laser desorption/ionization mass spectrometry imaging, MSI = mass spectrometry imaging, PFA = paraformaldehyde, SIMS = secondary ion mass spectrometry, TCA = trichloroacetic acid,  $\mu$ XRF = micro X-ray fluorescence.

Author (year)	Sample	Pretreatment	Embedding material	Sectioning specifications	Washing	MSI specifications	Results
Seeley, <i>et al.</i> (2014) <sup>131</sup>	Mice with tumor-induced bone disease	-	Ice	Whole sections Thickness: 15 $\mu$ m Sections collected using Instrumedics, Inc. Macro Tape Transfer system (Leica), whereby a polymer is used to transfer section from tape to slide	70%, 90% and 95% ethanol for 30 s each	MALDI-MSI, positive ion mode, $m/z$ range 2,000-40,000	Mass spectra could be acquired from bone marrow, but not from bone.

**Table 3.1 (continued):** Overview of MALDI-MSI and similar techniques studies performed on bone tissue.

Author (year)	Sample	Pretreatment	Embedding material	Sectioning specifications	Washing	MSI specifications	Results
Fujino, <i>et al.</i> (2016) <sup>97</sup>	Mice femurs and tibia	Decalcification using formic acid, EDTA-NH <sub>4</sub> , or TCA. Fixation using 4% PFA, Carnoy fluid, or TCA.	2% CMC	Kawamoto method Thickness: 10 µm Tape: Electrical conducting double-sided tape	70% and 100% ethanol	MALDI-MSI, positive and negative ion mode, <i>m/z</i> range of 100-1000	Each and decalcification ion and/or fixation method has its own characteristic peaks. No significant difference in number of peaks per method. Using cryotape reduces the number of peaks in the mass spectra.

Table 3.1 (continued): Overview of MALDI-MSI and similar techniques studies performed on bone tissue.

Author (year)	Sample	Pretreatment	Embedding material	Sectioning specifications	Washing	MSI specifications	Results
Scheape, <i>et al.</i> (2018) <sup>90</sup>	Human femoral heads	-	First, big blocks in 4% PHA. Second, smaller pieces in SCEM-L1 embedding medium from SECTION-LAB Co.	Kawamoto method Thickness: 4 $\mu$ m Knife: SL-30 tungsten carbide blade Tape: cryofilm of type 2C(9) from SECTION-LAB Co.	-	APS-MALDI-MSI, positive ion mode, $m/z$ range 250-1000 SIMS, positive and negative ion mode,	Different distributions of major lipid classes could be shown, including glycerolipids, glycerolphospholipids, and sphingolipids. In addition, triacylglycerols could be found in bone marrow.

Table 3.1 (continued): Overview of MALDI-MSI and similar techniques studies performed on bone tissue.

Author (year)	Sample	Pretreatment	Embedding material	Sectioning specifications	Washing	MSI specifications	Results
Svirikova, et al. (2018) <sup>98</sup>	Chicken digits	-	20% gelatin with 5% CMC	Ullberg method Thickness: 12 µm Knife: non-disposable tungsten carbide knife Tape: double-sided tape and polyimide one sided tape made with DuPont™ Kapon®	-	MALDI-MSI, positive ion mode, $m/z$ range 300-1000 µXRF	Lipid distributions were shown in surrounding tissues using MALDI-MSI and elements in the bone using µXRF.
Khodjanliyazova, et al. (2019) <sup>130</sup>	Mice humeri	-	Half of the bone in plaster of Paris, in addition, other embedding materials were tested	The cutting surface at half the bone was imaged. The bone was trimmed using a Surgipath high-profile disposable blade at 20 µm).	-	IR-MALDESI-MSI, positive ion mode, $m/z$ range 250-1000	Lipid distribution images were shown from bone tissue, including a ceramide, phospholipid, and cholesterol.

MALDI-MSI without any pretreatment. We will focus on the evaluation of the potential of MALDI-MSI for targeted and untargeted applications, namely the detection of small exogenous molecules (i.e., drugs of abuse) for the forensic field and endogenous ones (i.e., lipids) for the (pre)clinical field in longitudinal bone tissue sections.

During the last decade, the interest in the usage of skeletal tissue as an alternative specimen in forensic toxicology has seen a revival.<sup>132-134</sup> It is shown that the bone tissue acts as a depot for certain drugs.<sup>132</sup> However, the analysis of bone tissue is still in its infancy. Nowadays, the gold standard for analysis of skeletal tissue is the usage of liquid or gas chromatography MS.<sup>135</sup> Although it is of great value, this technique requires sample clean-up and extractions steps. MALDI-MSI could prove a more time efficient alternative for the detection of certain drugs. Therefore, in this study, the targeted detection of methadone and its metabolite 2-ethylidene-1,5-dimethyl-3,3-diphenylpyrrolidine (EDDP) in skeletal tissue will be studied using MALDI-MSI.

In the clinical field, the application of MALDI-MSI related to skeletal diseases can have a great potential, as the current molecular understanding of the underlying processes of, for example, bone fracture healing and non-union development is very limited.<sup>4,10,136</sup> The application of MALDI-MSI on undecalcified bone tissue can be of additional value for improved understanding of molecular pathways involved in different bone diseases. The untargeted application will be focused on different lipid classes, because lipids have a regulatory function in healthy bone and repair processes and are present in bone marrow as well as in bone.<sup>90,137</sup> In this study, a method for untargeted detection of a broad range of lipid classes with MALDI-MSI in bone tissue will be optimized by comparing the efficiency of different matrices.

### 3.3 Materials and methods

#### 3.3.1 Chemical and materials

Analytical reference standards of EDDP (1 mg/mL) and methadone (1 mg/mL) were purchased from Cerilliant (Round Rock, TX, USA). Aqueous standard stocks of different concentrations were prepared by mixing reference standards. All standard solutions were stored at  $-20\text{ }^{\circ}\text{C}$ . Acetone, acetonitrile (ACN), methanol, isopropanol, and water were purchased from Biosolve BV (Valkenswaard, The Netherlands) with HPLC grade (acetone) or ULC/MS-CC/SFC grade (other solvents). Red phosphorus was obtained from Sigma-Aldrich (St. Louis, MO, USA). Tragacanth, carboxymethyl cellulose (CMC) sodium salt, and gelatin were purchased from Sigma-Aldrich (St. Louis, MO, USA). Conductive indium tin oxide (ITO)-coated

microscope glass slides were purchased from Delta Technologies (Loveland, MN, USA) for the drug measurements. For the lipid measurements, SuperFrost Plus microscopic glass slides were purchased from VWR International BV (Radnor, PA, USA). All MALDI matrices, 2,5-dihydroxybenzoic acid  $\geq$  98% (DHB), 2,4,6-trihydroxyacetophenone hydrate  $\geq$  98% (THAP),  $\alpha$ -cyano-4-hydroxycinnamic acid  $\geq$  98% ( $\alpha$ -CHCA), 2',6'-dihydroxyacetophenone (DHA), 1',5'-diaminonaphthalene (DAN), norharmane, N-(1-naphthyl)ethylenediamine dihydrochloride (NEDC), and sinapic acid  $\geq$  98% (SA) were purchased from Sigma-Aldrich. Different supportive tapes were purchased: double-sided conductive copper tape and double-sided carbon tape, double-sided Tesa® tape; double-sided Scotch® tape all manufactured by 3M (MN, USA).

### 3.3.2 Sample collection

Male Wistar rats were obtained from the animal facility of Gasthuisberg (KU Leuven, Belgium) to facilitate targeted drug experiments by spiking blank bones with a methadone:EDDP (1:1) aqueous mixture. The animals served solely for breeding purposes and were not involved in any prior experiments. Samples of dosed rats were obtained from an experiment concerning chronic dosing of rats with methadone.<sup>138</sup> All applicable international, national, and institutional guidelines for the care and use of the animals were followed. All experiments were in accordance with ethical standards as approved by the Ethical Committee for Animal Experimentation of the University of Leuven (P 113/2011). The animals were euthanized using CO<sub>2</sub>. Bones were removed by dissection and stored at -20 °C until future use.

Human postmortem samples were obtained at autopsy of legal cases at UZ Leuven (Belgium). Approval for this study was received from the Medical Ethics Committee of the faculty of Medicine of the University Hospital of Leuven, Belgium. Cases were selected after a positive screening result for methadone. The clavicle was chosen as the specimen of choice due to the high accessibility during autopsy. After removal of the breastplate, a ring of 1-cm width was serrated 1 cm from the center of the distal clavicle head. The bones were cleaned by scraping the soft tissue off with a scalpel. Bone marrow was not removed prior to cutting. Samples were stored at -20 °C.

For the untargeted lipid experiments, the control (not fractured) hind legs of a mouse study were used. These mice received pulsed electromagnetic field (PEMF) therapy for 0, 1, 4, or 8 h per day for 14 days. The animals were euthanized by cardiac puncture. The samples were stored on ice and transported to the freezer. Approval for this study was received from the Animal Experiments Committee of

Maastricht University (2014-030). Before embedding and sectioning, the fur was removed, while the surrounding soft tissue and bone marrow remained. The samples were stored at  $-80\text{ }^{\circ}\text{C}$ .

### 3.3.3 Tissue sectioning

Based on previous experiments,<sup>98</sup> different embedding media were tested for thin rat bone sections: (A) an aqueous mixture of 20% gelatin, 5% CMC (w/v); (B) an aqueous mixture of 20% gelatin, 7.5% CMC (w/v); and (C) an aqueous mixture of 20% gelatin, 10% CMC (w/v). Also, different adhesive tapes were evaluated for supporting the tissue sections. Four different tapes were evaluated: double-sided conductive copper tape, double-sided carbon tape, double-sided Tesa® tape, and double-sided Scotch® tape. For every tape separately, the optimal section thickness and temperature were determined. The sample was mounted on the specimen disc using 10% tragacanth (w/v). Tissue sectioning was performed on CryoStar NX50 (Thermo Scientific) or Leica CM1860 UV (Wetzlar, Germany) using a Shandon™ Tungsten Carbide D-Profile (Thermo Scientific). The tape was attached using the second adhesive side to a conductive indium tin oxide (ITO)-coated microscope glass slides from Delta Technologies (Loveland, MN, USA) for the drug experiment and on SuperFrost Plus microscopic glass slides (VWR International BV, Radnor, PA, USA) for the lipid experiments. For the lipid experiments, the samples were stored at  $-80\text{ }^{\circ}\text{C}$  until future use. The sample was vacuum-dried in a desiccator overnight at room temperature for the drug experiments and 30 min in the desiccator at room temperature for the lipid experiments before matrix application. For the application of the drug standards, it was necessary that the sections were completely dry to prevent water-based drops from spreading due to capillary forces while a short drying time for lipids is preferred due to the natural degradation of lipids at room temperature. When the sections were completely dried, drug standards with different concentrations of an aqueous methadone:EDDP mixture were applied to bone sections using manually spotting of 0.5- $\mu\text{L}$  drops. The spiked sections were vacuum-dried for 15 min in a desiccator before matrix application.

### 3.3.4 MALDI matrix selection with dried droplet

For the drug experiments, four matrices were evaluated and prepared as follows: 7 mg of DHB and 10 mg of NaCl dissolved in 1 mL of  $\text{H}_2\text{O}/\text{ACN}$  (70:30 v/v); 10 mg of THAP and 10 mg of NaCl dissolved in 1 mL of methanol; and 5 mg of SA and 1 mg of NaCl dissolved in 1 mL of  $\text{H}_2\text{O}/\text{ACN}$  (40:60 v/v) and 5 mg of  $\alpha\text{-CHCA}$  in 1 mL of  $\text{H}_2\text{O}/\text{ACN}$  (70:30 v/v). Matrix solutions were deposited 1:1 (v/v; 0.5  $\mu\text{L}$  each) together with a methadone:EDDP mixture on a stainless steel target and dried at room temperature. All experiments were performed in duplo.

### 3.3.5 MALDI matrix sublimation

The different matrices were either sublimated on a home-built sublimation unit at TU Wien using experimental parameters as described previously<sup>139</sup> for preliminary experiments or on the HTX Sublimator (HTX Technologies, Chapel Hill, NC, USA). For the analysis of methadone and its metabolite, DHB was sublimated. For the matrix selection for the lipid experiments, CHCA, DAN, DHA, DHB, and norharmane were compared in positive ion mode, while DAN, NEDC, and norharmane were compared in negative ion mode. The sublimation details per matrix can be found in Table 3.2.

### 3.3.6 MALDI-MSI instrumentation

A Waters SYNAPT G2 system was used for preliminary experiments before switching to the more sensitive SYNAPT G2-Si system equipped with a prototype uMALDI source, both provided with a Nd:YAG laser (Waters Corporation, Manchester, UK) (for more information about the uMALDI source, see Barré *et al.*<sup>106</sup>). The data acquiring was performed using MassLynx version 4.1 and HDImaging version 1.5 software (Waters Corporation). The measurements were performed in sensitivity mode with a scan rate of 1.0 s per scan. Different mass ranges were acquired:  $m/z$  50–500 in positive ion mode for drug experiments,  $m/z$  100–1200 in positive ion mode for lipid experiments, and  $m/z$  100–2000 in negative ion mode for lipid experiments. The instrument was calibrated with red phosphorus for both positive and negative ion modes before each measurement. The laser fluence was dependent on the matrix used as well as the application type. It varied between 150 and 350 arbitrary units set in the control software, and no absolute fluence measurement was performed. The spatial resolution was 150  $\mu\text{m}$   $\times$  150  $\mu\text{m}$  for the drug experiments and 100  $\mu\text{m}$   $\times$  100  $\mu\text{m}$  for the lipid experiments.

**Table 3.2:** Matrix sublimation details for the HTX sublimator unit. Per matrix, the amount of matrix, solvent, sublimation temperature, and sublimation time are provided.

Matrix	Amount (mg)	Solvent ( $\pm 5$ mL)	Sublimation temperature ( $^{\circ}\text{C}$ )	Sublimation time (s)
CHCA	55 $\pm$ 1	ACN:H <sub>2</sub> O (70:30)	180	300
DAN	30 $\pm$ 1	Methanol	120	80
DHA	50 $\pm$ 1	Isopropanol	160	300
DHB	50 $\pm$ 1 (lipid) 70 $\pm$ 1 (drug)	Acetone	180	280
NEDC	40 $\pm$ 1	Methanol	160	150
Norharmane	50 $\pm$ 1	Methanol	140	200

### 3.3.7 Data analysis

For the data analysis of the measurements, HDImaging (version 1.4, Waters Corporation), MassLynx (version 4.1, Waters Corporation), LipostarMSI (version 1.1.0b17, Molecular Horizon), and mMass (Open Source Mass Spectrometry Tool, version 5.5.0) were used. All data analysis is performed on total ion current (TIC)-normalized data and the shown distribution images are TIC-normalized.

### 3.3.8 Lipid identifications

The selected  $m/z$  values (shown in the overlay images in “3.4 Results”) were chosen from the merged dataset created in LipostarMSI (version 1.1.0b17, Molecular Horizon). In this dataset, all measurements of one ion mode were merged and the  $m/z$  values were averaged over the different measurements. For each merged  $m/z$  value as displayed in the figure, the corresponding  $m/z$  value from the average mass spectrum for the specific matrix was obtained, as this value correlates to the shown distribution. These average mass spectra were recalibrated to the high-intensity matrix peaks and some general lipids using the manual mass warping option during data import in LipostarMSI. For tentative identifications of selected  $m/z$  values (from the average mass spectrum), the experimental  $m/z$  values were searched in the LIPID MAPS® Structure Database (LMSD) and ALEX<sup>123</sup> lipid calculator with a maximum ppm error of 15 ppm, including all lipid classes and all single charged adducts.<sup>140,141</sup>

## 3.4 Results

This study consists of three parts: (1) the optimization of a sample preparation method of undecalcified bone tissue for MSI, focused on the embedding material and sectioning method; (2) a targeted approach measuring drug concentrations in rat and human bone tissue, and more specifically on the detection of methadone and its metabolites to determine the limit of detection (LOD) and detection of these molecules in dosed bones; and (3) an untargeted approach to select the most suitable matrix for measuring lipids in mouse bone tissue.

### 3.4.1 Method optimization for tissue sectioning

Cutting undecalcified bone tissue without embedding resulted in shattered fragments. Therefore, embedding bone tissue proved necessary to maintain sample integrity during sectioning. In a previous study, gelatin and CMC has been used as embedding materials for chicken digits.<sup>98</sup> Chicken digits differ from rat and mouse bone, the latter being harder and more brittle. An optimal embedding material and sectioning protocol for undecalcified bone tissue of rats and mice focusing only on MALDI-MSI has not been determined yet. Three different

embedding media were tested with different concentrations of CMC to maintain the integrity of the sample. Of these embedding media, 7.5% proved to provide the best sections, while 10% CMC showed to exceed the solubility threshold. Tissue sections were visually assessed by a light microscope to evaluate their integrity. Optimal section parameters were chosen based on a surface homogeneity. As the embedded samples still shattered during sectioning, double-sided tapes were used to increase the support. The section thickness and temperature were optimized for each of the four tapes. Optical images of a section obtained with different tapes are shown in Figure 3.1. The Tesa® tape gave the most homogenous sections. The final workflow for the sample preparation and MALDI-MSI measurements for undecalcified bone tissue is shown in Figure 3.2.

### 3.4.2 Targeted detection of methadone and EDDP

#### 3.4.2.1 Matrix selection for drugs

The limit of detection (LOD) was determined based on a signal-to-noise (S/N) ratio of more than 3. In a common MALDI-MS experiment using the dried droplet method on a stainless steel target, the LOD was estimated to approximately 2.5 µg for methadone and 1 µg for EDDP using DHB as a matrix. The corresponding mass spectra are shown in Figure 3.3. Using SA as a matrix, the LODs were estimated to approximately 50 µg for methadone and 30 µg for EDDP. CHCA showed to have an overlapping mass with EDDP. THAP did not co-crystallize with methadone and gave no signal. The amount of DHB for detection of methadone and EDDP was optimized, resulting in 70 mg of DHB. This latter resulted in 3.3 mg DHB on the ITO slide.

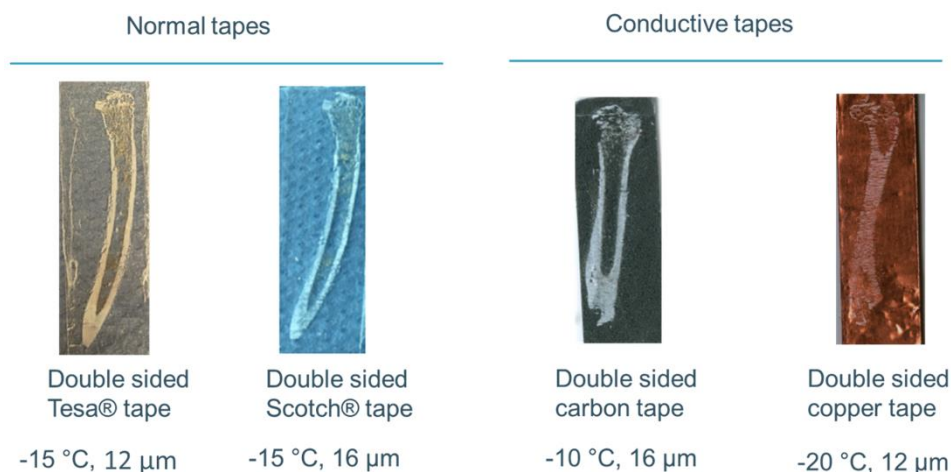
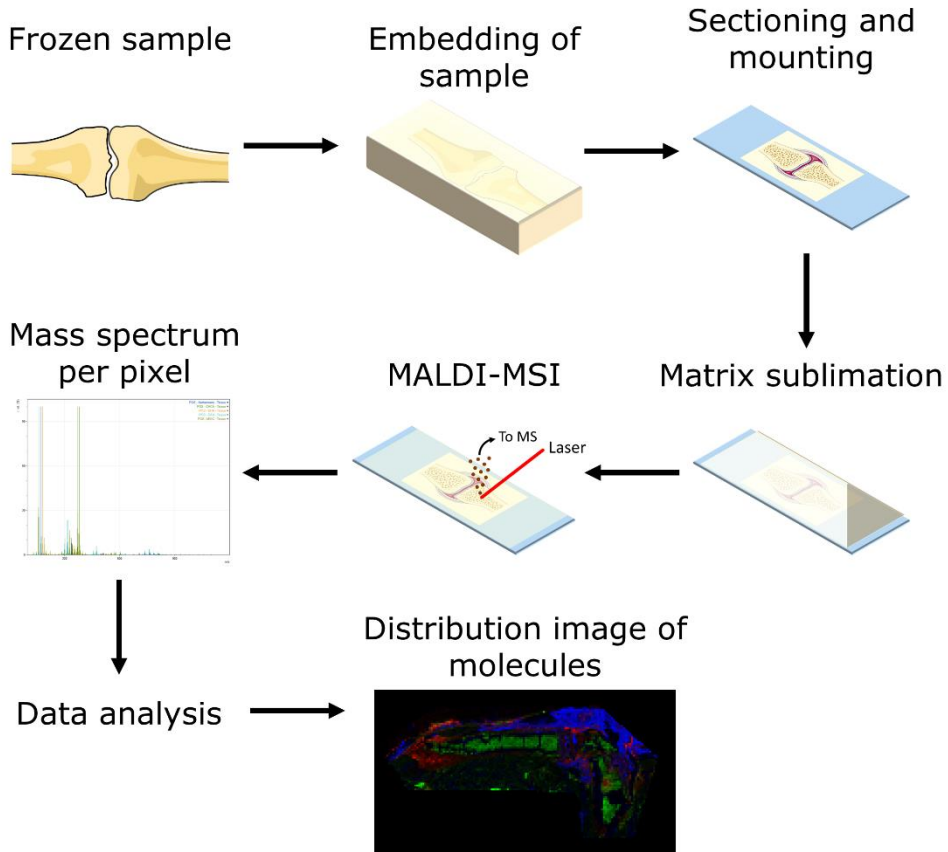


**Figure 3.1:** Optical images of rat bones mounted on each of the four tapes used during sectioning with optimized section thickness and temperature.

## Sample preparation of bone tissue for MALDI-MSI



3

**Figure 3.2:** Analytical workflow for the analysis of bone tissue with MALDI-MSI. Samples were collected and stored in the freezer until further use. Samples were embedded in 20% gelatin with 7.5% CMC (w/v), sectioned at 12  $\mu\text{m}$  with the support of double-sided tapes, and mounted with the other side of the tape on a glass slide such that the tissue was available for analysis. The matrix was applied on the sample via sublimation. After matrix sublimation, the MALDI-MSI measurement was performed, during which a mass spectrum per pixel is obtained for the region of interest. After data processing and analysis of these spectra, for example, intensity and signal-over-noise (S/N) values could be obtained and distribution images of selected  $m/z$  values could be created that can provide information about the location of these molecules.

### 3.4.2.2 Sensitivity test

On the SYNAPT G2-Si, the copper tape as well as the normal tape gave sufficient signal intensities. Because the quality of the sections was better using the normal Tesa® tape, the latter was used for future experiments. Different calibration series were constructed to compare the influence of the different parameters (ITO slide,

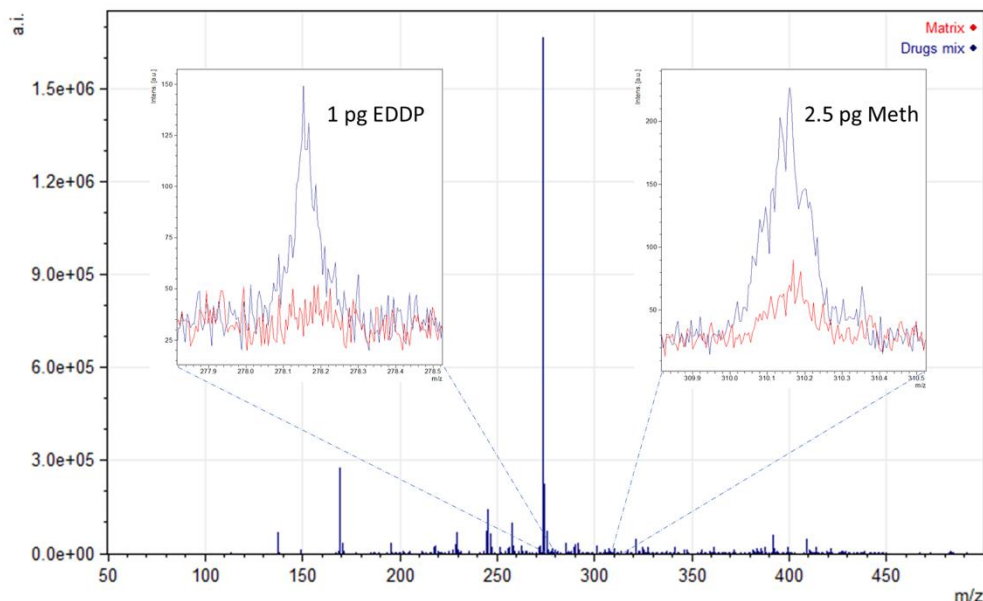


**Figure 3.3:** Detection of methadone and EDDP using DHB as matrix in positive ion mode. In blue the mass spectrum of the measured droplet with a drug mixture of 1pg EDDP ( $m/z$  278.18) and 2.5 pg methadone ( $m/z$  310.21) and in red the spectrum of DHB.

tape, and bone tissue). Methadone and EDDP were detectable as  $[M+H]^+$  ions in MS mode in all calibration series. A significant decrease in intensity could be observed from bone tissue compared with ITO glass slides exemplifying the significantly reduced desorption/ionization efficiency of analytes. The LOD of detection for methadone was estimated to approximately 5 pg, 25 pg, and 50 pg in a drop on the ITO slide, the tape with gelatin, and the bone tissue, respectively. For EDDP, LODs were estimated to approximately 25 pg on bone, 25 pg on tape with gelatin, and 5 pg on the ITO slide. On the ITO slide and the tape, methadone and EDDP generated characteristic ion fragment signatures in MS/MS mode. On the bone tissue, below 500 pg, no specific MS/MS spectra could be generated. The calibration series are shown in Figure 3.4. The mass spectra of a 50-pg spot on bone tissue are shown in Figure 3.5.

#### 3.4.2.3 Detection of methadone and metabolite in dosed rat bone

A femoral bone of a rat dosed with methadone was sectioned longitudinal and imaged as described. The methadone concentration and EDDP concentration in the bone were determined respectively at 14 ng/g and 4 ng/g as described by Vandenbosch *et al.*<sup>138</sup> The intensity of methadone in the bone was very low. The

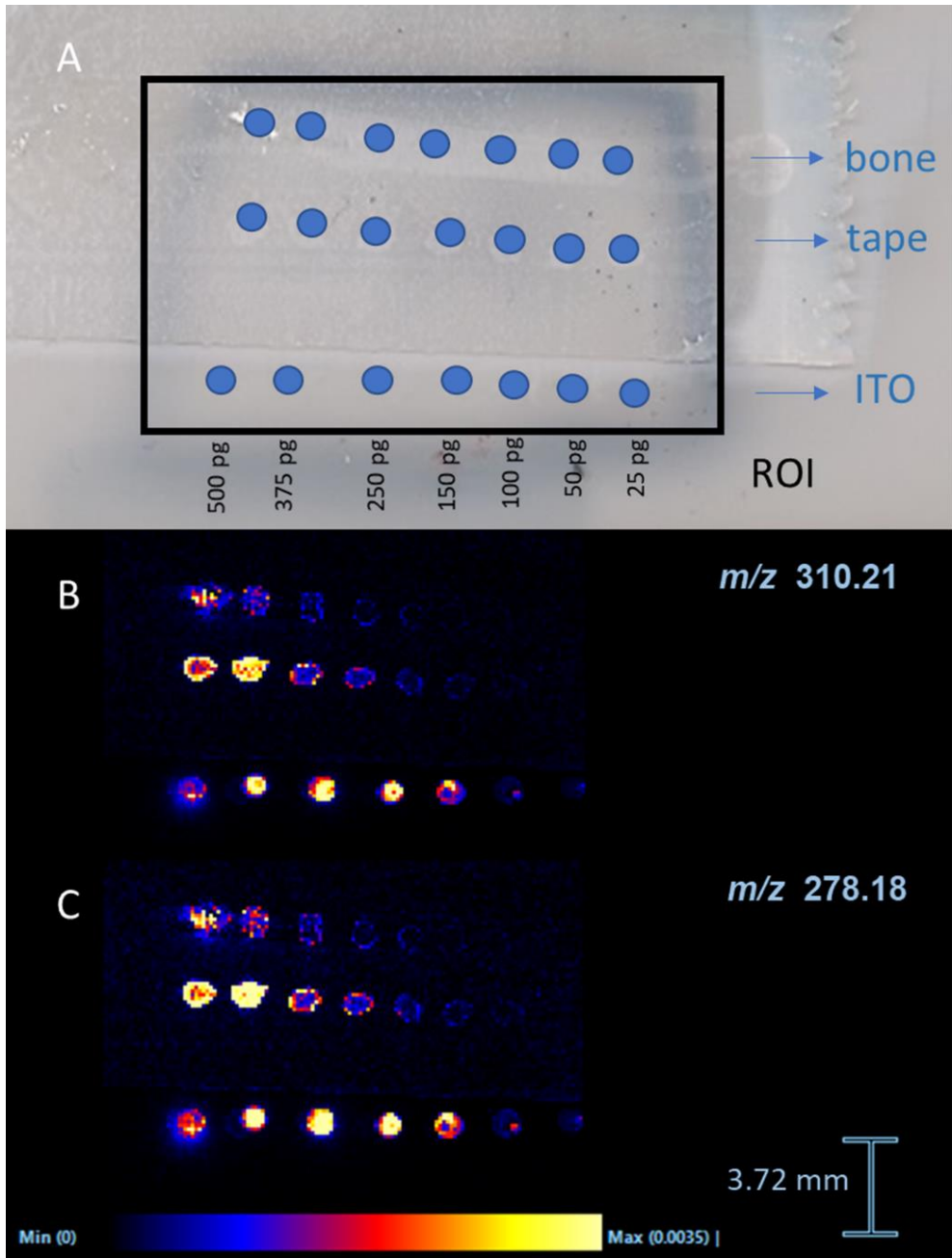


**Figure 3.4:** Calibration series for methadone and EDDP. **A** Longitudinal bone section spiked with methadone dilution series region of interest (ROI) in blue. **B** MALDI-MSI image of methadone ( $m/z = 310.21$ ) and **C** EDDP ( $m/z = 278.18$ ). The distribution images are total ion current (TIC)-normalized. Scale bar shows relative intensities.

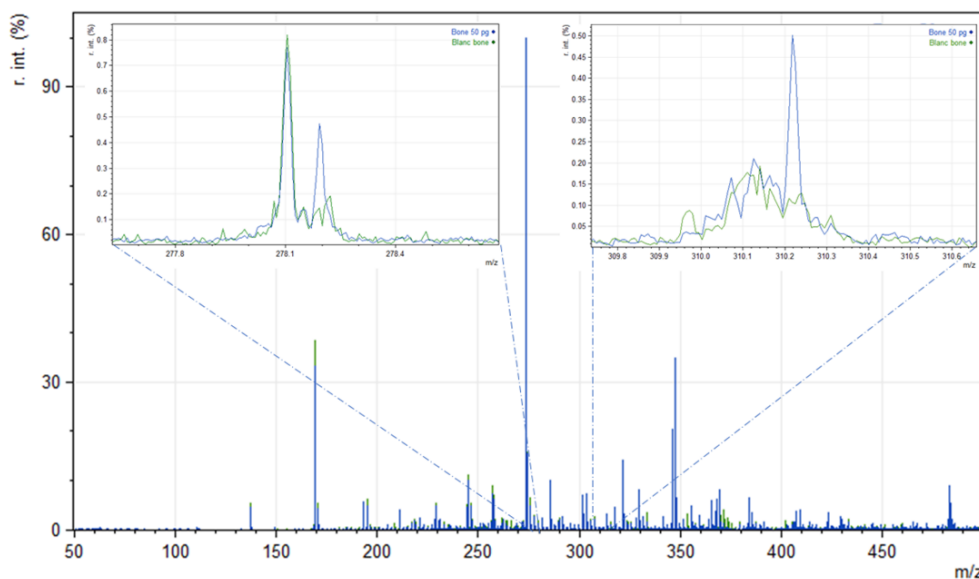


**Figure 3.5:** Detection of methadone and EDDP using DHB as matrix in positive ion mode. In blue the mass spectrum of a spot with 50 pg methadone ( $m/z = 310.21$ ) and 50 pg EDDP ( $m/z = 278.18$ ) on bone tissue and in green a mass spectrum of blank bone tissue.

methadone intensity in the bone marrow could clearly be distinguished from the surrounding bone. The surrounding bone showed a slight intensity difference with the surrounding matrix, but this difference is not significant. For the metabolite EDDP, the same pattern was seen and the signals were more intense at some spots. The bone tissue could be distinguished from the surrounding matrix, but this difference is not significant. The distribution images of methadone and EDDP are shown in Figure 3.6.

#### 3.4.2.4 Detection of methadone and metabolite in postmortem forensic human bone

A clavicular bone of a 37-year-old male who died of an overdose of methadone was sectioned cross-sectional and imaged as described. Blood concentrations of methadone and EDDP were respectively 3727.4 ng/mL and 32.9 ng/mL as described in Vandenbosch *et al.*<sup>142</sup> When looking at the distribution image of methadone, the bone marrow could be distinguished from the surrounding bone (see Figure 3.7). In addition, the bone tissue could clearly be distinguished from the surrounding matrix. Similar observations were made for EDDP (see Figure 3.7).

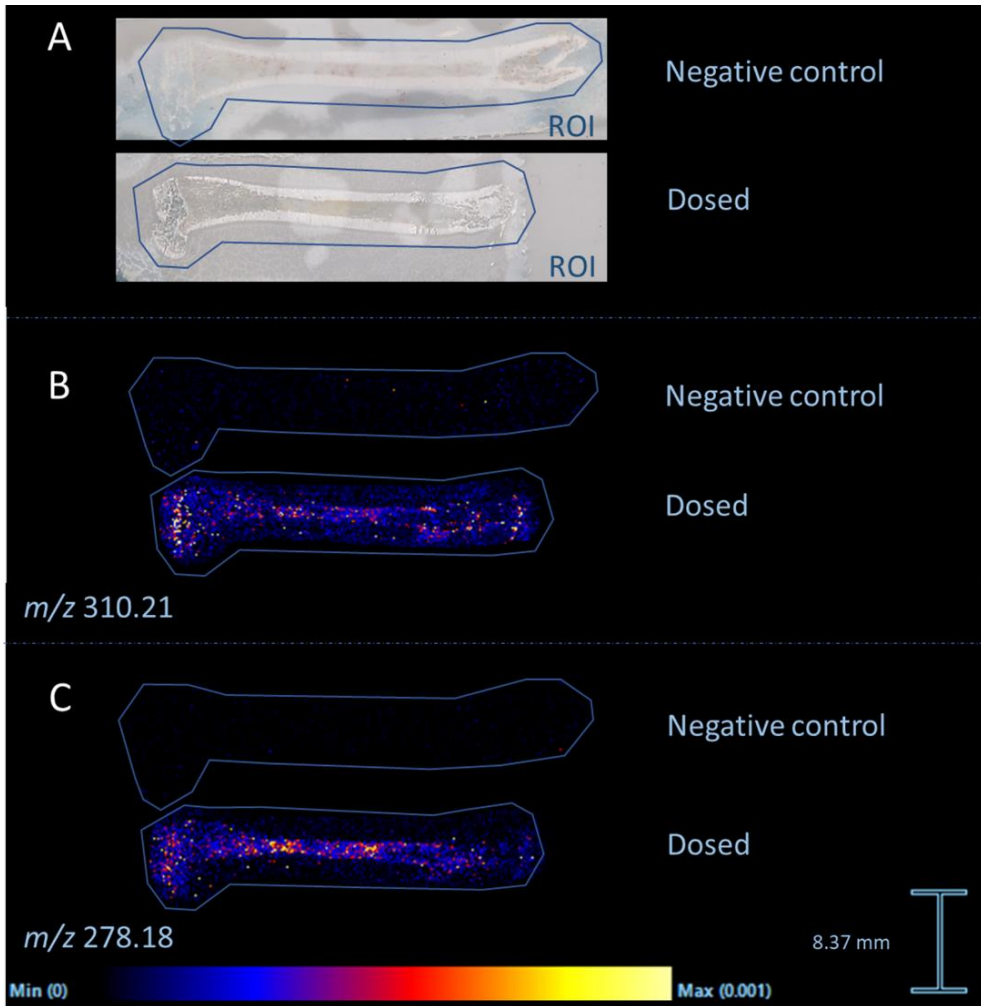


**Figure 3.6:** Distribution images of methadone and EDDP in a rat femur dosed with methadone. **A** Longitudinal section of rat femur with region of interest (ROI) in blue. **B** MALDI-MSI distribution image of methadone ( $m/z$  310.21). **C** MALDI-MSI distribution image of EDDP ( $m/z$  278.18). The distribution images are total ion current (TIC)-normalized. Scale bar shows relative intensities.

### 3.4.3 Untargeted detection of lipids

In previous studies of MALDI-MSI on undecalcified bone tissue, CHCA, DHB, and dithranol have been reported as matrices for the detection of metabolites and lipids from bone tissue, but limited information is available on lipids and the efficiency of these matrices to desorb and ionize different lipid classes.<sup>90,97,98</sup>

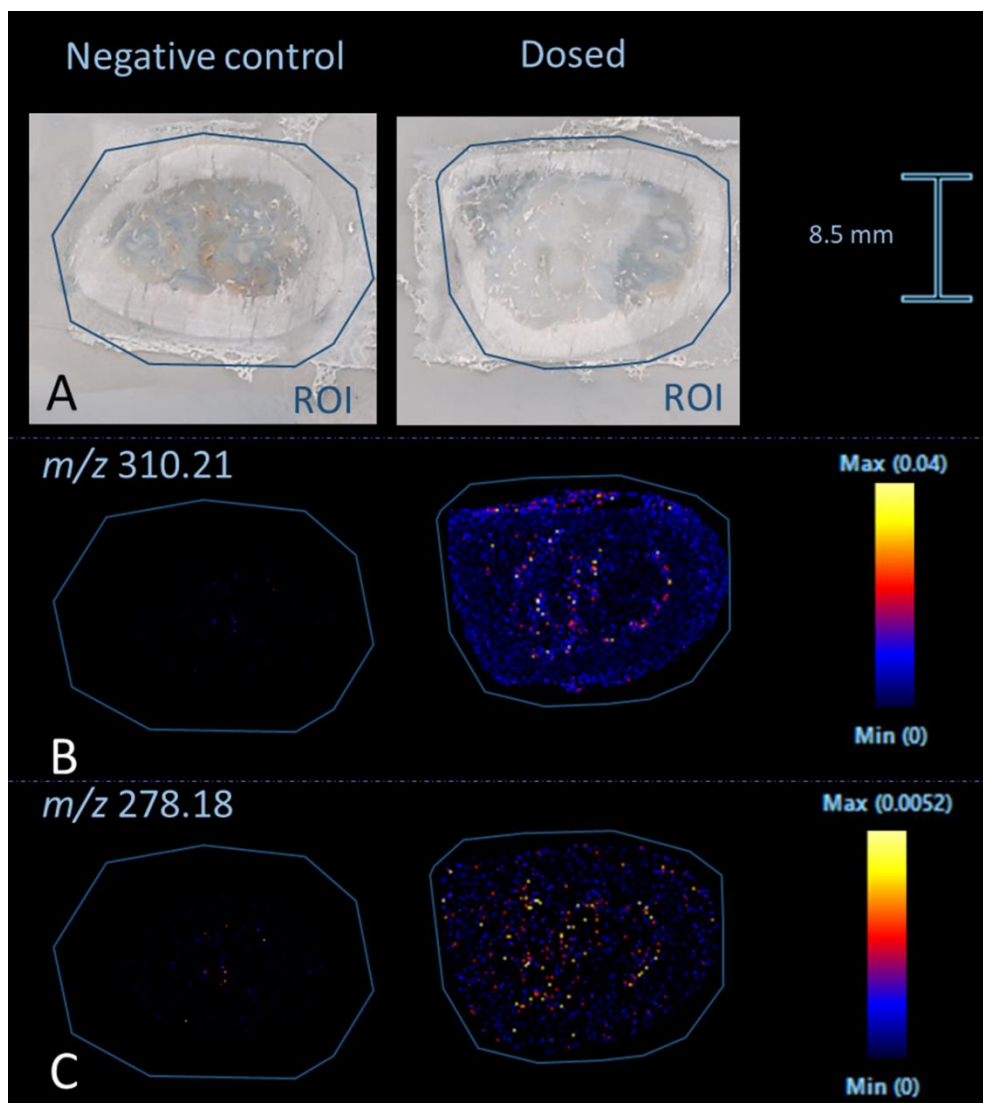


**Figure 3.7:** Distribution images of methadone and EDDP in a human clavicle from someone who overdosed on methadone. **A** Cross-section of the clavicle with the region of interest (ROI) in blue. **B** MALDI-MSI distribution image of methadone ( $m/z$  310.21). **C** MALDI-MSI distribution image of EDDP ( $m/z$  278.18). The distribution images are total ion current (TIC)-normalized. Scale bar shows relative intensities.

Studying the different lipid classes present in bone is of great interest, because of their regulatory role in bone health and repair.<sup>90,137</sup> To test the different matrices for the detection of lipids in bone tissue, the following matrices were assessed: CHCA, DAN, DHA, DHB, and norharmane for positive ion mode; and DAN, NEDC,

and norharmane in negative ion mode. NEDC was included in this analysis although it is more often used for the detection of metabolites than for lipids, as multiple molecules in the lower mass range were seen during initial analysis.

#### 3.4.3.1 Positive ion mode

In positive ion mode, different matrices allowed for the detection of different molecules from the bone and bone marrow, although some  $m/z$  values were represented in multiple matrices (see Figure 3.8). For DAN, DHA, and norharmane, it was not possible to obtain specific  $m/z$  values from bone, although for norharmane some  $m/z$  values showed higher intensities in bone tissue compared with the bone marrow and surrounding tissue. For CHCA and DHB, it was possible to obtain  $m/z$  values specific for bone and bone marrow. In addition, CHCA and DHB had the highest number of  $m/z$  values specific for bone or bone marrow (see Table 3.3). DAN and norharmane resulted in a high number of specific  $m/z$  values for bone marrow compared with DHA. For CHCA, the specific  $m/z$  values were roughly half divided between bone and bone marrow, while for DHB, the majority of the specific  $m/z$  values were obtained from bone (see Table 3.3). DHB has relatively low signal intensities (TIC-normalized) and signal-to-noise (S/N) ratios (see Table 3.3 and mass spectra in Figure 3.9) for bone as well as bone marrow compared with the base peak, while CHCA has low signal intensities and S/N ratios for bone in contrast to data collected from bone marrow. DAN provided the highest S/N ratios for signals derived from bone marrow, but in the positive ion mode, this matrix showed significant interference with the tissue-related peaks. DHB and norharmane show some interferences, and for CHCA and DHA, the interference is low (Figure 3.9).

#### 3.4.3.2 Negative ion mode

In negative ion mode, different matrices allowed for the detection of different ions from the bone and bone marrow and most  $m/z$  values were only presented in one measurement (see Figure 3.10). For DAN and norharmane, it was only possible to obtain specific signals for bone marrow, while for NEDC, it was possible to observe specific signals from both, bone and bone marrow. NEDC had the highest number of  $m/z$  values specific for bone or bone marrow, of which most of the  $m/z$  values were obtained from the bone (see Table 3.5). However, these specific  $m/z$  values are only in the lower mass range ( $m/z < 500$ ). DAN resulted in the highest number of specific  $m/z$  values for bone marrow. Furthermore, NEDC has higher signal intensities for bone and relatively high S/N values for bone marrow (see Table 3.5), while the intensities and S/N values for bone marrow are higher in DAN and norharmane. DAN showed the highest S/N values for bone marrow. In negative ion

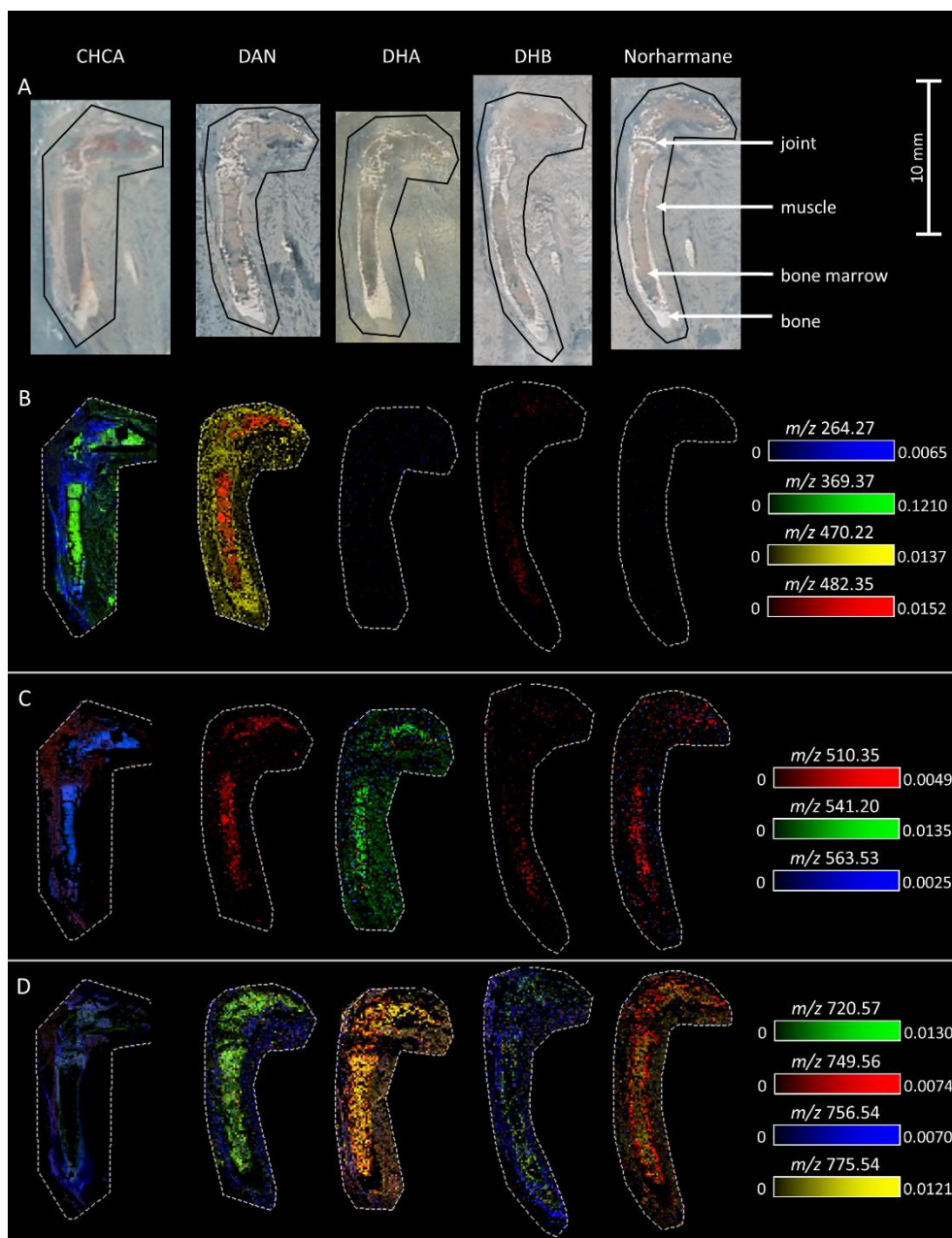


**Figure 3.8:** Overlay images of selected  $m/z$  values for CHCA, DHA, DAN, DHB, and norharmane in positive ion mode measured with MALDI-MSI of mouse hind legs for the untargeted detection of lipids. The  $m/z$  values were selected to show the similarities and differences between the matrices in terms of desorption and ionization efficiency. **A** Optical

**Figure 3.8 (legend continued):** scan of the section with the measured area indicated with a black line. Overlay images of the distributions of selected  $m/z$  values in the range 200-500 (B), 500-600 (C), and 700-800 (D). The distribution images are total ion current (TIC)-normalized and the intensity scale shows the maximum relative intensity of the specific  $m/z$  value (for tentative identifications of the selected  $m/z$  values, see Table 3.4).

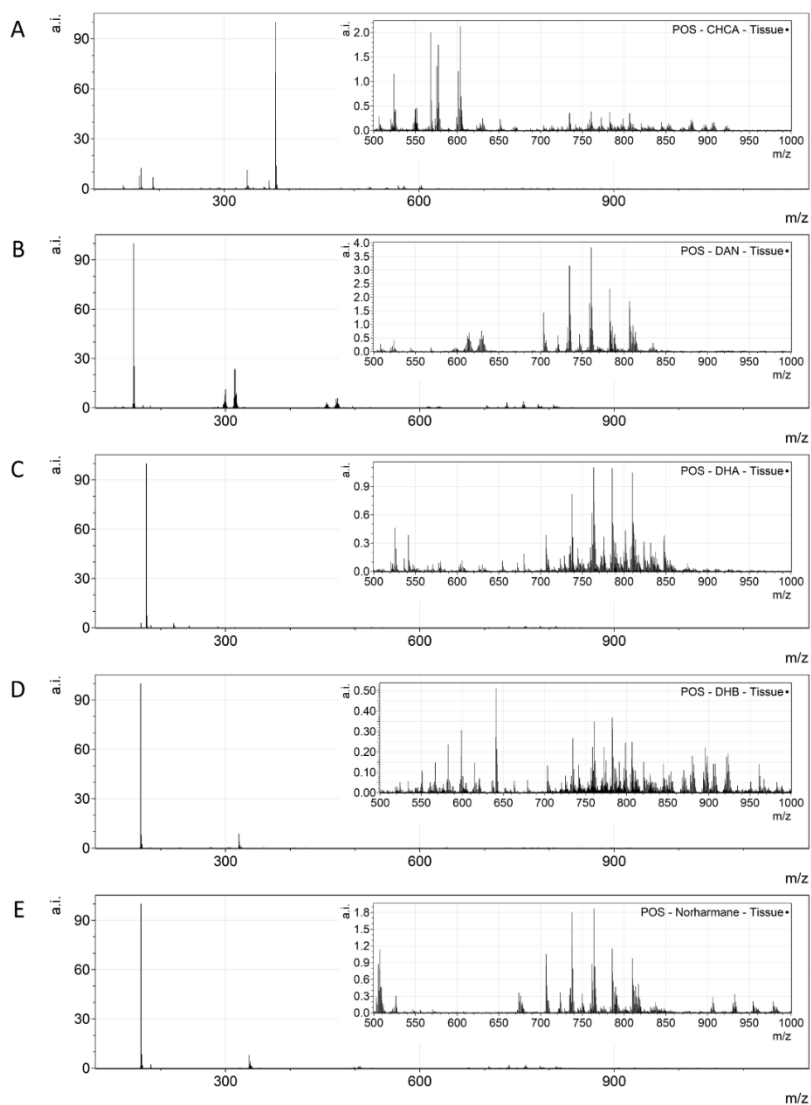


**Figure 3.9:** Profile mass spectra of the measured area for the different matrices in positive ion mode using mice bone for the untargeted application. Full range ( $m/z$  100-1200) mass spectra with an insertion of a zoom in of the  $m/z$  range 500-1000 for CHCA (A), DAN (B), DHA (C), DHB (D), and norharmane (E). Mass spectra represent the combined signal from bone, bone marrow, surrounding (muscle) tissue and some surrounding background signal.

**Table 3.3:** Comparison of CHCA, DAN, DHA, DHB, and norharmane in positive ion mode using mice hind legs for the untargeted application.

The number of specific  $m/z$  values is given for bone as well as bone marrow, which are the number of specific  $m/z$  values from the 2000 most intense peaks as selected by HDImaging (version 1.4, Waters Corporation). From these specific  $m/z$  values, values potentially related to the matrix and background were removed by comparing them to a measurement of the background. The average signal-to-noise (S/N) is calculated for the specific  $m/z$  values and the ratio to the background is calculated in comparison to the highest background peak, based on the S/N-values obtained after peak picking using mMass (Open Source Mass Spectrometry Tool, version 5.5.0). In addition, the interference of the matrix with signals from the tissue is given based on the average mass spectra looking at the amount of background signal and the overlap of background peaks with peaks specific for tissue.

Matrix	Specific $m/z$ values			Signal-to-noise (S/N) ratio			Interference of matrix with tissue signal	
	Bone	Bone marrow	Total	Average bone	Ratio to background (%)	Ratio to background (%)		
CHCA	50	57	107	257.62	0.04	895.20	0.14	Low
DAN	0	35	35	-	-	966.37	0.29	High
DHA	0	5	5	-	-	388.13	0.17	Low
DHB	96	7	103	223.51	0.05	81.51	0.02	Middle
Norharmane	0	23	23	-	-	138.22	0.09	Middle

**Table 3.4:** Tentative identifications of selected  $m/z$  values in positive ion mode.

Per  $m/z$  value from the merged dataset, the experimental  $m/z$  value from the average mass spectrum of the corresponding matrix, the  $m/z$  value for a random pixel (from the corresponding matrix), the matched molecular formula, the theoretical  $m/z$  value, the  $\Delta m$  ( $m/z_{exp} - m/z_{theo}$ ), the ppm error ( $\frac{m/z_{exp} - m/z_{theo}}{m/z_{theo}} \times 10^6$ ), the potential matching lipid(s), and the detected ion are provided.

Abbreviations lipid classes: CerP = ceramide phosphate; CerPE = glycerophosphoethanolamine ceramide; DAG = di(acyl/alkyl)glycerol; EPC = ethanolaminephosphoceramide; FA = fatty acids; HexCer = hexosyl ceramide; LIPC = lyso-inositolphosphoceramide; LPI = lyso-glycerophosphoinositols; MGDG = monogalactosylmonoacylglycerol; MGMG = monogalactosylmonoacylglycerol; PA = glycerophosphate; PAA = glycerophospholipid class; PC = glycerophosphocholine; PE = glycerophosphoethanolamine; PG = glycerophosphoglycerols; PI = glycerophosphoinositols; PS = glycerophosphoserine; SM = sphingomyelin; SPB = sphingoid base; SQMG = sulfoquinovosyl monoacylglycerol; ST = sterols; TAG = tri(acyl/alkyl)glycerol

Merged dataset $m/z$ value*	Experimental $m/z$ value average spectrum (matrix)	$m/z$ value random pixel (matrix)	Molecular formula	Theoretical $m/z$	$\Delta m$	Ppm error	Possible lipid	Ion
264.2711	264.2712 (CHCA)	264.2808 (CHCA)	C <sub>18</sub> H <sub>34</sub> N	264.2686	0.0026	9.84	SPB 18:2;O	[M+H-H <sub>2</sub> O] <sup>+</sup>
369.3721	369.3721 (CHCA)	369.3763 (CHCA)	C <sub>24</sub> H <sub>48</sub> O <sub>2</sub>	369.3727	-0.0006	-1.62	FA 24:0	[M+H] <sup>+</sup>
470.2184	470.2084 (DAN)	470.2063 (DAN)	C <sub>19</sub> H <sub>37</sub> NO <sub>10</sub> P	470.2150	-0.0066	-14.04	LIPC 13:2;O2	[M+H] <sup>+</sup>
482.3470	482.3409 (DAN)	482.3486 (DAN)	C <sub>27</sub> H <sub>48</sub> NO <sub>6</sub>	482.3476	-0.0067	-13.89	ST 27:2;O6	[M+NH <sub>4</sub> ] <sup>+</sup>
510.3497	510.3694 (DAN)	510.3800 (DAN)	C <sub>25</sub> H <sub>52</sub> NO <sub>9</sub>	510.3637	0.0057	11.17	MGMG 16:0	[M+NH <sub>4</sub> ] <sup>+</sup>

\* As displayed in Figure 3.8.

Table 3.4 (continued): Tentative identifications of selected  $m/z$  values in positive ion mode.

Merged dataset $m/z$ value*	Experimental $m/z$ value average spectrum (matrix)	$m/z$ value random pixel (matrix)	Molecular formula	Theoretical $m/z$	$\Delta m$	Ppm error	Possible lipid	Ion
541.2046	541.2724 (DHA)	541.2345 (DHA)	C <sub>24</sub> H <sub>45</sub> O <sub>11</sub> S	541.2677	0.0047	8.68	SQMG 15:1	[M+H] <sup>+</sup>
			C <sub>24</sub> H <sub>46</sub> O <sub>11</sub> P	541.2772	-0.0048	-8.87	LPI 15:0	[M+H-H <sub>2</sub> O] <sup>+</sup>
			C <sub>27</sub> H <sub>41</sub> O <sub>11</sub>	541.2643	0.0081	14.96	ST 21:2;O5;GlcA	[M+H] <sup>+</sup>
563.5326	563.4944 (CHCA)	563.5432 (CHCA)	C <sub>34</sub> H <sub>68</sub> O <sub>4</sub> Na	563.5010	-0.0066	-11.71	DAG O-3:1:0	[M+Na] <sup>+</sup>
			C <sub>41</sub> H <sub>80</sub> NO <sub>5</sub> PNa	720.5667	0.0034	4.72	CerP 41:2;O	[M+Na] <sup>+</sup>
			C <sub>41</sub> H <sub>79</sub> NO <sub>7</sub> Na	720.5749	-0.0048	-6.66	HexCer 35:1;O	[M+Na] <sup>+</sup>
							CerPE 36:2;O3	
720.5671	720.5701 (DAN)	720.5379	C <sub>38</sub> H <sub>79</sub> N <sub>3</sub> O <sub>7</sub> P	720.5650	0.0051	7.08	EPC 36:2;O3	[M+NH <sub>4</sub> ] <sup>+</sup>
							SM 33:2;O3	
			C <sub>43</sub> H <sub>78</sub> NO <sub>7</sub>	720.5772	-0.0071	-9.85	TAG 40:4;O	[M+NH <sub>4</sub> ] <sup>+</sup>
			C <sub>39</sub> H <sub>78</sub> NO <sub>10</sub>	720.5620	0.0081	11.24	HexCer 33:0;O4	[M+H] <sup>+</sup>
			C <sub>39</sub> H <sub>78</sub> NO <sub>10</sub>	720.5620	0.0081	11.24	MGDG 30:0	[M+NH <sub>4</sub> ] <sup>+</sup>
			C <sub>41</sub> H <sub>79</sub> N <sub>2</sub> O <sub>6</sub> PNa	749.5568	0.0024	3.20	SM 36:3;O2	[M+Na] <sup>+</sup>
			C <sub>41</sub> H <sub>82</sub> O <sub>9</sub> P	749.5691	-0.0099	-13.21	PG O-35:1	[M+H] <sup>+</sup>
749.5561	749.5592 (DHA)	749.4490 (DHA)	C <sub>46</sub> H <sub>78</sub> O <sub>6</sub> Na	749.5691	-0.0099	-13.21	TAG 43:5	[M+Na] <sup>+</sup>
			C <sub>46</sub> H <sub>78</sub> O <sub>5</sub> K	749.5481	0.0111	14.81	DAG 43:6	[M+K] <sup>+</sup>
			C <sub>44</sub> H <sub>78</sub> O <sub>7</sub> P	749.5480	0.0112	14.94	PA 41:4	[M+H-H <sub>2</sub> O] <sup>+</sup>

\* As displayed in Figure 3.8.

Table 3.4 (continued): Tentative identifications of selected  $m/z$  values in positive ion mode.

Merged dataset $m/z$ value*	Experimental $m/z$ value average spectrum (matrix)	$m/z$ value random pixel (matrix)	Molecular formula	Theoretical $m/z$	$\Delta m$	Ppm error	Possible lipid	Ion
756.5372	756.5274 (CHCA)	756.5330 (CHCA)	C <sub>40</sub> H <sub>80</sub> NO <sub>7</sub> PK	756.5304	-0.0030	-3.97	PC O-32:1 PE O-35:1	[M+K] <sup>+</sup>
			C <sub>39</sub> H <sub>75</sub> NO <sub>11</sub> Na	756.5232	0.0042	5.55	HexCer 33:1;O5	[M+Na] <sup>+</sup>
			C <sub>45</sub> H <sub>75</sub> NO <sub>6</sub> P	756.5326	-0.0052	-6.87	PE O-40:8	[M+H-H <sub>2</sub> O] <sup>+</sup>
			C <sub>48</sub> H <sub>70</sub> NO <sub>6</sub>	756.5198	0.0076	10.05	TAG 45:13	[M+NH <sub>4</sub> ] <sup>+</sup>
			C <sub>41</sub> H <sub>75</sub> NO <sub>9</sub> P	756.5174	0.0100	13.22	PS 35:2	[M+H-H <sub>2</sub> O] <sup>+</sup>
			C <sub>41</sub> H <sub>75</sub> NO <sub>9</sub> P	756.5174	0.0100	13.22	PAA 36:3	[M+H] <sup>+</sup>
			C <sub>40</sub> H <sub>79</sub> NO <sub>9</sub> K	756.5386	-0.0112	-14.80	HexCer 34:0;O3	[M+K] <sup>+</sup>
			C <sub>40</sub> H <sub>76</sub> N <sub>2</sub> O <sub>10</sub> P	775.5232	-0.0039	-5.03	PS 34:3	[M+NH <sub>4</sub> ] <sup>+</sup>
			C <sub>43</sub> H <sub>77</sub> O <sub>8</sub> PNa	775.5248	-0.0055	-7.09	PA 40:4	[M+Na] <sup>+</sup>
			C <sub>40</sub> H <sub>81</sub> O <sub>9</sub> PK	775.5250	-0.0057	-7.35	PG O-34:0	[M+K] <sup>+</sup>
775.5374	775.5193 (DHA)	775.5063 (DHA)	C <sub>41</sub> H <sub>76</sub> O <sub>11</sub> P	775.5120	0.0073	9.41	PI O-32:2	[M+H-H <sub>2</sub> O] <sup>+</sup>
			C <sub>45</sub> H <sub>76</sub> O <sub>8</sub> P	775.5272	-0.0079	-10.19	PA 42:7	[M+H] <sup>+</sup>

\* As displayed in Figure 3.8.

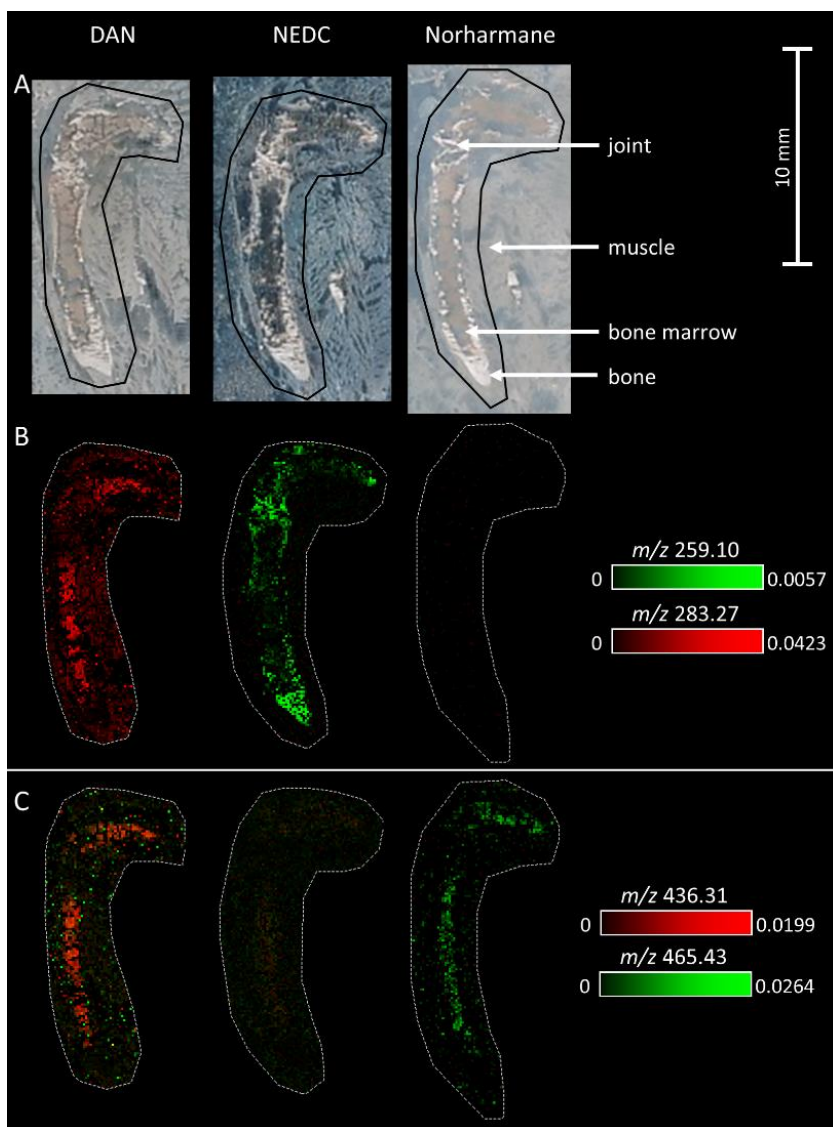


**Figure 3.10:** Overlay images of selected  $m/z$  values for DAN, NEDC, and norharmane in negative ion mode measured with MALDI-MSI of mice hind legs for the untargeted detection of lipids. The  $m/z$  values were selected to show the agreement and differences between the matrices in terms of desorption and ionization efficiency. **A** Optical scan of the section with the measured area indicated with a black line. Overlay images of the distributions of selected  $m/z$  values in the range 200-300 (**B**), and 300-500 (**C**). The distribution images are total ion current (TIC) normalized and the intensity scale show the maximum relative intensity of the specific  $m/z$  value. For tentative identifications of the selected  $m/z$  values see Table 3.6.

**Table 3.5:** Comparison of DAN, NEDC, and norharmane in negative ion mode using mice hind legs for the untargeted application

The number of specific  $m/z$  values is given for bone as well as bone marrow, which are the number of specific  $m/z$  values from the 2000 most intense peaks as selected by HDImaging (version 1.4, Waters Corporation). From these specific  $m/z$  values, values potentially related to the matrix and background were removed by comparing them to a measurement of the background. The average signal-to-noise (S/N) is calculated for the specific  $m/z$  values and the ratio to the background is calculated in comparison to the highest background peak, based on the S/N-values obtained after peak picking using mMass (Open Source Mass Spectrometry Tool, version 5.5.0). In addition, the interference of the matrix with signals from the tissue is given based on the average mass spectra looking at the amount of background signal and the overlap of background peaks with peaks specific for tissue.

Matrix	Specific $m/z$ values		Signal-to-noise (S/N) ratio			Interference of matrix with tissue signal		
	Bone	Bone marrow	Total	Average bone	Ratio to background (%)		Ratio to background (%)	
DAN	0	14	14	-	-	17186.58	0.63	Middle
NEDC	20	6	26	25773.37	4.61	2990.28	0.54	Extremely high
Norharmane	0	9	9	-	-	5846.46	0.02	Middle

**Table 3.6:** Tentative identifications of selected  $m/z$  values in negative ion mode.

Per  $m/z$  value from the merged dataset, the experimental  $m/z$  value from the average mass spectrum of the corresponding matrix, the  $m/z$  value for a random pixel (from the corresponding matrix), the matched molecular formula, the theoretical  $m/z$  value, the  $\Delta m$  ( $m/z_{exp} - m/z_{theo}$ ), the ppm error ( $\frac{m/z_{exp} - m/z_{theo}}{m/z_{theo}} \times 10^6$ ), the potential matching lipid(s), and the detected ion are provided.

Abbreviations lipid classes: CAR = acyl carnitine; FA= fatty acids; LPA = lyso-glycerophosphate; LSM = lyso-sphingomyelin; NAE = N-acyl ethanolamines; ST = sterols

Merged dataset $m/z$ value*	Experimental $m/z$ value average spectrum (matrix)	$m/z$ value random pixel (matrix)	Molecular formula	Theoretical $m/z$	$\Delta m$	Ppm error	Possible lipid	Ion
259.1009	259.0982 (NEDC)	259.0036 (NEDC)	C <sub>15</sub> H <sub>15</sub> O <sub>4</sub>	259.0976	0.0006	2.32	FA 14:7	[M+HCOO] <sup>-</sup>
283.2673	283.2640 (DAN)	283.2640 (DAN)	C <sub>18</sub> H <sub>35</sub> O <sub>2</sub>	283.2643	-0.0003	-1.06	FA 18:0	[M-H] <sup>-</sup>
436.3118	436.3096 (DAN)	436.3124 (DAN)	C <sub>25</sub> H <sub>42</sub> NO <sub>5</sub>	436.3069	0.0027	6.19	CAR 18:3;O	[M-H] <sup>-</sup>
			C <sub>25</sub> H <sub>42</sub> NO <sub>5</sub>	436.3069	0.0027	6.19	NAE 21:4;O	[M+CH <sub>3</sub> COO] <sup>-</sup>
			C <sub>25</sub> H <sub>42</sub> NO <sub>5</sub>	436.3069	0.0027	6.19	NAE 22:4;O	[M+HCOO] <sup>-</sup>
			C <sub>25</sub> H <sub>42</sub> NO <sub>5</sub>	436.3069	0.0027	6.19	NAE 21:4	[M+CH <sub>3</sub> OCCO] <sup>-</sup>
			C <sub>29</sub> H <sub>41</sub> O <sub>3</sub>	437.3061	0.0039	8.92	ST 27:5;O	[M+CH <sub>3</sub> COO] <sup>-</sup>
437.3100 (Norharmane)	437.3100 (Norharmane)	437.3044 (Norharmane)	C <sub>21</sub> H <sub>46</sub> N <sub>2</sub> O <sub>5</sub> P	437.3150	-0.0050	-11.39	LSM 16:0;O2	[M-H] <sup>-</sup>
			C <sub>22</sub> H <sub>46</sub> O <sub>8</sub> P	437.3038	0.0063	14.29	LPA O-19:0	[M-H] <sup>-</sup>

\* As displayed in Figure 3.10.

mode, DAN and NEDC have the most interference of matrix peaks with the tissue-related peaks, while there is some interference for norharmane (see mass spectra in Figure 3.11).

## 3.5 Discussion

### 3.5.1 Method optimization for sectioning of undecalcified bone tissue

Here, we present a sample preparation protocol for undecalcified bone tissue developed and optimized for analysis with MALDI-MSI. Embedding in an aqueous solution of 20% gelatin (w/v) and 7.5% carboxymethyl cellulose (CMC, w/v) in combination with the use of double-sided tape proved to be necessary to maintain sample integrity during sectioning. It is of utmost importance to avoid bubbles of any kind (air, water from melting crystals in tissue) in the medium during embedding of the tissue. Bubbles will result in holes in the embedding which cause less support during sectioning and thus low-quality sections. While at 60 °C, the embedding material is poured in a mold. The tissue sample is immersed

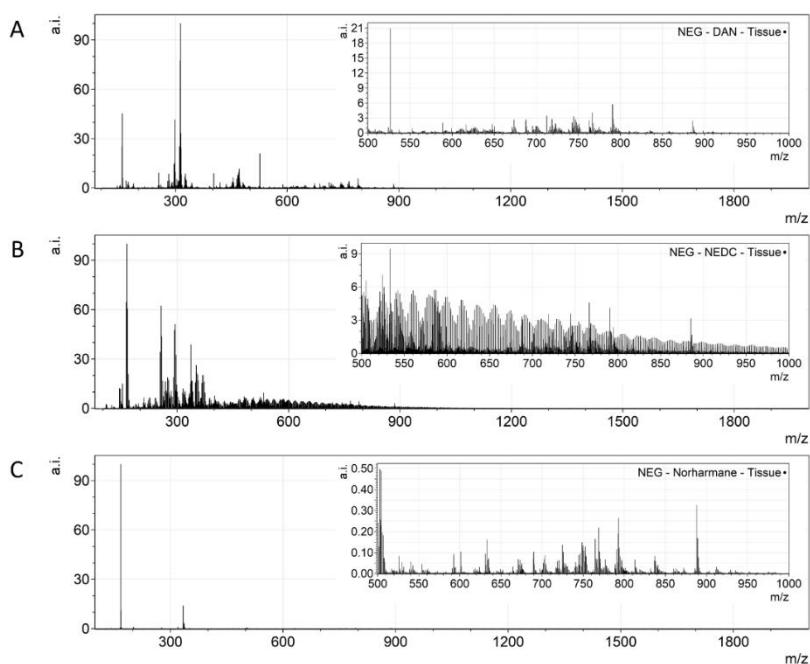


**Figure 3.11:** Profile mass spectra of the measured area for the different matrices in negative ion mode using mice bone for the untargeted application. Full range ( $m/z$  100-2000) mass spectra with an insertion of a zoom in of the  $m/z$  range 500-1000 for DAN (A), NEDC (B), and norharmane (C). Mass spectra represent the combined signal from bone, bone marrow, surrounding (muscle) tissue and some surrounding background signal.

immediately. As a result, the frozen sample will start melting. It is recommended to immediately start polymerization after sample embedding by freezing at  $-20\text{ }^{\circ}\text{C}$  to avoid tissue degeneration due to the heat. Only the tungsten carbide knife was found to be robust enough to cut bone tissue without permanent deformation of the blade. Different amounts of CMC were tested. The amount of CMC was increased compared with that in previous studies to ensure a smooth transition from embedding to bone tissue while sectioning. Increased amounts of CMC gave more homogenous sections with less relief compared with lower CMC concentrations. Above 7.5% (w/v), the solution was saturated and CMC could not dissolve anymore. Still the sections were not completely homogenous. An embedding medium with characteristics closer to those of bone tissue would have been even better, but this medium still has to be MSI-compatible, making conventionally used resins unsuitable. For example, other research groups use tragacanth or SCEM-L1 embedding medium for sectioning bone tissue.<sup>90,143</sup> Unfortunately, tragacanth is hygroscopic, making it not fit for use after storage in a freezer. On the contrary, the gelatin/CMC-embedded samples could be easily reused for at least 5 times after storage. Samples were stored in aluminum foil and frozen at  $-20\text{ }^{\circ}\text{C}$  or  $-80\text{ }^{\circ}\text{C}$ . Although the gelatin/CMC mixture is MS-compatible, it has the disadvantage of being used at higher temperature than the frozen tissue during embedding, which can cause heat stress and/or affect the molecular composition of the bone.<sup>130</sup>

Four different double-sided tapes were evaluated for suitability, specifically two non-conductive normal tapes and two conductive tapes. When choosing a tape as a support during sectioning, different parameters should be taken into consideration. The first one is the capability of the tape to stick to the frozen gelatin/CMC block. While the temperature affects the adherence of the tape, it is important to have a good adherence to the frozen sample to create a homogenous sample. As a result, the adherence will determine the optimal temperature for sectioning as well as the thickness of the sections. A tape with a good adherence makes it possible to generate thinner sections. In addition, the thickness of the sections should be considered carefully. On one side, a thin section will give less insulation and hence a higher overall signal intensity. On the other side, thinner sections also mean that less analyte will be available for extraction into the MALDI matrix and subsequent desorption.<sup>126</sup> Thicker sections will take more time to dry in the desiccator. It is noteworthy that some mass spectrometers, such as linear ToF, conductive samples/tape, and therefore the tape selected here, would be unsuitable. The double-sided Tesa<sup>®</sup> tape resulted in the most homogenous sections at a thickness of  $12\text{ }\mu\text{m}$ .

### 3.5.2 Targeted detection of methadone and EDDP

The targeted detection of methadone and its metabolite EDDP requires the right matrix which crystallizes with the chosen analyte but does not provide too many background peaks overlapping with the peaks of interest. This is important since most matrices show molecular ion signals, multiple adduct ions, as well as aggregates in the lower mass range ( $m/z < 1000$ ). A method for detection and visualization of methadone and its metabolites was developed and optimized. Matrix selection was performed using the dried droplet technique. Four common matrices were tested, of which DHB gave the best results. DHB showed the lowest LOD of 2.5 pg for methadone and 1 pg for EDDP. Additionally, no interfering peaks with the small molecules from methadone and EDDP were found. SA showed to ionize the analyte of interest, but increased LODs. CHCA also showed to ionize the analyte of interest but an interfering peak was close to the mass of the metabolite EDDP. THAP did not work for this application. The sensitivity of MALDI-MSI technology was tested by investigating the LODs. Significant ion suppression was noticed when spiking standards on bone tissue compared with ITO slides. In this study, a deliberate choice was made for a sample preparation protocol without any pretreatment of the bone tissue to reduce interfering molecules or other contaminants. This is required to maintain the molecular distribution and to retain the presence of minerals and lipids in the bone tissue. As lipids desorb/ionize relatively easily, they are the dominant fraction of ions in every MALDI-MSI spectrum. Thereby, lipids suppress molecular ion fractions of lower abundance or molecular ion fractions that desorb/ionize with more difficulty.<sup>36</sup> The intensities of methadone and EDDP decrease on the tape and even further on the bone tissue when compared to the ITO glass slide (Figure 3.4). The obtained findings indicate that bone tissue and the supporting tape have a significant negative effect on the grade of desorption/ionization. These negative effects can partly be accounted for by the high content of minerals, e.g., hydroxyapatite, and lipids present in the bone. When comparing the intensities between the spots on tape and those on the ITO slide, also a diminishing effect on the desorption/ionization rate is seen solely due to the tape.

Another factor of impact could be height differences in the sample surface. The samples consisted of heterogeneous tissues such as bone tissue, bone marrow, and even surrounding tissue. Due to drying, the thickness of the section can change in nanometers. Bone does not shrink when dried, but bone marrow does. As a result, minor peak shifts can occur. This problem was countered by the usage of an orthogonal ToF system, in which the source is decoupled from the mass analysis. This causes the mass analysis to be independent of the height of the sample, making

it better suited for the analysis of non-homogenous samples, such as bone.<sup>40</sup> Nevertheless, ionization efficiency may be affected as the laser is not optimally focused on each part of the tissue if height differences occur.<sup>144</sup>

In the MALDI-MSI experiments, methadone ( $m/z$  310.21) and EDDP ( $m/z$  278.18) were distinguishable from background signals in the bone marrow of the rat and human bone (see Figures 3.6 and 3.7). Confirmatory MS/MS experiments were not performed due to the low intensities of our analytes, but high mass accuracy of the oToF system strongly corroborates our so far tentative assignment. Internal calibration of the instrument was performed daily in the mass range 50–650 Da (< 1 ppm) using red phosphorus. Afterwards, the mass accuracy was checked with quality control samples in the form of calibration series spiked on blank bone sections. Aside to that, the untreated and dosed bones were analyzed in the same experimental run to ensure a consistent mass accuracy.

When looking at the cross section of human bone tissue, it still looked slightly shattered. This is in part caused by the histological structure of bone tissue. Compact bone mostly consists of osteons or Haversian systems, which are cylindrical structures. They are aligned parallel to the long axis of the bone. Therefore, sections made in parallel with the osteons give the best results, while sectioning perpendicular to the osteons causes fragmentation, as seen in the human clavicle. Another important factor is that the sample sectioning method is optimized using rat bone. Rat bone is less hard than human bone which causes more fractions in the human sections.

### 3.5.3 Untargeted detection of lipids

As only a few studies have been performed on undecalcified bone using MALDI-MSI, it is important to compare different matrices in their ability to desorb and ionize a broad range of lipids from bone and bone marrow. Different lipid classes are of interest in (pre)clinical research, because of their important regulating role in maintaining bone health and fracture healing.<sup>90,137</sup> This broad range of lipids can contribute to improve the understanding of the lipid pathways in bone healing and impaired bone healing. Here, different matrices were compared based on the number of specific  $m/z$  values from bone as well as bone marrow, the intensity of the specific  $m/z$  values in comparison with the matrix peaks, the amount of background signal from the matrix, and the interference of the matrix peaks with signal from the tissue.

In positive ion mode, five matrices for measurement of lipids were compared, namely CHCA, DAN, DHA, DHB, and norharmane. Of these matrices, DAN was the

only matrix that showed an unwanted reaction with components of the double-sided tape over time after the measurement was performed. The tape became untransparent, which can cause complications with staining of the same section after the MALDI-MSI measurement. Besides, DAN showed the highest interference of the matrix and background peaks with the tissue-related peaks of all the matrices (Table 3.3). For all matrices in positive ion mode, it was possible to obtain ion distribution images up to  $m/z$  800 (see Figure 3.8). The bone and bone marrow-specific  $m/z$  values could be found over the complete measured mass range, although these intensities were lower for  $m/z$  values above 800. This broad range of values indicated that different lipid classes could be obtained with these matrices, which have been shown to be present in bone and bone marrow and contribute to bone health.<sup>137</sup> With DAN, DHA, and norharmane, no specific  $m/z$  values could be obtained from only bone tissue in the 2000 most abundant peaks, which makes these matrixes less suitable for the (pre)clinical research related to fracture healing. CHCA and/or DHB showed to be the best matrices for the analysis of lipids in bone and bone marrow, as these matrices resulted in the highest number of  $m/z$  values specific for bone as well as bone marrow with low interference of the matrix and background peaks with the tissue-specific peaks. Nevertheless, the intensities and S/N values of the specific  $m/z$  values for bone and bone marrow are relatively low.

In Figure 3.8, it can be seen that most of the selected  $m/z$  values are not present in all the different matrices. Most of the detected  $m/z$  values specific for bone or bone marrow were found in only one of the compared matrices or showed different distributions between matrices, for example, surrounding muscle tissue versus bone marrow. This can indicate that the detected molecules at the same  $m/z$  value might not be the same between matrices, emphasizing the fact that the desorption and ionization mechanism of each matrix is different, resulting in the ionization of different lipid classes.<sup>145</sup> Therefore, matrix selection depends on the lipid class of interest. For positive ion mode, CHCA and DHB showed to be able to absorb and ionize a broad range of lipid classes from bone and bone marrow. These matrices could be used in future preclinical studies about different skeletal diseases.

For the matrices tested in negative ion mode, it was possible to create distribution images up to  $m/z$  500 (see Figure 3.10). For DAN and norharmane, a few specific  $m/z$  values for bone marrow could be found above  $m/z$  500, but not for NEDC. With limited or no detection of lipids in bone and bone marrow, major lipid classes can be missed, for example, certain subclasses phospholipids that ionize better in negative ion mode.<sup>145</sup> Although these subclasses have been shown to play a role in

bone health.<sup>137</sup> No specific  $m/z$  values for bone tissue could be obtained with DAN and norharmane. Based on specific  $m/z$  values, NEDC is the only matrix for which specific  $m/z$  values for bone as well as bone marrow could be obtained. However, the background signal and interference of this matrix is high (see Figure 3.11). In negative ion mode, none of the tested matrices provided the desired result in terms of detection of  $m/z$  values specific for bone and bone marrow in combination with low interference of the matrix with the signal from the tissue. Therefore, further testing of the best matrix in negative ion mode is necessary.

For most of the matrices, the intensities and S/N values for the detected molecules were relatively low, especially compared with the high intensities of matrix peaks. It is expected to obtain an improvement in these values by applying the matrix by spraying it with an automated sprayer. Spraying the matrix is a wetter matrix application method allowing for a better extraction of analytes from the tissue.<sup>146</sup> In addition, trifluoroacetic acid (TFA) can be added when spraying CHCA or DHB to further enhance the extraction of molecules from the tissue.<sup>36,65</sup> An advantage of matrix sublimation in comparison with spraying of a matrix is the lower diffusion of analyte and, therefore, less delocalization.<sup>36</sup> In addition, sublimation results in smaller crystals than when a matrix is sprayed, which can be an advantage for measurements at lower spatial resolution.<sup>36</sup> In general, the application of a matrix by sublimation is faster than spraying and should provide good detection of different lipid classes, which is why for this study sublimation was selected. Nevertheless, whether or not spraying of the matrix will improve detection and intensity of different lipid classes for bone tissue should be studied.

### 3.6 Conclusion

This study describes the optimization of the sample preparation protocol for MALDI-MSI of undecalcified bone tissue in close contact with soft tissue like bone marrow or muscle tissue. Embedding of the sample in combination with a supportive tape to transfer the section to the sample holder is necessary to obtain high-quality bone sections. As height differences may occur between bone and bone marrow, mass spectrometers that are not affected by these differences are more appropriate for analysis of bone tissue. Experiments can be performed on mass spectrometers where the ionization is decoupled from the mass analysis. This optimized bone tissue preparation protocol for MALDI-MSI was applied in a targeted and untargeted approach. The sample preparation protocol was shown to be applicable for the targeted detection of methadone and its metabolites as well as the untargeted detection of lipids from bone tissue. MALDI-MSI has been used to estimate the limits of detection and the distribution of the methadone and its

### Sample preparation of bone tissue for MALDI-MSI

metabolites in rat and human bone tissue. In addition, CHCA and/or DHB showed to be the best matrix for lipid detection in positive ion mode. The optimized sample preparation protocol and these targeted and untargeted approaches clear the path for future forensic and (pre)clinical investigations.



# Chapter 4: Lipid analysis of fracture hematoma with MALDI-MSI - Specific lipids are associated to bone fracture healing over time

# 4

Rald V.M. Groven\*

Sylvia P. Nauta\*

Jane Gruisen

Britt S.R. Claes

Johannes Greven

Martijn van Griensven

Martijn Poeze

Ron M.A. Heeren

Tiffany Porta Siegel

Berta Cillero-Pastor

Taco J. Blokhuis

\*Shared first authorship

Frontiers in Chemistry

2022; 9:780626



## 4.1 Abstract

Fracture healing is a complex process, involving cell-cell interactions, various cytokines, and growth factors. Although fracture treatment improved over the last decades, a substantial part of all fractures shows delayed or absent healing. The fracture hematoma (fxh) is known to have a relevant role in this process, while the exact mechanisms by which it influences fracture healing are poorly understood. To improve strategies in fracture treatment, regulatory pathways in fracture healing need to be investigated. Lipids are important molecules in cellular signaling, inflammation, and metabolism, as well as key structural components of the cell. Analysis of the lipid spectrum in fxh may therefore reflect important events during the early healing phase. This study aims to develop a protocol for the determination of lipid signals over time, and the identification of lipids that contribute to these signals, with matrix-assisted laser desorption/ionization mass spectrometry imaging (MALDI-MSI) in fxh in healthy fracture healing. Twelve fxh samples (6 porcine; 6 human) were surgically removed, snap frozen, sectioned, washed, and analyzed using MALDI-MSI in positive and negative ion mode at different time points after fracture (porcine: 72 h; human samples: range 1-19 days). A tissue preparation protocol for lipid analysis of fxh sections was developed and optimized. Although hematoma is a heterogeneous tissue, the intra-variability within fxh was smaller than the inter-variability between fxh. Distinctive  $m/z$  values were detected that contributed to the separation of three different fxh age groups: early (1-3 days), middle (6-10 days), and late (12-19 days). Identification of the distinctive  $m/z$  values provided a panel of specific lipids that showed a time dependent expression within fxh. This study shows that MALDI-MSI is a suitable analytical tool for lipid analysis in fxh and that lipid patterns within fxh are time-dependent. These lipid patterns within fxh may serve as a future diagnostic tool. These findings warrant further research into fxh analysis using MALDI-MSI and its possible clinical implications in fracture treatment.

## 4.2 Introduction

Fracture healing is a complex process in which a great variety of cells, signaling molecules, and cellular signaling pathways are involved.<sup>147</sup> Although fracture treatment has advanced greatly over the past decades, a substantial portion of fractures still suffers from impaired healing in the form of delayed healing or non-union.<sup>147,148</sup> Treatment of these complications often consists of multiple surgical interventions and, even if the interventions are successful, a long trajectory of rehabilitation.<sup>149</sup> Therefore, insights in fracture healing processes at an early stage may help to prevent or treat these complications.<sup>7,150,151</sup>

The fracture healing process can be divided into three main phases: inflammation, bone repair, and bone remodeling.<sup>148</sup> The first phase starts immediately after the fracture occurs, with the formation of the fracture hematoma (fxh). The fxh is considered to play a pivotal role in proper fracture healing, since it initiates the inflammatory response and creates a microenvironment to which a variety of cells is attracted by means of chemotaxis. Studies have shown that the removal or debridement of the fxh as well as an overshoot in the inflammatory response can induce adverse effects on fracture healing.<sup>12,147,148,152,153</sup> Cytokines and growth factors within the fxh facilitate the influx of inflammatory and mesenchymal stem cells and regulate capillary growth, which is necessary to replace extracellular matrix with granulation tissue.<sup>147,150,153</sup> Therefore, the molecular environment in fxh changes based on this cellular trafficking.<sup>150,154,155</sup>

During the following phases of fracture healing, the fxh acts as a basis for the formation of granulation tissue, also known as callus, which will gradually ossify as time progresses to bridge the fracture gap. Being an important initiator of the fracture healing cascade, investigating the molecular environment of the fxh at different time points after trauma could provide more insight into early fracture healing processes. Mass spectrometry offers potential advantages in understanding these dynamic molecular patterns and their regulatory effects on fracture healing as well as their possible complications.

Matrix-assisted laser desorption/ionization mass spectrometry imaging (MALDI-MSI) is a suitable imaging modality that allows for the untargeted, spatially resolved detection of a variety of molecules in tissue sections. The applicability of this technique to many research fields derives from its intrinsic property to detect a broad range of molecular classes, such as lipids or proteins, in a single experiment, without prior knowledge or hypothesis on the composition of a sample.<sup>33</sup>

A schematic overview of the MALDI-MSI workflow is depicted in Figure 4.1. A tissue section is covered with a matrix, which co-crystallizes with the analyte molecules. The matrix-analyte mixture absorbs the energy of the focused laser beam hitting the sample surface. This results in the local desorption and ionization of the analytes into the gas phase. The analysis of these ions with a mass spectrometer provides a mass spectrum, which depicts their mass-to-charge ratio ( $m/z$ ). The analysis of mass spectra of multiple laser spots (or pixels) allows for the determination of the spatial distribution of certain molecules in the sample.<sup>33,34,156-159</sup> Histological staining of the same section after MSI enables the correlation of the detected molecules to a certain anatomical region within the sample.

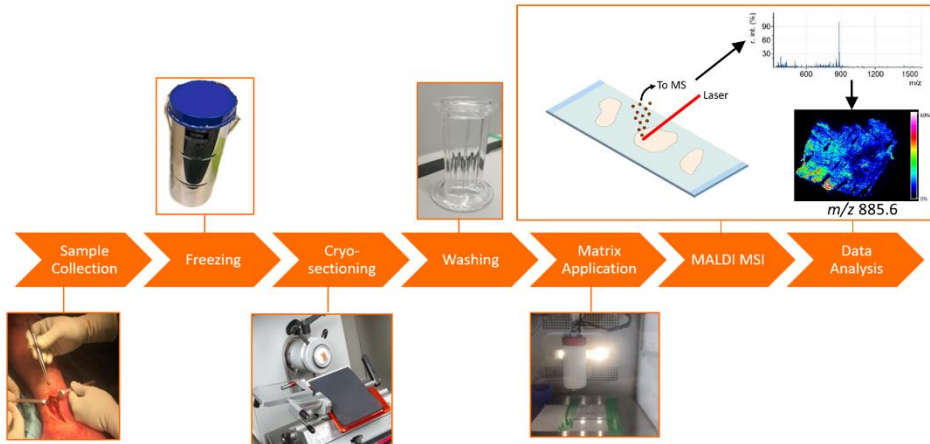


**Figure 4.1:** General MALDI-MSI workflow, applied to fracture hematoma analysis. The fxh was surgically removed and snap frozen in liquid nitrogen. The fxh was cryo-sectioned and thaw mounted on ITO slides. The slides were washed by submerging them in either ammonium formate or acetone. Afterwards, norharmane was homogenously sprayed onto the slides. The coated slides were analyzed by MALDI-MSI after which the data were processed and visualized.

To our knowledge, MALDI-MSI has not yet been reported for the analysis of fracture healing processes. Using MALDI-MSI to analyze fxh at different time points during the fracture healing process could help to understand changes in molecular patterns throughout different phases of fracture healing. Lipids are suitable target molecules for the examination of potential use and application of MALDI-MSI for fxh analysis since they are key molecules in cellular signaling, inflammation, and metabolism, as well as important structural components of the cell.<sup>160-166</sup>

In this study, we used MALDI-MSI to investigate the lipid signature and its spatial distribution in fxh samples taken at different time points between trauma and surgery. A sample preparation procedure was developed to improve lipid signal intensities. One of the key challenges in this sample preparation was the removal of blood from the fxh with a washing step, since it contains large quantities of heme. Heme is easily ionized and therefore negatively affects the ionization of lipids and other molecules, a process called ion suppression. The washing step should improve lipid signal intensities without delocalization. Furthermore, the intra-variability of the detected molecules within the fxh was evaluated to establish if differences in molecular patterns occur based on their specific location within the fxh. Thus, the aims of this study are to: 1) Develop a methodology for analysis of

fxh with MALDI-MSI, 2) Investigate the intra-variability of the molecular profile within fxh, and 3) Identify fxh time-dependent molecular patterns between the fxh.

### 4.3 Materials and methods

#### 4.3.1 Materials

Ammonium formate, norharmane, Mayer's hematoxylin, and eosin were purchased from Sigma Aldrich (St. Louis, MO, USA). Acetone (HPLC grade), chloroform (HPLC grade), ethanol (HPLC grade), n-hexane (HPLC grade), methanol (ULC/MS-CC/SFC grade), and deionized water (ULC/MS-CC/ SFC grade) were purchased from Biosolve B.V. (Valkenswaard, the Netherlands).

#### 4.3.2 Samples—Fracture hematoma

Fxh were obtained from pigs for method development and investigation of the intra-variability. Fxh were obtained from humans for the method validation and the investigation of time-dependent molecular patterns. An overview of the fxh tissue and age used for the different objectives can be found in Table 4.1. The fxh age is defined as the number of days between the bone fracture and surgical intervention.

##### 4.3.2.1 Porcine fxh

Porcine fxh were collected from closed tibia shaft fractures that were created during animal experiments, as previously published by Guo *et al.* (2020).<sup>167</sup> In short, a multi-trauma model was used to study hematological and chemical profiles in a porcine model of severe multi-trauma over a time period of 72 h after trauma. During the experiments, all animals were kept sedated and fxh were harvested 72 h after fracture induction. All procedures were approved by the animal care and use office of the state of Nordrhein-Westfalen (approval number: LANUV AZ 81–02.04.2017.A412).

##### 4.3.2.2 Human fxh

The human fxh were collected during open surgical reduction and internal fixation of metaphyseal long bone fractures. For the detection of molecular patterns, samples were gathered from male patients with metaphyseal bone fractures, without further known comorbidities, that showed uneventful fracture healing, with a mean age of  $51 \pm 20$  years. Due to patient-specific reasons, fracture surgery was performed at different time points after trauma which enables harvesting of a range of fxh of different ages (2-19 days). The Medical Ethical Committee of the MUMC+ approved this study (approval number: MEC 16-4-251).

**Table 4.1:** Overview of fxh tissues and ages used for the different objectives.

Objective	fxh tissue	fxh age
Tissue washing comparison	1 Human	3 days
	1 Porcine	3 days
Intra-hematoma variability	4 Porcine	3 days
Detection of molecular patterns	2 Human	2 days
	2 Human	9 days
	2 Human	19 days

### 4.3.3 General sample preparation and MALDI-MSI protocol

The workflow for the sample preparation and MALDI-MSI analysis of fxh can be described in six steps (Figure 4.1). H&E staining was performed after MALDI-MSI analysis. The general protocol was used for the different experiments with minor adaptations when specified.

#### 4.3.3.1 Sample collection and freezing

The fxh were harvested and snap-frozen in aluminum containers dipped in liquid nitrogen to stop cellular biological processes.<sup>36</sup> The fxh were stored at  $-80^{\circ}\text{C}$  until further use. The containers were put on ice when transferring for a short period of time.

#### 4.3.3.2 Cryo-sectioning

Indium tin oxide (ITO) slides were cleansed for 10 min each by sonicating them in n-hexane and ethanol, consecutively. The fxh were cryo-sectioned at  $12\ \mu\text{m}$  using a Leica CM1860 UV cryostat (Leica microsystems, B.V., Amsterdam, the Netherlands) between  $-22$  and  $-24^{\circ}\text{C}$ . The sectioned fxh were thaw mounted on ITO slides (Delta Technologies, Colorado, USA). Afterwards, the slides with fxh sections were dried with nitrogenous gas. The slides were stored at  $-80^{\circ}\text{C}$ , until further use.

#### 4.3.3.3 Washing

The ITO slides with tissues sections were submerged for a defined amount of time (15–120 s) in either ammonium formate or acetone. After submersion, the slides were dried by nitrogen gas. More details about this step can be found in the paragraph ‘4.3.4 Comparison of different tissue washing methods’.

#### 4.3.3.4 Matrix application

In this study, 7 mg/ml norharmane in 2:1 chloroform and methanol (v:v) was applied for the extraction of lipids. This matrix solution was sonicated for 15 minutes and applied to the slides using an HTX TM sprayer (HTX technologies, LC, North Carolina, USA). Ten layers of matrix were applied with a drying time of 30 s

between each layer using a nozzle temperature of 30 °C and a flow rate of 0.12 mL/min. The velocity was set at 1200 mm/min with a track spacing of 3 mm.

### 4.3.3.5 MALDI-MSI

Experiments were performed with a RapifleX MALDI TissueTyper mass analyzer system (Bruker, Bremen, Germany) in reflector mode. The data were acquired at a 50 µm by 50 µm raster size with 200 laser shots/pixel at a laser frequency of 10 kHz. Positive and negative ion mode spectra were acquired to analyze lipids over a mass range of  $m/z$  340-1200 and 340-1600, respectively. The system was calibrated with red phosphorus before acquisition.

### 4.3.3.6 Data analysis

FlexImaging v4.1 (Bruker Daltonik GmbH, Bremen, Germany) was used to visualize the molecular distributions. SCiLS lab 2016b (SCiLS GmbH, Bremen, Germany) was used for data analysis and data conversion. Principal component analysis—linear discriminant analysis (PCA-LDA) was performed and visualized with an in-house built ChemomeTricks toolbox for MATLAB (version 2014a, The MathWorks, Natick, USA) to compare different groups.

### 4.3.3.7 H&E staining

After the MSI analysis, the matrix was removed from the slides with 70% ethanol. The slides were hematoxylin-eosin (H&E) stained. The stained slides were scanned with a M8 Microscope and Scanner (PreciPoint, Freising, Germany) at ×20 magnification and co-registered with the MALDI-MSI distribution images.

## 4.3.4 Comparison of different tissue washing methods

Different tissue washing methods were compared to increase lipid signal intensities after washing of heme. In addition, the possible delocalization of molecules caused by the washing of the lipids was assessed. Slides with porcine or human fxh were submerged in ammonium formate (50 mM in water, pH 7) or acetone. In-between washing steps and at the end, slides were dried with a gentle flow of nitrogen gas. Unwashed samples served as a control. An overview of the different washing methods compared for negative and positive ion modes can be found in Table 4.2. The number of washing methods tested for positive ion mode was reduced based on the results in negative ion mode, as the longest washing methods resulted in reduced lipid intensity and increased lipid delocalization. Three technical replicates were acquired per washing method. The remaining tissue preparation protocol and analyses were as described above in the general methods.

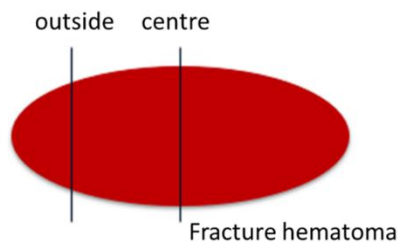
**Table 4.2:** Overview of the different washing methods that were applied to the fxh, including the polarity.

Washing solvent	Washing time	Negative ion mode	Positive ion mode
Ammonium formate	30 s	X	X
	15 s twice	X	X
	30 s twice	X	-
	15 s four times	X	-
Acetone	30 s twice	X	X
	30 s four times	X	-
No-wash (control)	-	X	X

Comparison of the washing methods was done based on the mean signal-to-noise (S/N) values of ten selected ion peaks and the heme peak ( $m/z$  value based on literature). In addition, the ratios of the intensity of selected  $m/z$  values over the heme ion intensity (M/H) were compared. The  $m/z$  values were selected based on the highest intensities (excluding isotopes) and to cover the mass range of  $m/z$  650–950. The optimal washing method was selected based on the combination of high ratios, adequate blood removal, and minimal lipid delocalization.

#### 4.3.5 Intra-variability of fxh

A comparison of the molecular profiles of the outside and center of the fxh was performed to study the heterogeneity of the samples. For this purpose, multiple slides were created with three consecutive sections of the outside and the center for four porcine fxh (see Figure 4.2). The sections for the outside were sectioned as close to the border of the sample as possible after minimal trimming. The center of the fxh was determined based on visual observation of size and shape, as the center differs distinctively for each fracture hematoma due to their differences in size and shape. The remaining tissue preparation protocol and analyses were as described above in the general method.

**Figure 4.2:** Schematic view of fxh and the location of sectioning for the outside and center sections.

#### 4.3.6 Identify fxh age-dependent molecular patterns

One of the objectives was to compare the molecular profiles of human fxh of different fxh ages. The selected fxh ages were two, nine, and 19 days after bone fracture to represent different time points in the early stages of the fracture healing cascade. Per sample at least five technical replicates were acquired. The slides were used for acquisition in negative and positive ion mode. The remaining tissue preparation protocol and analyses were as described above in the general method.

The different fxh ages were compared in both negative and positive ion mode using PCA-LDA. This analysis defines discriminant functions (DFs) that maximize the variance between classes while minimizing the variance within classes. The DF-score plots show which groups can be separated using that DF while the scaled loadings plot provides the corresponding  $m/z$  values. The scaled loadings are a combination of the intensity of the  $m/z$  value and the extent to which the molecule contributes to the separation of classes across the specified discriminant function. The scaled loadings on the positive side contribute more to the class at the positive side of the DF score and vice versa.

#### 4.3.7 Lipid identification

Molecules of interest were determined based on the PCA-LDA analysis of human fxh of different fxh ages. These molecules of interest were identified based on the highest scaled loadings for the different classes. Background peaks, matrix clusters, and isotopes were removed from the lists of  $m/z$  values with high scaled loadings. The molecules were identified by MS/MS analysis using collision-induced dissociation (CID) to fragment molecules of interest. Data for lipid identification were acquired using a data-dependent acquisition (DDA)-imaging method, as described previously.<sup>168</sup> Shortly, MSI and MS/MS data were acquired on an Orbitrap Elite hybrid ion trap mass spectrometer (Thermo Fisher Scientific GmbH, Bremen, Germany) using a stage step size of  $25 \times 50 \mu\text{m}^2$ . MSI (MS1) data of  $m/z$  300-2000 were acquired at a nominal mass resolution of 240,000 (at  $m/z$  400) using an injection time of 250 ms for both positive and negative ion mode. In parallel, the MS/MS data were acquired using the ion trap with an isolation window of 1 Da; a normalized collision energy of 30.0 (manufacturer units) with an activation  $q$  value of 0.17 in positive ion mode, and 38.0 and 0.25 in negative ion mode, respectively. Data analysis and lipid assignments were performed using Thermo Xcalibur (version 4.2, Thermo Fisher Scientific) and LipostarMSI<sup>169</sup> (version 1.1.0b26, Molecular Horizon, Bettona, Italy).

## 4.4 Results

### 4.4.1 Comparing different tissue washing methods

#### 4.4.1.1 Porcine fxb

The ratios between the mean intensities of selected  $m/z$  values and heme, as well as the S/N values of the selected  $m/z$  values of porcine fxb in both ion modes, were increased after washing the sections in either ammonium formate or acetone (Figures 4.3A, B, and Tables 4.3A, B).

In negative ion mode, submerging the sections in ammonium formate for 15 seconds twice resulted in the highest ratios for most  $m/z$  values, as seen in Figure 4.3A. Washing the sections in acetone for 30 seconds twice enhanced the S/N value for heme compared to no wash, while for the other washing methods the heme S/N value decreased (Table 4.3A). The highest S/N values for most of the selected  $m/z$  values were obtained with washing in ammonium formate for 30 seconds once or 15 seconds twice.

In positive ion mode, submerging the sections in ammonium formate for 15 seconds twice resulted in the highest ratios for most  $m/z$  values (Figure 4.3B). Only washing twice with ammonium formate for 15 seconds decreased the S/N value for heme compared to no wash (Table 4.3B). For the other methods, the S/N value of heme increased. The highest S/N values for most of the selected  $m/z$  values were obtained with washing in ammonium formate for 30 seconds once or 15 seconds twice.

#### 4.4.1.2 Human fxb

MSI results of human fxb also improved in both ion modes. The ratios between the mean intensities of selected  $m/z$  values and heme as well as the S/N values of the selected  $m/z$  values were increased after washing the sections in either ammonium formate or acetone, as for the porcine samples (Figures 4.3C, D, and Tables 4.3C, D).

In negative ion mode, submerging the sections in ammonium formate for 15 seconds four times resulted in the highest ratios for most  $m/z$  values (Figure 4.3C). Washing the sections in ammonium formate for 30 seconds twice or 15 seconds four times resulted in a decreased S/N value of heme compared to unwashed controls, while the other washing methods resulted in an increased heme S/N value (Table 4.3C). The highest S/N values for all the selected  $m/z$  values were obtained with washing in ammonium formate for 30 seconds once or 15 seconds twice, despite the S/N ratios being the highest for ammonium formate for 15 seconds four times.

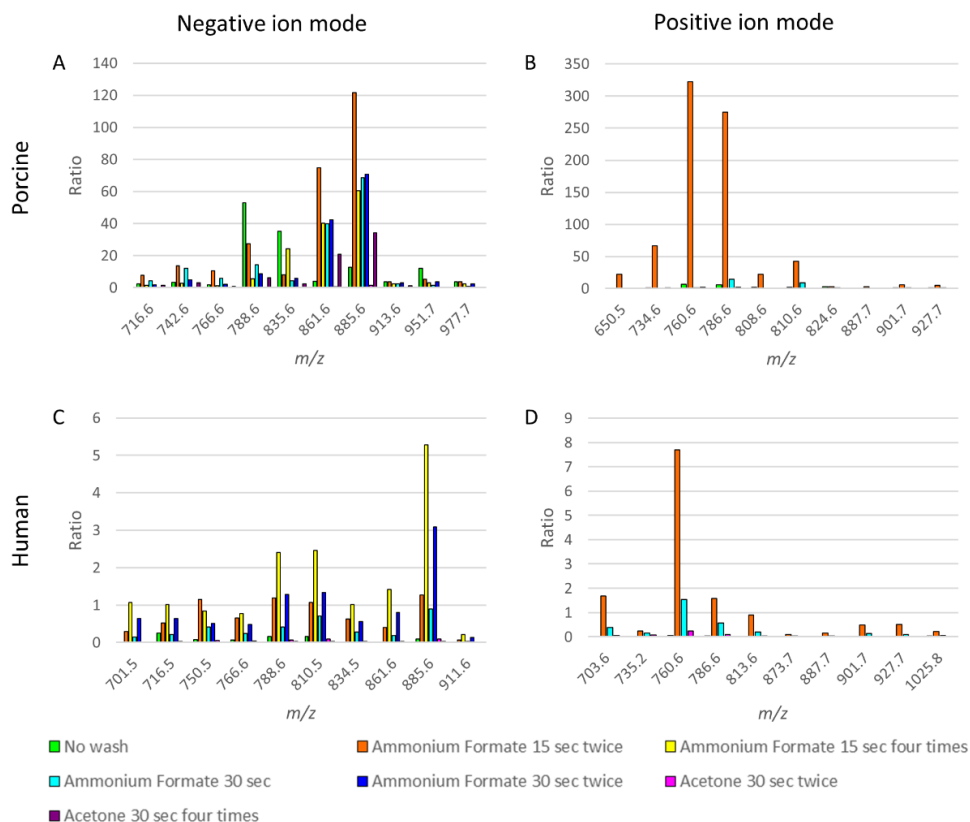


**Figure 4.3:** Comparison of the ratios between heme and selected  $m/z$  values for different washing methods for negative and positive ion mode for porcine and human fracture hematoma. The ratios represent the ion intensities of selected  $m/z$  values over the heme ion intensity. The  $m/z$  values were selected based on the highest intensities (excluding isotopes) and to cover the mass range of lipids ( $m/z$  650–950). **A** Ratios for 10  $m/z$  values for the six washing methods and the control (no wash) for porcine fxh in negative ion mode. **B** Ratios for 10  $m/z$  values for the three washing methods and the control (no wash) for porcine fxh in positive ion mode. **C** Ratios for 10  $m/z$  values for the six washing methods and the control (no wash) for human fxh in negative ion mode. **D** Ratios for 10  $m/z$  values for the three washing methods and the control (no wash) for human fxh in positive ion mode.

In positive ion mode, submerging the sections in ammonium formate for 15 seconds twice resulted in the highest ratios for all of the  $m/z$  values (Figure 4.3D). All the washing methods resulted in an increased heme S/N value compared to no wash, but this increase was the smallest for an ammonium formate wash of 15 seconds twice (Table 4.3D). The highest S/N values for all the selected  $m/z$  values

**Table 4.3:** Comparison of the signal-to-noise (S/N) values for the different washing methods for negative and positive ion mode for porcine and human fracture hematoma (fxh). No wash = control; Wash 1 = Ammonium formate 15 sec twice; Wash 2 = Ammonium formate 15 seconds four times; Wash 3 = Ammonium formate 30 seconds; Wash 4 = Ammonium formate 30 seconds twice; Wash 5 = Acetone 30 seconds twice; Wash 6 = Acetone 30 seconds four times.

**A** S/N values for heme ( $m/z$  615.2 = [Heme-H]<sup>+</sup>) and ten  $m/z$  values for the six washing methods and the control for porcine fxh in negative ion mode.

$m/z$	<b>615.2</b>	<b>716.6</b>	<b>742.6</b>	<b>766.6</b>	<b>788.6</b>	<b>835.6</b>	<b>864.6</b>	<b>885.6</b>	<b>913.6</b>	<b>951.7</b>	<b>977.7</b>
No wash	7.1	15.0	7.5	11.0	300.8	188.8	20.4	67.6	21.5	69.3	21.4
Wash 1	31.8	124.8	206.9	148.7	383.9	109.3	1051.8	1832.7	57.7	99.2	72.1
Wash 2	42.0	41.8	70.5	31.2	142.5	140.9	1002.4	1581.6	66.9	87.5	74.8
Wash 3	51.4	106.9	288.2	141.0	327.5	99.8	972.6	1839.4	73.5	42.8	28.7
Wash 4	37.0	43.6	101.7	38.9	1177.6	117.6	895.3	1563.8	67.9	84.5	61.6
Wash 5	717.0	61.1	196.0	79.1	168.6	45.2	385.0	920.6	37.5	2.0	0.0
Wash 6	16.5	20.1	42.2	13.3	81.2	33.3	312.1	570.1	19.8	0.0	0.0

**B** S/N values for heme ( $m/z$  616.2 = [Heme]<sup>+</sup>) and ten  $m/z$  values for the three washing methods and the control (no washing) for porcine fxh in positive ion mode.

$m/z$	<b>616.2</b>	<b>650.5</b>	<b>734.6</b>	<b>760.6</b>	<b>786.6</b>	<b>808.6</b>	<b>810.6</b>	<b>824.6</b>	<b>887.7</b>	<b>901.7</b>	<b>927.7</b>
No wash	26.8	5.1	21.1	95.7	83.2	31.9	30.6	41.7	10.3	15.9	16.4
Wash 1	11.7	152.6	270.1	1059.3	931.2	54.2	173.7	8.7	16.1	43.2	37.4
Wash 3	600.8	125.0	195.4	1125.2	971.5	72.0	168.9	22.4	17.6	46.8	49.1
Wash 5	381.6	56.8	174.3	358.3	320.8	86.0	85.2	117.1	0.0	0.0	0.0

**Table 4.3 (continued):** Comparison of the signal-to-noise (S/N) values for the different washing methods for negative and positive ion mode for porcine and human fracture hematoma (fxh).

C S/N values for heme ( $m/z$  615.2 = [Heme-H]<sup>+</sup>) and ten  $m/z$  values for the six washing methods and the control (no washing) for human fxh in negative ion mode.

$m/z$	<b>615.2</b>	<b>701.5</b>	<b>716.5</b>	<b>750.5</b>	<b>766.6</b>	<b>788.6</b>	<b>810.5</b>	<b>834.5</b>	<b>861.6</b>	<b>885.6</b>	<b>911.6</b>
No Wash	254.6	0.0	13.4	4.2	5.8	26.0	27.1	10.4	13.0	46.5	0.0
Wash 1	634.1	107.2	176.2	351.9	200.1	369.6	335.4	131.0	129.7	459.5	27.1
Wash 2	60.6	48.3	46.8	36.8	34.2	107.6	115.9	51.2	75.6	305.6	14.4
Wash 3	1008.0	108.9	149.8	260.3	149.6	259.9	437.0	176.0	128.3	527.6	23.1
Wash 4	72.8	42.6	43.4	32.3	31.6	89.6	96.4	42.8	64.4	273.8	13.2
Wash 5	1878.2	30.4	42.9	83.3	50.1	92.7	95.8	56.3	47.0	219.7	8.6
Wash 6	846.7	9.1	11.9	7.4	8.6	22.7	25.4	8.9	11.7	40.2	0.0

D S/N values for heme ( $m/z$  616.2 = [Heme]<sup>+</sup>) and ten  $m/z$  values for the three washing methods and the control (no washing) for human fxh in positive ion mode.

$m/z$	<b>616.2</b>	<b>703.6</b>	<b>735.2</b>	<b>760.6</b>	<b>786.6</b>	<b>813.6</b>	<b>873.7</b>	<b>887.7</b>	<b>901.7</b>	<b>927.7</b>	<b>1025.8</b>
No wash	331.1	6.2	0.0	38.0	15.0	0.0	0.0	6.7	14.8	15.3	18.5
Wash 1	436.1	460.6	55.7	1535.5	498.6	198.6	28.5	46.3	173.2	146.6	116.5
Wash 3	1476.9	384.0	145.8	1349.9	492.3	173.9	26.1	47.8	168.6	146.8	101.5
Wash 5	1707.2	53.3	67.5	236.0	93.4	29.1	0.0	0.0	0.0	0.0	0.0

were obtained with washing in ammonium formate for 30 seconds once or 15 seconds twice.

#### 4.4.1.3 Delocalization

Figures 4.4 and 4.5 show example images of MALDI-MSI distribution images for different washing methods for selected washing methods. The ammonium formate wash shows less delocalization than the acetone wash (Figures 4.4 and 4.5). Almost

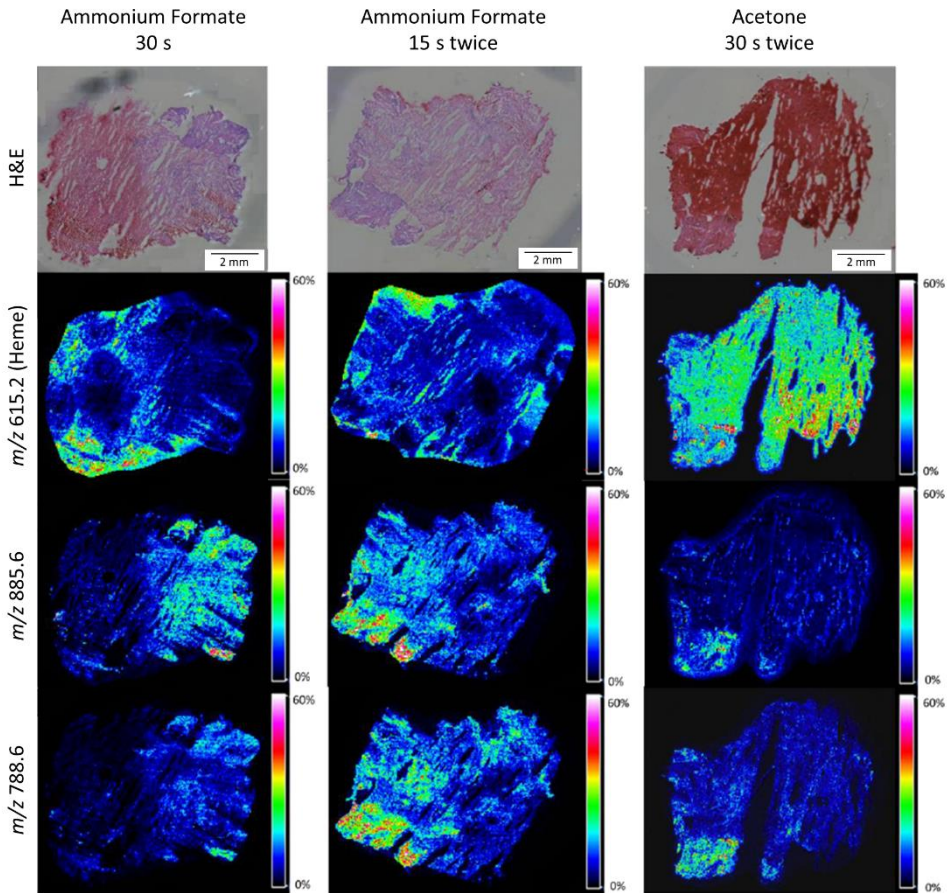


**Figure 4.4:** H&E stained and MALDI-MSI distribution images for three different washing methods for human fxh. MALDI-MSI images are shown for the distribution of heme ( $m/z$  615.2) and lipids with  $m/z$  values 885.6 and 788.6 in negative ion mode for the washing methods: ammonium formate for 30 s (left column), ammonium formate for 15 s twice (middle column), and acetone for 30 s twice (right column). All shown intensities are total ion current (TIC) normalized.

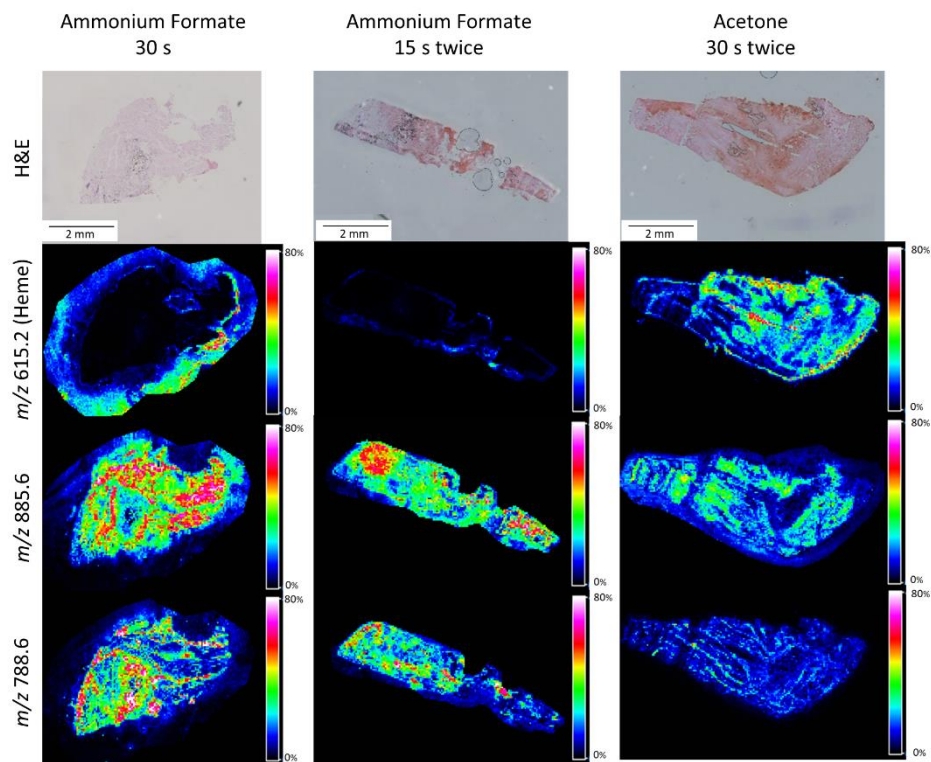


**Figure 4.5:** H&E stained and MALDI-MSI distribution images for three different washing methods for porcine fxh. MALDI-MSI distribution images are shown for heme ( $m/z$  615.2) and  $m/z$  values 885.6 and 788.6 in negative ion mode for the washing methods: ammonium formate for 30 seconds (left column), ammonium formate for 15 seconds twice (middle column), and acetone for 30 seconds twice (right column). All shown intensities are total ion current (TIC) normalized.

no heme was present within the fxh tissue for the tissue washing method with ammonium formate, in contrast to washing with acetone (Figures 4.4 and 4.5). Nevertheless, the intensity of heme is relatively high outside the tissue for the ammonium formate washing methods, which is attributed to the removal of the heme from the tissue with these methods. Increased delocalization was observed with increasing washing time, for example, the delocalization was larger for ammonium formate wash 15 s four times than for 15 s twice. In addition, it was observed that the delocalization for the selected  $m/z$  values was minimal and the highest intensities were present within the tissue for the ammonium formate wash.

Taking the above-mentioned results into account, the optimal fxh washing method is the ammonium formate wash for 15 s twice based on the increased intensity of

the selected  $m/z$  values, the decreased heme intensity, and minimum delocalization of the molecules of interest. This washing method was further applied throughout this study.

#### 4.4.2 Intra-variability of fxh

Fxh is a very heterogeneous tissue due to the presence of different cell types, which affects the molecular profile as well. The molecular profiles of the outside and center of fxh are compared to examine the intra-variability of this profile throughout the fxh. This is important to prevent bias based on sampling location within a fxh.

Four porcine fxh were used to determine if the molecular profiles differed based on the sampling location within the fxh, which reflects the intra-variability of the fxh. Figure 4.6A shows that molecular profiles of the outside and center of fxh cannot be distinguished in negative ion mode, as the graphs for the outside and center section per sample mostly overlap. For positive ion mode, the same holds, although the intra-variability for sample 2 is bigger than for the other samples, as those graphs overlap less (see Figure 4.6B). The DF-2 scores (see Figures 4.6C, D) show the same trend for both negative and positive ion mode. In general, the results from the PCA-LDA analysis show that the inter-variability between samples is higher than the intra-variability within a sample.

#### 4.4.3 Identification of fxh age-dependent molecular patterns

Human fxh of different fxh ages (2, 9, and 19 days) were analyzed to compare the differences in molecular profiles at an early, middle, and late stage during fracture healing. Changes in the molecular profiles can help to improve the understanding of molecular changes during bone fracture healing.

##### 4.4.3.1 Negative ion mode

In negative ion mode, DF-1 explains 1.47% of the total variance of the dataset and can be used to separate day 2 from day 19 (Figure 4.7A). Figure 4.7C shows the corresponding scaled loading plot. In the range from  $m/z$  600 to 830, the peaks are more distinctive of day 2, while the peaks in the range  $m/z$  830 to 1000 and some peaks in the mass range above that are more distinctive of day 19. The results of the identification of the peaks with the highest scaled loadings can be found in Table 4.4 (labeled with DF-1). For the separation between day 2 and day 19, certain phosphatidylinositols (PIs) and cardiolipins (CLs) are more characteristic of day 19, while a phosphatidylethanolamine (PE) is more characteristic of day 2. Phosphatidic

## Chapter 4

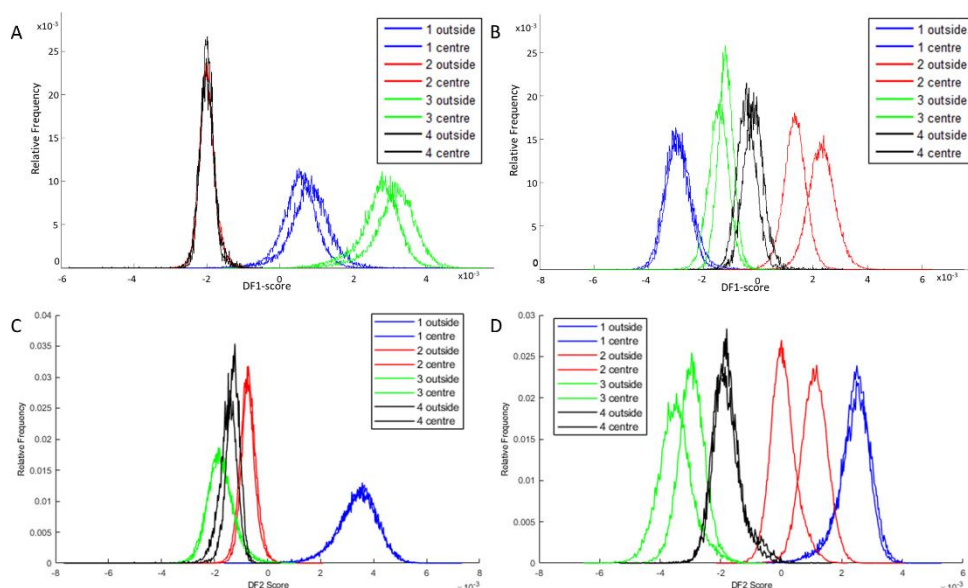


**Figure 4.6:** DF-1 and DF-2 scores for comparison of the intra-variability of fracture hematoma for negative and positive ion mode. The DF-1 score explains the biggest variance in the data set as determined by a PCA-LDA of the mass spectra of the outside and center sections of different porcine fxh. The DF-2 score explains the second biggest variance in the data set as determined by a PCA-LDA of the mass spectra of the outside and center sections of different porcine fxh. **A** DF-1 score for the outside and center sections of four porcine fxh in negative ion mode. **B** DF-1 score for the outside and center sections of four porcine fxh in positive ion mode. **C** DF-2 score for the outside and center sections of four porcine fxh in negative ion mode. **D** DF-2 score for the outside and center sections of four porcine fxh in positive ion mode.

acids (PAs) and phosphatidylserines (PSs) are present on both day 2 and 19, but the specific fatty acid chain composition and degree of saturation differ between both classes.

DF-2 explains 2.39% of the total variance and can be used to separate day 2 from day 9 (Figure 4.7B). The corresponding scaled loading plot (Figure 4.7D) shows that most of the peaks in the mass range up to  $m/z$  880 are more distinctive of day 9, while most peaks above this value are more distinctive of day 2 except for the peaks just above  $m/z$  1515, which correspond to day 9. The results of the identification of the peaks with the highest scaled loadings can be found in Table 4.4 (labeled with DF-2). For the separation between days 2 and 9, certain PAs, PEs, and PSs are more characteristic of day 9, while certain CLs are more characteristic of day 2. PIs are

## Lipid analysis of fracture hematoma with MALDI-MSI

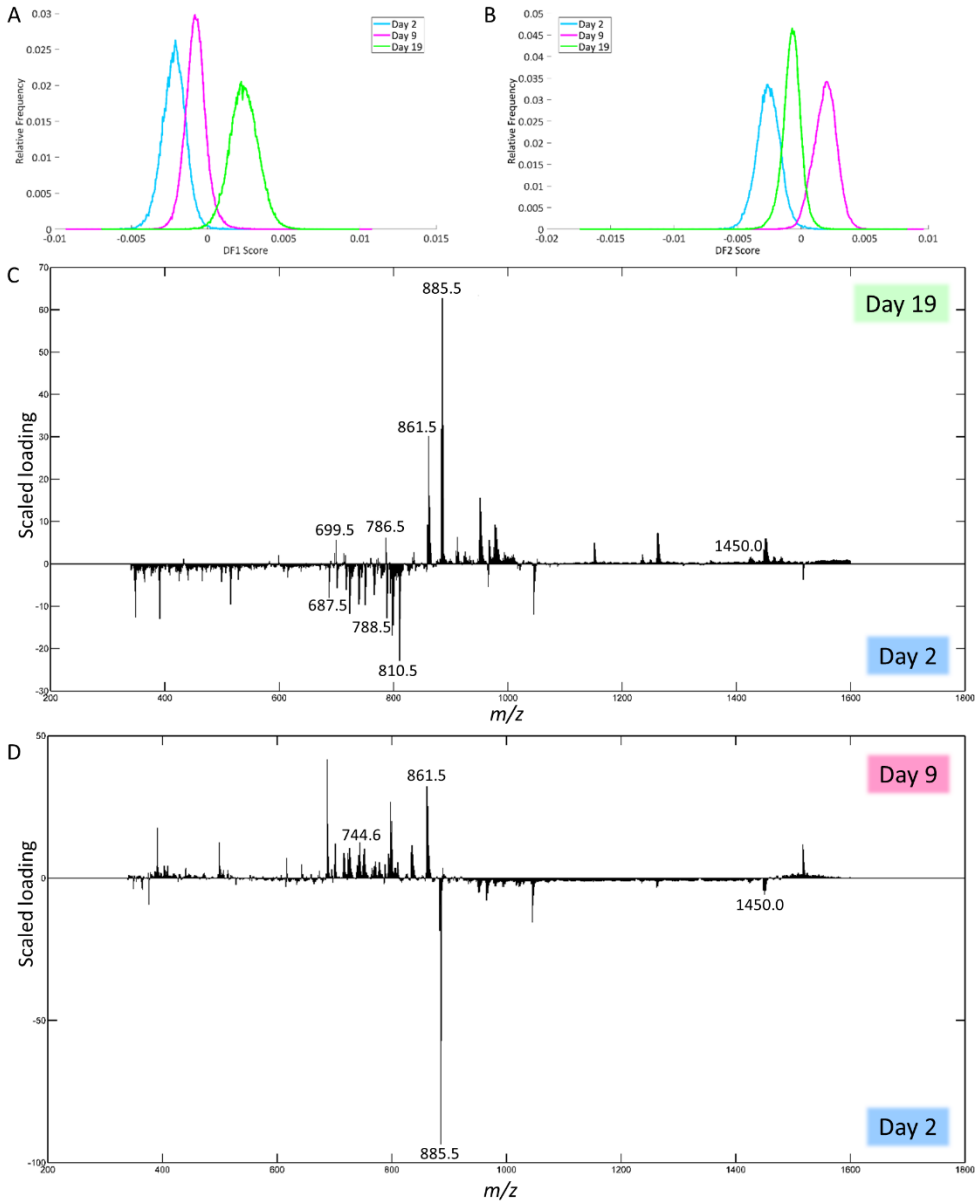


**Figure 4.7:** Results of the PCA-LDA of the human fxh of different fxh age (2, 9, and 19 days) for negative ion mode. DF-scores and their corresponding scaled loading plots are shown. The scaled loading is a combination of the intensity of the  $m/z$  value with how much the molecule contributes to the separation of classes across the specified discriminant function. The positive side for the DF-score plot is related to the positive side of the scaled loading plots. This indicates that the  $m/z$  values at a certain side have a higher contribution in the

**Figure 4.7 (legend continued):** class at that side. **A** DF-1 score representing the first discriminant function, which corresponds to the highest variance in the dataset. **B** The DF-2 score representing the second discriminant function. **C** Scaled loading plot of the full mass range for DF-1. **D** Scaled loading plot of the full mass range for DF-2.

**Table 4.4:** Lipid assignments based on MS/MS data and high mass resolution experiments in negative ion mode. For each assignment, the  $m/z$  value obtained with the high mass resolution mass spectrometer (Orbitrap Elite), the lipid assignment, the detected ion, the ppm error, the condition to which the  $m/z$  value contributes, and the DF are provided.

$m/z$ value	Assignment	Ion	$\Delta$ ppm error	Condition	DF
687.54	SM 16:0_18:1;O2	[M-CH <sub>3</sub> ] <sup>-</sup>	0.5	Day 2	DF-1
699.50	PA 18:0_18:2 and PA 18:1_18:1	[M-H] <sup>-</sup>	0.5	Day 19	DF-1
701.51	PA 18:0_18:1	[M-H] <sup>-</sup>	0.5	Day 2	DF-1
				Day 9	DF-2
716.52	PE 16:0_18:1	[M-H] <sup>-</sup>	0.7	Day 9	DF-2
723.50	PA 18:0_20:4	[M-H] <sup>-</sup>	0.4	Day 2	DF-1
				Day 9	DF-2
742.54	PE 18:0_18:2 and PE 18:1_18:1	[M-H] <sup>-</sup>	0.5	Day 9	DF-2
744.60	PE 18:0_18:1	[M-H] <sup>-</sup>	0.6	Day 9	DF-2
766.54	PE 18:0_20:4	[M-H] <sup>-</sup>	0.9	Day 2	DF-1
770.57	PE 18:0_20:2 and PE 18:1_20:1 and PE 18:2_20:0	[M-H] <sup>-</sup>	1.8	Day 9	DF-2
786.53	PS 18:0_18:2 and PS 18:1_18:1	[M-H] <sup>-</sup>	0.5	Day 19	DF-1
788.54	PS 18:0_18:1	[M-H] <sup>-</sup>	0.6	Day 2	DF-1
				Day 9	DF-2
810.53	PS 18:0_20:4	[M-H] <sup>-</sup>	0.5	Day 2	DF-1
				Day 9	DF-2
833.52	PI 16:0_18:2 and PI 16:1_18:1 and PI 16:2_18:0	[M-H] <sup>-</sup>	0.6	Day 9	DF-2
835.53	PI 16:1_18:0 and PI 16:0_18:1	[M-H] <sup>-</sup>	1.1	Day 19	DF-1
				Day 9	DF-2
859.53	PI 18:1_18:2	[M-H] <sup>-</sup>	0.1	Day 19	DF-1
861.54	PI 18:0_18:2 and PI 18:1_18:1	[M-H] <sup>-</sup>	0.6	Day 19	DF-1
				Day 9	DF-2

**Table 4.4 (continued):** Lipid assignments based on MS/MS data and high mass resolution experiments in negative ion mode.

<i>m/z</i> value	Assignment	Ion	$\Delta$ ppm error	Condition	DF
863.56	PI 18:0_18:1	[M-H] <sup>-</sup>	0.8	Day 19	DF-1
				Day 9	DF-2
883.53	PI 18:1_20:4	[M-H] <sup>-</sup>	0.8	Day 19	DF-1
				Day 2	DF-2
885.55	PI 18:0_20:4	[M-H] <sup>-</sup>	0.8	Day 19	DF-1
				Day 2	DF-2
909.55	PI 18:0_22:6	[M-H] <sup>-</sup>	0.9	Day 19	DF-1
911.56	PI 18:0_22:5 and PI 18:1_22:4	[M-H] <sup>-</sup>	1.0	Day 19	DF-1
1447.96	CL 18:2_18:2_18:2_18:2	[M-H] <sup>-</sup>	0.4	Day 19	DF-1
				Day 2	DF-2
1449.98	CL 18:1_18:2_18:2_18:2	[M-H] <sup>-</sup>	1.0	Day 19	DF-1

present on both day 2 and 9, but the specific fatty acid chain composition and degree of saturation differ between both classes.

#### 4.4.3.2 Positive ion mode

In positive ion mode, DF-1 explains 2.23% of the total variance of the dataset and can be used to separate day 2 from day 19 after trauma (Figure 4.8A). Based on the scaled loadings (Figure 4.8C), most of the peaks are more distinctive of day 2 up to *m/z* 925, except for a few peaks, most notably 3 clusters of peaks in the range of *m/z* 700 to 800. Most of the peaks above *m/z* 925 are more distinctive of day 19. The results of the identification of the peaks with the highest scaled loadings can be found in Table 4.5 (labeled with DF-1). For the separation between day 2 and day 19, it seems that certain lysophosphatidylcholines (LPCs) have a higher presence on day 2. The main class of identified lipids is phosphatidylcholines (PCs), PCs are present in both the day 2 and day 19. However, the specific fatty acid chain composition and degree of saturation differ between day 2 and day 19.

DF-2 explains 2.79% of the total variance and can be used to separate day 9 from day 2 + 19 (Figure 4.8B). The corresponding scaled loading plot (Figure 4.8D) shows that clusters of peaks are more distinctive of day 9 or day 2 + 19. For the mass range up to *m/z* 850 and from *m/z* 1020, most peaks are related to day 2 + 19, while for the mass range *m/z* 850 to 1020 most peaks are related to day 9. The results of the identification of the peaks with the highest scaled loadings can be found in Table

## Chapter 4

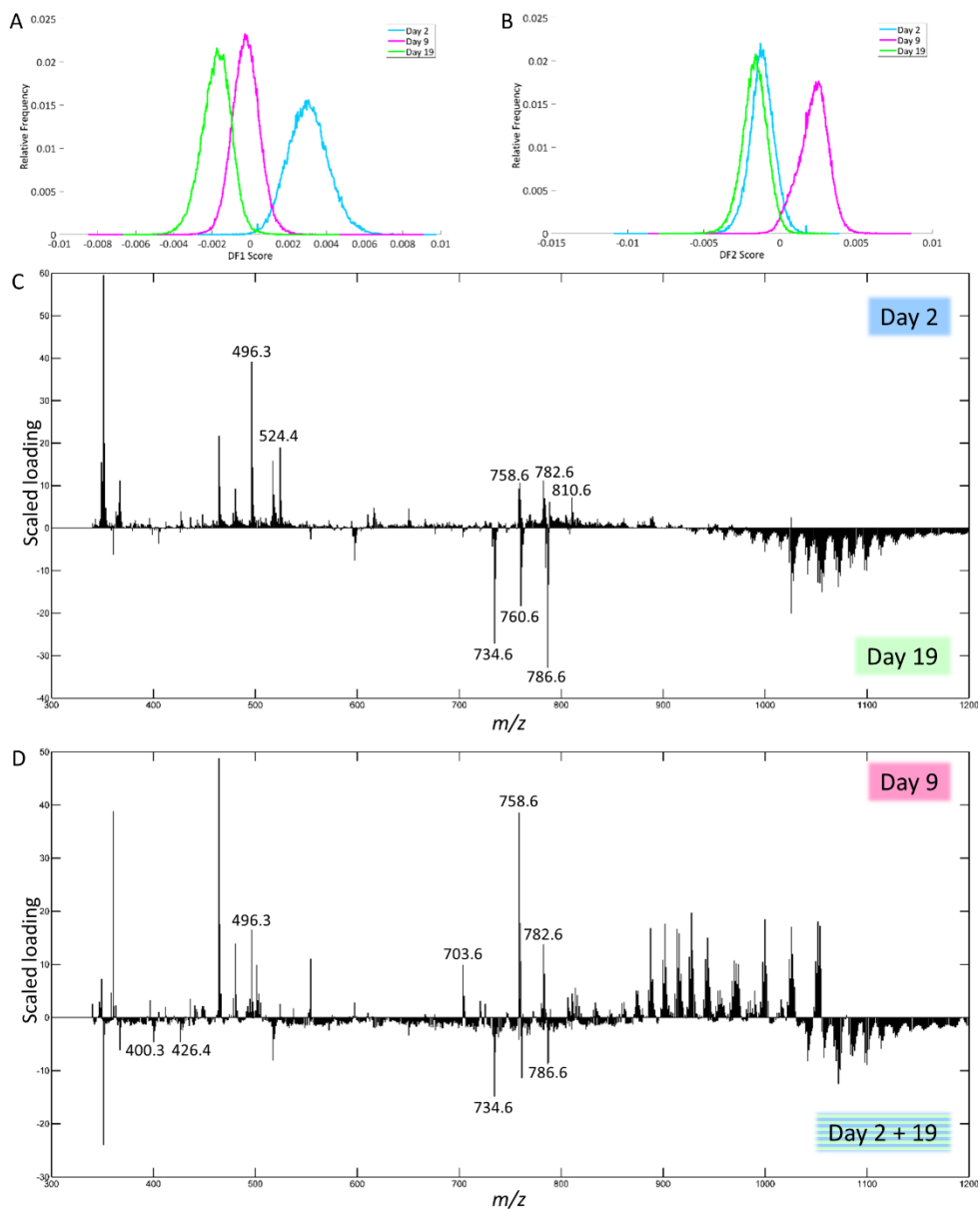


**Figure 4.8:** Results of the PCA-LDA of the human f1xh of different f1xh age (2, 9, and 19 days) for positive ion mode. DF-scores and their corresponding scaled loading plots are shown. The scaled loading is a combination of the intensity of the  $m/z$  value with how much the molecule contributes to the separation of classes across the specified discriminant function. The positive side for the DF-score plot is related to the positive side of the scaled loading plots. This indicates that the  $m/z$  values at a certain side have a higher contribution in the

**Figure 4.8 (legend continued):** class at that side. **A** DF-1 score representing the first discriminant function, which corresponds to the highest variance in the dataset. **B** The DF-2 score representing the second discriminant function. **C** Scaled loading plot of the full mass range for DF-1. **D** Scaled loading plot of the full mass range for DF-2.

**Table 4.5:** Lipid assignments based on MS/MS and high mass resolution experiments in positive ion mode. For each assignment, the  $m/z$  value obtained with the high mass resolution mass spectrometer (Orbitrap Elite), the lipid assignment, the detected ion, the ppm error, the condition to which the  $m/z$  value contributes, and the DF are provided.

$m/z$ value	Assignment	Ion	$\Delta$ ppm error	Condition	DF
400.34	CAR 16:0	[M+H] <sup>+</sup>	1.0	Day 2 + 19	DF-2
426.36	CAR 18:1	[M+H] <sup>+</sup>	0.4	Day 2 + 19	DF-2
496.34	LPC 16:0	[M+H] <sup>+</sup>	0.7	Day 2	DF-1
				Day 9	DF-2
524.37	LPC 18:0	[M+H] <sup>+</sup>	1.5	Day 2	DF-1
703.57	SM 34:1;O2	[M+H] <sup>+</sup>	0.4	Day 9	DF-2
734.57	PC 16:0_16:0	[M+H] <sup>+</sup>	0.4	Day 19	DF-1
				Day 2 + 19	DF-2
758.57	PC 16:0_18:2	[M+H] <sup>+</sup>	0.5	Day 2	DF-1
				Day 9	DF-2
760.58	PC 16:0_18:1	[M+H] <sup>+</sup>	0.7	Day 19	DF-1
				Day 9	DF-2
768.59	PC O-36:4	[M+H] <sup>+</sup>	0.7	Day 2	DF-1
782.57	PC 16:0_20:4	[M+H] <sup>+</sup>	0.6	Day 2	DF-1
				Day 9	DF-2
784.58	PC 16:0_20:3 and PC 18:1_18:2	[M+H] <sup>+</sup>	0.7	Day 19	DF-1
				Day 2 + 19	DF-2
786.60	PC 18:0_18:2 and PC 18:1_18:1	[M+H] <sup>+</sup>	0.7	Day 19	DF-1
				Day 2 + 19	DF-2
788.62	PC 18:0_18:1	[M+H] <sup>+</sup>	1.4	Day 2	DF-1
810.60	PC 18:0_20:4	[M+H] <sup>+</sup>	0.7	Day 2	DF-1

4.5 (labeled with DF-2). For the separation between day 9 and day 2 + 19, it seems that certain acyl carnitines (CARs) are more present at day 2 + 19, while an LPC and sphingomyelin (SM) are more present at day 9. Just as for DF-1, the main class of identified lipids is PCs, which are present on both day 9 and day 2 + 19. Again, the specific fatty acid chain composition and degree of saturation differ between day 9 and day 2 + 19.

## 4.5 Discussion

In this study, the use of MALDI-MSI as a tool to examine the molecular events in fxh was explored. A methodology was developed for the analysis of fxh with MALDI-MSI with a focus on defining the optimal washing method. The intra-variability of the molecular profile in fxh was shown to be smaller than the inter-variability using this method. Lastly, fxh age-dependent lipid patterns within the fxh were identified. These age-dependent lipid patterns might be applied in predicting fracture healing outcome in the future.

### 4.5.1 Tissue preparation

A two-step washing protocol with ammonium formate followed by an intermediary drying step is most effective in reducing the heme signal, minimizing lipid delocalization, and enhancing lipid signal intensities. Our results are in line with the study by Angel *et al.* (2012), which shows that longer washing times go hand in hand with increased lipid delocalization.<sup>170</sup>

In general, most molecular intensities were enhanced after tissue washing with either ammonium formate or acetone, compared to no tissue washing at all. This result is in line with the study by Seeley *et al.* (2008), which also showed enhanced heme signal intensities after tissue washing with acetone as compared to not washing tissue sections.<sup>171</sup> In this study, acetone proved to be less effective, as acetone tissue washing resulted in a higher heme signal as compared to ammonium formate tissue washing or no washing. Additionally, more residual heme was located within the tissue after acetone wash in comparison to the ammonium formate wash.

### 4.5.2 Fracture hematoma intra-variability

For the sample location of the fxh, it was shown that the intra-variability within a fxh was smaller than the inter-variability between fxh based on DF-1. No marked regions within the fxh could be identified that exhibit a specific function based on their spatial distribution. This is in line with expectations since the fxh is a very dynamic and diverse environment in which, depending on the phase of the fracture healing process, a great variety of cells is present.<sup>147,150</sup>

### 4.5.3 Comparison of human fxh of different fxh age

Using MALDI-MSI, distinct lipid patterns were identified in fxh samples that were indicative of fxh age. Five lipid classes in negative ion mode and four lipid classes in positive ion mode showed to contribute most to differentiating the three age-based fxh groups. Herein, we focus on the lipid classes with the highest differentiating contribution.

#### 4.5.3.1 Lipid patterns in negative ion mode

In negative ion mode, days 2 and 19 could predominantly be separated by the relatively higher presence of PIs and CLs on day 19 as compared to a higher presence of PEs on day 2 (Table 4.4).

PIs serve as precursors of signaling molecules within both the Inositol-3-phosphate/diacylglycerol (IP3/DAG), as well as the phosphatidylinositol-3-Kinase/protein kinase B (PI3K/AKT) signaling pathway and assist in the effective regulation of angiogenesis.<sup>172</sup> Regarding bone formation, another important aspect is the recruitment and release of calcium through the binding of IP3 to the endoplasmic reticulum. Calcium release results in a positive feedback loop on the production of DAG, which is counteracted by diacylglycerol kinase due to the conversion to PA, a key molecule in the mammalian target of rapamycin (mTOR) signaling pathway, as described below.<sup>173</sup> Placing the above-mentioned functions of PIs into perspective, it can be expected that regulation of angiogenesis and calcium mobilization will be more present at day 19 as compared to day 2.

Furthermore, days 2 and 9 could be distinguished from each other by the increased presence of CLs on day 2 as compared to a higher presence of PAs, PSs, and PEs on day 9 (Table 4.4). PA, a metabolite of phosphatidylcholine, plays a role in the mTOR signaling pathway, which acts as a pivotal nutrient sensing mechanism and partakes in regulating cellular differentiation, survival, growth, and division. Within this pathway, PA proposedly serves as an indicator for the presence of its lipid precursor molecules within the cell since these are important for the before-mentioned processes.<sup>174</sup> Additionally, PA has shown to be an important component in the induction of angiogenesis through activating the HIF-1 $\alpha$ -VEGF pathway.<sup>175</sup> Lastly, PA enhances inflammation through mTOR signaling, both *in vitro* as well as *in vivo*.<sup>176,177</sup> The higher presence of PA on day 9 as compared to day 2 is in line with physiological fracture healing due to its roles in the regulation of cell fate and angiogenesis, as well as a more widespread, regulated inflammatory response that would more likely take place around day 9 after fracture as compared to day 2.

PEs, like PCs, are important precursor molecules of phosphoethanolamine, which on its turn is catalyzed by phosphoethanolamine/phosphocholine phosphatase (PHOSPHO1) to serve as a donor of inorganic phosphate in the production of hydroxyapatite. Furthermore, they are involved in the glycine and serine metabolism, two key amino acids in the production of collagen.<sup>178</sup> Increased presence of PEs on day 9, combined with relatively large scaled loadings, matches its role in both collagen metabolism, as well as a phosphate donor for hydroxyapatite production.

#### 4.5.3.2 Lipid patterns in positive ion mode

In positive ion mode, day 2 and day 19 were mostly distinguishable by the presence of specific PCs on days 2 or 19. Furthermore, a higher presence of LPCs was observed on day 2 as compared to day 19 (Table 4.5).

PCs are amongst the most abundant phospholipids in mammalian cell membranes and are known to play important roles in cellular metabolism and energetic state.<sup>179</sup> They also regulate endochondral bone formation by promoting chondrocyte differentiation and cartilage matrix degradation in growth plates.<sup>163</sup> Furthermore, PCs play a role in the glycine and serine metabolism, which are key amino acids in collagen synthesis, and act as precursors of phosphocholines, important inorganic phosphate donors in the production of hydroxyapatite and thus influence bone mineralization.<sup>178,180,181</sup> A study by Øyen *et al.* (2017) showed that dietary supplementation of choline, an essential nutrient that is predominantly supplied as PC, was directly associated with increased bone mineral density.<sup>165</sup> Since PCs are the most abundant phospholipids within mammalian cell membranes, it was to be expected that their presence in fxh would be validated on both days 2 and 19. However, it has yet to be revealed what causes the shift in specific lipid isoforms amongst the different time points. Unfortunately, information about the presence of specific lipids throughout fracture healing is lacking. The shift in specific PCs might be due to certain osteogenic processes that can be expected to be more present during day 19 as compared to day 2.

LPCs are known to elicit a seemingly contradictory effect on osteoclasts by inhibiting their formation whilst enhancing their function. Besides, although predominantly investigated in valvular calcification, LPCs enhance cellular mineralization.<sup>182-184</sup> The dual (opposite) effect of LPCs on both osteoclast formation and function could contribute to adequate osteoclast turnover and functionality in the early fracture environment.

Furthermore, day 9 could be separated from day 2 + 19 due to the higher presence of certain long chain CARs on day 2 + 19, whilst SM and LPC were more characteristic of day 9 (Table 4.5).

SMs are important cellular signaling molecules that play a role in bone formation and apoptosis. A deficiency in the enzyme that converts SM to PC has been shown to impair bone and cartilage mineralization.<sup>185</sup> Additionally, a lack of SM due to the knockdown of sphingomyelin synthase 1 (SMS1) has been shown to impair bone development and case growth retardation due to the regulatory role of SMS1 in osteoblast development.<sup>164</sup> An increased presence of SM is, therefore, more likely

to occur during day 9 after fracture since osteoblast development is initiated around that time.<sup>186</sup>

#### 4.5.4 Limitations and future research

This study showed that MALDI-MSI allows for the identification of a fxh age-dependent lipid signature. Still, a larger sample cohort is needed to validate these data. Especially the lipid signature in fxh of fractures that develop impaired healing would be of interest. Due to the limited sample size and the fact that all fractures in our cohort healed without adverse events, no conclusions in relation to clinical outcome can be drawn at this stage. Theoretically, the fracture location within a bone could influence the presence of lipids in the fracture hematoma. However, since all included fractures were located in the metaphyseal bone, we expect this influence to be minimal. Moreover, analysis of metabolites or proteins, being key players in bone healing and formation, could further provide insights into the molecular mechanisms in fracture healing. Future research should therefore focus on validating the results of the present study in a larger cohort and developing a method for analyzing the protein signature of the fxh.

#### 4.6 Conclusion

For the first time, our approach revealed the potential of MALDI-MSI as an analytical tool for the assessment of lipid patterns in fxh samples over time. An ammonium formate wash for 15 s twice was shown to adequately remove the heme from the porcine and human fxh and increase the overall molecular signal for negative and positive ion mode with minimum delocalization. The sample location within fxh is of less importance, as it was shown that the intra-variability within fxh was smaller than the inter-variability between fxh. Lastly, fxh age-dependent lipid patterns were identified, which showed to be involved in various processes that are important during fracture healing, such as angiogenesis, inflammation, cellular differentiation, mineralization, hydroxyapatite production, and collagen synthesis. Proper bone regeneration is in part dependent on the successful integration of the above-mentioned processes, and our results emphasize the important contributing role that lipids play. Assessment of specific molecular patterns within the fxh could provide insights into fracture healing processes and could potentially serve as a future source of theragnostic information on fracture healing.



# Chapter 5: Effect of citrulline supplement on lipid and protein profiles during bone fracture healing in a rat model

# 5

Sylvia P. Nauta

Martijn Hofman

Johannes Greven

Frank Hildebrand

Ronny J.C. Mohren

Tiffany Porta Siegel

Eva Cuypers

Ron M.A. Heeren

Martijn Poeze

*In preparation*



## 5.1 Abstract

Bone fracture healing is a complex process that occurs after a bone fracture and consists of four overlapping phases. The exact molecular regulation and importance of specific molecules throughout the different fracture healing phases is still poorly comprehended, despite the improvement in understanding of fracture healing over the past decades. The citrulline-arginine-nitric oxide metabolism is one of the pathways involved in fracture healing and enrichment of this pathway via citrulline supplement can enhance fracture healing. This study investigated the effect of citrulline supplement on the lipid and protein profiles during different fracture healing phases in a rat model. Matrix-assisted laser desorption/ionization mass spectrometry imaging (MALDI-MSI) and liquid-chromatography tandem mass spectrometry (LC-MS/MS) were used for lipid and protein analyses, respectively. The observed lipid profiles contributing to the citrulline supplement compared to the control group and vice versa were distinct for the different stages of fracture healing and differed between bone and bone marrow. The main lipid classes observed were phosphatidylcholines (PCs) and lysophosphatidylcholines (LPCs), while also acyl carnitines (CARs), triacyl/alkylglycerides (TGs), and a sphingomyelin (SM) contributed to the separation between the treatment and control group. The more abundant proteins in the citrulline supplement and control group were different during the fracture healing phases. The citrulline supplement had a changing effect throughout the different fracture healing phases, as limited overlap between more abundant proteins at different time points was seen. An enhancement of fracture healing in the citrulline supplement group was seen in comparison to the control group based on the activation of different pathways. In addition, multiple pathways related to the citrulline-arginine-nitric oxide metabolism were more active in citrulline supplement group. This study showed that citrulline supplement results in distinct differences in the lipid and protein profiles during different fracture healing stages, especially during the first three phases of fracture healing. In addition, enhancement of fracture healing was seen as a result of citrulline supplementation.

## 5.2 Introduction

Bone fracture healing is a complex but well-defined process that occurs after a bone fracture.<sup>5,7,10,13,14,187</sup> The optimal outcome is the achievement of biological/metabolic and structural restoration of the bone.<sup>4,5,7,187,188</sup> A sequence of biological phases with different mechanical and biological requirements is part of the regular fracture healing process.<sup>4,5,12-14</sup> The different phases, the overlap between the phases, and the crosstalk between different cell types result in a

constantly changing cellular and molecular environment around the fracture site.<sup>4,5,10,12,188-190</sup> Fracture healing is usually divided into four overlapping phases: 1) hematoma (fibrin clot) formation and inflammation phase, 2) soft callus formation, 3) hard callus formation, and 4) bone remodeling.<sup>4,5,12,187,190,191</sup> The majority of bone fractures will heal normally, but the healing process is impaired in 1 to 10% of the fractures resulting in delayed healing or non-union formation.<sup>4,7,10,12,13,188-190,192,193</sup> The treatment of impaired healing cases is a complex, individualized, and lengthy process, despite the improvements in treatment over the past decades.<sup>4,13,193</sup> Prevention and treatment of impaired healing can be improved by further insights into the fracture healing processes.

Some key molecules that affect the outcome of fracture healing are known and can be associated with impaired fracture healing in case of alternation of the local or systemic regulation.<sup>5,7,10,13,194</sup> The most abundant class of molecules in bone are proteins with collagen being the largest group.<sup>190,195,196</sup> Different protein classes play an important role during fracture healing, such as pro-inflammatory cytokines, growth and differentiation factors, inhibitory molecules, and angiogenic factors.<sup>4,5,7,10,12,13,188</sup> Lipids are other key molecular players, as they are structural components of a cell as well as involved in cellular signaling, inflammation, metabolism, and bone mineralization.<sup>137</sup> Lipids are mainly present in bone marrow, but small amounts are present in the mineralized bone as well.<sup>137</sup> Lipid mediators, like prostaglandins and leukotrienes, are important during bone regeneration and regulate inflammation.<sup>194,197</sup>

The citrulline-arginine-nitric oxide metabolism (see Figure 5.1) is one of the pathways that is important during fracture healing.<sup>189,190,192</sup> It has been shown that disruption of this metabolism can result in impaired healing.<sup>189,191-193</sup> Citrulline is the precursor of arginine.<sup>189,190,192</sup> Arginine can be converted back into citrulline via the different nitric oxide synthases (NOS1, NOS2, and NOS3), which results in the production of nitric oxide.<sup>189-193,198-201</sup> Arginine is the only amino acid precursor of nitric oxide.<sup>190,192,193,198</sup> Nitric oxide is important for fracture healing, as it affects the inflammatory responses, stimulates regulation of bone remodeling, and capillary growth.<sup>189-193,198,200</sup> In addition, arginine can also be converted into ornithine.<sup>189,190,192,193</sup> Ornithine is important in collagen synthesis via polyamine production.<sup>189,190,192,193</sup> Previous studies showed that the supplementation of citrulline can improve fracture healing via stimulation of callus formation and improvement of the inflammatory response and results in improved biomechanical properties.<sup>192,202</sup> However, the exact affected and involved pathways are still not fully explored.

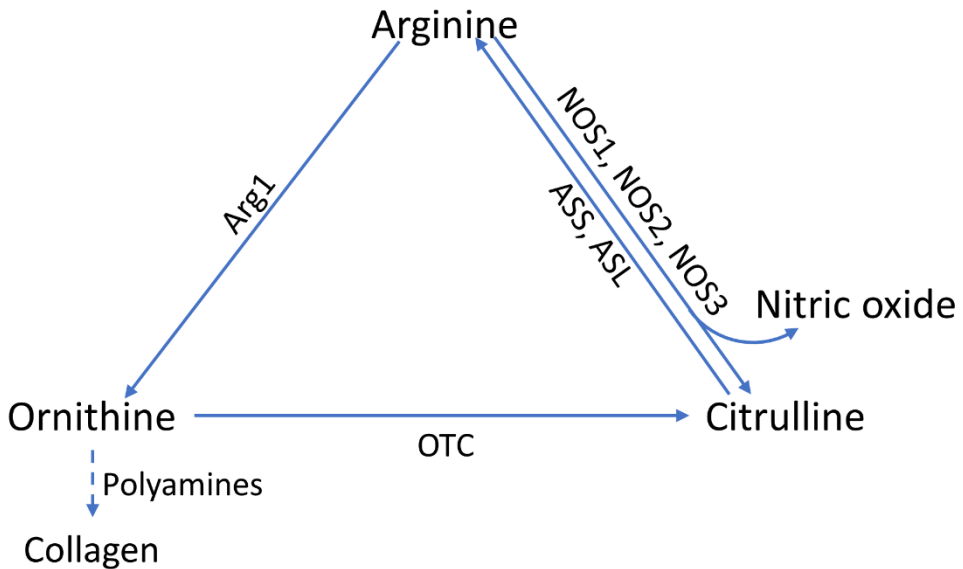


**Figure 5.1:** Schematic overview of citrulline-arginine-nitric oxide metabolism. Abbreviations: Arg1 = arginase 1; ASS = argininosuccinate synthetase; ASL = argininosuccinate lyase; NOS = nitric oxide synthase; OCT = ornithine transcarbamylase.

Mass spectrometry (MS) is a powerful analytical technique to explore the molecular pathways that are affected by citrulline supplement. MS allows for the detection of different molecular classes, including lipids and proteins, from a wide range of tissue types without prior knowledge about the sample composition when conducted in an untargeted fashion.<sup>90,97,98,130,131,203,204</sup> Matrix-assisted laser desorption/ionization mass spectrometry imaging (MALDI-MSI) is often used to study the molecular distributions in tissue sections, including lipid analysis.<sup>97,98,130,131,203,204</sup> MALDI-MSI has only recently been applied on undecalcified bone tissue, including for lipid analysis, due to the complicated sample preparation protocol.<sup>90,97,98,130,131,203,204</sup> Additionally, tandem mass spectrometry in combination with liquid chromatography (LC-MS/MS) has been shown to be a powerful technique to investigate proteome changes.<sup>99,205-207</sup> Crushed tissue or tissue homogenates are needed for the analysis with this technique, which results in the loss of distribution information.<sup>97</sup> LC-MS/MS has been applied the analysis of bone tissue to study proteins, lipids, and drugs in various application fields.<sup>99,133,142,205-207</sup> Therefore, the combination of lipid analysis with MALDI-MSI and protein analysis with LC-MS can contribute to improving molecular understanding in bone fracture healing.

The objective of this paper is to study the molecular effects of citrulline supplement during bone fracture healing on the lipid and protein profiles by applying two different MS techniques on undecalcified bone. Fracture healing in the citrulline supplement group was expected to be enhanced in comparison to the control group based on these profiles. MALDI-MSI was applied for the analysis of the lipid composition in the affected bone. In addition, protein analysis was performed on bone tissue using LC-MS/MS. The lipid and protein profiles were compared between the citrulline supplement and control group for the different time points. In addition, the more abundant proteins in the citrulline supplement and control group per time point were used for analysis of activated pathways.

### 5.3 Materials and methods

#### 5.3.1 Chemicals and materials

Gelatin, carboxymethyl cellulose (CMC) sodium salt, tragacanth, red phosphorus,  $\alpha$ -cyano-4-hydroxycinnamic acid  $\geq 98\%$  (CHCA), sulfosalicylic acid (SSA), ammonium bicarbonate (ABC), dithiothreitol (DTT), iodoacetamide (IAM), and trifluoroacetic acid (TFA, ULC grade) were purchased from Sigma-Aldrich (Zwijndrecht, the Netherlands). Phosphate buffered saline (PBS) was purchased from Thermo Fisher Scientific (Inc. Waltham, United States of America (USA)). SuperFrost Plus microscopic glass slides were purchased from VWR International (Amsterdam, the Netherlands). Urea was purchased from GE Healthcare (Chicago, IL, USA). The enzyme mixture of Trypsin and LysC (mass spectrometry grade) was purchased from Promega (Leiden, the Netherlands). Methanol, acetonitrile (ACN), formic acid (FA), and water with ULC/MS-CC/SFC grade were purchased from Biosolve BV (Valkenswaard, the Netherlands).

#### 5.3.2 Animal study and sample collection

Female, adult Sprague Dawley rats (approximately 250 g) were obtained from Envigo (Horst, the Netherlands) for this study. The animals were housed under controlled environmental conditions with a 12-hour light-dark cycle and food and water ad libitum. An intramedullary wire was inserted and a standardized femoral fracture was generated at the right side under general anesthesia. General anesthesia was induced with ketamine (100 mg/kg i.p.), xylazine (2%; 10 mg/kg i.p.) and, if necessary, extended with isoflurane inhalation (2.0–2.5 vol.%). The intramedullary wire (1-mm stainless-steel intramedullary Kirschner wire, Königsee Implantate GmbH, Allendorf, Germany) was inserted in a retrograde manner. The standardized fracture were created using the blunt guillotine method, as described by Bonnarens and Einhorn.<sup>208</sup> Fluoroscopic evaluation was performed after placement of the intramedullary pin and the fracture induction. Pre- and post-

operative analgesia were ensured with buprenorphine hydrochloride (0.03–0.05 mg/kg s.c.) 30 minutes before the operation and every 6 hours for the first 24–48 hours after the operation, respectively. Afterwards, buprenorphine hydrochloride was administered in the same way twice daily during the first three weeks. In addition, the drinking water was supplemented with metamizole (1 mL/300 mL) during the first post-operative week. The rats were assigned to the citrulline supplement or control group at random. The citrulline supplement group received a citrulline-supplemented diet for 14 days post-operative (DPO) and an isocaloric normal diet for the remainder of the study protocol. The citrulline-supplemented diet consisted of 10 g/kg/day citrulline-suspension administered per os over a bend metal feeding tube. The control group received an isocaloric normal diet throughout the study protocol.

Samples were collected at four different time points, namely 3, 7, 14, and 28 DPO corresponding to the different phases in bone fracture healing: inflammation phase, soft callus formation, hard callus formation, and bone remodeling, respectively. At these time points, six rats per treatment group were exsanguinated by cardiac puncture under anesthesia and analgesia. Three rats were excluded because of premature death. An isotope administration was performed after anesthesia induction with a bolus infusion of two tracers L-[guanidino-<sup>15</sup>N<sub>2</sub>]-arginine (146 nmol/10 g body weight) and L-[ureido-<sup>13</sup>C-<sup>2</sup>H<sub>2</sub>]-citrulline (44 nmol/10 g body weight) dissolved in NaCl over the tail vein. An infusion of these tracers (L-[guanidino-<sup>15</sup>N<sub>2</sub>]-arginine at 960 nmol/10 g body weight and L-[ureido-<sup>13</sup>C-<sup>2</sup>H<sub>2</sub>]-citrulline at 90 nmol/10 g body weight) was performed for 60 minutes before exsanguination. The integral whole femur was collected, soft tissue was removed, and the femurs were washed 3 times with PBS. The Kirschner wire was carefully removed and 0.5 cm of the callus at the fracture site was collected. The sample was divided in two pieces with a wire saw while cooling with ice-cold PBS. One piece was used for lipid analysis and the other piece was homogenized and used for protein analysis. The samples were rapidly frozen and stored at -80 °C until further use. An overview of the number of samples collected for each group is provided in Table 5.1. The samples containing pieces of bone were used for lipid analysis with MALDI-MSI and the homogenized samples were used for protein analysis with LC-MS/MS, as shown in the overview of the study workflow in Figure 5.2. The Governmental Animal Care and Use Committee of the state Nordrhein-Westfalen approved this study (approval number: LANUV NRW 84-02.04.2015.A078).

**Table 5.1:** Overview of sample group references and number of samples collected from citrulline supplement rat study.

Days post-operative	Citrulline group	Control group
3	C1: 6 samples	F1: 6 samples
7	C2: 6 samples	F2: 6 samples
14	C3: 6 samples	F3: 4 samples
28	C4: 5 samples	F4: 6 samples

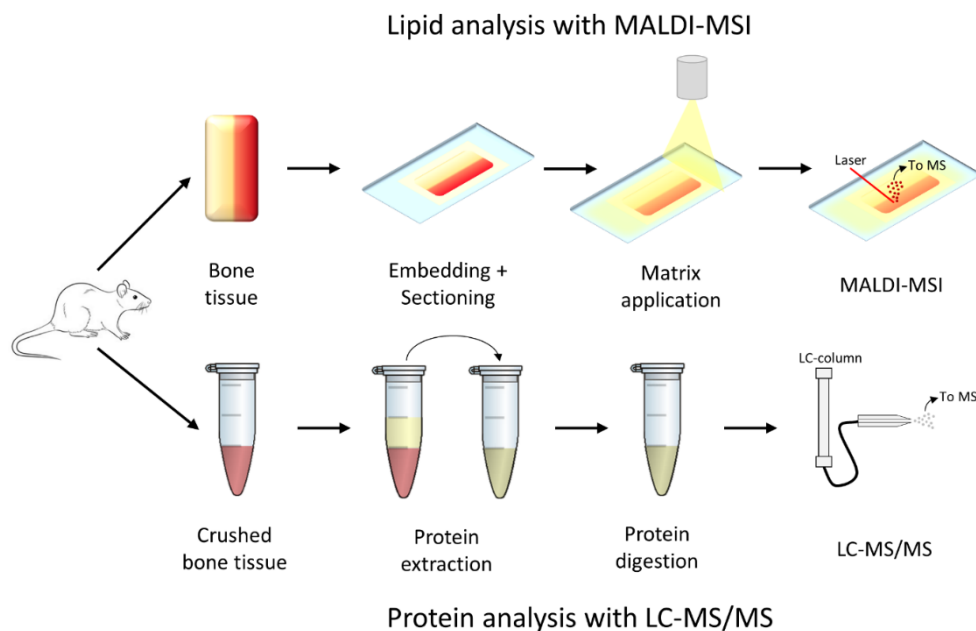


**Figure 5.2:** Overview of the study analytical workflow combining the analysis of lipids using MALDI-MSI and proteins using LC-MS/MS. Small pieces of bone were used for lipids analysis. These pieces were embedded and sectioned during sample preparation. Matrix was sprayed onto the section before MALDI-MSI analysis. Crushed bone tissue was used for the protein analysis. Proteins were extracted from the crushed bone tissue and subsequently digested using enzymes. The resulting peptides were analyzed with LC-MS/MS.

### 5.3.3 Lipid analysis with MALDI-MSI

#### 5.3.3.1 Sample preparation and matrix application

The lipid distribution in bone tissue, consisting of bone and bone marrow, were analyzed with MALDI-MSI. The embedding and sectioning of these samples followed the protocol described by Vandebosch *et al.* (2021).<sup>204</sup> In short, samples were embedded in 20% gelatin and 7.5% CMC dissolved in water (w/v) and directly frozen. 10% tragacanth was used to mount the samples on the specimen disc of the

cryotome to ensure firm attachment. Tissue sectioning was performed in a Leica CM1860 UV (Wetzlar, Germany) using a Shandon™ Tungsten Carbide D-profile knife (Thermo Scientific Emergo, Landsmeer, the Netherlands). The samples were sectioned at -15 °C and at a thickness of 12 µm. The sections were supported during sectioning using double-sided tape (Tesa®), and transferred and thaw-mounted on SuperFrost Plus microscopic glass slides. The samples were stored at -80 °C until further use.

Slides with tissue sections were dried in the desiccator for 35 minutes. Matrix application was performed using a TM-sprayer (HTX Technologies, Chapel Hill, NC, USA). CHCA was dissolved in methanol:water (70:30) at a concentration of 5 mg/mL. Thirteen layers were sprayed with a drying time of 10 s between layers using a nozzle temperature of 30 °C, a flow rate of 0.12 mL/min, nozzle velocity of 1300 mm/min, track spacing of 1.5 mm, and CC pattern.

#### 5.3.3.2 MALDI-MSI

A 9.4T Solarix Fourier Transform Ion Cyclotron Resonance (FT-ICR) Mass Spectrometer (Bruker Daltonik GmbH, Bremen, Germany) was used for MALDI-MSI acquisition operated with FTMS control (version 2.2.0, Bruker). The pixel size was set to 50 µm with SmartWalk enabled with a width of 25 µm and grid increment of 5 µm. The laser focus was set to a minimum (<30 µm), the laser power at 25% and 750 laser shot were fired per pixel at a frequency of 2000 Hz. 1M data points were acquired for each pixel for a  $m/z$  range of 100.44 to 1200. The lower cut-off frequency was set to  $m/z$  350 by setting the Q1 mass to 350 to reduce the intensity of the matrix peaks in the lower mass range. A data reduction factor of 95% was used to save the reduced profile spectra. FlexImaging (version 5.0, Bruker) was used for setting up regions of interest for acquisition. The calibration of the instrument was performed before each measurement using red phosphorus. The Solarix mass spectrometer has a large depth of laser focus and the ionization and mass analysis are consecutive, which makes the instrument less susceptible to height differences.

#### 5.3.3.3 Data analysis

All measurements were imported into SCiLS Lab 2022a (SCiLS GmbH, Bremen, Germany) using the centroided mass spectra. Annotations of bone and bone marrow were manually performed in QuPath (v0.2.3)<sup>209</sup> and imported into SCiLS. Peak picking was performed on the overview spectrum of all regions using mMass (Open Source Mass Spectrometry Tool, version 5.5.0)<sup>210</sup>. The distribution images of  $m/z$  values from this list were inspected to remove background peaks, due to the high number of matrix clusters and other background peaks. The obtained peak list included detected isotopes and was used in further data analysis. The imzml files

including only the peaks of the reduced peak list were exported per region of interest, with separate files for the bone and bone marrow regions. These imzml files were converted into MATLAB compatible files using an in-house-written R-script. The in-house-built ChemomeTricks toolbox (version 2.71c) for MATLAB (version 2014a, The MathWorks, Natick, USA) was used to perform principal component analysis-linear discriminant analysis (PCA-LDA) for comparison of the citrulline supplement and control group per time point. These analyses were performed separately for bone and bone marrow based on the exported information of the different regions.

### 5.3.3.4 Lipid identification

$m/z$  values of interest were selected based on the PCA-LDA analyses of the comparison of the citrulline supplement and control group for each time point. These  $m/z$  values were selected based on the highest unscaled loadings for each sample group per PCA-LDA analysis. Isotopic and low intensity peaks were removed from the lists with interesting  $m/z$  values, as detection is challenging after fragmentation. MS/MS analysis was used for the identification of the molecules using collision-induced dissociation (CID) fragmentation. Data for lipid identification were manually acquired on a SYNAPT HDMS G2-Si coupled with a prototype uMALDI source (Waters Corporation, Manchester, UK) operated with MassLynx (version 4.1, Waters), which has been described by Barré *et al.*<sup>106</sup> The MS/MS measurements were performed in sensitivity mode with a scan rate of 1.0 s per scan. The instrument was calibrated with red phosphorus twice a day. The laser fluence was set to 250 on bone marrow and 300 on bone arbitrary units set in the control software. The MS/MS isolation window was optimized per  $m/z$  value and was between 1 and 1.5 Da, depending on peak intensity and potentially interfering background and matrix cluster peaks. The trap collision energy varied between 15 and 25 arbitrary units. Lipid identifications were performed using a combination of MassLynx (version 4.1), LipostarMSI (version 1.3.0, Molecular Horizon, Bettona, Italy),<sup>169</sup> and database searches in ALEX<sup>123</sup> lipid calculator.<sup>140</sup>

## 5.3.4 Protein analysis with LC-MS

### 5.3.4.1 Protein extraction

Pieces of bone tissue, consisting of bone and bone marrow, per animal were homogenized using a pestle and mortar on liquid nitrogen. At least 30 mg of sample (range 37 to 238.7 mg) was placed into an Eppendorf tube containing 250  $\mu$ L 5% SSA. Samples were stored at -80 °C until further use.

The homogenized sample was thawed and centrifuged. The SSA was removed and 500  $\mu$ L of 5 M Urea/50 mM ABC was added. The proteins from the bone pellet were dissolved by shortly sonicating in an ultrasonic bath and 10 minutes at 10 °C in a thermoshaker at 750 rpm. Undissolved particles and the bone pellets were removed by centrifugation and the proteins in the solution were transferred to 3 kDa filters. The dissolved proteins were filtered three times using centrifugation and adding 400  $\mu$ L of 5 M Urea/50 mM ABC. The remaining volume was centrifuged to remove any remaining undissolved particles and the proteins in the solution were transferred to new Eppendorf tubes. The protein concentration of each sample was determined using Bradford Protein Assay (Bio-Rad Laboratories, Hercules, CA, USA) according to the manufacturer's protocol by measuring the absorption at 595 nm (optical density). Samples were stored at -80 °C until further use.

#### 5.3.4.2 Protein digestion

A total of 50  $\mu$ g protein was used per sample for the protein digestion. The sulfur bridges were broken with 20 mM DTT for 45 minutes at room temperature. The protein samples were alkylated with 40 mM IAM for 45 minutes at room temperature in the dark. The alkylation was terminated using 20 mM DTT for 45 minutes.

A mixture of Trypsin and LysC was used for protein digestion and was added at a ratio of 1:25 (enzyme:protein). The proteins were digested for 2 hours at 37 °C in a thermoshaker at 250 rpm. The urea concentration of the samples was reduced to 1 M by adding 50 mM ABC. Further digestion took place overnight at 37 °C in a thermoshaker at 250 rpm. The addition of FA with a final relative concentration of 1% was used to terminate the digestion. The samples were centrifuged to remove any remaining particles, transferred to new Eppendorf tubes, and stored at -80 °C until analysis.

#### 5.3.4.3 LC-MS/MS

A LC-MS based bottom-up proteomics experiment was conducted on the digested protein extract from the crushed bone samples. The peptide separation was performed on a Thermo Scientific Ultimate 3000 Rapid Separation UHPLC system (Dionex, Amsterdam, the Netherlands) equipped with a PepSep C18 analytical column (15 cm, ID 75  $\mu$ m, 1.9  $\mu$ m Reprosil, 120Å). The peptide samples were desalted on an online installed C18 trapping column and were separated on the analytical column with a 90 minutes linear gradient from 5% to 35% ACN with 0.1% FA at a flow rate of 300 nL/min. The UHPLC system was coupled to an Orbitrap QExactive HF mass spectrometer (Thermo Scientific, GmbH, Bremen, Germany).

Data-dependent acquisition (DDA) was used for the measurement of full mass spectrometry (MS) and MS/MS spectra. The full MS scans were acquired for  $m/z$  250-1250 at a resolution of 120 000 and were followed by MS/MS scans of the top 15 most intense ions at a resolution of 15 000.

### 5.3.4.4 *Data analysis and protein identification*

The DDA spectra were processed and analyzed with Proteome Discoverer (PD, version 2.2, Thermo Scientific) for the identification and quantification of the proteins. The search engine Sequest was used within the PD software applying the rat protein database (*Rattus norvegicus*, SwissProt TaxID= 10116, 8150 proteins included). The following settings were selected for the database search: trypsin as the enzyme, a maximum of 2 missed cleavages, minimum peptide length of 6, precursor mass tolerance of 10 ppm, fragment mass tolerance of 0.02 Da, dynamic modifications of methionine oxidation and protein N-terminus acetylation, and static modification of cysteine carbamidomethylation. In addition, two dynamic modifications were added to account for the administered labeled amino acids, namely  $^{15}\text{N}_2$  or  $^{13}\text{C}_1\text{-}^2\text{H}_2$  label both for arginine. The label of citrulline was included for arginine, as citrulline is not one of the amino acids used for proteins, but it is a precursor of arginine. The default Label Free Quantification (LFQ) settings in PD were used for protein quantification. In short, the peptide precursor intensities were used for peptide abundancies. Normalization was performed on the total peptide amount. Protein ratios were calculated based on pairwise peptide ratios. Background-based ANOVA was applied for hypothesis testing.

One of the samples of the citrulline supplement day 7 group (C2) was excluded from the data analysis and LFQ after the initial data analysis. These analyses showed a much lower number (less than 40% compared to other samples) of proteins identified with high confidence in this sample. The cause of this was an issue during protein digestion. Data analysis, including principal component analysis (PCA), and LFQ were performed using the remaining five samples for C2. The number of identified proteins was a total of 1186 for all samples combined, of which 883 proteins were identified with high confidence, after the exclusion of one of the samples. The more abundant proteins for the citrulline supplement and control group were determined per time point by protein ratio analyses. Proteins were considered as more abundant in one of the groups in the ratio with a fold change of 1.5 ( $\log_2$  of  $\geq 0.58$  or  $\leq -0.58$ ) and an adjusted p-value of  $\leq 0.05$ .

### 5.3.4.5 *Pathway analysis*

Pathway analysis was performed to identify the biological processes that differ between the citrulline supplement and respective control groups, based on the

more abundant proteins found during data analysis of the proteomics data. Pathway analysis was performed using Reactome Pathway Database.<sup>211</sup> The gene names related to the more abundant proteins were used for analysis to obtain a higher coverage compared to the use of UniProt accession codes. The p-value was set to  $\leq 0.05$  for the selection of involved pathways. In addition, the threshold for the false discovery rate (FDR) was set to  $\leq 0.25$  for possible involved pathways. This FDR threshold was set to  $\leq 0.05$  for involved pathways with high confidence. In case multiple pathways that were connected in the pathway overview of Reactome were noticed to have the same matched gene name, one of these pathways was selected based on the specificity that could be expected based on the matched gene names.

## 5.4 Results

### 5.4.1 Comparison of lipids between citrulline supplement and control group

#### 5.4.1.1 Lipid profiles in cortical bone

The PCA-LDA analyses for the reduced peak list showed no complete separation for 3, 7, 14, and 28 DPO between the citrulline supplement and control group for bone, as represented in Figure 5.3A, B, C, and D, respectively. The citrulline supplement and control group distributions show quite some overlap in their discriminant distributions for the different time points, indicating small differences between the treatment and control group. The lipids in the top 30 unscaled loadings per time point contributing to the separation between the treatment and control group were identified (Table 5.2). The major classes of identified lipids are phosphatidylcholines (PCs) and lysophosphatidylcholines (LPCs). Furthermore, some acyl carnitines (CARs), triacyl/alkylglycerides (TGs), and a sphingomyelin (SM) contributed to the difference between the citrulline supplement and respective control group. Certain lipids were identified with different adducts and the sample groups overlapped between the different adducts in most cases, except for PC 32:0. The LPCs with an alkyl group are contributing more to the lipid profiles of the citrulline supplement group at different time points. On the contrary, the TGs are only contributing to the control group at 28 DPO. The other lipid classes contribute to both the treatment and control group depending on the lipid and the time point, as the some lipids contribute the lipid profile of both the treatment and control group depending the time point. Some lipids show the same pattern in contributions, like SM 34:1;O2 and PC 34:1 for the  $[M+H]^+$  ions. The overlap between the lipids contributing to the different time points in the citrulline supplement and control group are displayed in Figure 5.4A and B, respectively.

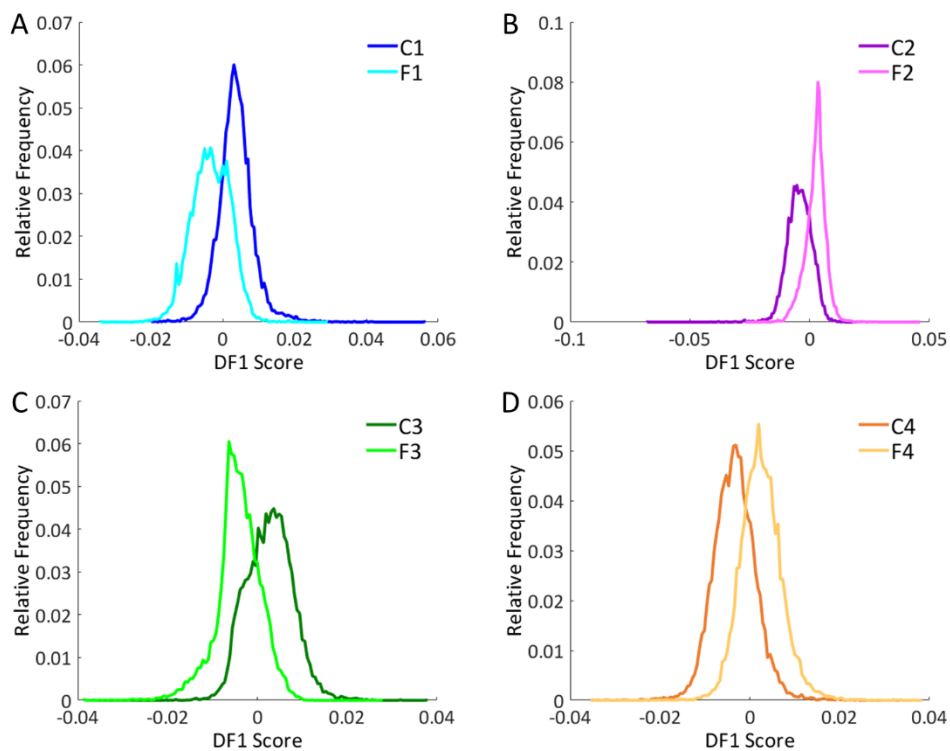


**Figure 5.3:** The first discriminant function (DF1) for the lipid comparison of the citrulline supplement (C) and control (F) group per time point for bone representing the results of the PCA-LDA analyses. DF1 plots are shown for **A** 3, **B** 7, **C** 14, and **D** 28 DPO representing 2.20, 1.47, 1.94, and 1.61% of the variance in the dataset, respectively. C1, C2, C3, and C4 represent 3, 7, 14, and 28 DPO in the citrulline supplement group, respectively. F1, F2, F3, and F4 represent 3, 7, 14, and 28 DPO in the control group, respectively.

Interestingly, most of the lipids contributing to 3, 7, and 28 DPO overlap in the citrulline supplement group, while no overlap is seen for 14 DPO. Quite a high number of lipids contributing to the control group displays overlap with other time points, especially overlap between 7 DPO with other time points can be noticed. Some lipids contribute to two or more consecutive time points. No lipid is contributing to all time points in either the treatment and control group.

#### 5.4.1.2 Lipid profiles in bone marrow

Figure 5.5A, B, C, and D shows the separation between the citrulline supplement and control group for bone marrow for 3, 7, 14, and 28 DPO, respectively, based on the PCA-LDA analyses for the reduced peak list. The separation between the

**Table 5.2:** Lipid assignments based on high mass resolution data and MS/MS data for bone. For each assignment, the  $m/z$  value obtained with the high mass resolution mass spectrometer (Solarix), the lipid assignment, the detected ion, the ppm error, and the sample group, in which the assigned lipid has a higher presence, are provided. The higher lipid contribution for a sample group is in comparison to the other treatment group at the same time point. C1, C2, C3, and C4 represent 3, 7, 14, and 28 DPO in the citrulline supplement group, respectively. F1, F2, F3, and F4 represent 3, 7, 14, and 28 DPO in the control group, respectively.

$m/z$ value	Assignment	Ion	$\Delta$ ppm error	Sample group
400.343	CAR 16:0	[M+H] <sup>+</sup>	2.25	C1 C4
426.359	CAR 18:1	[M+H] <sup>+</sup>	2.81	F3 C4
478.330	LPC O-16:2	[M+H] <sup>+</sup>	1.67	C1 C2 C4
496.341	LPC 16:0	[M+H] <sup>+</sup>	2.42	F2
504.346	LPC O-18:3	[M+H] <sup>+</sup>	2.18	C1 C4
506.362	LPC O-18:2	[M+H] <sup>+</sup>	2.96	C1 C2 C4
522.357	LPC 18:1	[M+H] <sup>+</sup>	3.06	C1
524.372	LPC 18:0	[M+H] <sup>+</sup>	1.72	F2 F3
546.354	LPC 18:0	[M+Na] <sup>+</sup>	1.83	F3
562.328	LPC 18:0	[M+K] <sup>+</sup>	1.96	F3
703.577	SM 34:1;O2	[M+H] <sup>+</sup>	3.13	F1 F2 C3
706.540	PC 30:0	[M+H] <sup>+</sup>	2.69	F1 C3
725.558	SM 34:1;O2	[M+Na] <sup>+</sup>	1.65	F1 C3
732.556	PC 32:1	[M+H] <sup>+</sup>	3.00	F2 C3
734.570	PC 32:0	[M+H] <sup>+</sup>	0.82	F2 C3
756.554	PC 32:0	[M+Na] <sup>+</sup>	3.44	C3 F4
758.571	PC 34:2	[M+H] <sup>+</sup>	2.64	F2 F4

**Table 5.2 (continued):** Lipid assignments based on high mass resolution data and MS/MS data for bone.

<i>m/z</i> value	Assignment	Ion	$\Delta$ ppm error	Sample group
760.587	PC 34:1	[M+H] <sup>+</sup>	2.50	F1
				F2
				C3
772.527	PC 32:0	[M+K] <sup>+</sup>	2.20	C3
780.553	PC 34:2	[M+Na] <sup>+</sup>	2.05	F1
				F4
782.571	PC 36:4	[M+H] <sup>+</sup>	2.04	F1
				F2
				C3
				F4
804.554	PC 36:4	[M+H] <sup>+</sup>	3.23	F1
808.587	PC 38:5	[M+H] <sup>+</sup>	2.35	F1
810.603	PC 38:4	[M+H] <sup>+</sup>	2.84	F1
				F2
820.528	PC 36:4	[M+K] <sup>+</sup>	3.29	F1
832.585	PC 38:4	[M+Na] <sup>+</sup>	2.76	F1
853.730	TG 52:5	[M+H] <sup>+</sup>	2.34	F4
879.745	TG 54:6	[M+H] <sup>+</sup>	1.59	F4

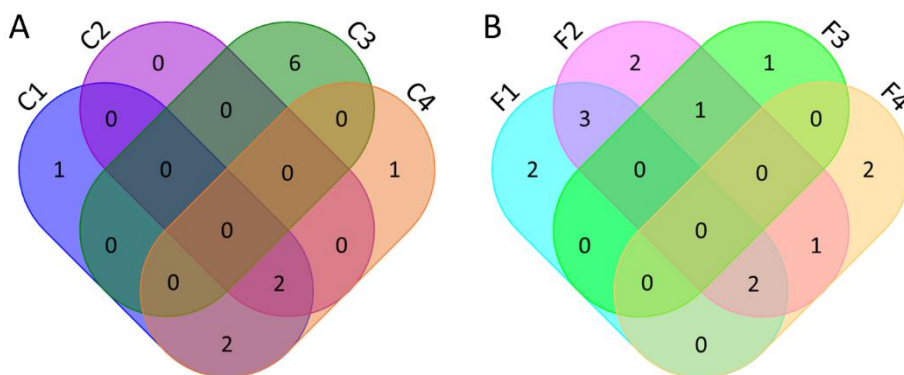


**Figure 5.4:** Venn diagrams of the lipids from bone contributing at the different time points for citrulline supplement and control group. Lipids detected with different adducts were grouped together per sample group. **A** Overlap in the contributing lipids in the citrulline supplement group (C). **B** Overlap in the contributing lipids in the control group (F). The number depicted in the overlapping areas indicate the contribution of a lipid to all the related time points. C1, C2, C3, and C4 represent 3, 7, 14, and 28 DPO in the citrulline supplement group, respectively. F1, F2, F3, and F4 represent 3, 7, 14, and 28 DPO in the control group, respectively.

citrulline supplement and control group is better for 7 and 14 DPO than for 3 and 28 DPO, as the overlap between the discriminate distributions of the citrulline supplement and respective control group is less. Therefore, the difference between the treatment groups at 7 and 14 DPO are probably bigger than at 3 and 28 DPO. The lipids in the top 30 unscaled loadings per time point contributing to the separation between treatment groups were identified and can be found in Table 5.3. No identifications were included for the citrulline supplement group 28 DPO (C4), as the top 30 unscaled loadings included only the isotopes of molecules and unidentified peaks. PCs and LPCs are the major classes of identified lipids, but also one CAR, one SM, and two TGs contribute to the separation between treatment and control group. The different identified adducts per lipid show little similarity

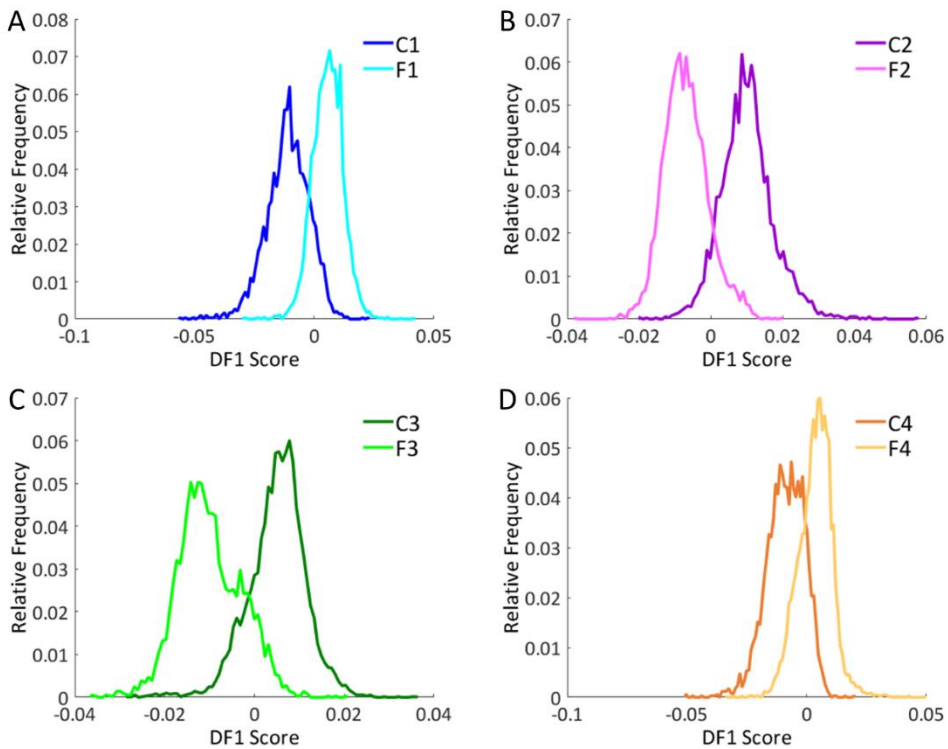


**Figure 5.5:** The first discriminant function (DF1) for the lipid comparison of the citrulline supplement (C) and control (F) group per time point for bone marrow representing the results of the PCA-LDA analyses. DF1 plots are shown for **A** 3, **B** 7, **C** 14, and **D** 28 DPO representing 2.69, 3.46, 3.53, and 2.75% of the variance in the dataset, respectively. C1, C2, C3, and C4 represent 3, 7, 14, and 28 DPO in the citrulline supplement group, respectively. F1, F2, F3, and F4 represent 3, 7, 14, and 28 DPO in the control group, respectively.

between them in terms of the sample groups they contribute to, which is same as for the lipids in the cortical bone. The CAR and LPCs with an alkyl group are only contributing to the lipid profile of the citrulline supplement group, while the TGs contribute to the control group, specifically at 28 DPO. The LPCs and PCs seem to contribute to both groups during their separation on different time points. Interestingly, the LPCs are contributing mainly to the citrulline supplement group, while the PCs contribute more the control group. Some lipids contribute to both the treatment and control group, but their contribution to the lipid profile of each group is at different time points. A few lipids show the same pattern in contribution throughout the different time points, for example PC 36:6 and PC 38:8 for the  $[M+H]^+$  ions. Figure 5.6A and B show the overlap between the lipids contributing to the different time points for the citrulline supplement and control group, respectively. Only overlap of three lipids between 3 and 14 DPO can be noticed for the citrulline supplement group. More overlap in contributing lipids between the different time points can be seen for the control group. Especially the lipids contributing to 3 DPO overlap with different time points. In addition, some overlap can be seen between 14 and 28 DPO. No lipid is contributing to all time points in either the treatment and control group.

The separation between the citrulline supplement and control group is better for bone marrow than for bone when comparing Figures 5.3 and 5.5. A pattern of medium separation at 3 DPO, good separation at 7 and 14 DPO, and limited separation at 28 DPO is seen for bone marrow. However, this pattern was not present for cortical bone. A high number of lipids can be seen that are contributing to treatment group separation in bone and bone marrow based on a comparison between Tables 5.2 and 5.3. In general, the identified lipid classes overlap between bone and bone marrow and the main classes are LPC and PC in both. Four, zero, three, and zero lipids overlap between bone and bone marrow for the citrulline supplement group for 3, 7, 14, and 28 DPO, respectively. Four, six, zero, and three lipids overlap between bone and bone marrow for the control group for 3, 7, 14, and 28 DPO, respectively.

### 5.4.2 Comparison of proteins and pathways between citrulline supplement and control group

#### 5.4.2.1 Protein profiles in cortical bone and bone marrow

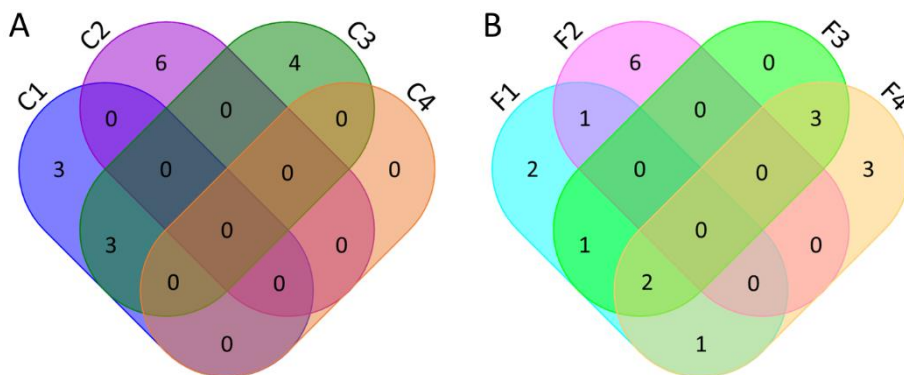
Protein profiles were obtained for each sample group from the mix of crushed cortical bone and bone marrow. PCAs were performed to compare the protein profiles between the citrulline supplement and control groups per time point. The

**Table 5.3:** Lipid assignments based on high mass resolution data and MS/MS data for bone marrow. For each assignment, the  $m/z$  value obtained with the high mass resolution mass spectrometer (Solarix), the lipid assignment, the detected ion, the ppm error, and the sample group, in which the assigned lipid has a higher presence, are provided. The higher lipid contribution for a sample group is in comparison to the other treatment group at the same time point. C1, C2, C3, and C4 represent 3, 7, 14, and 28 DPO in the citrulline supplement group, respectively. F1, F2, F3, and F4 represent 3, 7, 14, and 28 DPO in the control group, respectively.

$m/z$ value	Assignment	Ion	$\Delta$ ppm error	Sample group
400.343	CAR 16:0	[M+H] <sup>+</sup>	2.25	C3
478.330	LPC O-16:2	[M+H] <sup>+</sup>	1.67	C1
496.341	LPC 16:0	[M+H] <sup>+</sup>	2.42	C1 C3
504.346	LPC O-18:3	[M+H] <sup>+</sup>	2.18	C1
506.362	LPC O-18:2	[M+H] <sup>+</sup>	2.96	C1
518.323	LPC 16:0	[M+Na] <sup>+</sup>	2.51	F2
522.357	LPC 18:1	[M+H] <sup>+</sup>	3.06	C1 C3
524.372	LPC 18:0	[M+H] <sup>+</sup>	1.72	C3
534.297	LPC 16:0	[M+K] <sup>+</sup>	2.62	C3
546.354	LPC 18:0	[M+Na] <sup>+</sup>	1.83	F2
703.577	SM 34:1;O2	[M+H] <sup>+</sup>	3.13	F2 C3
706.540	PC 30:0	[M+H] <sup>+</sup>	2.69	C1 C3
720.592	PC O-32:0	[M+H] <sup>+</sup>	2.78	F2
734.570	PC 32:0	[M+H] <sup>+</sup>	0.82	F2 C3
754.538	PC 32:1	[M+Na] <sup>+</sup>	3.05	C2
756.554	PC 32:0	[M+Na] <sup>+</sup>	3.44	F2
758.571	PC 34:2	[M+H] <sup>+</sup>	2.64	C2 F4
766.578	PC O-36:5	[M+H] <sup>+</sup>	4.57	F1 C2
768.592	PC O-36:4	[M+H] <sup>+</sup>	2.34	F2
778.541	PC 36:6	[M+H] <sup>+</sup>	3.72	C2 F3 F4
802.540	PC 38:8	[M+H] <sup>+</sup>	2.37	C2 F3 F4
804.554	PC 36:4	[M+Na] <sup>+</sup>	3.23	F1 F3

**Table 5.3 (continued):** Lipid assignments based on high mass resolution data and MS/MS data for bone marrow.

<i>m/z</i> value	Assignment	Ion	$\Delta$ ppm error	Sample group
806.572	PC 38:6	[M+H] <sup>+</sup>	3.22	F3
				F4
808.587	PC 38:5	[M+H] <sup>+</sup>	2.35	F1
810.603	PC 38:4	[M+H] <sup>+</sup>	2.84	F2
820.528	PC 36:4	[M+K] <sup>+</sup>	3.29	F1
				F3
				F4
828.557	PC 40:9	[M+H] <sup>+</sup>	3.86	F1
				C2
				F3
				F4
830.572	PC 40:8	[M+H] <sup>+</sup>	3.13	F1
				F4
832.585	PC 38:4	[M+Na] <sup>+</sup>	2.76	F1
853.730	TG 52:5	[M+H] <sup>+</sup>	2.34	F4
856.588	PC 42:9	[M+H] <sup>+</sup>	3.39	F1
				F3
879.745	TG 54:6	[M+H] <sup>+</sup>	1.59	F4

**Figure 5.6:** Venn diagrams of the lipids from bone marrow contributing at the different time points for citrulline supplement and control group. Lipids detected with different adducts were grouped together per sample group. **A** Overlap in the contributing lipids in the citrulline supplement group (C). **B** Overlap in the contributing lipids in the control group (F). The number depicted in the overlapping areas indicate the contribution of a lipid to all the related time points. C1, C2, C3, and C4 represent 3, 7, 14, and 28 DPO in the citrulline supplement group, respectively. F1, F2, F3, and F4 represent 3, 7, 14, and 28 DPO in the control group, respectively.

## Effect of citrulline supplement on lipid and protein profiles during fracture healing

PCA plots of the first two principal components (PC1 and PC2) do not show separation between the citrulline supplement and the control group, as displayed in Figure 5.7. Higher PCs did not contribute to improved separation between the citrulline supplement groups and respective control groups.

The more abundant proteins were determined by comparing the citrulline supplement and control group per time point. Ten, thirteen, nine, and five proteins

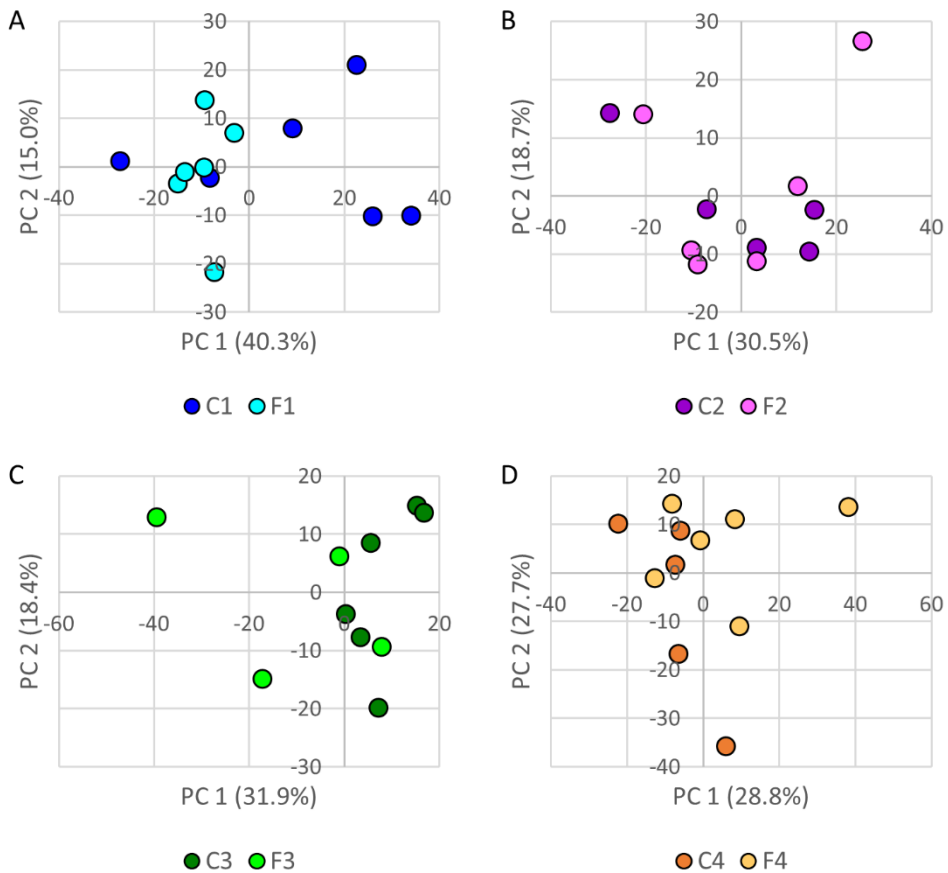


**Figure 5.7:** Principal component analysis (PCA) of protein profiles of the citrulline supplement (C) and control groups (F) per time point. Each dot represents one sample. The first two principal components are shown, namely PC1 and PC2, for **A** 3, **B** 7, **C** 14, and **D** 28 DPO. C1, C2, C3, and C4 represent 3, 7, 14, and 28 DPO in the citrulline supplement group, respectively. F1, F2, F3, and F4 represent 3, 7, 14, and 28 DPO in the control group, respectively.

were more abundant in the citrulline supplement group compared to the control group at 3, 7, 14, and 28 DPO, respectively. Five, sixteen, nineteen, and nineteen proteins were more abundant in the control group compared to the citrulline supplement group at 3, 7, 14, and 28 DPO, respectively. An overview of these proteins for each sample group in comparison to the other treatment group per time point can be found in Table 5.4. The overlap between proteins with higher abundance within the citrulline supplement and control group is limited between different time points, as shown in Figures 5.8A and B, respectively. This can be attributed to the different fracture healing phases that take place at different time points. The overlap of proteins between the different time points is higher for the control group than for the citrulline supplement group. Seven DPO shows the most overlap with the other time points, especially for the control group. In addition, the more abundant proteins of 28 DPO for the control group overlap quite a bit with the other time points. Comparison of the more abundant proteins between the treatment and control group shows that only four proteins overlap between the citrulline supplement and control group, namely Cathepsin G (Ctsg), Guanine deaminase (Gda), Proteasome subunit beta type-2 (Psmb2), and Slit homolog 1 protein (Slit1). The abundance of these proteins was higher at a later time point in the control group than in the citrulline supplement group.

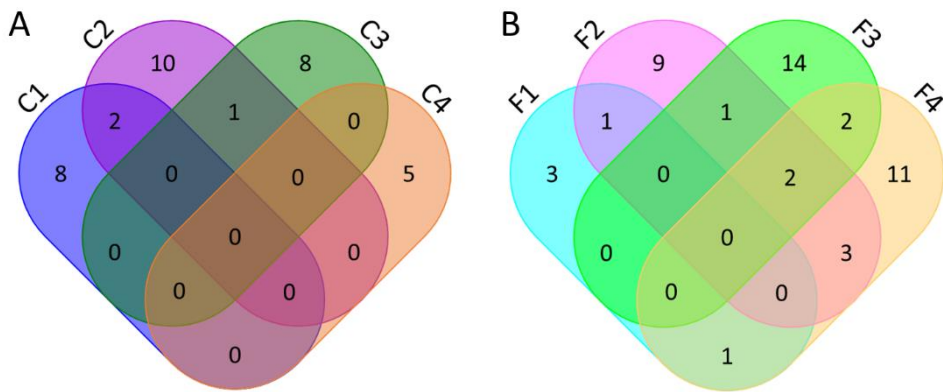


**Figure 5.8:** Venn diagrams of the more abundant proteins at the different time points for citrulline supplement and control group. **A** Overlap in the more abundant proteins in the citrulline supplement group in comparison to the respective control group. **B** Overlap in the more abundant proteins in the control group in comparison to the respective citrulline supplement group. The number depicted in the overlapping areas indicate the higher abundance of the same protein at different time points. C1, C2, C3, and C4 represent 3, 7, 14, and 28 DPO in the citrulline supplement group, respectively. F1, F2, F3, and F4 represent 3, 7, 14, and 28 DPO in the control group, respectively.

**Table 5.4:** Proteins with higher abundance from the comparison of citrulline supplement group with the respective control group per time point. Only proteins with an abundance ratio (log2) of  $\geq 0.58$  or  $\leq -0.58$  (fold change of 1.5) and an adjusted p-value of  $\leq 0.05$  were considered more abundant in the corresponding sample group. Positive and negative abundance ratios were related to proteins in the citrulline supplement (C) and control (F) group, respectively. The protein name, related gene name, sample group in which the protein is more abundant, the used ratio between the citrulline supplement and control group, the abundance ratio (log2), and adjusted p-value are provided. C1, C2, C3, and C4 represent 3, 7, 14, and 28 DPO in the citrulline supplement group, respectively. F1, F2, F3, and F4 represent 3, 7, 14, and 28 DPO in the control group, respectively.

Protein name	Gene name	Sample group	Ratio	Abundance ratio (log2)	Adjusted p-value
60S acidic ribosomal protein P1	Rplp1	C2	C2/F2	0.7	0.033
60S ribosomal protein L27	Rpl27	C1	C1/F1	1.03	0.028
Acidic leucine-rich nuclear phosphoprotein 32 family member B	Anp32b	F2	C2/F2	-0.88	0.024
Actin, alpha cardiac muscle 1	Actc1	C1	C1/F1	1.03	0.028
Acyl-protein thioesterase 1	Lyp1a1	C3	C3/F3	1.31	0.017
ADP-ribosylation factor-like protein 3	Arl3	F1	C1/F1	-6.64	$8.071e^{-16}$
		F2	C2/F2	-6.64	$4.404e^{-16}$
Alpha-1B-glycoprotein	A1bg	C2	C2/F2	0.78	0.012
Alpha-crystallin B chain	Cryab	F4	C4/F4	-1.00	0.012
Annexin A6	Anxa6	C4	C4/F4	1.17	0.041
Band 3 anion transport protein	Slc4a1	C2	C2/F2	0.99	$6.731e^{-3}$
Calmodulin-3	Calm3	F3	C3/F3	-1.17	0.041
Calnexin	Canx	C2	C2/F2	0.93	$3.609e^{-3}$
		F2	C2/F2	-0.91	$6.037e^{-3}$
Carbonic anhydrase 3	Ca3	F4	C4/F4	-1.09	$5.002e^{-3}$
Carboxylesterase 1D	Ces1d	F2	C2/F2	-1.03	0.015
		C2	C2/F2	1.1	$4.266e^{-5}$
Cathepsin G	Ctsg	F3	C3/F3	-1.18	0.036

**Table 5.4 (continued):** More abundant proteins from the comparison of citrulline supplement group with the respective control group per time point.

Protein name	Gene name	Sample group	Ratio	Abundance ratio (log2)	Adjusted p-value
Collagen alpha-1(II) chain	Col2a1	F3	C3/F3	-1.93	2.401e <sup>-5</sup>
Collagen alpha-1(XII) chain (Fragment)	Col12a1	C1	C1/F1	1.31	4.258e <sup>-4</sup>
Desmin	Des	F4	C4/F4	-0.92	0.027
Deoxyuridine 5'-triphosphate nucleotidohydrolase	Dut	F3	C3/F3	-1.38	7.582e <sup>-3</sup>
Dynein light chain roadblock-type 1	Dynlrb1	F3	C3/F3	-1.29	0.015
Elongation factor 1-alpha 2	Eef1a2	F4	C4/F4	-0.88	0.037
Eukaryotic translation initiation factor 3 subunit A	Eif3a	F2	C2/F2	-1.16	1.857e <sup>-3</sup>
		F3	C3/F3	-1.45	4.052e <sup>-3</sup>
		F3	C3/F3	-1.52	2.179e <sup>-3</sup>
Ferritin light chain 1	Ftl1	F4	C4/F4	-0.96	0.017
Fibromodulin	Fmod	C1	C1/F1	1.06	0.022
Follistatin-related protein 1	Fstl1	C4	C4/F4	6.64	4.222e <sup>-16</sup>
Fructose-bisphosphate aldolase A	Aldoa	C3	C3/F3	1.21	0.036
Galectin-5	Lgals5	C2	C2/F2	0.66	0.050
Gamma-enolase	Eno2	F3	C3/F3	-1.22	0.028
Glucose-6-phosphate isomerase	Gpi	C3	C3/F3	1.61	1.237e <sup>-3</sup>
		C2	C2/F2	1.01	0.013
Glycogen phosphorylase, muscle form	Pygm	C3	C3/F3	6.64	4.596e <sup>-16</sup>
		C2	C2/F2	1.08	3.179e <sup>-4</sup>
Guanine deaminase	Gda	F4	C4/F4	-0.95	0.019
Heat shock protein beta-6	Hspb6	F4	C4/F4	-1.05	6.933e <sup>-3</sup>
Heat shock protein beta-7 (Fragment)	Hspb7	F4	C4/F4	-1.14	2.940e <sup>-3</sup>
Heat shock protein beta-8	Hspb8	F4	C4/F4	-1.08	5.254e <sup>-3</sup>
Hemogen	Hemgn	C1	C1/F1	6.64	8.071e <sup>-16</sup>

**Table 5.4 (continued):** More abundant proteins from the comparison of citrulline supplement group with the respective control group per time point.

Protein name	Gene name	Sample group	Ratio	Abundance ratio (log2)	Adjusted p-value
Histone H3.3	H3-3b	C1	C1/F1	6.64	8.071e <sup>-16</sup>
		C2	C2/F2	1.06	0.026
Junctophilin-2	Jph2	C2	C2/F2	1.05	4.730e <sup>-3</sup>
Keratin, type I cytoskeletal 14	Krt14	C4	C4/F4	2.41	7.092e <sup>-10</sup>
Keratin, type II cytoskeletal 1	Krt1	F3	C3/F3	-2.00	1.057e <sup>-5</sup>
Keratin, type II cytoskeletal 5	Krt5	F1	C1/F1	-0.64	9.643e <sup>-4</sup>
		F4	C4/F4	-1.12	3.273e <sup>-3</sup>
Lactadherin	Mfge8	F3	C3/F3	-1.57	1.401e <sup>-3</sup>
Leukemia inhibitory factor receptor	Lifr	F1	C1/F1	-1.23	5.166e <sup>-10</sup>
Leukocyte cell-derived chemotaxin 1	Cnmd	F3	C3/F3	-1.72	2.755e <sup>-4</sup>
Mitochondrial fission 1 protein	Fis1	F2	C2/F2	-1.05	5.352e <sup>-3</sup>
Myosin-6	Myh6	F4	C4/F4	-2.00	4.814e <sup>-9</sup>
Myosin-7	Myh7	F3	C3/F3	-1.49	2.780e <sup>-3</sup>
Myosin-binding protein C, slow-type (Fragment)	Mybpc1	F4	C4/F4	-1.62	4.272e <sup>-6</sup>
		F4	C4/F4	-1.45	5.367e <sup>-5</sup>
Myosin light chain 3	MyI3	F2	C2/F2	-0.76	0.043
		F3	C3/F3	-1.22	0.030
Myosin light chain 4	MyI4	F4	C4/F4	-1.51	2.025e <sup>-5</sup>
		F1	C1/F1	-0.58	2.404e <sup>-3</sup>
Myosin regulatory light chain 2, ventricular/cardiac muscle isoform	MyI2	F2	C2/F2	-1.05	5.819e <sup>-4</sup>
		F3	C3/F3	-1.44	4.312e <sup>-3</sup>
Myristoylated alanine-rich C-kinase substrate	Marcks	F4	C4/F4	-1.87	5.466e <sup>-8</sup>
		C4	C4/F4	1.18	0.039

**Table 5.4 (continued):** More abundant proteins from the comparison of citrulline supplement group with the respective control group per time point.

Protein name	Gene name	Sample group	Ratio	Abundance ratio (log2)	Adjusted p-value
NADH dehydrogenase [ubiquinone] iron-sulfur protein 4, mitochondrial	Ndufs4	C3	C3/F3	1.52	2.778e <sup>-3</sup>
NADH-ubiquinone oxidoreductase 75 kDa subunit, mitochondrial	Ndufs1	C2	C2/F2	0.73	0.043
Neutrophil gelatinase-associated lipocalin	Lcn2	C2	C2/F2	0.77	0.014
Nexilin	Nexn	C1	C1/F1	1.09	0.014
N(G),N(G)-dimethylarginine dimethylaminohydrolase 2	Ddah2	C1	C1/F1	0.99	0.043
Nuclear autoantigenic sperm protein	Nasp	F3	C3/F3	-6.64	4.596e <sup>-16</sup>
Nucleolar protein 3	Nol3	F2	C2/F2	-0.85	0.039
Phosphoglucomutase-1	Pgm1	C3	C3/F3	1.77	2.429e <sup>-4</sup>
Plasma kallikrein	Klkb1	F1	C1/F1	-0.63	1.145e <sup>-3</sup>
Programmed cell death protein 6	Pdcd6	F3	C3/F3	-1.24	0.024
Proteasomal ubiquitin receptor ADRM1	Adrm1	C3	C3/F3	6.64	4.596e <sup>-16</sup>
Proteasome subunit beta type-2	Psmb2	F2	C2/F2	-6.64	4.404e <sup>-16</sup>
		C3	C3/F3	6.64	4.596e <sup>-16</sup>
Protein disulfide isomerase Creld2	Creld2	C4	C4/F4	1.29	0.014
Protein phosphatase 1G	Ppm1g	F2	C2/F2	-6.64	4.404e <sup>-16</sup>
Protein RoBo-1 (Rodent bone protein)	LOC24906	F3	C3/F3	-1.64	6.362e <sup>-4</sup>
Protein S100-A8	S100a8	F3	C3/F3	-1.51	2.324e <sup>-3</sup>
Protein S100-B	S100b	F2	C2/F2	-0.82	0.047
Serine/arginine-rich splicing factor 2	Srsf2	F4	C4/F4	-0.86	0.043
Serine/arginine-rich splicing factor 6	Srsf6	C1	C1/F1	1.36	1.372e <sup>-4</sup>
		C1	C1/F1	6.64	8.071e <sup>-16</sup>
		C2	C2/F2	6.64	4.404
Slit homolog 1 protein	Slit1	F3	C3/F3	-6.64	4.596e <sup>-16</sup>

**Table 5.4 (continued):** More abundant proteins from the comparison of citrulline supplement group with the respective control group per time point.

Protein name	Gene name	Sample group	Ratio	Abundance ratio (log2)	Adjusted p-value
Spondin-1	Spon1	F2	C2/F2	-0.75	0.047
Thrombospondin-4	Thbs4	F2	C2/F2	-1.44	3.615e <sup>-6</sup>
		F4	C4/F4	-1.24	8.924e <sup>-4</sup>
Troponin I, slow skeletal muscle	Tnni1	F4	C4/F4	-1.18	1.860e <sup>-3</sup>
Troponin T, slow skeletal muscle	Tnnt1	F2	C2/F2	-0.98	1.857e <sup>-3</sup>
		F4	C4/F4	-1.41	9.272e <sup>-5</sup>
Vitamin K-dependent protein C	Proc	F2	C2/F2	-1.01	0.013
Vomerol type-1 receptor 95	Vom1r95	C3	C3/F3	1.83	1.245e <sup>-4</sup>

## 5.4.2.2 Pathway analysis

The pathways related to the more abundant proteins can be found in Table 5.5A-D for the different time points. Figure 5.9A and B show the overlap between the more active pathways for the citrulline supplement and control group, respectively. The overlap between the pathways of the citrulline supplement group is limited, while the pathways of the control group show a higher number overlapping pathways, despite the different fracture healing processes going on at the different time points. Interestingly, the striated muscle contraction pathway is more active at all time points in the control group (Table 5.5). Most overlap of more active pathways is seen for 7 DPO for citrulline supplement and control group and 28 DPO for the control group, similar to the more abundant proteins.

The comparison of the overlap in proteins (Figure 5.8) and pathways (Figure 5.9) shows that overlap in more abundant proteins does not indicate overlap in pathways, as each protein can be part of many different pathways. On the other hand, the overlap between more active pathways between time points can be seen in Figure 5.9 that is not related to overlap in the more abundant proteins at the same overlapping area in Figure 5.8. This indicates that different proteins with higher abundance contribute to these overlapping pathways at different time

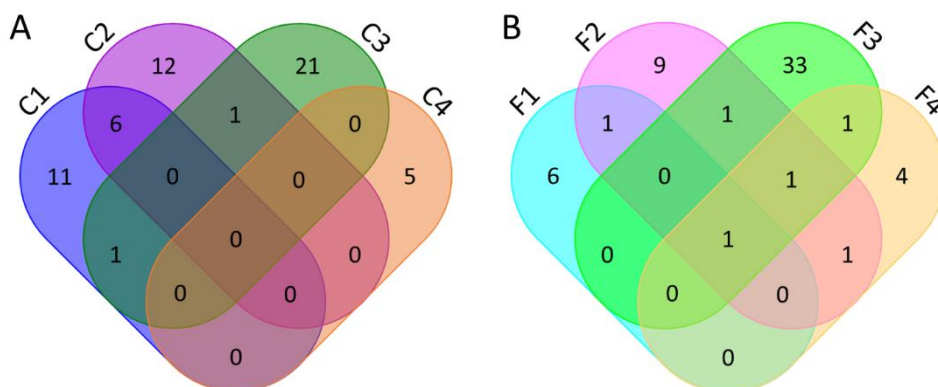


**Figure 5.9:** Venn diagrams of the more active pathways at the different time points for citrulline supplement and control group. **A** Overlap in the more active pathways in the citrulline supplement group in comparison to the respective control group. **B** Overlap in the more active pathways in the control group in comparison to the respective citrulline supplement group. The number depicted in the overlapping areas indicate the higher activity of the same pathway at different time points. C1, C2, C3, and C4 represent 3, 7, 14, and 28 DPO in the citrulline supplement group, respectively. F1, F2, F3, and F4 represent 3, 7, 14, and 28 DPO in the control group, respectively.

**Table 5.5:** More active reactome pathways from the comparison of citrulline supplement group with the respective control group per time point based on the more abundant proteins. Only pathways with a p-value of  $\leq 0.05$  were considered more activated in the corresponding sample group. The pathway name, p-value, false discovery ratio (FDR), and matched gene names are provided per time point.

**Table 5.5A** More active reactome pathways for 3 DPO in the citrulline supplement and control group.

Citrulline supplement group				Control group			
Pathway name	p-value	FDR	Gene names	Pathway name	p-value	FDR	Gene names
RNA Polymerase II Transcription Termination	0.002	0.086	Srsf6	RUNX1 regulates transcription of genes involved in interleukin signaling	<0.001	<0.001	Lifr
eNOS activation	0.010	0.086	Ddah2	Formation of Fibrin Clot (Clotting Cascade)	<0.001	0.002	Klkb1
Signaling by ROBO receptors	0.017	0.086	Slit1, Rpl27	Trafficking of myristoylated proteins to the cilium	0.004	0.012	Arl3
Processing of Capped Intron-Containing Pre-mRNA	0.022	0.086	Srsf6	Keratinization	0.007	0.020	Krt5
RNA Polymerase I Promoter Opening	0.030	0.086	H3-3b	Interleukin-6 family signaling	0.018	0.033	Lifr
DNA methylation	0.032	0.086	H3-3b	Activation of Matrix Metalloproteinases	0.021	0.033	Klkb1
Keratan sulfate/keratin metabolism	0.032	0.086	Fmod	Striated Muscle Contraction	0.024	0.033	Myl4
Striated Muscle Contraction	0.034	0.086	Actc1	Retrograde transport at the Trans-Golgi-Network	0.032	0.033	Arl3
Activated PKIN1 stimulates transcription of AR (androgen receptor) regulated genes KLK2 and KLK3	0.034	0.086	H3-3b				

**Table 5.5A (continued)** More active reactome pathways for 3 DPO in the citrulline supplement and control group.

Citrulline supplement group				Control group			
Pathway name	p-value	FDR	Gene names	Pathway name	p-value	FDR	Gene names
SIRT1 negatively regulates rRNA expression	0.034	0.086	H3-3b				
Assembly of the ORC complex at the origin of replication	0.035	0.086	H3-3b				
Synthesis of PA	0.036	0.086	Nexn				
PRC2 methylates histones and DNA	0.039	0.086	H3-3b				
Collagen chain trimerization	0.041	0.086	Col12a1				
Condensation of Prophase Chromosomes	0.042	0.086	H3-3b				
ERCC6 (CSB) and EHMT2 (G9a) positively regulate rRNA expression	0.042	0.086	H3-3b				
Inhibition of DNA recombination at telomere	0.045	0.086	H3-3b				
Netrin-1 signaling	0.046	0.086	Slit1				

**Table 5.5B** More active reactome pathways for 7 DPO in the citrulline supplement and control group.

Citrulline supplement group				Control group			
Pathway name	p-value	FDR	Gene names	Pathway name	p-value	FDR	Gene names
Glycogen breakdown (glycogenolysis)	<0.001	0.066	Pygm	Striated Muscle Contraction	<0.001	0.007	Tnnt1, Myl2, Myl3
Neutrophil degranulation	0.002	0.103	Ctsg, Pygm, A1bg, Lcn2	Reversible hydration of carbon dioxide	<0.001	0.027	Ca3
Activation, myristoylation of BID and translocation to mitochondria	0.004	0.116	Ctsg	Reactions specific to the hybrid N-glycan synthesis pathway	0.004	0.147	Myl2
Signaling by Interleukins, incl. IL-1, IL-4, IL-13, IL-27, IL-35	0.005	0.116	Ctsg, Canx, Lcn2	Signaling by ERBB4	0.006	0.147	S100b
Antimicrobial peptides	0.008	0.116	Ctsg, Lcn2	Trafficking of myristoylated proteins to the cilium	0.010	0.147	Ar13
Bicarbonate transporters	0.016	0.116	Slc4a1	Interleukin-1 signaling	0.014	0.147	Psmb2, S100b
Coenzyme A biosynthesis	0.023	0.116	Gda	Signaling by NTRK1 (TRKA)	0.018	0.147	Arc
O2/CO2 exchange in erythrocytes	0.027	0.116	Slc4a1	Advanced glycosylation endproduct receptor signaling	0.023	0.147	S100b
Signaling by ROBO receptors	0.028	0.116	Rplp1, Slit1	Gamma-carboxylation, transport, and amino-terminal cleavage of proteins	0.023	0.147	Proc
Metabolism of Angiotensinogen to Angiotensins	0.030	0.116	Ctsg	Physiological factors	0.026	0.147	Ces1d

**Table 5.5B (continued)** More active reactome pathways for 7 DPO in the citrulline supplement and control group.

Citrulline supplement group				Control group			
Pathway name	p-value	FDR	Gene names	Pathway name	p-value	FDR	Gene names
RNA Polymerase I Promoter Opening	0.037	0.116	H3-3b	Class I peroxisomal membrane protein import	0.029	0.147	Fis1
Pyroptosis	0.037	0.116	Ctsg	Common Pathway of Fibrin Clot Formation	0.036	0.147	Proc
Activation of Metalloproteinases	0.039	0.116	Ctsg	Metabolism of Angiotensinogen to Angiotensins	0.039	0.147	Ces1d
DNA methylation	0.040	0.116	H3-3b	TRAF6 mediated NF-κB activation	0.043	0.147	S100b
Signaling by NOTCH2	0.042	0.116	Ctsg				
Assembly of the ORC complex at the origin of replication	0.044	0.116	H3-3b				
Calnexin/calreticulin cycle	0.045	0.116	Canx				
PRC2 methylates histones and DNA	0.048	0.116	H3-3b				
SIRT1 negatively regulates rRNA expression	0.049	0.116	H3-3b				

**Table 5.5C** More active reactome pathways for 14 DPO in the citrulline supplement and control group.

Citrulline supplement group				Control group			
Pathway name	p-value	FDR	Gene names	Pathway name	p-value	FDR	Gene names
Glycogen metabolism	<0.001	<0.001	Pygm, Pgm1	Striated Muscle Contraction	<0.001	0.012	Myl2, Myl3, Myh7
Neutrophil degranulation	0.001	0.015	Gpi, Pygm, Aldoa, Pgm1	Reactions specific to the hybrid N-glycan synthesis pathway	0.002	0.112	Myl2
Glucose metabolism	0.003	0.049	Gpi, Aldoa	Regulation of cortical dendrite branching	0.008	0.112	Slit1
Galactose catabolism	0.003	0.052	Pgm1	Cam-PDE 1 activation	0.008	0.112	Calm3
eNOS activation	0.009	0.073	Lyp1a1	Activation, myristoylation of BID and translocation to mitochondria	0.008	0.112	Ctsg
Deubiquitination	0.023	0.073	Adrm1, Psmb2	Neutrophil degranulation	0.014	0.112	Ftl1, Ctsg, Krt11, S100a8
RAF/MAP kinase cascade	0.025	0.073	Lypla1, Psmb2	Activation of RAC1 downstream of NMDARs	0.014	0.112	Calm3
Regulation of activated PAK-2p34 by proteasome mediated degradation	0.042	0.073	Psmb2	Antimicrobial peptides	0.015	0.112	Ctsg, S100a8
Cross-presentation of soluble exogenous antigens (endosomes)	0.042	0.073	Psmb2	CREB1 phosphorylation through the activation of CaMKII/CaMKIV cascade	0.016	0.112	Calm3

**Table 5.5C (continued)** More active reactome pathways for 14 DPO in the citrulline supplement and control group.

Citrulline supplement group				Control group			
Pathway name	p-value	FDR	Gene names	Pathway name	p-value	FDR	Gene names
Regulation of ornithine decarboxylase (ODC)	0.043	0.073	Psmb2	Glucose metabolism	0.016	0.112	Eno2
GSK3B and BTRC:CUL1-mediated degradation of NFE2L2	0.044	0.073	Psmb2	Calcineurin activates NFAT	0.018	0.112	Calm3
p53-Independent DNA Damage Response	0.044	0.073	Psmb2	Activation of Kainate Receptor	0.020	0.112	Calm3
Ubiquitin-dependent degradation of Cyclin D	0.044	0.073	Psmb2	CaMK IV-mediated phosphorylation of CREB	0.020	0.112	Calm3
Autodegradation of the E3 ubiquitin ligase COP1	0.044	0.073	Psmb2	Tetrahydrobiopterin (BH4) synthesis, recycling, salvage and regulation	0.020	0.112	Calm3
FBXL7 down-regulates AURKA during mitotic entry and in early mitosis	0.046	0.073	Psmb2	Regulation of commissural axon pathfinding by SLIT and ROBO	0.020	0.112	Slit1
SCF-beta-TrCP mediated degradation of Emi1	0.046	0.073	Psmb2	CLEC7A (Dectin-1) induces NFAT activation	0.022	0.112	Calm3
Degradation of AXIN	0.046	0.073	Psmb2	eNOS activation	0.022	0.112	Calm3
Negative regulation of NOTCH4 signaling	0.046	0.073	Psmb2	Sodium/Calcium exchangers	0.022	0.112	Calm3
Regulation of RUNX3 expression and activity	0.046	0.073	Psmb2	CREB1 phosphorylation through the activation of Adenylate Cyclase	0.023	0.112	Calm3
AUF1 (hnRNP D0) binds and destabilizes mRNA	0.047	0.073	Psmb2	Reduction of cytosolic Ca++ levels	0.023	0.112	Calm3

**Table 5.5C (continued)** More active reactome pathways for 14 DPO in the citrulline supplement and control group.

Citrulline supplement group				Control group			
Pathway name	p-value	FDR	Gene names	Pathway name	p-value	FDR	Gene names
Degradation of DVL	0.048	0.073	Psmb2	NOTCH2 intracellular domain regulates transcription	0.023	0.112	Ctsg
Complex I biogenesis	0.048	0.073	Ndufs4	Regulation of Insulin-like Growth Factor (IGF) transport and uptake by Insulin-like Growth Factor Binding Proteins (IGFBPs)	0.025	0.112	Ctsg, Mfge8
NIK->noncanonical signaling	0.050	0.073	Psmb2	Degradation of the extracellular matrix	0.031	0.112	Col2a1, Ctsg
				Protein methylation	0.033	0.112	Calm3
				PKA activation	0.035	0.112	Calm3
				Metabolism of Angiotensinogen to Angiotensins	0.035	0.112	Ctsg
				Scavenging by Class A Receptors	0.037	0.112	Ftl1
				VEGFR2 mediated cell proliferation	0.039	0.112	Calm3
				Negative regulation of NMDA receptor-mediated neuronal transmission	0.041	0.112	Calm3
				Ras activation upon Ca2+ influx through NMDA receptor	0.041	0.112	Calm3
				Unblocking of NMDA receptors, glutamate binding and activation	0.041	0.112	Calm3

**Table 5.5C (continued)** More active reactome pathways for 14 DPO in the citrulline supplement and control group.

<b>Citrulline supplement group</b>				<b>Control group</b>			
Pathway name	p-value	FDR	Gene names	Pathway name	p-value	FDR	Gene names
				RHO GTPases activate PAKs	0.041	0.112	Calm3
				Regulation of TLR by endogenous ligand	0.041	0.112	S100a8
				DARPP-32 events	0.046	0.112	Calm3
				RHO GTPases Activate NADPH Oxidases	0.046	0.112	S100a8
				Long-term potentiation	0.048	0.112	Calm3
				Glycogen metabolism	0.048	0.112	Calm3

**Table 5.5D** More active reactome pathways for 28 DPO in the citrulline supplement and control group.

Citrulline supplement group				Control group			
Pathway name	p-value	FDR	Gene names	Pathway name	p-value	FDR	Gene names
Keratinization	0.005	0.023	Krt14	Striated Muscle Contraction	<0.001	<0.001	Des, Mybpc1, Myl2, Myl3, Myh6, Myh7, Tnni1, Tnnt1
Acetylcholine regulates insulin secretion	0.005	0.023	Marcks	Reversible hydration of carbon dioxide	<0.001	0.006	Ca3
Type I hemidesmosome assembly	0.006	0.023	Krt14	Reactions specific to the hybrid N-glycan synthesis pathway	0.002	0.024	Myl2
Signaling by BMP	0.014	0.043	Fstl1	Coenzyme A biosynthesis	0.016	0.142	Gda
Smooth Muscle Contraction	0.023	0.055	Anxa6	Type I hemidesmosome assembly	0.022	0.151	Krt5
				Formation of the cornified envelope	0.027	0.182	Krt5
				Scavenging by Class A Receptors	0.037	0.182	Ftl1
				Purine catabolism	0.039	0.182	Gda

points, which makes sense considering the number of proteins involved in each pathway.

## 5.5 Discussion

Two different MS techniques were applied to explore the effect of citrulline supplement on the molecular profiles during bone fracture healing. MALDI-MSI analyses showed distinct lipid profiles for bone and bone marrow at the different time points for both the citrulline supplement and control groups. LC-MS/MS was used to identify the more abundant proteins in the citrulline supplement group compared to the control group per time point and vice versa. The more abundant proteins showed limited overlap between time points for both the treatment and the control group. Pathway analyses were based on these more abundant proteins and showed different activated pathways for both the citrulline supplement and control group at different time points. These pathways included pathways involved in the citrulline-arginine-nitric oxide metabolism.

### 5.5.1 Lipid analyses: Different lipids contribute to the citrulline supplement and control group

The separation between the citrulline supplement and control group is better for bone marrow in comparison to bone, as shown in Figures 5.3 and 5.5. The best separations between the citrulline supplement and control group are for 7 and 14 DPO and a slightly less at 3 DPO for bone marrow. This could indicate that the largest effect of the citrulline supplement during fracture healing on the lipid profiles is during these days. While the differences between the treatment and control group are smaller at 28 DPO, indicating the citrulline supplement has less effect at the final phase of the fracture healing process. This can also be related to the citrulline supplement time, as this was stopped after 14 days. These separations could also be a combination of differences in lipid content and involvement in the fracture healing process between bone and bone marrow. On one hand, this could indicate that the differences in lipid profiles between the citrulline supplement and control group are bigger in bone marrow compared to bone. This could hint at a more important involvement of lipids in bone marrow during the fracture healing process than in bone. At the other hand, these differences could be related to the intrinsic composition of bone and bone marrow as well as the experimental setup. Bone marrow contains a higher percentage of lipids than bone and the extraction of lipids from bone is more challenging than from bone marrow due to the mineralization of the tissue.<sup>137</sup> These differences could reduce the desorption and ionization efficiency from bone in comparison to bone marrow, as the bone tissue was not demineralized during sample preparation.<sup>129</sup> The mass spectra obtained

from bone marrow contained more and higher intensity peaks of interest than bone, while the mass spectra from bone included more matrix cluster and background peaks. The differences in separation between the treatment and control group between bone and bone marrow could potentially be attributed to differences in desorption and ionization efficiencies affecting the lipid profile obtained.

The lists identified lipids that contribute to the separation between the citrulline supplement and control group show a great amount of overlap between bone and bone marrow (Tables 5.2 and 5.3). The overlap between bone and bone marrow for the lipids contributing to each sample group is limited, despite the overlap in the overall lists. There are even lipids that contribute to the citrulline supplement group in one tissue type while contributing to the control group in the other tissue type at a specific time point. The lack of overlap and differences between bone and bone marrow could indicate that different lipid patterns are involved in the fracture healing process in both tissue types and these patterns are affected by citrulline supplement differently. The analysis of the lipid processes that are affected by citrulline supplement throughout the different time points is challenging because of among others the different contribution patterns of lipids and even between the different adducts of the same lipid. Therefore, no conclusive changes lipid class or changes in sum composition of the fatty acid chains between different time points were observed for bone or bone marrow. The overlap between the contributing lipids for different time points is different between bone and bone marrow. There is more overlap between contributing lipids in the control group than in the citrulline supplement group (Figures 5.4 and 5.6). However, no lipid is contributing to all time points in both treatment groups for both tissue types. This could indicate a changing effect throughout fracture healing of citrulline supplement on the contributing lipids, depending on the stage of fracture healing. In general, CARs and LPCs with an alkyl group contribute more to the citrulline supplement group in both bone and bone marrow. TGs are specifically contributing to the control group at 28 DPO. The LPCs, PCs, and SM contribute to the citrulline supplement and control group depending on the time point and in different patterns between specific lipids. Furthermore, potentially contributing lipids might have been missed due to the manual removal of matrix cluster and background peaks from the peak list. Overall, the lipid profiles of bone and bone marrow show specific lipids contributing to each treatment group at different time points during the fracture healing process, as a result of the citrulline supplement.

Recently, we published a paper describing different lipid profiles throughout fracture healing in the fracture hematoma.<sup>212</sup> Different lipids from fracture hematoma in positive ion mode contributed more at different time points after fracture. Most of these lipids were also observed to be contributing to the separation between the citrulline supplement and control group per time point. The time points of the contributing lipids do not always match. However, direct comparison of the lipid profiles per time point is impossible, due to the different aims of the analyses performed to get the lists of contributing lipids (time point comparison versus treatment comparison). The presence of the same lipids and their contribution to different time points in both studies show that these lipids are involved in fracture healing. In addition, this could indicate the importance of CARs, LPCs, PCs, and SMs for normal fracture healing, although this should be confirmed in future research.

Unfortunately, the knowledge about the involvement and importance of lipids during fracture healing is limited and usually generalized per lipid class. Early evidence of changes in the phospholipid composition in the callus throughout fracture healing were provided by Boskey *et al.*<sup>213</sup> They showed that the ratio of different phospholipid classes changed when comparing different time points, although most of these changes were insignificant. The two main observed lipid classes that contribute to the separation between the citrulline supplement and control group are LPCs and PCs. PCs are one of the most abundant phospholipids in mammals and are an important part of in cell membranes.<sup>137,179,214</sup> PCs are an essential source of lipid-derived secondary messengers and play a role in cellular metabolism and energy production, in which the fatty acid chain composition can be of importance.<sup>137,179,214</sup> PCs are involved in the regulation of soft callus formation via promotion of chondrocyte proliferation and differentiation and during the replacement of the soft callus by the hard callus.<sup>163</sup> The production and function PCs are essential for osteoblast proliferation and function, especially mineralization.<sup>215</sup> Furthermore, PCs are potentially involved in the recruitment of osteoclasts.<sup>163</sup> LPCs inhibit osteoclast formation, but promote osteoclast function.<sup>212</sup> The dietary intake of choline, which is required for the synthesis of PCs, improved bone mineral density.<sup>165</sup> PCs containing a 20:5 fatty acid chain have been shown to enhance the formation of bone via the promotion of osteoblast differentiation.<sup>216</sup> Besides LPCs and PCs, some CARs, a SM, and TGs were contributing to the separation between the citrulline supplement and control group at different time points. SMs are an important source of ceramides and phosphocholine, which is relevant in the production of PCs, as well as parts of lipid membranes and secondary messengers.<sup>137,164,185</sup> Impairment of the SM metabolism

can result in abnormal cartilage development and reduction of bone mineralization.<sup>137,164,185</sup> Furthermore, insufficient levels of SM can result in impaired bone development via the regulation of osteoblast differentiation and mineralization.<sup>164</sup> TGs are commonly used for energy storage mainly in bone marrow.<sup>137</sup> This matches well with the observation that this lipid class only contributes to the control group in the separation between the treatment and control group at 28 DPO, as during the bone remodeling phase also the energy storage is restored. Most of the observed lipid classes are involved in the different fracture healing phases, and, therefore, differences in expression can be expected. However, the role of specific lipids during fracture healing are unknown and extrapolation to the effect of citrulline supplement impossible, consequently. In addition, the differences in expression and role for lipids from bone and bone marrow are largely unknown. The effect of the specific identified lipids and their potential importance and role as lipid mediators in different pathways should be explored in future research.

This research highlights the distinct effect of citrulline supplement on lipids during the different phases of fracture healing, because of the different lipid profiles for cortical bone and bone marrow for the citrulline supplement and respective control group at the different time points. Although the effect of each specific lipid is unknown at the moment. The specific lipid profiles and patterns for bone and bone marrow for the citrulline supplement and control group for the different time points should be confirmed in future research and the role further explored.

### 5.5.2 Protein analyses: Citrulline supplement has a changing effect throughout the fracture healing process

The PCA analyses did not show a good separation between the citrulline supplement and control groups at the different time points based on the complete protein profile (Figure 5.7). This indicates that the citrulline supplement did not result in a completely different protein profile throughout the fracture healing process. A different protein profile could have indicated that the treatment groups were in different stages of the fracture healing process at the same time point. The effect of citrulline supplement on the protein profiles throughout fracture healing is thus expectedly more subtle. The small differences between the treatment and control group are also reflected in the low numbers of more abundant proteins for the citrulline supplement and control group at the different time points. Interestingly, a decreasing trend in the number of more abundant proteins in the citrulline supplement group can be seen over the different time points, while an increasing trend can be noticed for the control group. This could indicate a bigger

effect of the citrulline supplement during the early stages of the fracture healing. Previous research has shown enhancement of fracture healing by citrulline supplement via improved angiogenesis and callus formation.<sup>192,202</sup> The higher number of more abundant proteins in the citrulline supplement group at the early phases of fracture healing seem to match with these results. The higher numbers of more abundant proteins in the control group at the later time points could indicate a more active fracture healing process in comparison to the citrulline supplement group.

The overlap between the more abundant proteins in the citrulline supplement group throughout the different time points is limited, as shown in Figure 5.8A. There is some overlap in more abundant proteins in consecutive time points in the citrulline supplement group, as Histone H3.3 (H3-3b) and Slit homolog 1 protein (Slit1) are more abundant at 3 and 7 DPO, and Glycogen phosphorylase (Pygm) is more abundant at 7 and 14 DPO. The limited overlap between time points can be expected, as they represent different phases of fracture healing. In addition, this indicates that citrulline supplement does not have a constant effect on the protein profile throughout the different phases of fracture healing. The overlap of the more abundant proteins between the different time points for the control group is also limited, although the total number of proteins overlapping between groups is higher (Figure 5.8B). Most overlap between abundant proteins is between consecutive time points, although one protein (Keratin, type II cytoskeletal 5 (Krt5)) is more abundant at 3 and 28 days in the control group. The limited overlap between the different time points in the control group is related to the different phases of fracture healing, similar to the citrulline supplement group. Therefore, the effect of citrulline supplement on the protein expression throughout the fracture healing process is not constant and does not have a consistent effect in the citrulline supplement or the control group. This indicates that citrulline supplement might have a distinct effect in different processes throughout fracture healing.

The more abundant proteins per sample group listed in Table 5.4 provide an overview, but an extensive discussion of each protein separately is beyond the scope of this paper. Some molecules that are a known part of the extracellular matrix (ECM) of bone tissue are more abundant throughout the fracture healing process in the treatment or control group. These include different collagens, fibromodulin, and thrombospondin, which have a role in regulation of bone formation and resorption via effects on the osteoblast and osteoclast function.<sup>196,217</sup> Furthermore, for example, different myosins, myosin light chains, and troponins are more abundant in the control group at different time points,

while an actin and annexin are more abundant in the citrulline supplement group. Involvement of actin and different myosins during fracture healing is not surprising, due to their role in the cytoskeleton. For example, myosins have been shown to play an important role in osteoclast differentiation and function, while annexins are important in osteoblast differentiation and function.<sup>218-220</sup> However, little is known about the role of these proteins and many other more abundant proteins during fracture healing. In general, it is more informative to examine the different pathways related to the combination of the more abundant proteins per sample group, because of the involvement of proteins in main different pathways. Therefore, the more active pathways will be discussed in the next section.

Four proteins are more abundant in both the treatment and control group, although at different time point, namely 1) Cathepsin G (Ctsg) is more abundant in the citrulline supplement group at 7 DPO and in the control group at 14 DPO, 2) Guanine deaminase (Gda) in the citrulline supplement group at 7 DPO and in the control group at 28 DPO, 3) Proteasome subunit beta type-2 (Psmb2) in the citrulline supplement group at 7 DPO and in the control group at 14 DPO, and 4) Slit homolog 1 protein (Slit1) in the citrulline supplement group at 3 and 7 DPO and in the control group at 14 DPO. These proteins are involved in main different pathways and do not have one general effect. For example, Slit homolog 1 protein (Slit1) is a known member of the Slit/Robo signaling pathway, which is involved during different phases in fracture healing.<sup>221,222</sup> Each of these four proteins is more abundant at an earlier time point in the citrulline supplement group than in the control group. This could imply an enhancement of the fracture healing process in the citrulline supplement group in comparison to the control group.

### 5.5.3 Pathway analyses: Citrulline supplement results in enhanced fracture healing

This part focuses on pathways with biological meaning in bone fracture healing. One of the reasons for this decision is the high number of more active pathways in the different sample groups, which is partly caused by the low number of proteins with higher abundance. In addition, only one matched gene name is found for most pathways, which is also related to the low number of proteins. For these reasons, the pathway analyses should be considered with caution and be confirmed in future research.

#### 5.5.3.1 3 days post-operative: inflammatory phase

One of the interesting more active pathways in the citrulline supplement group is eNOS activation (see Table 5.5A). eNOS is also known as NOS3 and its activation is

important in the production of nitric oxide.<sup>190,191</sup> Previous research has shown that citrulline supplement can enhance fracture healing among other by improvement of the inflammatory response.<sup>192</sup> Nitric oxide is important during the inflammatory phase, because of its role as secondary messenger in inflammatory pathways, in increasing blood flow at the fracture site, and potentially in infection prevention.<sup>5,198,199,201</sup> The activation of eNOS at this time point does match previous research, as Corbett *et al.* (1999) showed increased eNOS expression 1 day after fracture.<sup>199</sup> However, Zhu *et al.* (2001, 2002) found a higher protein expression of iNOS(/NOS2) than eNOS at 4 days.<sup>200,201</sup> Nevertheless, activation of eNOS is the only form of NOS that is incorporated in the Reactome Pathway Database for nitric oxide metabolism. A more active nitric oxide metabolism via activation of eNOS is important in the inflammatory phase and can directly be related to the citrulline supplementation of the rats. Furthermore, signaling by ROBO receptors and Netrin-1 is more active in the citrulline supplement group. Both these pathways are known for their role in axon guidance and cell migration during nervous system development, but have also other functions.<sup>221,222</sup> The ROBO receptors are part of the Slit/Robo signaling pathway.<sup>221,222</sup> This pathway has a regulatory role in inflammation due to its inhibition of inflammatory cell infiltration.<sup>222</sup> In addition, the Slit/Robo signaling pathway can promote angiogenesis, which is important for regulation of bone formation and nutrients and other supplies.<sup>221,222</sup> Netrin-1 has been shown to be involved in angiogenesis as well as differentiation of and interaction between osteoblasts and osteoclasts.<sup>221</sup> The higher activity of the signaling by ROBO receptors and Netrin-1 in the citrulline supplement group are connected and can potentially indicate faster healing in this group, due to the inhibition of inflammation and promotion of angiogenesis. Furthermore, pathways related to PA and collagen synthesis are more active in the citrulline supplement group. PA is important in the regulation of inflammation via the secretion of inflammatory cytokines, like interleukins (ILs).<sup>177</sup> Upregulation of iNOS expression by PA was shown in macrophages by Lim *et al.* (2003).<sup>177</sup> The activation of PA synthesis indicates an active regulation of the inflammatory response and could potentially be related to the citrulline supplement. Collagen has a critical role in fracture healing, also because of its essential role in ECM of bone and hydroxyapatite formation.<sup>195,217</sup> Collagen formation during the inflammatory phase is essential for cell anchoring and in the formation of callus.<sup>195,217</sup> Activation of this pathway in the citrulline supplement group could indicate an earlier start of the formation of the soft callus in comparison to the control group.

Two related more active pathways in the control group are regulation of interleukin gene transcription by RUNX1 (runt-related transcription factor 1) and interleukin-6

(IL-6) signaling. IL-6 is one of the pro-inflammatory cytokines that is secreted by, among others, macrophages to recruit mesenchymal stem cells and promote angiogenesis.<sup>5,7,10,12,14,188</sup> ILs and other pro-inflammatory cytokines show a peak expression during the first days of fracture healing.<sup>7,10</sup> Activation of the IL-6 signaling matches with its role in the fracture healing process, while higher activation in the control group could indicate a more active inflammatory response than in the citrulline supplement group. The activation of IL gene transcription by RUNX1 is probably related to IL-6 signaling, as these pathways have the same single matched gene name. Pathways related to fibrin clot formation are more active in the control group. The formation of a fibrin clot is the start of the fracture healing process and form the hematoma, which is the scaffold for soft callus formation.<sup>5,12,223</sup> Higher activity of these pathways in the control group can indicate a faster completion of the clot formation in the citrulline supplement group compared to the control group and, therefore, this pathways is more active in the control group. Furthermore, matrix metalloproteinases (MMPs) are activated in the control group. MMPs are enzymes that are important in ECM degradation, which are especially important in soft callus degradation and bone remodeling.<sup>195,224</sup> In addition, they facilitate cell migration the formation of blood vessels through the bone matrix, also by releasing growth factors from the remaining ECM.<sup>195,224</sup> MMPs play a role in chondrocyte proliferation and differentiation.<sup>224</sup> Activation of MMPs in the control group could indicate a slower angiogenesis and chondrocyte differentiation in comparison to the citrulline supplement group.

#### 5.5.3.2 7 days post-operative: soft callus formation

One of the pathways more active in the citrulline supplement group at 7 DPO is glycogen breakdown (see Table 5.5B). Glycogen breakdown results in glucose 1-phosphate and is important in the glucose homeostasis, which can enter glycolysis for energy production.<sup>225</sup> However, the glycolysis pathway was not more active in the citrulline supplement group in comparison to the control group. Higher activation of the glycogen breakdown in the citrulline supplement group could indicate a higher need for glucose related to, for example, cell differentiation in comparison to the control group. Neutrophil degranulation is more active in the citrulline supplement group. Neutrophils are the first inflammatory cells that arrive at the damaged tissue site and their number decrease after the first days.<sup>154,223,226</sup> Neutrophils presence increases again in later phases of fracture healing in blood and their presence is related with normal fracture healing.<sup>154</sup> Neutrophils release the contents of their granules during degranulation.<sup>226</sup> The importance of neutrophil presence and degranulation during later stages of fracture healing is not clear. Antimicrobial peptides show a higher activity in the citrulline supplement

group. Antimicrobial peptides are an important part of the innate immune system and can be produced by, among others, neutrophils.<sup>226,227</sup> Besides this role, antimicrobial peptides can promote wound healing via modulation of cytokine production, cell migration and proliferation, angiogenesis, and ECM production, especially collagen.<sup>227</sup> Antimicrobial peptide could potentially have a similar role in fracture healing, because of the similarities in early phases of wound and fracture healing. The antimicrobial peptides could potentially promote cell proliferation, ECM formation, and angiogenesis during the soft callus formation, indicating a higher activity of these processes in the citrulline supplement group in comparison to the control group. Different signaling pathways are more active in the citrulline supplement group, namely multiple interleukins, including IL-1 and IL-13, NOTCH2 (neurogenic locus notch homolog 2), and ROBO receptors. IL-1 promotes the formation of the soft callus by the recruitment of cells and differentiation of osteoblasts and osteoclasts as well as promotion of angiogenesis.<sup>7,10,12,14</sup> IL-13 enhances osteoblast differentiation and function resulting in bone formation.<sup>12</sup> Based on these functions the activation of interleukin signaling matches well with the fracture healing phase. NOTCH signaling pathways have different functions during fracture healing that can be contradicting and are depending on cell and receptor-ligand combination.<sup>228-230</sup> At one hand, these pathways are important for promotion of proliferation of progenitor cells during the early stage of osteoblast formation, but can inhibit osteoblast differentiation.<sup>229,230</sup> At the other hand, NOTCH2 enhances osteoclast formation and activation emphasizing its double role in fracture healing.<sup>228-230</sup> Furthermore, NOTCH signaling pathways have a critical role in angiogenesis during bone development.<sup>228-230</sup> Higher activity of NOTCH2 at this stage can be related to proliferation of osteoblast progenitor cells or is potentially a sign of early osteoclast formation for remodeling of the soft callus. The Slit/Robo signaling pathway regulates bone formation and resorption, especially soft callus formation by promoting chondrocyte differentiation via the inhibition of  $\beta$ -catenin in the Wnt pathway.<sup>221</sup> In addition, the Slit/Robo signaling pathway can promote angiogenesis, which is an important event occurring during soft callus formation.<sup>221</sup> Higher activity of the Slit/Robo signaling pathway in the citrulline supplement group can indicate more soft callus formation and angiogenesis in comparison to the control group. Two pathways related to the transport of small molecules are more active in the citrulline supplement group, namely bicarbonate transporters and  $O_2/CO_2$  exchange in erythrocytes. The more active pathway of reversible hydration of  $CO_2$  in the control group is related to these pathways. Erythrocytes are important for the transport and exchange of the waste  $CO_2$  for  $O_2$ .<sup>231</sup> Bicarbonate equilibrates the production of  $CO_2$ , as reversible hydration of  $CO_2$

results in the production of bicarbonate and protons via carbonic anhydrases.<sup>231</sup> In addition, bicarbonate transporters have a role pH-regulation during acid secretion occurring during formation of hydroxyapatite during fracture healing.<sup>231</sup> Interpretation of the higher activation of these pathways is challenging due to the limited knowledge in the fracture healing processes. These activations could potentially indicate more cell activity in the citrulline supplement group compared to the control group. However, it could be related to differences in amount of blood containing bone marrow between sample groups. MMPs are more activated in the citrulline supplement group. MMPs play a role in angiogenesis, and osteoblasts and osteoclast recruitment and functioning, besides their role in ECM degradation, which is important in the replacement of the soft callus by a hard callus and bone remodeling.<sup>224</sup> Higher activity in the citrulline supplement group could indicate more angiogenesis and recruitment of osteoblasts and osteoclasts, which can suggest earlier start of the hard callus formation compared to the control group.

The metabolism of angiotensinogen to angiotensins is activated in both the citrulline supplement and control group, although the matched gene name is different. Angiotensinogen and angiotensins are part of the renin-angiotensin-aldosterone system (RAAS), which affects bone metabolism via activation of osteoclasts and inhibition of osteoblasts.<sup>232</sup> Expression of components of the RAAS have been shown in mature chondrocytes and osteoblast during callus formation.<sup>233</sup> This matches with the activation of this pathway during soft callus formation in both the treatment and control group, although the exact role is poorly understood.

Different signaling pathways are more active in the control group for 7 DPO, namely IL-1, ERBB4, and NTRK1 (neurotrophic receptor tyrosine kinase 1, TRKA). IL-1 is one of the interleukins that is also activated in the citrulline supplement group and, therefore, its role has been described above. Activation of IL-1 can be related to its role in angiogenesis and soft callus formation and potentially in callus remodeling in the control group. ERBB4 is a tyrosine kinase receptor for different angiogenic factors, which is related to the epidermal growth factor receptor (EGFR).<sup>234</sup> ERBB4 plays a role in cell migration and angiogenesis.<sup>234</sup> NTRK1 is a tyrosine kinase receptor for nerve growth factor (NGF) and is expressed in, among others, bone.<sup>235</sup> NTRK1 has been suggested to play a role in the proliferation and differentiation of chondrocytes and osteoblasts as well as to potentially promote angiogenesis.<sup>235</sup> Activation of ERBB4 and NTRK1 signaling in the control group can indicate delayed angiogenesis and chondrogenesis compared to the citrulline supplement group. Advanced glycosylation end-product receptor signaling and TRAF6 (TNF receptor

associated factor 6) mediated NF- $\kappa$ B (nuclear factor kappa B) activation are two related pathways in the control group that show higher activation. Receptor for advanced glycation end-products (RAGE) is one of the receptors regulating the immune response and is involved in bone metabolism via osteoblast and osteoclast differentiation and function.<sup>236</sup> The NF- $\kappa$ B signaling pathway can be stimulated after activation of RAGE resulting in the secretion of pro-inflammatory cytokines.<sup>236,237</sup> Besides, the TRAF6 mediated activation of NF- $\kappa$ B is important in the osteoclast differentiation and function.<sup>236-238</sup> Higher activation of these pathways could indicate that the inflammation phase is not completely finalized in the control group, while at the other hand, it can indicate differentiation of osteoclasts, although these cells are usually not active during this phase. One of the fibrin clot formation pathways is more active in the control group. Fibrin clot formation is the part of the first phase of the fracture healing process.<sup>5,12,223</sup> The activation of this pathway could indicate that this process is still ongoing or the remaining presence of a fibrin clot, which could imply a delayed fracture healing process in comparison to the citrulline supplement group.

### 5.5.3.3 14 days post-operative: hard callus formation

Interestingly, the eNOS (NOS3) is activated in both the treatment and control group at 14 DPO, while in the citrulline supplement group the regulation of ornithine decarboxylase (ODC) is also activated (see Table 5.5C). Nitric oxide production by NOSs is important in the regulation of fracture callus and bone remodeling, because of its effect on the proliferation, differentiation, and functioning of osteoblasts and osteoclasts.<sup>192,198-201,239</sup> The eNOS activation at this time point for both groups matches with the eNOS mRNA found at 15 days by Diwan *et al.* (2000) and peak protein levels of eNOS at 14 days by Zhu *et al.* (2001, 2002).<sup>191,200,201</sup> Rajfer *et al.* (2017) demonstrated an increased iNOS expression during fracture healing at 14 days for COMB-4 supplement group, which included citrulline, in comparison to the control group.<sup>202</sup> Nevertheless, the pathways of iNOS are not included in the Reactome Pathway Database. The activation of eNOS in both the treatment and control group can be related with stage of fracture healing. The matched gene names are different between the groups. The regulation of ODC is directly related to the metabolism of polyamines. Polyamines are a precursor of in the formation of collagen and are related to the arginine-citrulline-nitric oxide metabolism via the formation of ornithine.<sup>192</sup> The activation of the regulation of ODC might be related to the citrulline supplement of the rats in this group, as more citrulline is available that can be converted to ornithine via arginine (see Figure 5.1). Tetrahydrobiopterin (BH4) metabolism is more active in the control group. BH4 is important in the regulation of NOS activity as necessary cofactor.<sup>240</sup> Based on this

function and the same matched gene name, the activation of this pathway is related to the eNOS activation in the control group at this time point.

The metabolisms of different carbohydrates are activated in the citrulline supplement group, namely glycogen, glucose, and galactose, of which the glucose and glycogen metabolisms are activated in the control group as well. These different carbohydrates can be metabolized from the other carbohydrates and, therefore, are related.<sup>225</sup> These carbohydrates are important in the energy production, but also are involved in the production of, among others, fatty acids, glycolipids, and proteoglycans.<sup>225</sup> Interpretation of these activated carbohydrate pathways is irrelevant, as most of them are activated in both the treatment and control group. Another pathway that is activated in both the citrulline supplement and control group is neutrophil degranulation. Neutrophil degranulation results in the release of, among others, proteases and cytokines.<sup>226</sup> However, the importance and role of this process in fracture healing is poorly understood, as indicated above.

Deubiquitination is one of the pathways that is more active in the citrulline supplement group at 14 DPO. Deubiquitination is the process of removal of ubiquitin from target proteins by deubiquitinases (DUBs).<sup>241</sup> DUBs have been shown to be essential for the regulate differentiation and functioning of osteoblasts and osteoclasts during bone remodeling.<sup>237,241</sup> The higher activity in the citrulline supplement group and the importance of deubiquitination during bone remodeling could indicate an earlier start of the bone remodeling phase in this group in comparison to the control group. The RAF/MAP kinase cascade and NF-κB signaling are more active in the citrulline supplement group. The mitogen-activated protein (MAP) kinase signaling pathway has a wide range of biological effects and play a regulatory role in bone development and homeostasis due to the regulation and stimulation of differentiation and maturation of osteoblasts as well as osteoclasts.<sup>238</sup> The activation of NF-κB is also involved these effects.<sup>237,238</sup> Activation of the RAF/MAP kinase cascade and NF-κB signaling matches with the hard callus formation at this time point, due to their role on osteoblast and osteoclast differentiation and function. Especially, the activation of NF-κB could indicate early osteoclast activation for bone remodeling before the start of this phase in the control group. Furthermore, Hou *et al.* (2009) demonstrated increased iNOS expression via RAF/MAPK and NF-κB signaling pathways in ultrasound stimulated pre-osteoblasts.<sup>242</sup> Therefore, the activation of these pathways might be directly related to citrulline supplement, also in relation to the eNOS activation. NFE2L2 (nuclear factor erythroid 2-related factor 2, NRF2) degradation is a more active pathway in the citrulline supplement group. NFE2L2 plays a role in different

fracture healing phases as key regulator of antioxidants enzyme expression and has been suggested to play a role in fracture callus formation via chondrocyte and osteoblast differentiation, although its role is poorly understood.<sup>243</sup> NFE2L2 degradation at this time point can be related to this role, as its higher activity in the citrulline supplement group can indicate earlier completion of osteoblast differentiation compared to the control group. Degradation of AXIN and Disheveled (DVL) is more active in the citrulline supplement group. AXIN and DVL both play a role in the Wnt/ $\beta$ -catenin signaling pathway, which is important in the differentiation of mesenchymal stem cells (MSCs) into osteoblasts or chondrocytes.<sup>244,245</sup> AXIN is part of a multi-protein complex that phosphorylates  $\beta$ -catenin in absence of Wnt ligands, which results in degradation.<sup>244,245</sup> DVL is an intercellular protein that transduces the signal after binding of Wnt to its receptor and results in the accumulation of  $\beta$ -catenin that is followed by increased gene transcription.<sup>244,245</sup> Activation of the degradation of both AXIN and DVL is unexpected due to their opposite roles. However, this is caused by the same single matched gene name for both pathways. Degradation of AXIN would be expected at this time point in the fracture healing process, as this would result in enhance Wnt signaling via DVL resulting in increased osteoblast differentiation. Furthermore, negative regulation of NOTCH4 signaling was more active in the citrulline supplement group. The effects of NOTCH4 signaling on osteoblasts and osteoclasts as well as its role during fracture healing are unclear, due to the low expression levels in bone.<sup>228,229</sup> The activation of this pathway can currently not linked to bone fracture healing, and further research is necessary.

The signaling by ROBO receptors is a more active pathway in the control group at 14 DPO. The Slit/Robo signaling pathway regulates bone remodeling via inhibition of osteoclasts formation and function as well as stimulating osteoblast migration and proliferation and, therefore, plays an important role in regulation of bone formation and resorption.<sup>221</sup> In addition, the protein Robo-1 was more abundant in the control group at this time point. This protein is probably also involved in the Slit/Robo signaling pathway, but the gene name did not match with the Reactome database. The Robo-1 protein has been shown to play a role in bone homeostasis and remodeling.<sup>246</sup> Activation of the signaling by ROBO receptors pathway is related to replacement of the soft callus with the hard callus. The higher activation of this signaling is in the control group later than in the citrulline supplement group could potentially indicate a slower healing process in the control group compared to the citrulline supplement group. Different calmodulin induced events are more active in the control group, namely Cam-PDE1 activation, CaMK IV-mediated phosphorylation of CREB, and PKA activation. There are seven more active

pathways in the control group related to the activation and regulation of NMDA receptors, which is an ion channel for among others  $\text{Ca}^{2+}$ . Also, the activation of Ca-permeable Kainate receptor, sodium/calcium exchange, and reduction of cytosolic  $\text{Ca}^{2+}$  levels are more active pathways in the control group. All these different pathways are related to calcium ions and/or calmodulin. Calmodulin mediates many of the cellular effects of  $\text{Ca}^{2+}$  and one of the target proteins of  $\text{Ca}^{2+}$ /calmodulin is calcineurin.<sup>247,248</sup> The signaling of calcium/calmodulin via calcineurin is also more active in the control group via two pathways.  $\text{Ca}^{2+}$ , calmodulin, and calcineurin play an important role in proliferation and differentiation of osteoblasts.<sup>248</sup>  $\text{Ca}^{2+}$ , calmodulin, and calcineurin stimulate in osteoclast differentiation as well, while changes in  $\text{Ca}^{2+}$  regulate bone resorption in mature osteoclasts.<sup>247</sup> Higher activation of these calcium-related pathways in the control group could indicate a later differentiation of osteoblasts and osteoclasts, which are needed for hard callus formation and bone remodeling, in comparison to the citrulline supplement group. Antimicrobial peptides is another pathway with a higher activity in the control group. Antimicrobial peptides can be generated by neutrophils.<sup>226,227</sup> Because of this reason and the overlap in matched gene names, the activity of this pathway might be related to the activation of neutrophil degranulation. In addition, antimicrobial peptides might play a role in fracture healing via cell proliferation and ECM production, as their role in promotion of wound healing has already been shown.<sup>227</sup> The higher activation of this pathway in the control group is at a later time point than in the citrulline supplement group, which could indicate a slower fracture healing process in the control group. NOTCH2 regulation of transcription is more active in the control group. The NOTCH signaling pathways have different target genes, including Hes1, which is involved in bone remodeling and regulation of bone mass.<sup>228,229</sup> Activation of the NOTCH2 regulation of transcription can result in increased bone resorption.<sup>228,229</sup> Bone resorption is important during the formation of the hard callus, but the formation of new bone is also important. Activation of this pathway in the control group can indicate more bone resorption in this group compared to the citrulline supplement group. The regulation of IGF transport and uptake of IGFBPs is more active in the control group. IGFs promote bone matrix formation during fracture healing via osteoblast differentiation and their actions are modulated by IGF-binding proteins (IGFBPs).<sup>7,10</sup> The higher activity of the regulation of IGF transport and uptake of IGFBPs matches with the time point in the fracture healing process, but could indicate a delay in bone matrix formation in the control group in comparison to the citrulline supplement group. Degradation of the ECM is another pathway with higher activity in the control group. The degradation of ECM is mainly performed by MMPs.<sup>224</sup> This process is important

during the replacement of the soft callus by the hard callus. Activation of ECM degradation in the control group could indicate slower healing in this group than in the citrulline supplement group. Another more active pathway is the metabolism of angiotensinogen to angiotensins in the control group. Angiotensinogen and angiotensins activate osteoclasts and inhibit osteoblasts via de RAAS, and are expressed by osteoblasts, as indicated.<sup>232,233</sup> The activation of this pathway can be matched with this role, as bone remodeling starts at the end of the hard callus formation. The longer activation of this pathway in the control group in comparison to the citrulline supplement group could indicate higher amounts of callus resorption in the control group. VEGFR2 mediated cell proliferation is more active in the control group. Vascular endothelial growth factor (VEGF) is important in the formation of blood vessels and is expressed by osteoblasts and chondrocytes.<sup>7,10,14</sup> Angiogenesis starts already during the inflammation phase via the angiopoietin-dependent pathway, while VEGF-mediated angiogenesis occurs at during the hard callus formation.<sup>7,10,14,223</sup> Activation of this pathway can indicate that the angiogenesis in the control group is behind in comparison to the citrulline supplement group. More activity of the pathways related to RHO GTPases (RAS homolog family member of nucleotide guanosine triphosphate-ases) results in the activation of PAKs and NADPH oxidases in the control group. Activation of PAKs via GTPases plays an important part in the cytoskeletal reorganization and promotes bone resorption by osteoclasts.<sup>219,249</sup> NADPH oxidases are important in the controlled formation of reactive oxygen species (ROs) and ROs can contribute to osteoblast and osteoclast differentiation.<sup>250</sup> Activation of these pathways can be related to the formation of the hard callus and the start of bone remodeling, in which both osteoblasts and osteoclasts are active. Higher activity of these pathways in the control group can indicate delayed osteoblast and osteoclast differentiation in comparison to the citrulline supplement group.

#### *5.5.3.4 28 days post-operative: bone remodeling*

Regulation of insulin secretion by acetylcholine is more active in the citrulline supplement group at 28 DPO in comparison to the respective control group (see Table 5.5D). One of the functions of bone is its contribution to regulation of the energy metabolism.<sup>251,252</sup> Especially, osteoblasts are involved in the regulation of the secretion of insulin, which might be related to the constant bone remodeling.<sup>251,252</sup> The higher activation of this pathway in the citrulline supplement group could indicate higher activation of the bone remodeling pathways compared to the control group. Signaling by BMP (bone morphogenetic protein) is more active in the citrulline supplement group. BMPs are an important class of molecules involved in different phases of fracture healing.<sup>14</sup> Different BMPs have been shown

to be upregulated during the bone remodeling phase of fracture healing, which indicates their involvement in this phase.<sup>7,10,14</sup> Higher activity of the signaling by BMPs in the citrulline supplement group in comparison to the control group could indicate a higher amount of ongoing bone remodeling.

Reversible hydration of CO<sub>2</sub> is more active in the control group at 28 DPO. This process results in the production of bicarbonate, which can be equilibrate an acidic environment.<sup>231</sup> An acidic environment is created by osteoclasts during bone resorption.<sup>231</sup> The higher activity of the reversible hydration of CO<sub>2</sub> in the control group could indicate a higher osteoclast activity and a less complete bone remodeling phase in comparison to the citrulline supplement group. Purine catabolism is another pathway with higher activity in the control group. Bone remodeling and the functioning of osteoblasts and osteoclasts is mediated by extracellular purines, while their effect is highly dependent on the activated receptors.<sup>253</sup> Nevertheless, the role of purine catabolism during bone remodeling is unclear.

#### 5.5.3.5 *Citrulline supplement versus control group*

The paragraphs above discuss the more active pathways in the citrulline supplement and respective control group per time point post-operation. These pathways are discussed individually or in sets of closely related pathways. However, there is a great amount of interplay between the different pathways and different pathways affect each other or are part of one larger signaling pathway in some cases. These interplays between the different pathways are of great importance in the fracture healing process. Higher activity of different related pathways confirms their importance in the fracture healing process of the related treatment group, although caution is necessary in cases with the same single matching gene name. Besides, some pathways show higher activity in both the treatment and control group at the same time point. This can be related to differences in more abundant proteins (and their related gene names) between the citrulline supplement and control group. However, these proteins from different the treatment and control group are part of the same pathway in these cases.

The combination of the pathway analyses for all time points suggests an enhanced fracture healing process in the citrulline supplement group compared to the control group. This difference is less pronounced during the bone remodeling phase, as a lower number more active pathways are different at 28 DPO. This could be related to the end of citrulline supplement after 14 DPO. The fracture healing process seems to be enhanced via improved angiogenesis and earlier formation of the soft and hard callus as a result of the citrulline supplement. These results are in

agreement with the previous citrulline supplement study performed in mice by Meesters *et al.*<sup>192</sup> On the contrary, the inflammation phase and angiogenesis take longer in the control group. The production of nitric oxide is more activated in the citrulline supplement group at different time points via NOS activation. In addition, there are different pathways with higher activity that can be linked to the NOS activation in the citrulline supplement group.

### 5.5.4 Limitations and future research

This study provided insight in the effect of citrulline supplement during bone fracture healing on lipids and proteins. Nevertheless, there are some methodological limitations that merit discussion. A relative wet matrix spraying protocol was used during the sample preparation for lipid MSI. This protocol was optimized to enhance desorption and ionization of the molecules of interest from the tissue, especially since extraction from bone is challenging. A consequence of a wet spraying protocol can be the delocalization of molecules.<sup>36,254</sup> Some delocalization of the lipids was indeed observed in the samples, but this was limited and accepted for the sake of desorption and ionization efficiency. Lipid MSI was only performed in positive ionization mode, as we have previously shown that this ionization provides better results than negative ionization mode.<sup>204</sup> Acquisitions in only positive ion mode, will affect which lipid classes can be extracted.<sup>255-257</sup> Mainly PCs and LPCs were detected in this study, but also some CARs, a SM, and two TGs were observed. The extracted lipid composition of a rat bone and bone marrow consist mainly of TGs and different phospholipid classes, of which PCs are the major class.<sup>137</sup> We believe MALDI-MSI acquisition only in positive ionization mode provides sufficient information in this study, as the major lipid classes present in bone and bone marrow are more commonly detected in this mode. However, additional information about the contribution of and changes in specific lipid classes during bone fracture healing can be provided by MALDI-MSI in negative ionization mode.

The protein extractions were performed on crushed pieces of bone and, therefore, no separate analysis of bone and bone marrow proteins could be performed, unlike for the lipid analysis. The composition and function of bone and bone marrow are different.<sup>258</sup> Separate analysis would have allowed to protein compositional changes for bone and bone marrow, which was not implemented in this study. The collection of bone and bone marrow for analysis resulted in differences in the ratio between them. This might have affected the data analysis due to differences in composition, although housekeeping proteins showed similar abundances between samples. In addition, protein digestion was performed using a

combination of LysC and Trypsin, which cut the proteins at amino acids lysine and arginine.<sup>259</sup> The efficiency of LysC and Trypsin on ECM proteins is limited by their post-translational modifications and structural organization.<sup>259</sup> Improved digestion of ECM proteins, like collagen and elastin, have been shown with collagenase and MMP.<sup>259</sup> The use of MMPs as enzyme is not recommended in proteomics studies of bone fracture healing due to their important role in this process.<sup>5,7,13</sup>

This study showed the effect of citrulline supplement on lipids and proteins during fracture healing in a rat model by applying different mass spectrometry techniques. The effect of citrulline supplement on lipid changes in bone and bone marrow should be confirmed in future, as little is known about specific lipids during fracture healing. In addition, the role of the different lipid classes and specific lipids during fracture healing should be explored to improve understanding of the effect of citrulline supplement. Furthermore, the observed activated pathways as result of the citrulline supplement or the lack of citrulline supplement should be validated, especially the ones that have only a single matched gene name. The high number of pathways with a single matched gene name was related to the low number of more abundant proteins in each sample group, indicated a limited effect of citrulline supplement on the overall protein profile throughout fracture healing, which should be confirmed in future research. Furthermore, it would be interesting to study the effect of citrulline supplement in a non-union animal model, as this supplement seems to enhance fracture healing. Lastly, a clinical study would be necessary to see the effect of citrulline supplement during bone fracture healing in human patients. Traditional methods to track fracture healing in clinical studies should be used, as obtaining samples from the fracture site is not desirable due to potential disturbance of normal fracture healing. However, there are some additional challenges related to human samples, in case they can be obtained from the fracture site, for example, during reduction or fixation surgeries. Bone samples will be more difficult to section for MALDI-MSI or crush for LC-MS/MS, due to the size and hardness of a human bone. Another option is the use of the fracture hematoma, as we have shown previously.<sup>212</sup> However, the molecular effects of citrulline supplement will need to be confirmed in this tissue type. Comparison between the treatment and control group in a clinical study will be more challenging than in an animal study, due to the wide variety of fracture types and differences in healing rates between patients.

## 5.6 Conclusion

The effect of citrulline supplement on fracture healing was explored by using different mass spectrometry techniques to analyze lipids and proteins at different

time points after operation in a rat model. An summary of these results can be found in Figure 5.10. Lipid analysis with MALDI-MSI showed different lipids contributing to the citrulline supplement and control group. The observed lipid profiles for the citrulline supplement and control group were distinct for bone and bone marrow at the different time points. Protein analysis with LC-MS/MS displayed different abundant proteins at the different time points in the citrulline supplement and control group. The overlap between abundant proteins at different time points was limited, which indicates a changing effect of citrulline supplement during the stages of fracture healing. The analysis of activated pathways based on the abundant proteins indicated an enhancement of the fracture healing process in the citrulline supplement group via improved angiogenesis and earlier formation of the soft and hard callus. The differences between the treatment and control group were smaller during the bone remodeling phase for the pathway analysis, which was also observed for the lipid profiles. The animals were no longer supplemented with citrulline at this stage. In addition, different pathways in the citrulline-arginine-nitric oxide metabolism and related pathways were more active in the citrulline supplement group. Overall, citrulline supplement results in a distinct effect on the lipid and protein profiles during fracture healing and pathway analysis showed an enhancement of fracture healing in the citrulline supplement group.

Effect of citrulline supplement on lipid and protein profiles during fracture healing

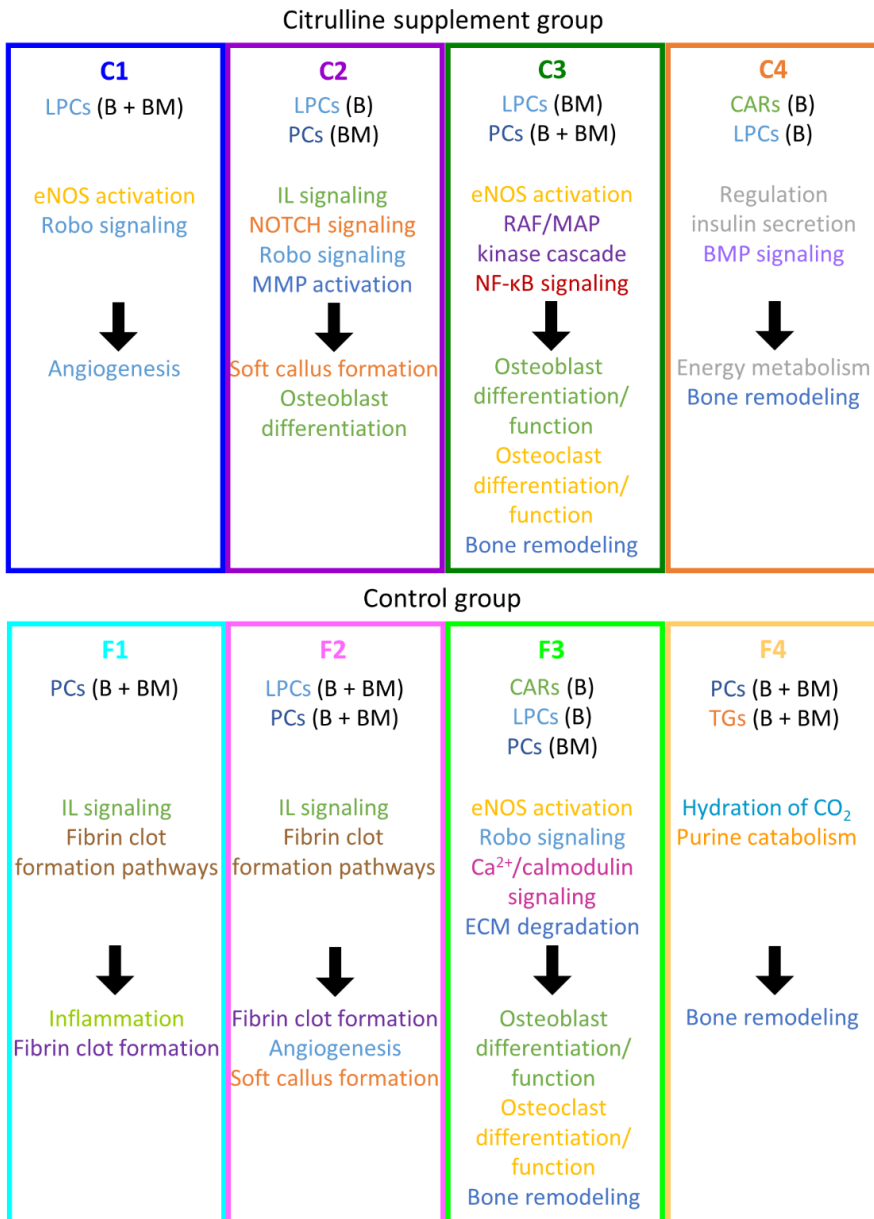


**Figure 5.10:** Overview of the results of the lipid and pathway analyses and the resulting processes for the citrulline supplement and control group. B and BM represent bone and bone marrow, respectively, for the lipid rows. C1, C2, C3, and C4 represent 3, 7, 14, and 28 DPO in the citrulline supplement group, respectively. F1, F2, F3, and F4 represent 3, 7, 14, and 28 DPO in the control group, respectively. The colors show the same lipid class, pathway, or related process, but the colors for the lipid, pathway, and resulting processes rows are not related.



## Chapter 6: Automated 3D sampling and imaging of uneven sample surfaces with LA-REIMS



Sylvia P. Nauta

Pascal Huysmans

Gabriëlle J.M. Tuijthof

Gert B. Eijkel

Martijn Poeze

Tiffany Porta Siegel

Ron M.A. Heeren

Journal of the American Society for Mass Spectrometry (JASMS)

2022; 33(1): 111-122



## 6.1 Abstract

The analysis of samples with large height variations remains a challenge for mass spectrometry imaging (MSI), despite many technological advantages. Ambient sampling and ionization MS techniques allow for the molecular analysis of sample surfaces with height variations, but most techniques lack MSI capabilities. We developed a 3D MS scanner for the automated sampling and imaging of a 3D surface with laser-assisted rapid evaporative ionization mass spectrometry (LA-REIMS). The sample is moved automatically with a constant distance between the laser probe and sample surface in the 3D MS Scanner. The topography of the surface was scanned with a laser point distance sensor to define the MS measurement points. MS acquisition was performed with LA-REIMS using a surgical CO<sub>2</sub> laser coupled to a qTOF instrument. The topographical scan and MS acquisition can be completed within 1 h using the 3D MS scanner for 300 measurement points on uneven samples with a spatial resolution of 2 mm in the top view, corresponding to 22.04 cm<sup>2</sup>. Comparison between the automated acquisition with the 3D MS scanner and manual acquisition by hand showed that the automation resulted in increased reproducibility between the measurement points. 3D visualizations of molecular distributions related to structural differences were shown for an apple, a marrowbone, and a human femoral head to demonstrate the imaging feasibility of the system. The developed 3D MS scanner allows for the automated sampling of surfaces with uneven topographies with LA-REIMS, which can be used for the 3D visualization of molecular distributions of these surfaces.

## 6.2 Introduction

Over the past decades, mass spectrometry imaging (MSI) has been increasingly used to investigate biological and biomedical samples. Nevertheless, the surface sampling of large areas with topographical height variations with 3D MSI is very limited. The analysis of samples with large and uneven surfaces has a potentially broad range of applications, including for the analysis of whole fruits or vegetables as well as clinically for analysis of large surface areas on bones and joints. The analysis of these types of surfaces can be of added value in reproducible molecular mapping of samples surfaces to study the molecular changes on the sample surface. For clinical applications, this can be used to improve molecular understanding of processes related to structural changes, which can be applied to tissue classification model building for identification of diseases. In addition, the number of sampling spots, and thus, tissue damage can be reduced by determining the optimal sampling point due to the improved molecular understanding of the sample surface for further applications.

Samples with uneven surfaces are more challenging to analyze with MSI, as mass analyzers, like time-of-flight (TOF) analyzers, are frequently affected by small height variations in the sample resulting in signal intensity variations or peak shifts.<sup>204</sup> For example, a linear TOF is more sensitive to height variation than an orthogonal TOF, as in an orthogonal TOF the ionization source is decoupled from the mass analysis.<sup>40</sup> Height variations of even a few micrometers in the sample can cause defocusing of the laser beam during analysis for MSI technique relying on laser beams, resulting in decreasing sensitivity.<sup>260</sup> Because of these challenges, most MSI techniques require a constant distance between the sample, the ionization source, and the extraction to the mass analyzer. Samples prepared for 2D MSI techniques, such as matrix-assisted laser desorption/ionization (MALDI) and desorption electrospray ionization (DESI), are often sectioned to create planar surfaces for easy analysis.<sup>144,260-262</sup> Nevertheless, sectioning is not always an option for certain tissue types or surface analyses. Some techniques have been developed that can compensate for small variations in sample height. These compensation techniques are based on obtaining surface height measurements by, for example, camera image analysis,<sup>263,264</sup> atomic force microscopy,<sup>265-268</sup> shear force microscopy,<sup>269</sup> scanning near-field optical microscopy,<sup>270,271</sup> laser triangulation,<sup>144,272</sup> or confocal distance sensor.<sup>260</sup> The height variation tolerance remains limited to only hundreds of  $\mu\text{m}$  and still requires the (biological) samples to be relatively flat for all these compensation techniques. Therefore, the analysis of biological sample surfaces with large height variations in terms of millimeters, for example, bones and joints removed during surgery, is not possible with these developments.

It is important to determine the topography of the surface that needs to be analyzed to achieve MSI of 3D surfaces. This topography will determine the position of the sample, ionization source, and MS inlet to keep a constant distance and orientation relative to each other by moving the sample or the ionization source and MS inlet. Only a few MSI studies have been performed on large 3D surfaces with sampling MS techniques that applied the concept of aligning the sampling probe with the uneven surface to create 3D distributions and, therefore, are described as 3D MSI. In 2014, Bennett *et al.* coupled direct analysis in real time (DART) with robotic probe surface sampling via a needle and showed the distribution of different dyes on the polystyrene hemisphere.<sup>261</sup> In 2018, Li *et al.* used a robotic arm with a needle probe combined with an open port sampling interface (OPSI) and showed the relative abundance of molecules on a plastic coffee cup cover, medicine blister pack, football, and six-well spot plate.<sup>262</sup> In 2021, Ogrinc *et al.* coupled a robotic arm with the SpiderMass (a water-assisted laser desorption ionization MS technique) for *in vivo* surgical applications.<sup>273</sup> In this setup, 3D

topographical imaging of the surface is combined with molecular surface sampling with the SpiderMass. Topological images and 3D mass distributions were shown *ex vivo* for a sponge spotted with lipid standards, an apple core with seeds, a skin biopsy, and parts of a whole-body mouse model and *in vivo* on a human fingertip. Although these prior methods are innovative, they have not been applied to samples that are difficult to sample, like bone and cartilage of joints.

The development of different ambient sampling and ionization mass spectrometry techniques, for *in vivo* applications, allows for the sampling of sample surfaces without sample preparation independent of the flatness of the sample.<sup>261,272,274</sup> One of these techniques is rapid evaporative ionization mass spectrometry (REIMS),<sup>46</sup> combined with either electrocautery or laser ablation sampling.<sup>38,39</sup> REIMS works by analyzing the smoke containing aerosolized molecules created when electrocautery or laser ablation is applied to biological tissue.<sup>38,46</sup> This smoke is rich in lipids and metabolites and is aspirated to a mass spectrometer via tubing connected to a Venturi pump.<sup>38,46</sup> Schäfer *et al.* showed that laser desorption ionization MS with a CO<sub>2</sub> laser could be applied to biological tissue to generate similar spectra as those created with electrocautery when combined with REIMS.<sup>39</sup> Recently, Genangeli *et al.* demonstrated the use of a CO<sub>2</sub> laser coupled with REIMS for the sampling of bone, cartilage, and bone marrow.<sup>38</sup> Of all the developed ambient techniques, the combination of a CO<sub>2</sub> laser with REIMS (LA-REIMS) and the SpiderMass are the only techniques that were demonstrated to be able to sample hard tissue samples, like bone and cartilage.<sup>38,121</sup> LA-REIMS was selected, as this technique is promising for the 3D MSI of samples with large height variations and can be used on bone and cartilage. Laser-assisted REIMS (LA-REIMS) has been used for different tissue classification, metabolic screening, and other applications.<sup>38,274-279</sup> LA-REIMS and similar techniques can be used for sampling of 3D surfaces, but the created mass spectra are often not spatially correlated back to the three-dimensional sample location to create distribution images. For LA-REIMS, a high-throughput and automated platform has been developed for the metabolic screening.<sup>274-279</sup>

Despite the promising field of applications, LA-REIMS has not yet been applied to the analysis of complex 3D sample surfaces, to the authors' knowledge. In addition, LA-REIMS currently lacks imaging capabilities, despite the development of automated screening platforms. The coordinates in the three-dimensional space of the sample locations as well as the order of the sampling locations need to be correlated back to the obtained mass spectra per sampling point to enable imaging capabilities for LA-REIMS. Automation of 3D surface sampling with LA-REIMS would

allow for 1) increased reproducibility between measurement points, as the distance and the angle between the sampling device and the sample surface is constant; 2) increased precision, as all sampling positions will be defined by a sampling grid with constant distances between measurement points; 3) faster analysis, as the sample or the laser probe is moved to the next measurement position automatically; and 4) the creation of molecular distribution images, as the spatial location of each measurement point can be coupled to the mass spectrum of the sample location. Besides, 3D MSI of the surfaces of, for example, bones and joints, can improve the generation of clinical classification models, as they will be more robust and small changes can be related back to the annotation of the sample surface.

Herein, we describe the development and demonstrate the effectiveness of such an automated device - the “3D MS scanner” - for the sampling of a 3D surface with LA-REIMS. We focus on the comparison between manual analysis of a 3D surface with LA-REIMS and the automated analysis. Furthermore, we show for the first time for LA-REIMS the added value of this automated sampling technique in terms of retaining spatial information on each sampling location, which allows for 3D visualization of the acquired area.

### 6.3 Materials and methods

#### 6.3.1 Materials and samples

2-Propanol and leucine-enkephalin were purchased from Honeywell (Seelze, Germany) and Sigma-Aldrich (St. Louis, MO), respectively. A 0.5 mM sodium formate solution was used for calibration of the mass spectrometer.

Apples and cow marrowbone were purchased at the local supermarket for different types of experiments with the 3D MS scanner. The apple and marrowbone were used without any further sample preparation, except for analysis of the bone of the marrowbone for which the remaining soft tissue was removed with a scalpel.

Human femoral heads were collected from five patients that underwent total hip replacement surgeries at Maastricht University Medical Center (MUMC+). The Medical Ethical Committee of the MUMC+ (approval number: 09-2-123) approved the use of “waste” materials from surgeries for scientific research without an additional written informed consent of the patient. The human femoral heads were stored in a  $-80\text{ }^{\circ}\text{C}$  freezer until analysis and were left to thaw at room temperature before analysis. No further sample preparation was performed.

### 6.3.2 Surgical CO<sub>2</sub> laser

An AcuPulse Class IV CO<sub>2</sub> surgical laser (Lumenis GmbH, Germany) with a wavelength of 10.6 μm was used for all experiments. The laser has a maximum power of 60 W and can be operated in the modalities continuous wave (CW), pulsed wave (PW), and super pulsed wave (SPW). The used laser settings depended on the sample type. An overview of the different laser settings used for the different samples (apple, cow marrowbone, and human femoral head) during the different experiments (comparison between manual and automated sampling, 3D visualization of molecular distributions, and MS/MS experiments) is provided in Table 6.1.

#### 6.3.2.1 Safety considerations

Appropriate safety measures were put in place, in accordance with local safety regulations when working with a Class IV laser CO<sub>2</sub> surgical laser. The laser was placed fully shielded in either the purposely designed and constructed mechanical CO<sub>2</sub> laser probe holder or the 3D MS scanner to prevent holding the laser in the hand while it fires. The experimental area was shielded with Class IV laser safety curtains, and all people inside this area wore CO<sub>2</sub> laser-grade safety goggles. An anodized aluminum plate was placed underneath the laser beam to prevent scattering of the CO<sub>2</sub> laser beam outside of the class II biosafety cabinet. All experiments were performed inside a class II biosafety cabinet that ventilated the created smoke safely. The CO<sub>2</sub> laser has a safety interlock to stop the laser on the laser body, which could be pressed in case of emergency.

#### 6.3.3 Manual setup: Mechanical CO<sub>2</sub> laser probe holder

A custom-built, articulated, mechanical arm was used to secure the CO<sub>2</sub> laser probe (the end of the laser arm through which the laser beam passes) for safety

**Table 6.1:** Overview of laser settings for different samples during the different experiments.

M is the operation mode, P is the laser power (in W), D is the laser pulse duration (in s), and E is the corresponding sampling energy (in J) per measurement point.

	Comparison				3D visualization				MS/MS			
	M	P	D	E	M	P	D	E	M	P	D	E
Apple	CW	25	0.1	2.5	CW	25	0.1	2.5	CW	25	0.4	10.0
Cow marrowbone	PW	30	0.4	12.0	CW	30	0.1	3.0	CW	30	0.4	12.0
Human femoral head	CW	20	0.3	6.0	CW	20	0.1	2.0	CW	20	0.4	8.0

considerations and to allow for operation of the laser at a fixed position when the laser was fired. This mechanical CO<sub>2</sub> laser probe arm has been previously described by Genangeli *et al.*<sup>38</sup> In short, the arm is made of aluminum alloy 6082, which was glass bead blasted. The moving parts of the arm were kept in place with air-powered breaks, which cause small movements in the position of the arm when releasing them. The laser probe in the holder could be moved by hand to the required position, where it remained while the laser was fired. The laser was fired with a two-button safety box outside of the biosafety cabinet for safety reasons. The sample is placed underneath the laser at a plate at the bottom of the biosafety cabinet.

### 6.3.4 Automated setup: 3D MS Scanner development

The 3D MS scanner was developed to measure the surface of a sample in an automated way using LA-REIMS. The main components of the 3D MS scanner are the different axes, the sample holder, distance sensor, clamps for fixation of the laser probe, and the control box (see Figure 6.1). For the operation of the 3D MS scanner, a sample is placed in a custom-designed sample holder positioned underneath the laser probe for safety considerations. The sample holder is positioned in the middle of the biosafety cabinet. The sample is automatically moved for each measurement point while maintaining a constant distance and angle between the laser probe and sample surface. The aim of this movement is to place the sample underneath the laser probe in such a way that the laser beam is aligned with the surface normal at the measurement point as perfect as achievable within the implemented degrees of freedom. The setup has four degrees of freedom: three translational axes (x, y, and z axes) and one rotational axis (around the x axis). Electric slides (models EGSK and EGSC, FESTO, Esslingen am Neckar, Germany) in combination with stepper motors (model EMMS, FESTO) were used for the motion along the translational axes. A rotary driver (model ERMO, FESTO) was used for the rotational motion with a manufacturer specified repeatability of  $\pm 0.05^\circ$ . A high-performance laser point distance sensor (model BA\_OM70, Baumer Holding AG, Frauenfeld, Switzerland) was used for the measurement of the topography of the surface sample. The distance sensor was placed at a fixed distance from the laser probe and has an optimal measurement range of 40 mm. Therefore, the maximum z-height variation in the acquisition areas should not extend this value. The laser probe was held by two magnetic clamps made of the plastic Stratasys-Verowhiteplus that would release the laser probe if a collision between the sample and laser probe occurred to prevent damage to the fragile laser arm. The base frame and sample holder of the 3D MS scanner were made of aluminum and an anodized aluminum plate was attached at the bottom.

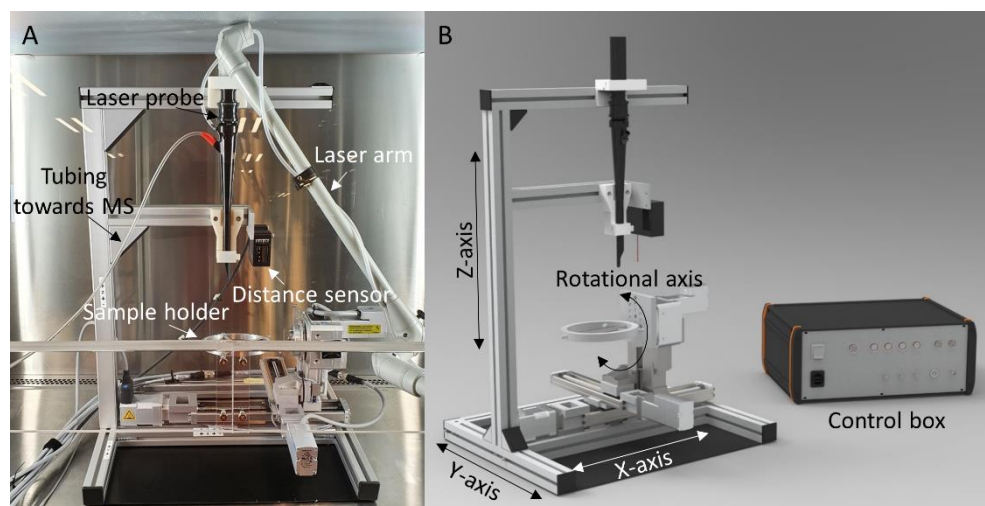


**Figure 6.1:** Images of the 3D MS scanner. **A** Picture of the 3D MS scanner setup in the biosafety cabinet with the CO<sub>2</sub> laser probe inserted. Besides the laser probe, the following elements are indicated: the tubing through which the created smoke is aspirated toward the mass spectrometer (MS), the distance sensor that is used for the topographical measurement, and the sample holder. **B** Design image of the 3D MS scanner with indication of the three translational axes, the rotational axis, and the control box.

The 3D MS scanner was operated using home-built control electronics that were programmed with custom LabVIEW software (version 2020, National Instruments). The control software was running on a Microsoft Surface Pro 6 using the custom-build LabVIEW application MS3D version 2.01.

#### 6.3.4.1 Analog laser trigger registration with mass spectral data

The position (in three dimensions) of a measurement point must be registered with the correct corresponding mass spectrum for each sampling event for correct processing of the data and the generation of images. Registration of an analogue laser trigger into the mass spectrometer next to the total ion current (TIC) signal is important for this alignment. An eSAT/IN box (D16EST083M, Waters Corp.) was used for the registration of an analog signal during the MS acquisition. An analogue trigger was registered next to the TIC chromatogram in MassLynx (version 4.1, Waters Corp.) during the MS measurement of the sample whenever the surgical CO<sub>2</sub> laser was fired. See Figure 6.2 for an example of an overlay image between the analogue signal and the TIC chromatogram.



measurement point. The topographical scan consists of two phases: 1) a quick scan of the sample surface where a spline is fitted through the points to define the mesh for the measurement points and 2) adjustment of the motor positions at each measurement point based on the mesh and optimization of the distance between the distance sensor and the surface. When the topographical scan is finished, the MS measurement is performed. The control box will send a trigger to the XEVO G2-XS to start the MS acquisition, which also starts the acquisition of the analogue laser trigger signal. The following steps are repeated for each measurement point: (a) the surgical CO<sub>2</sub> laser is triggered to fire one laser pulse and an analog trigger is registered at the eSAT/IN box at the same time, (b) the sample is held still for a short waiting period (optimized value: 0.1 s) to allow for the aspiration of the ablated smoke to the mass spectrometer and to prevent disturbance of the smoke by movement, and (c) the sample is repositioned to the next measurement point. A file is generated that contains the x, y, and z coordinates of each of the measurement points at the end of the acquisition. This file is used to assign the 3D coordinates to the mass spectral data of each measurement point in post-processing.

### 6.3.5 REIMS-qTOF instrumentation

The smoke created with the CO<sub>2</sub> laser was analyzed with REIMS by aspiration through a flexible tube by a Venturi pump to the source. A benchtop XEVO G2-XS qTOF (Waters Corp., Manchester, UK) equipped with a REIMS source was used for the ionization and detection of the molecules from this smoke. The measurements were acquired in negative ion mode, in sensitivity mode, and with a mass resolution of around 15 000 full width at half-maximum (fwhm) at  $m/z$  600. The acquired  $m/z$  range for all samples was 100-1500. The instrument was calibrated daily with a 0.5 mM solution of sodium formate. A lock mass solution of leucine-enkephalin (Leu-Enk) in 2-propanol (final concentration 0.075 ng/ $\mu$ L) was continuously infused at a flow rate of 150  $\mu$ L/min in the REIMS source using a syringe pump. A lock mass solution was constantly infused as it has been shown that infusion of a solvent matrix during the REIMS experiment can significantly improve the ion intensity.<sup>47</sup>

### 6.3.6 Optimization of the functioning of the 3D MS Scanner

#### 6.3.6.1 Optimization of the height between laser probe and sample surface

Seven distances between the laser probe and the sample surface were compared; 0.5 mm, 1.0 mm, 1.5 mm, 2.0 mm, 3.0 mm, 4.0 mm, and 10.0 mm. Fifty points were measured on an apple using the 3D MS Scanner for each distance. (Except for a distance of 3.0 mm, as the first 3 points were not recorded in the mass spectrometer due to an issue with aspiration.) The different distances were

compared based on the overall intensity and the intensity of nine  $m/z$  values specific for the apple signal defined over the measured mass range. The overall signal intensity was determined by 1) the maximum total ion current (TIC) peak value in the chromatogram trace of the measurement, and 2) the area of the TIC peak in the chromatogram trace of the measurement. The maximum of each of the TIC peaks corresponding to measurement points were determined to obtain the maximum TIC peak values. The TIC peak per measurement point was integrated to calculate the area of the TIC peak. The intensities of nine selected  $m/z$  values were compared using the areas of the extracted ion chromatograms (EICs). The areas under the peaks corresponding to measurement points in the EICs for the  $m/z$  values were calculated using integration. Results are represented as average  $\pm$  standard deviation (SD) and coefficient of variance (CV, %).

### 6.3.6.2 *Optimization of the waiting time after laser shot and before sample movement*

Seven waiting times between the laser shot and sample movement were compared; 0.1 s, 0.3 s, 0.5 s, 0.7 s, 1.0 s, 1.5 s, and 2.0 s. Twenty points were measured on an apple using the 3D MS Scanner for each waiting time. The different waiting times were compared based on the overall intensity and the intensity of nine  $m/z$  values specific for the apple signal defined over the measured mass range. The overall signal intensity was determined by 1) the maximum total ion current (TIC) peak value in the chromatogram trace of the measurement, and 2) the area of the TIC peak in the chromatogram trace of the measurement. The maximum of each of the TIC peaks corresponding to measurement points were determined to obtain the maximum TIC peak values. The TIC peak per measurement point was integrated to calculate the area of the TIC peak. The intensities of nine selected  $m/z$  values were compared using the areas of the EICs. The areas under the peaks corresponding to measurement points in the EICs for the  $m/z$  values were calculated using integration. Results are represented as average  $\pm$  standard deviation (SD) and coefficient of variance (CV, %).

### 6.3.7 Comparison between manual and automated measurements

Manual and automated measurements of 50 points were acquired to compare the reproducibility for the manual (see 6.3.3. Manual Setup) and automated (see 6.3.4 Automated Setup) setups in data acquisition. The manual data acquisition was always performed subsequent to the automated data acquisition, as the manual measurements points were placed in between the automated measurement points to prevent overlap between the sample location of the measurement points. The data acquisition for the manual and automated setups were performed within the

same rectangular acquisition area to keep the biological variance in both data sets similar. The comparisons were performed on an apple, the outside surface of a marrowbone (bone tissue), and five human femoral heads. Human femoral heads are molecularly more heterogeneous than apples and bone, and therefore, areas were selected that were homogeneous by eye.

The manual and automated setups were compared based on the overall intensity, the intensity of 10 selected  $m/z$  values, and the variance between measurement points. These  $m/z$  values were defined per sample to be specific for the sample signal and to cover the measured mass range. The overall signal intensity was determined by 1) the maximum TIC peak intensity value and 2) the area of the TIC peak. The maximum TIC peak intensity values corresponding to each measurement point were determined by taking the maxima in the chromatogram trace of the measurement. The TIC peak per measurement point in the chromatogram trace of the measurement was integrated to calculate the area of the TIC peak. The maximum TIC peak intensity value represents the maximum total signal intensity in one scan for each measurement point, while the TIC peak area represents the total signal intensity for the whole measurement point. Therefore, both values are compared between manual and automated measurements. The 10 selected  $m/z$  values were compared based on the calculated areas of the extracted ion chromatograms (EICs) for the measurement points. Results are reported as average  $\pm$  standard deviation (SD) and coefficient of variance (CV, %). The variance between measurement points was compared using principle component analysis (PCA) of the manual and automated setups per sample. The PCA plots can be related to the variance, as the closer the different measurement points (represented by spheres) are together the lower the variance in between them and vice versa.

MassLynx (version 4.1, Waters Corp.) was used for the analysis of the acquired MS data. The coefficients of variances (CV) for the manual and automated data were calculated to determine whether they were significantly different with a coefficient of variance test. The determination threshold for significance was set at  $p$ -values  $<0.05$ . Abstract Model Builder (AMX) (version 1.0.1581.0, Waters Corp.) was used for the PCA analyses. The mass spectra were binned with a bin size of  $m/z$  0.2 for the mass range of  $m/z$  100-1500. The mass spectra of each measurement point were lock mass corrected, background subtracted and removed, and normalized (TIC normalization) before building the a 10 component PCA model.

### 6.3.8 3D MSI measurements

Three experiments were set up to show the use of the 3D MS scanner for the 3D visualization of molecular distributions on different types of samples: 1) 300

measurements points on an apple of which part of the peel was removed, 2) 200 measurement points on the outside of a marrowbone, and 3) 150 measurement points on the outside of a human femoral head. The spatial resolution was set to 2 mm, and the MS acquisition time per measurement point was 5.0 s.

Home-built MATLAB (version 2018b, Mathworks) algorithms were used for data conversion and 3D visualization of the measurements acquired with the 3D MS scanner.

### 6.3.9 Molecular identifications

Tentative molecular identifications were performed on the basis of MS/MS and database searches for the  $m/z$  values that are displayed in the different figures in the Results. MS/MS fragmentation was performed on a REIMS-qTOF in negative ionization mode with varying collision energies (CEs) between 10 and 40 arbitrary units. Alex<sup>123</sup> lipid calculator, METLIN, LIPID MAPS Structure Database (LMSD), and MassLynx (version 4.1, Waters Corp.) were used for the identification of the  $m/z$  values. The data sets were lock-mass corrected using mMass (Open Source Mass Spectrometry Tool, version 5.5.0) when the internal lock mass (Leu-Enk) showed a ppm error above 10 ppm. The lock mass corrected  $m/z$  values were used for the identifications.

## 6.4 Results

This study consisted of three parts: 1) the optimization and characterization of the 3D MS scanner, 2) comparison between the mechanical CO<sub>2</sub> laser probe holder controlled by hand and the automated 3D MS scanner, and 3) 3D visualization of the data acquired with the 3D MS scanner.

### 6.4.1 Optimization and characterization of the 3D MS Scanner

The developed 3D MS scanner (see Figures 6.1 and 6.3) allows for the mass spectrometer analysis of sample surfaces with large topographical variations in 3D. The optimization and characterization of the 3D MS Scanner consists of three parts: 1) the optimization of the height between laser probe and sample surface, and the waiting time after laser shot and before sample movement; 2) the alignment of the analog laser trigger and raw TIC chromatogram; and 3) the speed of the whole process.

## Automated 3D sampling and imaging of uneven sample surfaces with LA-REIMS

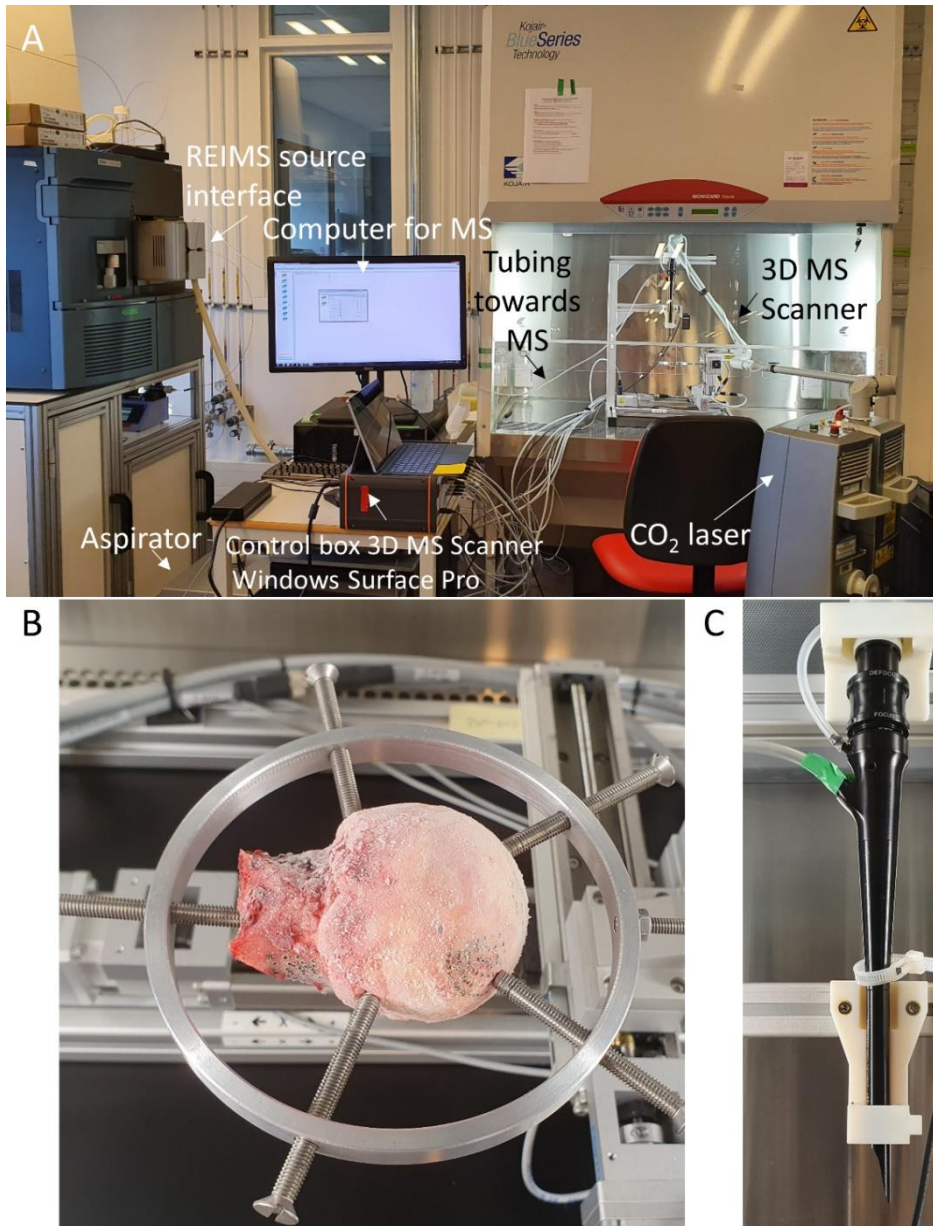


**Figure 6.3:** Details of the 3D MS Scanner setup. **A** Overview of the setup in the lab. The 3D MS Scanner is placed in the biosafety cabinet. The control box and the Windows Surface Pro, control the 3D MS Scanner and send the triggers to the laser, the mass spectrometer, and the eSAT/IN module. These are placed outside of the biosafety cabinet. The smoke created by the laser is aspirated through the tubing towards the mass spectrometer with the REIMS source. **B** Close up picture of the sample holder with a (frozen) femoral head. **C** Close up picture of the laser probe and aspiration tube.

### 6.4.1.1 Optimization of settings of the 3D MS Scanner

#### 6.4.1.1.1 Height between laser probe and sample surface

The distance between the laser probe and the sample surface is important for the amount of smoke that is aspirated into the mass spectrometer, as the increasing distance is expected to result in decreasing signal. Although no distance between the laser probe and the sample surface would result in the highest signal intensities, this is not preferred because of cross-contamination between sampling points. Besides, because of the shape of the laser probe (see Figure 6.3C), small distances between the laser probe and the sample surface can result in unwanted collisions between the laser probe and the sample.

The overall signal intensity decreases with an increasing height between the laser probe and the sample surface, which was as expected and can be seen from the peak TIC value (see Figure 6.4A) and the TIC peak area (see Figure 6.4B). In addition, the CVs show an upward trend with increasing height, which indicates a raising variation between TIC peaks in the chromatogram occur the further away the laser probe is from the sample surface. The most pronounced result is the big drop (almost 90% between 2.0 mm and 3.0 mm) in peak area for  $m/z$  value 833.5 from 3.0 mm onwards (see Figure 6.4C). The peak areas show a drop for the bigger heights (3.0, 4.0, and 10.0 mm) for the other  $m/z$  values as well. In general, an increasing trend can be seen with increasing distance between the laser probe and sample surface for the CVs of the different  $m/z$  values. Large CVs can be noted for  $m/z$  133.0 in comparison to other  $m/z$  values. The CVs for the distances 0.5, 1.0, 1.5, and 2.0 mm are in the acceptable range (<25 %) for all  $m/z$  values except  $m/z$  133.0, as they vary from 9.47 to 22.72 %. In addition, the absolute intensities of all  $m/z$  values decrease with increasing height and five of the  $m/z$  values show a big drop in absolute intensity for heights from 3.0 mm onwards (data not shown).

To conclude, the optimal height between the laser probe and the sample surface is 2.0 mm to avoid collision between the laser probe and sample surface while maintaining good signal intensities over the measured mass range.

#### 6.4.1.1.2 Waiting time after laser shot and before sample movement

The waiting time between the laser shot and the start of the sample movement to the next measurement point might affect the amount of aspirated smoke, as when the sample movement is too quick the created smoke might be disturbed before it is aspirated to the mass spectrometer. It is important to keep this waiting time as short as possible to reduce the overall speed of the acquisition of the mass spectra for each measurement point.

## Automated 3D sampling and imaging of uneven sample surfaces with LA-REIMS

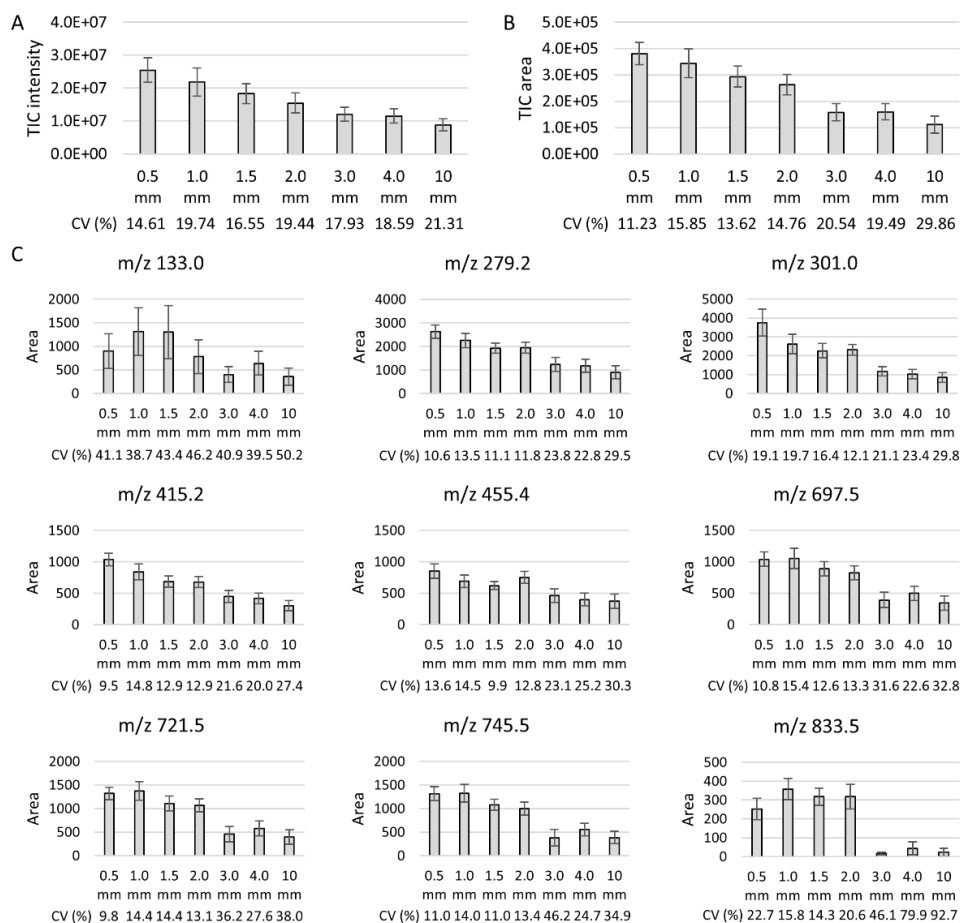


**Figure 6.4:** Comparison of heights between the laser probe and sample surface. Comparison of signal intensity between seven different distances between the laser probe and the sample surface, namely 0.5 mm, 1.0 mm, 1.5 mm, 2.0 mm, 3.0 mm, 4.0 mm, and 10.0 mm. **A** The average of the peak TIC values in the chromatogram per measurement point with the standard deviation. In addition, the coefficient of variation (CV) is provided as a percentage in the table underneath. **B** The average of the areas under the TIC peaks in the chromatogram determined with integration. Average with the standard deviation as well as the CV (%) are provided. **C** The average of the areas under the extracted ion chromatogram peaks for nine selected  $m/z$  values. The  $m/z$  values were selected based on their specificity for the sample and to cover the measured mass range as much as possible. For each  $m/z$  value, the average area with standard deviation and the CV (%) are provided.

No decreasing trend for the overall signal intensity was observed with decreasing the waiting time between the laser shot and the sample movement, as can be seen from the peak TIC value (see Figure 6.5A) and the TIC peak area (see Figure 6.5B). The overall signal intensity is even the highest for the shortest waiting time of 0.1 s, contradicting the expectations. The CVs for the TIC peak values and TIC peak areas show no clear trend with decreasing waiting time, indicating the variations in overall signal intensity vary between measurements, but are not dependent on the waiting time. No general trends can be seen in the peak areas for the nine selected  $m/z$  values (see Figure 6.5C), although the peak areas are quite stable or show a slightly decreasing trend for 2.0 s to 0.3 s for most  $m/z$  values. The waiting time of 0.1 s resulted in the highest peak area for  $m/z$  values 279.2, 301.0, 697.5, 721.5, 745.5, and 833.5, and is among the highest normalized intensities for  $m/z$  values 415.2 and 455.4 in comparison to the other waiting times. Only for  $m/z$  133.0, the peak areas is among the lowest values for all waiting times. No trends can be seen for the CVs of the different  $m/z$  values. Nevertheless, the CVs of the different  $m/z$  values is the lowest for 0.1 s for 6 of the 9  $m/z$  values.  $m/z$  133.0 shows a larger variation between measurement points even within one measurement than the other  $m/z$  values. The CVs for a waiting time of 0.1s are in the acceptable range (<20 %) for all  $m/z$  values except 133.0 and 301.0. In addition, for the absolute intensities of all the  $m/z$  values except 133.0, the waiting time of 0.1 s resulted in the highest intensity with an almost twofold increase for 0.1 s in comparison to the other waiting times (data not shown).

To conclude, the optimal waiting time between the laser shot and the sample movement is 0.1 s, as this allows for fast acquisition speeds and results in both a high signal intensity without disturbance of the smoke before aspiration.

### 6.4.2 Alignment between the laser trigger and raw TIC chromatogram

Alignment between the laser shots and the measurement points is important for the conversion of the data for 3D visualization, as only with the correct alignment between the 3D coordinates with the correct peak in the TIC chromatogram is the visualization representative of the sample surface. The registration of an analog signal together with a TIC chromatogram was used to achieve this. In the analog signal, peaks are recorded that corresponds to the trigger given to the CO<sub>2</sub> laser to fire per measurement point. In case a measurement point gives no signal, the misalignment between measurement points and coordinates can be prevented by using the alignment between the analog signal and the TIC chromatogram. Another

## Automated 3D sampling and imaging of uneven sample surfaces with LA-REIMS

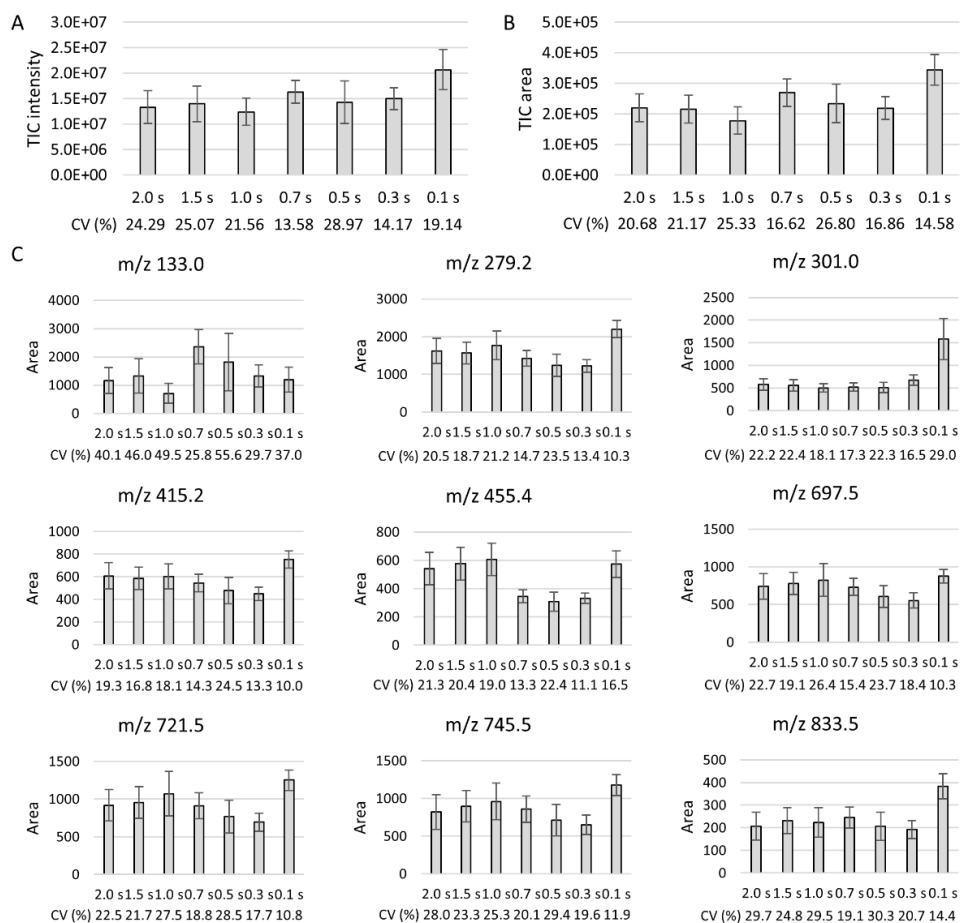


**Figure 6.5:** Comparison of waiting times between laser shot and sample movement. Comparison of signal intensity between seven different waiting times between the laser shot and the sample movement, namely 2.0 s, 1.5 s, 1.0 s, 0.7 s, 0.5 s, 0.3 s, and 0.1 s. **A** The average of the peak TIC values in the chromatogram per measurement point with the standard deviation. In addition, the coefficient of variation (CV) is provided as a percentage in the table underneath. **B** The average of the areas under the TIC peaks in the chromatogram determined with integration. Average with the standard deviation as well as the CV (%) are provided. **C** The average of the areas under the extracted ion chromatogram peaks for nine selected  $m/z$  values. The  $m/z$  values were selected based on their specificity for the sample and to cover the measured mass range as much as possible. For each  $m/z$  value, the average area with standard deviation and the CV (%) are provided.

added value is ensuring that no measurement points are missed during longer periods of only background signal in case the acquisition times vary between measurement points, despite the snake pattern that is implemented.

An example of the overlay between the analog signal and the TIC chromatogram can be seen in Figure 6.2A. The overlay shows that the TIC peak is recorded slightly after the peak in the analog signal representing the laser trigger. This can be explained by the time required for the smoke to be aspirated to the mass spectrometer. Each of the TIC peaks fits nicely between two peaks of the analog signal. Nevertheless, over time an increasing shift occurs between the analog signal and the TIC chromatogram (see Figure 6.2B). A comparison between the overlays of the start and the end of the measurement shows that the delay between the laser trigger and the TIC peak is increased. A possible explanation can be the difference in the registration of both signals, as the analog signal is acquired using an eSAT/IN module and TIC chromatogram is acquired by the mass spectrometer. Therefore, the maximum number of measurement points that can be acquired using this approach will be around 350 points (or half an hour acquisition time for the mass spectrometer) to prevent the falling edge of the TIC peak from occurring after the analog peak of the next measurement point.

### 6.4.3 Speed of the whole process of the 3D MS Scanner

The whole process of the 3D MS Scanner consists of multiple steps, namely homing the axes, performing the height scan, and performing the mass spectrometry measurement (see 6.3 Materials and methods). Each of the steps has been optimized to ensure the whole process is as quickly as possible. In general, the performance of the three stepper motors of the translational axes and the rotary driver of the rotational axis were optimized in terms of acceleration, deceleration, and maintaining position. The height scan consists of two phases: 1) a quick scan of the surface and a spline is fitted through the points, and 2) optimization of the motor positions at each measurement point. In the first step, twice as many points as the number of measurement points are quickly scanned to determine the distance for each of these points without the use of the rotational axis. A spline is fitted through these points to calculate the coordinates of each measurement and to correct for any inaccuracies or unexpected height differences. Based on these points, the motor positions are optimized for each measurement point by determining the distance for each point by movement to these points with the application of the rotational axis. After the height scan, the user can check the obtained topography for any unexpected height differences or other potential issues before the mass spectrometry analysis. For the mass spectrometry measurement, two different aspects define the speed of the measurement, namely how fast the sample can be moved to the next measurement point and how fast the mass spectrometry acquisition is performed. To reduce the required time to move to the next measurement point a snake pattern was implemented and the

performance of all motors was optimized (as indicated before). For the mass spectrometry acquisition, the limiting factor is the aspiration of the created smoke to the mass spectrometer, as this will always take a few seconds. In relation, the peak created in the TIC chromatogram is always a few seconds wide, as not all the molecules in the smoke are aspirated at the same speed. The smoke arrives more quickly at the mass spectrometer and the peaks in the TIC chromatogram are smaller by using small tubing for the aspiration than in comparison to the broader tubing. The measurement time required per point is 4 s when allowing the system to go back to the baseline background intensity after a measurement peak, but can be shorter when allowing overlap between measurement peaks in the TIC chromatogram.

The homing of the axes for alignment takes less than one minute, the topographical scan of the sample surface takes 5.1 s per measurement point, and the MS data acquisition using LA-REIMS takes 5.0 s per measurement point after optimization. Three hundred measurement points can be acquired within 1 h taking into account the whole process. The sample positions are defined based on the topography of the surface such that there is a constant distance and angle between the sample surface and the laser probe. The spatial resolution is constant in the top view with a distance of 2 mm between measurement points, which is difficult to achieve with manual analysis. The 3D MS scanner allows for the analysis of 3D sample surfaces in an automated and fast way with LA-REIMS.

### 6.4.4 Comparison between manual and automated measurements

The CVs were calculated as a representation of the reproducibility between measurement points. The reproducibilities of automated acquisitions were compared with the reproducibilities of manual acquisitions for different sample types. Three of the seven CVs were significantly lower for the automated setup using the 3D MS scanner in comparison to the manual setup looking at the TIC peak intensity values (see Table 6.2). In addition, the CVs for the TIC peak intensity for the manual setup for femoral heads 3 and 5 are lower than the CVs of the automated setup, but the CVs are not significantly different. The CVs for TIC peak area values (see Table 6.3) are lower for the automated setup than the manual setup with significant differences in the CVs for five samples. The results of the TIC peak intensities and TIC peak areas show the same trend, with lower CVs for the automated setup. These lower CVs for the TIC peak intensity and TIC peak area show the improved signal reproducibility between measurement points for the automated setup compared to the manual setup. This is further emphasized by the CVs for the selected  $m/z$  values, most of the CVs are lower or similar for the

automated setup in comparison to the manual setup (see Table 6.4). The variation between the measurement points for the whole mass range ( $m/z$  100-1500) for both setups can be assessed using PCA plots (see Figure 6.6). These plots display a smaller or similar variation between the measurement points of the automated setup than between those of the manual setup.

**Table 6.2:** Comparison of TIC peak intensities between automated and manual measurements. Comparison of the absolute maximum TIC peak values in the chromatogram per measurement point between automated and manual measurements for the different samples; apple, marrowbone, and five femoral heads. The average maximum TIC peak intensity value is given with the standard deviation as well as the coefficient of variance (CV) as a percentage. In addition, the result of the coefficient of variance test is provided, indicating if the CVs are significantly different ( $p < 0.05$ ).

	TIC peak intensity				P-value
	Automated		Manual		
	Average $\pm$ SD	CV (%)	Average $\pm$ SD	CV (%)	
<b>Apple</b>	5.97E7 $\pm$ 1.08E7	18.13	7.99E7 $\pm$ 1.47E7	18.46	0.9026
<b>Marrowbone</b>	1.27E8 $\pm$ 2.66E7	20.90	6.09E7 $\pm$ 2.76E7	45.31	<0.0001
<b>Femoral head 1</b>	1.25E8 $\pm$ 3.24E7	25.88	7.49E7 $\pm$ 2.70E7	36.08	0.0347
<b>Femoral head 2</b>	2.10E8 $\pm$ 3.25E7	15.48	1.02E8 $\pm$ 3.79E7	37.23	<0.0001
<b>Femoral head 3</b>	1.46E8 $\pm$ 3.51E7	23.98	1.19E8 $\pm$ 2.14E7	18.03	0.0577
<b>Femoral head 4</b>	2.04E8 $\pm$ 3.57E7	17.46	1.57E8 $\pm$ 3.35E7	21.41	0.1691
<b>Femoral head 5</b>	1.53E8 $\pm$ 3.21E7	20.99	1.23E8 $\pm$ 2.42E7	19.79	0.6916

**Table 6.3:** Comparison of TIC peak areas between automated and manual measurements. Comparison of the areas under the TIC peaks in the chromatogram per measurement point between automated and manual measurements for the different samples; apple, marrowbone, and five femoral heads. The areas are determined with integration of the TIC peaks. The average TIC peak area value is given with the standard deviation as well as the coefficient of variance (CV) as a percentage. In addition, the result of the coefficient of variance test is provided, indicating if the CVs are significantly different ( $p < 0.05$ ).

	TIC peak area				P-value
	Automated		Manual		
	Average $\pm$ SD	CV (%)	Average $\pm$ SD	CV (%)	
<b>Apple</b>	1.39E6 $\pm$ 1.42E5	10.17	1.45E6 $\pm$ 2.31E5	15.94	0.0024
<b>Marrowbone</b>	3.29E6 $\pm$ 3.20E5	9.73	1.35E6 $\pm$ 5.60E5	41.48	<0.0001
<b>Femoral head 1</b>	3.66E6 $\pm$ 7.23E5	19.74	1.52E6 $\pm$ 5.08E5	33.49	0.0007
<b>Femoral head 2</b>	5.83E6 $\pm$ 4.37E5	7.49	2.64E6 $\pm$ 1.13E6	42.70	<0.0001
<b>Femoral head 3</b>	4.29E6 $\pm$ 6.55E5	15.25	2.47E6 $\pm$ 4.22E5	17.05	0.4464
<b>Femoral head 4</b>	4.82E6 $\pm$ 4.57E5	9.48	4.39E6 $\pm$ 7.48E5	17.03	0.0001
<b>Femoral head 5</b>	4.00E6 $\pm$ 4.67E5	11.68	2.74E6 $\pm$ 6.09E5	22.24	<0.0001

**Table 6.4:** Comparison of selected  $m/z$  values between automated and manual experiments. For the different samples, apple, marrowbone, and five femoral heads, a comparison of signal intensity is provided between automated and manual experiments. This comparison is based on the average of the areas under the extracted ion chromatogram peaks with the standard deviation (SD) for 10 selected  $m/z$  values as well as the coefficient of variance (CV, %). The  $m/z$  values were selected based on their specificity for the sample and to cover the measured mass range as much as possible.

Apple						
$m/z$	Automated measurements			Manual measurements		
	Average	SD	CV	Average	SD	CV
147.0	89800	48091	53.55	70643	18123	25.65
279.2	309842	57597	18.59	444828	89840	20.20
301.0	828577	156155	18.85	1016699	214975	21.14
415.2	85173	14814	17.39	118220	25323	21.42
455.4	24671	4793	19.43	37554	7702	20.51
671.5	26194	5123	19.56	41958	10998	26.21
721.5	189082	35126	18.58	293713	64804	22.06
745.5	226378	41144	18.17	308987	69024	22.34
833.5	91428	17535	19.18	118533	29316	24.73
861.6	64850	13086	20.18	78707	20898	26.55

Marrowbone						
$m/z$	Automated measurements			Manual measurements		
	Average	SD	CV	Average	SD	CV
140.0	25279	11082	43.84	6666	5270	79.07
185.0	12057	3366	27.92	2619	1605	61.29
221.9	8901	1933	21.72	738	630	85.32
237.9	10202	3118	30.57	731	639	87.48
362.2	633	954	150.84	252	376	149.38
585.5	402	1087	270.06	488	1585	324.85
744.6	182	274	150.58	98	211	216.37
867.7	285	369	129.41	108	152	141.33
893.7	1026	1615	157.42	336	579	172.05
921.8	513	691	134.81	177	244	137.97

**Table 6.4 (continued):** Comparison of selected  $m/z$  values between automated and manual experiments.

<u>Femoral head 1</u>						
$m/z$	Automated measurements			Manual measurements		
	Average	SD	CV	Average	SD	CV
128.0	3040	1281	42.15	1283	725	56.49
189.9	553	776	140.16	113	373	329.49
281.2	71	28	39.04	1721	2193	127.42
303.2	1244	1217	97.83	633	809	127.89
559.5	1929	2053	106.45	186	465	250.60
642.5	853	226	26.52	625	286	45.76
687.5	1477	629	42.63	1170	695	59.45
744.5	913	434	47.60	563	263	46.73
893.7	486	313	64.54	124	76	61.56
1008.7	291	62	21.38	194	81	41.81

<u>Femoral head 2</u>						
$m/z$	Automated measurements			Manual measurements		
	Average	SD	CV	Average	SD	CV
128.0	2513	431	17.15	1048	567	54.15
189.9	563	570	101.26	46	77	167.15
281.2	19100	17277	90.46	1429	843	59.01
303.2	1119	622	55.57	691	344	49.84
572.5	1404	1018	72.52	1003	406	40.46
642.5	773	839	108.56	45	15	32.45
687.5	2155	3157	146.52	1744	921	52.79
744.5	831	600	72.23	689	346	50.23
893.7	1283	764	59.57	632	393	62.22
919.7	1001	602	60.13	514	325	63.11

<u>Femoral head 3</u>						
$m/z$	Automated measurements			Manual measurements		
	Average	SD	CV	Average	SD	CV
128.0	1576	446	28.29	803	273	33.94
186.0	332	74	22.41	113	68	60.43
281.3	13638	8251	60.50	1823	2025	111.04
303.2	651	260	39.97	450	416	92.45
572.5	2302	2281	99.06	2389	2233	93.46
642.5	1518	1450	95.52	1524	1649	108.19
687.6	4002	4383	109.54	4310	5100	118.33
797.7	682	592	86.72	672	663	98.55
893.7	744	344	46.17	217	136	62.57
919.8	576	243	42.12	184	120	65.08

**Table 6.4 (continued):** Comparison of selected  $m/z$  values between automated and manual experiments.

Femoral head 4						
$m/z$	Automated measurements			Manual measurements		
	Average	SD	CV	Average	SD	CV
128.0	2918	519	17.77	2423	734	30.30
189.9	247	130	52.75	103	63	61.06
281.3	18190	14891	81.86	11872	8208	69.14
303.2	611	213	34.90	537	172	32.10
572.5	1103	437	39.60	939	409	43.53
642.5	355	102	28.75	339	127	37.45
687.6	650	302	46.56	622	226	36.29
744.6	324	109	33.81	316	150	47.53
893.8	1024	458	44.71	684	515	75.20
919.8	894	392	43.84	600	418	69.64

Femoral head 5						
$m/z$	Automated measurements			Manual measurements		
	Average	SD	CV	Average	SD	CV
128.0	2866	750	26.17	1450	677	46.68
166.1	1586	292	18.40	911	283	31.05
281.2	14087	12702	90.16	6293	6373	101.27
303.2	1067	613	57.47	570	277	48.62
572.5	2085	528	25.32	1691	476	28.18
642.5	893	230	25.69	700	161	23.03
687.5	2189	617	28.19	1870	504	26.96
744.6	788	353	44.82	542	233	43.03
893.7	1277	672	52.67	503	356	70.80
919.8	865	452	52.25	361	251	69.61

#### 6.4.5 3D visualization of molecular distributions on sample surfaces

An advantage of data acquisition automation with LA-REIMS is the possibility of combining the mass spectra for each measurement point with the coordinates of that point. This allows the study of the molecular distributions of sample surfaces using LA-REIMS.

Comparison of the before (Figures 6.7A and 6.8A) and after (Figures 6.7B, 6.8B, and 6.9A) images shows regularly spaced patterns of the laser burning spots created during the acquisition. Optical differences in the laser burning spots are assumed to be related to the structural differences of the sample surface for all three samples. It was possible to select  $m/z$  values with different molecular distributions

## Chapter 6

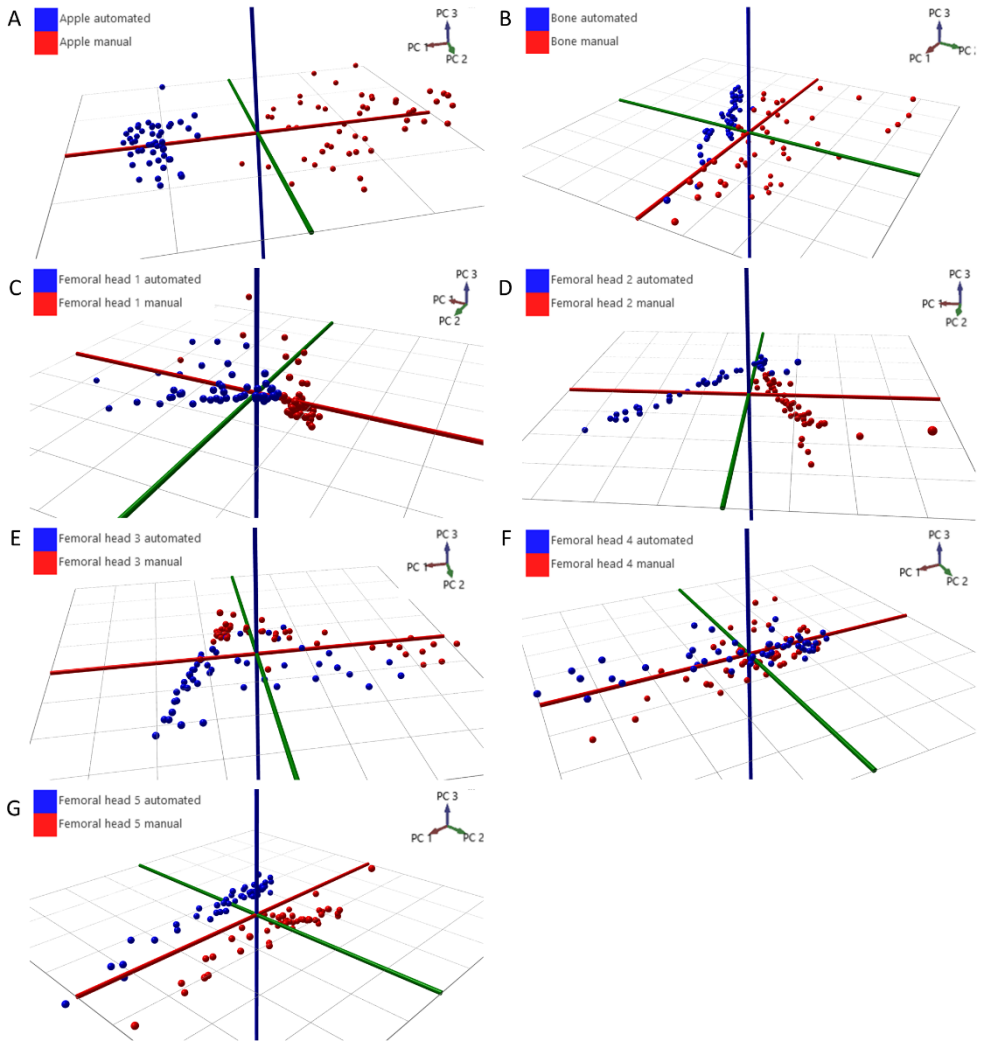


**Figure 6.6:** PCA plots displaying the variation in the automated and manual acquisitions. Principle component analysis (PCA) plots of the automated and manual acquisitions for the different samples, which display the variation between measurement points. These PCA plots can be related to the variation between measurement points, as the closer the different measurement points (represented by spheres) are together the lower the variance in between them and vice versa. **A** PCA plot for the apple acquisitions with PC1, PC2, and PC3 explaining 75.3%, 8.96%, and 2.94% of the variance, respectively. **B** PCA plot for the bone acquisitions with PC1, PC2, and PC3 explaining 49.26%, 28.57%, and 9.53% of the variance, respectively. **C** PCA plot for the femoral head 1 acquisitions with PC1, PC2, and PC3 explaining 58.07%, 20.67%, and 5.22% of the variance, respectively. **D** PCA plot for the femoral head 2 acquisitions with PC1, PC2, and PC3 explaining 55.10%, 26.24%, and 4.40%

**Figure 6.6 (legend continued):** of the variance, respectively. **E** PCA plot for the femoral head 3 acquisitions with PC1, PC2, and PC3 explaining 65.65%, 23.86%, and 1.64% of the variance, respectively. **F** PCA plot for the femoral head 4 acquisitions with PC1, PC2, and PC3 explaining 74.96%, 7.63%, and 3.86% of the variance, respectively. **G** PCA plot for the femoral head 5 acquisitions with PC1, PC2, and PC3 explaining 63.17%, 19.64%, and 4.14% of the variance, respectively.

that were related to structural differences visible by eye for each measurement. In addition,  $m/z$  values could be selected that showed molecular distributions that were related to structural differences not visible by eye. For the apple,  $m/z$  455.4 has a higher intensity in the peel of the apple,  $m/z$  671.5 has a higher intensity in the spots visible in the part without the peel and a bit higher intensity in the peel, and  $m/z$  846.6 has a higher intensity in the parts without the peel (see Figure 6.7C). For the outside of a marrowbone, for example,  $m/z$  393.3 seems to be related to the whiter part of the marrowbone with the highest intensities where the white tissue seems to be the thickest,  $m/z$  419.2 seems to be related to the nonwhite parts of the surface, and  $m/z$  717.5 seems to be related to the remaining muscle tissue at the edges of the measurement area (see Figure 6.8C). For the human femoral head, different structures can be seen, including a white/soft pink part at the right of Figure 6.9A that is the formation of bony tissue due to sclerosis, yellowish tissue in the middle of the image that is a small piece of cartilage, and red tissue toward the stem of the femoral head on the left of the image. For example,  $m/z$  205.9 seems to be more related to the red tissue on the femoral head,  $m/z$  744.5 seems to be related to part of the white, and  $m/z$  1080.9 seems to be related to the more yellow tissue and a bit of the red tissue (see Figure 6.9B).

## 6.5 Discussion

### 6.5.1 Development and optimization of the 3D MS Scanner

The 3D MS scanner was developed to analyze sample surfaces in 3D using LA-REIMS. Each of the three phases in the acquisition was optimized, and the acquisition rate of the 3D MS scanner is 300 points in approximately 1 h, corresponding to 22.04 cm<sup>2</sup> with a spatial resolution of 2 mm. After homing of the axes, the topographical scan and MS acquisition take 5.1 and 5.0 s per measurement point, respectively. This is faster than the surface sampling setups developed by Bennett *et al.* and Li *et al.*, which were on the order of minutes per measurement point.<sup>261,262</sup> The acquisition time for the 3D MS scanner is slower than the one reported by Ogrinc *et al.*, which was approximately 0.6 s per measurement point with optimized parameters and simultaneous collection of topographical and

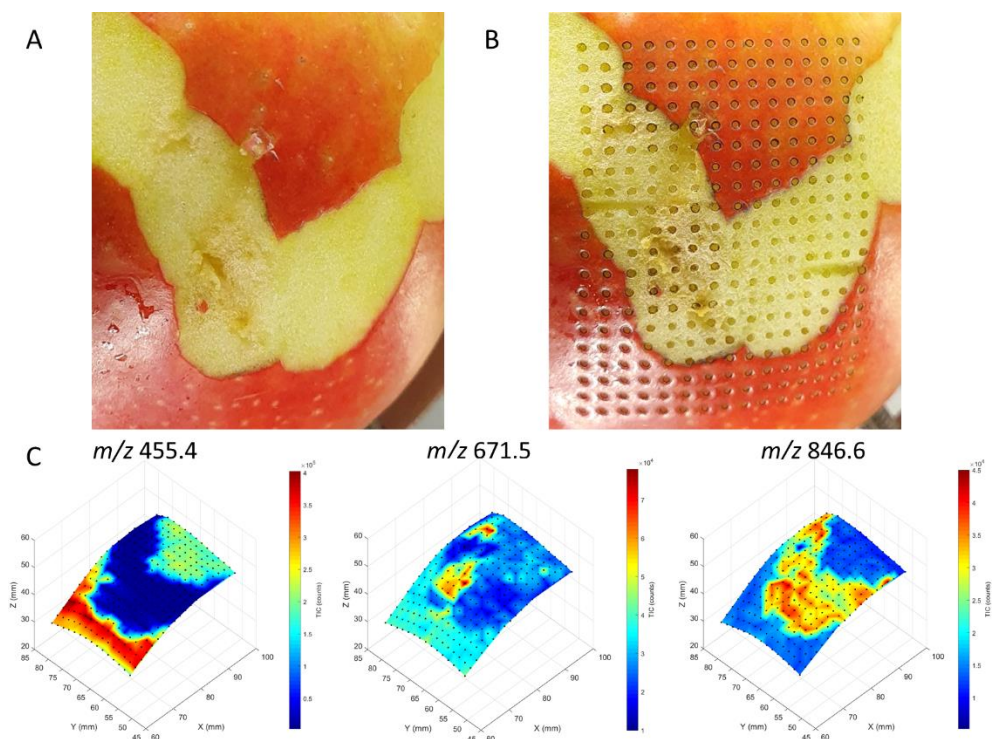


**Figure 6.7:** 3D visualization of molecular distributions obtained from an apple with the 3D MS scanner. **A** Apple before analysis with LA-REIMS using the 3D MS scanner. Parts of the peel have been removed to show different molecular patterns can be created. **B** Apple after analysis with LA-REIMS using the 3D MS scanner. The total number of measurement points acquired was 300 with a spatial resolution of 2 mm, thus covering an area of  $28 \times 38$  mm ( $15 \times 20$  measurement points). **C** 3D visualization of the molecular distributions (absolute intensities) of the imaging experiment on an apple. Three  $m/z$  values were selected based on their different distributions: 455.4, 671.5, and 846.6. Tentative identifications of the  $m/z$  values can be found in Table 6.5.

**Table 6.5:** Tentative assignments of  $m/z$  values of 3D visualization of molecular distributions of apple (Figure 6.7). Identifications are based on MS/MS in combination with the  $m/z$  value. For each identification, the experimental  $m/z$  value, the assignment, the detected ion, the ppm error, and level of identification are provided.

$m/z$	Assignment	Ion	ppm error	Level of identification
455.352	Ursolic acid	$[M-H]^-$	-2.41	MS
671.467	PA 16:0_18:2	$[M-H]^-$	1.89	MS/MS
846.552	PS 36:2	$[M+CH_3COO]^-$	2.13	MS

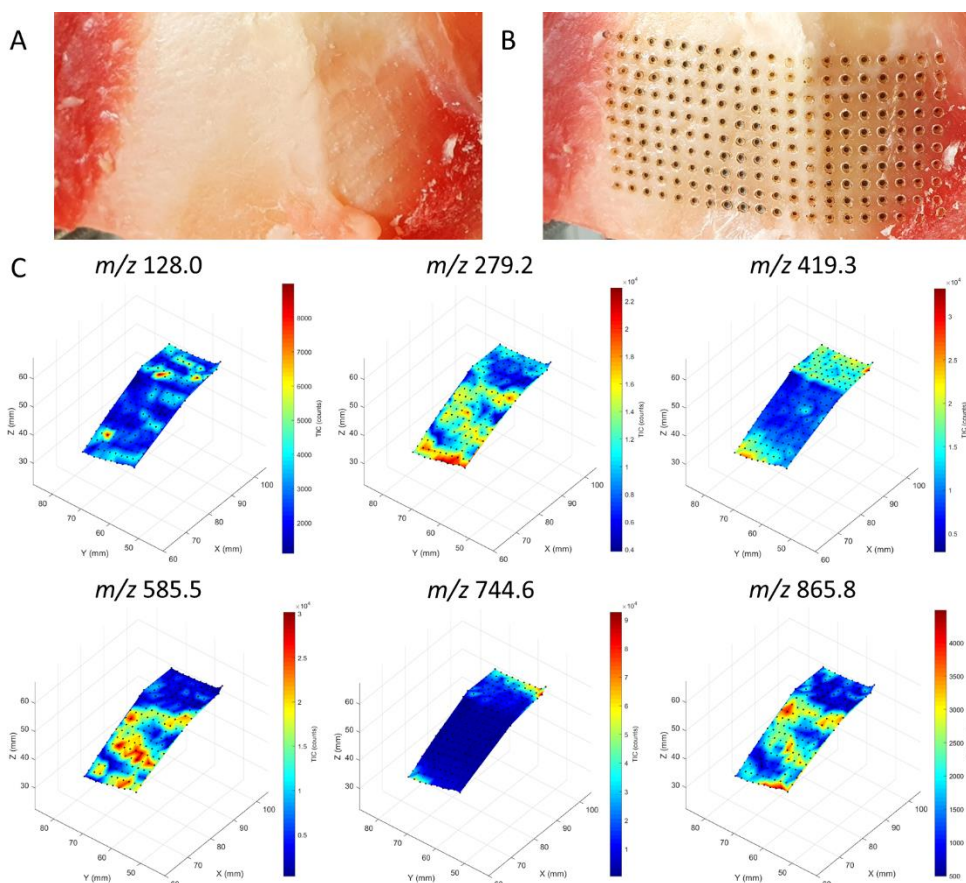


**Figure 6.8:** 3D visualization of molecular distributions obtained from the outside of a marrowbone with the 3D MS scanner. **A** Outside of a marrowbone before analysis with LA-REIMS using the 3D MS scanner. **B** Outside of the marrowbone after analysis with LA-REIMS using the 3D MS scanner. The total number of measurement points acquired was 200 with a spatial resolution of 2 mm, thus covering an area of 18 × 38 mm (10 × 20 measurement points). **C** 3D visualization of the molecular distributions (absolute intensities) of the imaging experiment on the outside of a marrowbone. Six  $m/z$  values were selected based on their different distributions: 128.0, 279.2, 419.3, 585.5, 744.6, and 865.8. Tentative identifications of the  $m/z$  values can be found in Table 6.6.

MS imaging data.<sup>273</sup> One of the reasons for the slower acquisition with the 3D MS scanner is the consecutive acquisition of the topographical scan and the MS measurement. Simultaneous collection is not possible with the 3D MS scanner due to the distance between the laser probe and laser point distance sensor. A risk in slower acquisitions could be molecular degradation of the biological samples, but

**Table 6.6:** Tentative assignments of  $m/z$  values of 3D visualization of molecular distributions of marrowbone (Figure 6.8). Identifications are based on MS/MS in combination with the  $m/z$  value. For each identification, the experimental  $m/z$  value, the assignment, the detected ion, the ppm error, and level of identification are provided.

$m/z$	Assignment	Ion	ppm error	Level of identification
128.035	C <sub>5</sub> H <sub>7</sub> NO <sub>3</sub>	[M-H] <sup>-</sup>	-2.34	MS
279.233	FA 18:2	[M-H] <sup>-</sup>	-3.58	MS
419.255	cLPA 18:0	[M-H] <sup>-</sup>	-4.29	MS/MS
585.486	DG O-35:5	[M-H] <sup>-</sup>	-4.84	MS
744.557	PE 36:1	[M-H] <sup>-</sup>	2.82	MS
865.753	TG 48:0	[M-H] <sup>-</sup>	3.24	MS

this is expected to be minimal within 1 h. However, molecular degradation should be taken into consideration for the acquisition of larger surfaces, which will have longer acquisition times.

The 3D MS scanner was developed to keep the distance and angle between the laser probe and sample surface consistent. With the implemented four degrees of freedom (three translational axes and one rotational axis) curvatures along the y-axis are fully compensated. Curvatures along the x- and z-axis cannot be fully compensated with these four degrees of freedom, as this would require additional degrees of freedom in the x- and z-axes. An angle of 10° along one of these axes will result in a decrease of only 3% in the laser fluency per measurement point, which is expected to not have a significant effect on the signal intensity in this setup due to the use of a CO<sub>2</sub> laser. Bennett *et al.*, Li *et al.*, and Ogrinc *et al.* used a robotic arm with six degrees of freedom for sampling of the surface.<sup>261,262,273</sup> Six degrees of freedom will allow for better compensation of the surface topography along all axes. Our in-house built setup with four degrees of freedom can still compensate for most topographical height variations, although the possibilities are more limited than for a robotic arm.

Another difference between the 3D MS scanner and previously published setups using robotic arms is the movement of the sample underneath the laser probe for the 3D MS scanner, while in previously published setups the sample lays still. The needle probe connected to the robotic arm needed to move from the sampling surface to DART ion source or the OPSI in the setup of Bennett *et al.* and Li *et al.*, respectively.<sup>261,262</sup> The SpiderMass probe was connected to the robotic arm together with the transfer line to the mass spectrometer for the robot-assisted SpiderMass setup.<sup>273</sup> The laser probe is moved relative to the sample in the setup

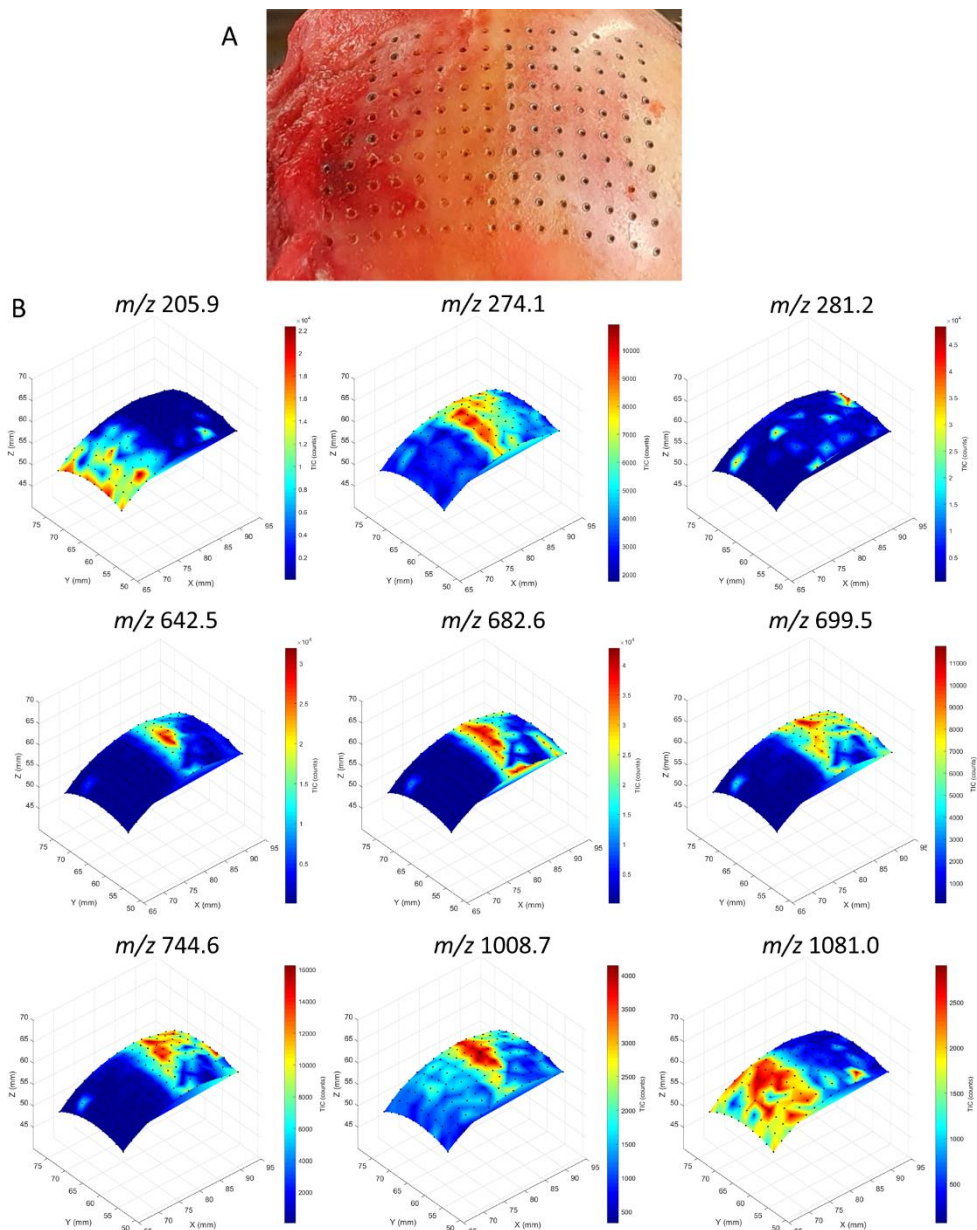


**Figure 6.9:** 3D visualization of molecular distributions obtained from part of a human femoral head with the 3D MS scanner. **A** Outside of a human femoral head after analysis with LA-REIMS using the 3D MS scanner. The total number of measurement points acquired was 150 with a spatial resolution of 2 mm, thus covering an area of  $18 \times 28$  mm ( $10 \times 15$  measurement points). **B** 3D visualization of the molecular distributions (absolute intensities) of the imaging experiment on the outside of a human femoral head. Nine  $m/z$

**Figure 6.9 (legend continued):** values were selected based on their different distributions: 205.9, 274.1, 281.2, 642.5, 682.6, 699.5, 744.6, 1008.7, and 1081.0. Tentative identifications of the  $m/z$  values can be found in Table 6.7.

**Table 6.7:** Tentative assignments of  $m/z$  values of 3D visualization of molecular distributions of femoral head (Figure 6.9). Identifications are based on MS/MS in combination with the  $m/z$  value. For each identification, the experimental  $m/z$  value, the assignment, the detected ion, the ppm error, and level of identification are provided. The data of the femoral head acquisition was recalibrated in mMass.

$m/z$	Assignment	Ion	ppm error	Level of identification
205.899	-			
274.119	C <sub>14</sub> H <sub>17</sub> N <sub>3</sub> O <sub>3</sub>	[M-H] <sup>-</sup>	-2.55	MS
281.248	FA 18:1	[M-H] <sup>-</sup>	-2.13	MS/MS
642.488	CerP 36:2;O2	[M-H] <sup>-</sup>	1.87	MS
682.591	Cer 42:2;O2	[M+Cl] <sup>-</sup>	-0.15	MS
699.498	PA 36:2	[M-H] <sup>-</sup>	1.43	MS
744.554	PE 36:1	[M-H] <sup>-</sup>	-1.21	MS
1008.684	Hex3Cer 34:0;O	[M-H] <sup>-</sup>	-1.98	MS
1081.011	-			

of Ogrinc *et al.*, as they aimed to develop a system that could potentially be used *in vivo* during surgeries in the future.<sup>273</sup> Our main consideration for a setup where the sample moves underneath the laser was safety, as the system is equipped with a Class IV CO<sub>2</sub> laser. Another reason for this setup of the 3D MS scanner is the focus on improved understanding of molecular distributions on sample surfaces with large height variations.

### 6.5.2 Comparison between manual and automated setup

Comparison between the manual and automated setups showed that the acquisition with the automated setup has a higher signal reproducibility between measurement points than with the manual setup. This was shown by the lower CVs for the TIC peak maximum intensities and areas for most of the automated acquisition than for the manual acquisitions (Tables 6.2 and 6.3), which is according to expectations. The lower CVs for the automated setup are caused by the higher reproducibility of the tissue ablation by the CO<sub>2</sub> laser due to the constant distance between the laser probe and the sample surface with the 3D MS scanner. In addition, the laser probe is placed as perpendicular to the sample surface as possible. Both considerations are more difficult to achieve with manual acquisitions, especially due to small movements of the laser probe holder caused by the air-powered breaks in the manual setup.

The reported CVs for the manual and automated setups are slightly higher than previously reported by Genangeli *et al.* for the CO<sub>2</sub> laser, especially for the manual setup.<sup>38</sup> Direct comparison between the CVs of both studies is complicated by the differences between the studies, which contribute to the CVs. In this study, more heterogeneous samples, especially the femoral heads, more measurement points per experiment, and different sizes of acquisition areas were used in comparison to the work of Genangeli *et al.* The CVs for the automated and manual setups were based on 50 measurement points, which covers a larger area than the 10 points acquired by Genangeli *et al.* Therefore, part of the higher CVs might be explained by small differences in the molecular composition and tissue ablation across the area. Another factor contributing to the high CVs can be LA-REIMS, although the whole setup is not changed during acquisitions. LA-REIMS is based on the analysis of the aspirated smoke created by laser ablation. The aspiration of the smoke might be different between measurement points, resulting in variations in the TIC peak intensities and TIC peak areas contributing to higher CVs. In addition, the surface sample will affect the aspiration of the smoke, as the topography of the surface will influence the flow of the smoke. For example, it has been observed that the aspiration of the smoke can be affected for samples with large height variations.

The TIC peak intensities and TIC peak area values were 8.82-58.94 % lower for the manual setup than for the automated setup, except for the apple acquisitions. A contributing factor to this might be the different positions of the sample in the biosafety cabinet in both setups. Changes in the aspiration of the smoke were observed based on sample position due to the airflow inside the biosafety cabinet. It is more difficult to keep the same distance between the sample and laser probe as well as the orientation of the laser probe compared to the sample with the manual setup, which can affect the aspiration of the smoke. Decreasing signal intensities with increasing distance between the sample surface and laser probe were shown for the automated setup (see Figure 6.4). Therefore, a larger distance between the sample surface and laser probe with the manual setup can contribute to the lower signal intensities.

The manual and automated setup both have their advantages. The manual setup is preferred if only a few measurements points, for example, for MS/MS data, need to be acquired, as no homing of the axis and topographical scan needs to be performed, making the manual acquisition faster than the automated one. Besides the higher signal reproducibility, one of the advantages of the automated setup is the larger area of the sample that is available for analysis. For the manual measurements, the sample is placed on a flat surface or could be placed in a clamp.

The fixed position of the sample in the manual setup limits the area available for data acquisition, which is not the case for the automated setup. The sample is fixated in the sample holder by tightening the screws for the automated measurements. The sample can be orientated and moved in such a way that the area of interest can be placed underneath the laser probe in the automated setup. The only limitation is that the screws should not be tightened at a position that might be of interest in later acquisitions. Another advantage of the automated acquisition is the automated movement to the next measurement point while maintaining a constant distance between the different measurement points, which prevents any overlap between the laser burning spots of different measurements points. Some overlap between the measurement points for the manual setup occurs sometimes due to the small movements of the holder due to the air-powered breaks. Therefore, the accuracy of the sampling position is higher for the automated setup due to the predefined sampling grit in comparison to the manual setup.

### 6.5.3 Comparison of 3D visualization between the 3D MS Scanner and similar technologies

3D visualization of molecular distributions in Figures 6.7, 6.8, and 6.9 demonstrates that different  $m/z$  values could be selected that represented molecular distributions related to visible structural differences, but also distributions that were not related to visible structural differences. The spaces between the laser burning spots were equal for the three different analyzed sample types when looking from the top view, but differences between laser burning spots were seen based on structural differences in the surface. Recently, Ogrinc *et al.* have shown that their robot-assisted SpiderMass setup allows for the visualization of 3D molecular distributions on different samples.<sup>273</sup> The robot-assisted Spider-Mass setup has not been applied to human bone and joints, like the human femoral heads used in this study. The SpiderMass is mini-invasive,<sup>273</sup> while the CO<sub>2</sub> laser leaves clear burning spots, due to the different equipped laser types. This is a result of differences in interaction between the biological tissue and the laser wavelength as well as different laser energies.

All the acquisitions with the 3D MS scanner were acquired with a spatial resolution of 2 mm. This is larger than the spatial resolution reported by Ogrinc *et al.*, which was 500  $\mu\text{m}$  without oversampling.<sup>273</sup> One of the factors that will limit the spatial resolution is the diameter of the laser focus point. The diameter of the focus point of a CO<sub>2</sub> laser is larger than the Nd:YAG laser used in the SpiderMass setup. Therefore, a spatial resolution of 500  $\mu\text{m}$  cannot be reached with a CO<sub>2</sub> laser

without major overlap between laser burning spots. It is noteworthy that the spatial resolution of the 3D MS scanner could be reduced to the size of the laser focus point, which is approximately 1 mm in this setup.

#### 6.5.4 Future applications

The 3D visualizations created from the data acquired with the 3D MS scanner allow for observing and correlating changes in molecular intensity to locations on the sample surface and, therefore, structural differences. The 3D correlative images can, for example, be used to study the different molecules present in the different tissue types of a femoral head and the transitions areas between them (see Figure 6.9). This can increase the molecular understanding of the processes underlying the structural changes in, for example, osteoarthritis of the femoral head. Large areas consisting of different tissue types should be acquired of a large cohort of femoral heads to achieve this. Furthermore, this molecular information on a large cohort of samples can be used to improve models build for clinical applications. Another potential application of the 3D molecular visualizations is to determine the optimal sampling spot for tissue classification for *in vivo* applications of LA-REIMS. On the basis of the molecular distributions, the most informative region for tissue classification can be determined, which can be specifically targeted during *in vivo* applications. This will reduce the amount of tissue damage created by the CO<sub>2</sub> laser as fewer sampling points will be required.

In addition to this specific potential clinical application for femoral heads, the 3D MS scanner has the potential to be used in a wide range of biomedical applications either as is or with small adjustments, for example, to the sample holder. Any type of sample could potentially be placed in the 3D MS scanner if it can be ablated with a CO<sub>2</sub> laser, although caution is advised to prevent contamination of the mass spectrometer. Adjustments could be made to include other types of ambient sampling probes that could be triggered in a similar way to also enable analysis of samples that cannot be ablated with a CO<sub>2</sub> laser. Two of the biggest advantages of this 3D MSI setup are the lack of sample preparation and the ambient conditions. Sectioning of the sample is commonly needed for 2D MSI techniques, which is not possible for all sample types or can be difficult to achieve. Furthermore, some samples are too large to fit on a microscope slide, which would not be an issue with the 3D MS scanner combined with LA-REIMS. In addition, the ambient conditions can allow for the analysis of samples that cannot withstand the vacuum used in, for example, MALDI-MSI. The 3D MS scanner could have a broad range of 3D MSI applications, for example, in the food industry as well as biomedical and preclinical applications, as shown in Figures 6.7, 6.8, and 6.9.

## 6.6 Conclusion

This study describes the development of the 3D MS scanner, which allows for the analysis of large and uneven 3D sample surfaces with LA-REIMS under ambient conditions. The 3D MS scanner automates the positioning of the sample underneath the laser probe and keeps the distance between them constant. This automated acquisition results in increased reproducibility of the obtained molecular information on the sample surface when compared to manual acquisitions. In addition, the data acquired with the automated setup can be used for the visualization of molecular distributions on the sample surface in 3D. This application was shown on an apple, a marrowbone, and a human femoral head, which showed distinct molecular distributions that could be related to structural differences. Therefore, the developed 3D MS scanner can be used to improve molecular understanding based on 3D molecular distributions and might have a potential application in determining optimal *in vivo* sampling points to reduce biological tissue damage.





## Chapter 7: General discussion and outlook





The pre-clinical application of different mass spectrometry techniques for the analysis of bone, fracture hematoma, and human femoral heads has been described in this thesis. The different biomedical studies focused on developments contributing to the clinical application of mass spectrometry and their applications in research into traumas to the skeletal system, like bone fractures and articular cartilage damage. In addition, the forensic application of mass spectrometry is briefly touched upon for bone tissue as well as possibilities for food samples analysis with one of the mass spectrometry techniques. This discussion focuses on the use of mass spectrometry as a biomedical and potential (pre)clinical tool in the fields of fracture healing and cartilage repair, also in relation to the impaired healing of these injuries. First, the application of matrix-assisted laser desorption and ionization mass spectrometry imaging (MALDI-MSI) for bone tissue and fracture hematoma will be discussed. The second part focuses on 3D imaging with laser-assisted rapid evaporative ionization mass spectrometry (LA-REIMS). Finally, the translation from the results presented in this thesis towards a (pre)clinical application will be explored by addressing the *ex vivo* application of MALDI-MSI and *ex vivo* and *in vivo* application of LA-REIMS.

## 7.1 Application of MALDI-MSI for bone tissue and fracture hematoma

Despite its growing number of biomedical applications, MALDI-MSI is only used in a limited number of studies for the analysis of undecalcified bone and has not yet been employed for the analysis of fracture hematoma. Methodological developments for the analysis of these tissue types are important to further extend the application field of MALDI-MSI into the research of the skeletal system after trauma as well as skeletal diseases. The possibility to investigate different molecular classes with MALDI-MSI in an untargeted manner offers diagnostic innovations and molecular understanding. The application of MALDI-MSI for bone tissue and fracture hematoma can contribute to improving molecular understanding of, for example, bone fracture healing and non-union development.

### 7.1.1 MALDI-MSI analysis of bone tissue

The methodological developments for the analysis of undecalcified bone tissue with MALDI-MSI and a targeted forensic and untargeted pre-clinical application are described in **Chapter 3**. The most important step in this development was the optimization of the sample preparation with a focus on the embedding and sectioning of the undecalcified bone tissue. The embedding material composition was optimized to contain 20% gelatin and 7.5% carboxymethyl cellulose (CMC) to overcome challenges related to sectioning bone tissue. Bone tissue needs to be

sectioned with a tungsten carbide knife longitudinally to limit the fracturing of bone in the sections. In addition, the sections need to be transferred to a glass slide with the support of double-sided tape to maintain the morphology. The optimized sectioning parameters were a sectioning thickness of 12  $\mu\text{m}$  and temperature of  $-15\text{ }^{\circ}\text{C}$  when using Tesa<sup>®</sup> double-sided tape. This sample preparation protocol was applied to mouse, rat, and human bone samples for the targeted detection of methadone and 2-ethylidene-1,5-dimethyl-3,3-diphenylpyrrolidine (EDDP) and untargeted detection of lipids, as described in **Chapter 3**. The best matrix for the detection of methadone and EDDP was DHB with a limit of detection of approximately 50 pg/spot on bone tissue. The presence of methadone and EDDP was shown in dosed rat and human bone. None of the tested matrices gave the desired lipid desorption and ionization results in negative ion mode. The best matrices for the detection of unknown lipids from bone and bone marrow in positive ion mode were CHCA and DHB.

The sample preparation protocol for lipid analysis with MALDI-MSI from **Chapter 3** was applied in **Chapter 5** in combination with protein analysis with liquid-chromatography tandem mass spectrometry (LC-MS/MS). These MS techniques were deployed to study the effect of citrulline supplementation during bone fracture healing throughout the fracture healing process. The observed lipid profiles were distinct at the different stages of fracture healing in the separation between the citrulline supplement and respective control group. Besides, these profiles were different between bone and bone marrow. Different lipid classes contributed to these separations, including phosphatidylcholines (PCs), lysophosphatidylcholines (LPCs), acyl carnitines (CARs), triacyl/alkylglycerides (TGs), and a sphingomyelin (SM). The protein analysis showed that the more abundant proteins in the citrulline supplement or control group were different throughout the different fracture healing phases. This indicates that the effect of citrulline supplementation is different throughout the different phases. The more abundant proteins per time point per treatment group were used for analysis of the activated pathways. This analysis indicated enhanced fracture healing in the citrulline supplement group in comparison to the control group, although the differences during the bone remodeling phase were less pronounced. Different pathways related to the citrulline-arginine-nitric oxide metabolism were more active in the citrulline supplement group and fracture healing enhancement was induced via improved angiogenesis and earlier soft and hard callus formation.

Despite the early evidence of changes in the ratio of the different phospholipid classes in the callus throughout fracture healing,<sup>213</sup> the knowledge about the role

and importance of lipids during fracture healing is limited and usually described per lipid class. Therefore, the understanding of the role of the lipid changes in the citrulline supplement versus control group observed in **Chapter 5** is limited. PCs play a role in cellular metabolism and energy production and are an essential source of secondary messengers.<sup>137,179,214</sup> For example, PCs are involved in chondrocyte and osteoblast proliferation, differentiation and function as well as osteoclast recruitment.<sup>163,215</sup> LPCs inhibit osteoclast formation, while promoting osteoclast function.<sup>212</sup> The fatty acid chain composition of the PCs and LPCs is of importance for the function, but details are often unknown in case of bone health and fracture healing. TGs are used for energy storage, especially in the bone marrow.<sup>137</sup> This matches with the fact that TGs only contribute to the separation between the citrulline supplement and control group during the bone remodeling phase, as in this phase the energy storage is restored. Different expression of lipids throughout fracture healing as well as between the citrulline supplement and control group can be expected based on the roles of different lipid classes. However, the effect of citrulline supplementation on the role of lipids during fracture healing and their role in bone versus bone marrow cannot be fully explained. Therefore, the role and effect of the different identified lipids for the citrulline supplement and control group should be further explored in future research.

**Chapter 5** also discusses the effect of citrulline supplementation during fracture healing on proteins and associated activated pathways. The comparative analysis of the more abundant proteins between the citrulline supplement and control group at different time points showed, among others, different collagens, fibromodulin, thrombospondin, annexin, and different myosins to be more abundant in of the treatment groups. These different proteins are part of the extracellular matrix (ECM) and affect the osteoblast and osteoclast function, which regulates the bone formation and resorption.<sup>196,217</sup> Annexin and myosins play an important role in osteoblast and osteoclast differentiation and function, respectively.<sup>218-220</sup> The activated pathways in the citrulline supplement and control group were explored using the more abundant proteins. For example, the increased production of nitric oxide was observed for the citrulline supplement group at 3 and 14 days post-operative (DPO) as well as 14 DPO in the control group. The regulation of ornithine decarboxylase is more active in the citrulline supplement group at 14 days DPO. These pathways can directly be related to the citrulline supplementation. Other pathways show activation of various fracture healing-related pathways for both the citrulline supplement and control group with different activations throughout the fracture healing process. An enhancement in fracture healing in the citrulline supplement group can be recognized in comparison

to the control group based on the protein and pathway analysis. The effects of citrulline supplementation on fracture healing are in agreement with previous research.<sup>192,202</sup> Nevertheless, the activation of the different pathways as result of citrulline supplementation should be validated in future research.

The sample preparation for bone tissue is a complex and challenging process due to the different structures.<sup>90,97,130,203,204</sup> Only a limited number of recent studies analyzed undecalcified bone with MALDI-MSI.<sup>90,97,98,130,131,203,204,280</sup> Despite all the optimization steps, the bone still substantially breaks into pieces during sectioning, although this is also depending on the sectioning direction. Sectioning in the longitudinal direction of the bone reduces bone fracturing, due to the structure of the bone matrix. In addition, the bone marrow cracks during thaw mounting and the sample drying steps afterwards, which can hamper the quality of the generated results. A recent publication by Good *et al.* (2021) showed reduced bone marrow cracking by freeze-drying the sample.<sup>203</sup> They were able to detect different lipids from bone marrow and surrounding tissues with matrix sublimation and recrystallization up to a spatial resolution of 10  $\mu\text{m}$ . Freeze-drying the sample extends the time required for the sample preparation even further. Another consideration related to the sample preparation protocol is the effect of the protocol on the molecular composition of the bone tissue. The exposure of the bone tissue to high temperature embedding material thaws the sample during embedding and the embedded sample is immediately thereafter frozen. The thawing of the sample to a high temperature can result in molecular degradation, especially for molecules that are unstable at higher temperatures, like lipids and metabolites.<sup>130,281-283</sup> Therefore, freezing of the sample is advisable to be as quickly as possible after embedding. It is important to consider the density of the embedding material during sample preparation, as the consistency of the embedding material should match the tissue as close as possible to provide enough support for easy sectioning.<sup>284</sup> In addition, the embedding material needs to be compatible with MALDI-MSI, as some embedding materials cause ion suppression or high background signals.<sup>36,284</sup> Finding the right embedding material for bone tissue is complex, due to the presence of the different tissue consistencies of bone and bone marrow and the brittleness of bone. The advice is to match the density of the hardest tissue, in this case the cortical bone, as this tissue is most fragile and is often the outward material. The density of bone can be different within a bone as well as between bones, as the amounts of cortical and trabecular bone changes throughout the body.<sup>285,286</sup> Bone density can be affected by disease and differs between species.<sup>286,287</sup> It might be necessary to optimize the embedding material's density for each different type of bone. The sectioning parameters also need to be

optimized per brand of double-sided tape, as described in **Chapter 3**. The attachment of the tape to the sample will be affected by the temperature and, thereby affect the sectioning thickness. Once the required optimization steps are completed, it is possible to obtain high-quality bone sections with limited fracturing using the sample preparation protocol developed in this thesis.

Matrix application for MALDI-MSI is performed after sample sectioning and there are several factors to consider during this step. The matrix can be applied using sublimation or spraying. The risk of tissue loss during sublimation of bone tissue is minimal, but the overall intensities of the lipid signals are relatively low in comparison to the matrix peaks as shown in **Chapter 3**. The relative intensities of lipids can be improved by spraying the matrix. Due to the flow and pressures during spraying, tissue was observed to detach from the tape (unpublished research). In addition, certain solvents should be avoided as they result in the increased loosening of tissue from the sample. For example, acetonitrile resulted in the loss of most of the bone during spraying (unpublished research). A relatively wet spraying method is needed to extract sufficient molecules from the sample, although this is at the risk of molecular delocalization.<sup>36,254</sup> A major disadvantage of spraying the matrix is the potential formation of matrix clusters on the bone and the surrounding tape and embedding material. This matrix cluster formation was observed for both CHCA and DHB after spraying, especially on bone, as indicated in **Chapter 5** and recently described by Kaya *et al.*, respectively.<sup>280</sup> The high-intensity matrix clusters have a potentially ion suppressing effect for bone-related molecules, although lipid peaks can still be observed. The desorption and ionization of lipids is more efficient in positive ion mode than in negative ion mode for both matrix sublimation, as shown in **Chapter 3**, and spraying, as applied in **Chapter 5**. The focus of MALDI-MSI in positive ion mode will affect the detected lipid classes, examples of lipid classes that are commonly identified in positive ion mode are acyl carnitines (CARs), sphingomyelins (SMs), phosphatidylcholines (PCs), and potentially triacylglycerols (TGs) and diacylglycerols (DGs).<sup>255-257,288</sup> Different commonly used matrices for lipid analysis in negative ion mode have been tested with sublimation in **Chapter 3** and with spraying (unpublished research). Nevertheless, desorption and ionization of lipids remained insufficient for the different matrices. An option for improvement of the desorption and ionization efficiency could be the adaption of the spraying protocol to create a more wet spray, although this is at the risk of increasing delocalization.<sup>36,254</sup> Other options to improve desorption and ionization efficiency of lipids in negative ion mode could be the use post-ionization using MALDI-2 or the application of other less commonly applied matrices, for example, novel matrices like anthranilic acid derivatives,

inorganic matrices like graphene oxide, or nanoparticles like silver nanoparticles.<sup>289-294</sup>

Some factors merit discussion related to MALDI-MSI acquisition. Not all mass spectrometers are suitable for the data acquisition from bone tissue samples, due to the isolating properties of the tissue and the use of non-conductive double-sided tape. In addition, height differences within the sample can occur due to the heterogeneity in sample morphologies.<sup>203,204</sup> The thickness of the section can vary throughout the tissue because of differences in shrinkage and drying. This can complicate the acquisition and data analysis, due to mass shifts and intensity variations.<sup>40,204</sup> A mass spectrometer is needed that does not require a conducting sample and is less affected by height differences for the analysis of non-homogeneous and isolating tissues, like bone. This is the case for mass spectrometers in which the ionization and mass analysis are consecutive by decoupling of the ionization source from the mass analyzer.<sup>40</sup> MALDI-MSI of bone tissue was performed on a qTOF instrument (**Chapter 3**) and an FT-ICR (**Chapter 5**) in this thesis. Both instruments were able to ionize and analyze molecules from the bone tissue despite the challenges described. Ionization efficiency might vary due to height differences that affect the laser focus height and associated laser fluence variations can cause intensity fluctuations.<sup>144,260</sup>

The combination of lipid and protein analyses was performed in **Chapter 5**. The benefit of this combination is the additional, increased amount of molecular information obtained from the samples. Limited literature usually only describes the involvement in pathways per lipid class. The effects of these pathways are quite general and can be linked to different phases throughout fracture healing. Therefore, describing the effects of specific lipids and relating those to pathways is still troublesome. The combined data analysis of lipids and proteins can be challenging, as software programs and web applications have been separately developed for both molecular classes, and the data formats and processing can differ.<sup>295,296</sup> Some databases allow for the combination of both datasets, but often require lipid names related to higher level of identification than commonly achieved with MALDI-MSI experiments. A limitation of the study in **Chapter 5** is the separation of the sample in two pieces to get one for each of the analyses. Recent studies have shown the potential of using the same tissue section for MALDI-MSI followed by LC-MS/MS with the use of laser capture microdissection (LMD) and the effects of different glass slides.<sup>297-299</sup> Kaya *et al.* showed the use LMD on undecalcified bone samples with adhesive cryofilm for quantitation of different drugs using LC-MS/MS.<sup>280</sup> This study shows the potential of combining MALDI-MSI

with LC-MS/MS on the same tissue section for undecalcified bone. Its applicability might be depending on the tape used during sample preparation. LC-MS/MS based on LMD can also be used to simplify the separate analyses of bone and bone marrow. In general, the combination of MALDI-MSI and LC-MS/MS offers the potential to analyze different molecular classes or the same molecular class in more detail.<sup>298,299</sup> A spatial-omics approach that combines different mass spectrometry techniques together is one of the directions in which the MSI field is moving in the recent years. The potential of spatial-omics for bone tissue is great, as it can contribute to improved understanding of molecular processes, especially related to changes in lipids.

The complex sample preparation protocol, matrix cluster formation, and challenges during MALDI-MSI raise the question of whether MALDI-MSI is a suitable technique for the molecular analysis of undecalcified bone tissue for (pre)clinical applications in impaired bone healing. The protocol developed in **Chapter 3** is most suitable for the analysis of lipids in positive ionization mode, while other molecular classes are of interest as well. Metabolites will probably suffer from the heat stress caused by the embedding. Another molecular class of potential interest is proteins, but the direct analysis or on-tissue digestion of this class requires washing of the tissue, which can result in loss of sample because of the composition of the tape. This considerably reduces the field of application of the sample preparation protocol. One could consider the use of decalcified bone tissues instead of undecalcified samples to overcome some of the limitations. Submerging in a solvent, usually, an acid such as ethylenediaminetetraacetic acid (EDTA), for days is required for decalcification.<sup>97,300</sup> This could result in substantial molecular delocalization or even removal, which will affect the obtained mass spectra and molecular information.<sup>97,204,300</sup> The use of undecalcified samples avoids the negative molecular effects of decalcification. Another option is the use of other molecular analytical techniques than MALDI-MSI for analysis of bone tissue, of which three are shortly discussed. A complementary MSI technique could be secondary ion mass spectrometry (SIMS). SIMS analysis of bone has been used to study the elemental and molecular distributions, for example, Ca, PO<sub>2</sub>, and fragments of hydroxyapatite and collagen have been shown.<sup>91,92,95,96,101,102</sup> SIMS can be used for the analysis of lipids and peptides, but the sensitivity for these molecules is limited compared to MALDI-MSI.<sup>33,93-96</sup> In addition, substantial fragmentation of larger organic molecules is observed due to the energetics of the primary ion beam and its interaction with the sample surface.<sup>33,93</sup> LC-MS is another MS technique that could be used for the analysis of bone tissue. LC-MS has been used to analyze, among others proteins, lipids, and drugs in bone tissue for different research fields and has

been applied for protein analysis in **Chapter 5**.<sup>133,142,205,206</sup> The advantage of LC-MS is the additional separation provided by the column, which can support getting more molecular information from the sample due to sample cleanup before introduction into the mass spectrometer.<sup>99,207</sup> Furthermore, LC-MS can provide more quantitative information on the molecules present in a sample than MALDI-MSI. A major drawback of LC-MS is that tissue homogenates and crushed tissue are commonly used. The creation of tissue homogenates of bone tissue is possible, but the extracted molecules depend on the composition of the homogenized tissue, for example, the ratio of bone and bone marrow. Homogenization of only bone will result in powder like material, due to the mineral composition of bone. These minerals from the bone can affect MS analysis if not separated out due to potential ion suppression effects. Lastly, immunohistochemistry (IHC) can be used to get additional functional and molecular information by the analysis of specific molecular distributions and pathological processes.<sup>301,302</sup> IHC is a targeted technique that requires knowledge about the molecular contents of the sample. IHC is applied to proteins and molecules targeted in bone tissue are, among others, osteocalcin, osteonectin, collagen, specific growth factors, and nuclear or membranous proteins concerning bone regeneration, bone tumors, and other bone diseases.<sup>300-303</sup> An advantage of IHC is the possibility to apply a counterstaining with IHC to get more information about the exact location of the targeted molecules.<sup>302</sup> IHC requires extensive sample preparation that can affect the immunostaining, but it is required for the staining to reach the target in bone tissue.<sup>300,302</sup> Immunohistochemistry on undecalcified bone tissue results in stronger immunostaining compared to decalcified bone, but the calcified tissue can affect the stainings.<sup>302</sup> So, lipid analysis using MALDI-MSI of undecalcified bone tissue allows for the separate analysis of molecular profiles and distributions in bone and bone marrow, while this might be limited with application of SIMS, LC-MS, or IHC. Separate analysis of bone and bone marrow is of interest, as the molecular composition and ionization efficacy of these two tissue types differ significantly. For example, the desorption and ionization of lipids with MALDI-MSI is more efficient from bone marrow than from cortical bone, as described in **Chapter 5**. The lower lipid content of cortical bone compared to bone marrow is also contributing to this.<sup>137</sup> Nevertheless, other analytical techniques can be combined with MALDI-MSI to provide additional molecular information depending on the research question.

A sample preparation protocol of bone tissue for the lipid analysis with MALDI-MSI has been developed that allows for the separation of molecular information from bone and bone marrow during data analysis. The molecular composition and/or changes in bone and bone marrow could be studied by separating these tissues, as

shown in **Chapter 5**. The application of MALDI-MSI on bone tissue using the developed methodology is not limited to the analysis of fracture healing and non-union development. Other clinical applications could be molecular analysis related to bone diseases, for example, osteoporosis and bone cancers, and the uptake and/or effect of drugs on bone tissue. The methodology could also be applied in bone tissue engineering, for example, to study if the molecular patterns of the engineered bone are the same as for healthy bone. The combination of developed MALDI-MSI protocol with LC-MS/MS can be adopted, for example, to explore multiple molecular classes, as displayed in **Chapter 5**. Furthermore, applications in forensics (as shown in **Chapter 3**) and paleontology are possible.

### 7.1.2 MALD-MSI analysis of fracture hematoma

**Chapter 4** describes the optimization of a washing method for the analysis of lipids with MALDI-MSI in bone fracture hematoma, the comparison of the intra-variability within fracture hematoma with the inter-variability between samples, and the exploration of time-dependent lipid patterns in fracture hematoma. An ammonium formate wash of 15 seconds twice showed to be the best washing method when focusing on lipids for both positive and negative ion mode. This washing method resulted in decreased heme intensity, increased intensities of potential lipid peaks, and minimal molecular delocalization. The intra-variability within a fracture hematoma was smaller than the inter-variability between samples and, therefore, the sampling location within a fracture hematoma is not affecting the molecular profile. Lastly, time-dependent lipid patterns were observed in both positive and negative ion modes. These patterns were able to separate fracture hematoma taken 2, 9, and 19 days after fracture. Phosphatidylethanolamines (PEs) had a higher presence on day 2, while phosphatidylinositols (PIs) and cardiolipins (CLs) on day 19 in negative ion mode when comparing day 2 and day 19. CLs had a higher presence on day 2 and phosphatidic acids (PAs), phosphatidylserines (PSs), and PEs on day 9 in negative ion mode when comparing day 2 and day 9. Specific phosphatidylcholines (PCs) and lysophosphatidylcholines (LPCs) had a higher presence on day 2 and other PCs on day 19 in positive ion mode when comparing day 2 and day 19. Acyl carnitines (CARs) had a higher presence on day 2 + 19 and sphingomyelins (SMs) and LPCs on day 9 in positive ion mode when comparing day 2 + 19 and day 9.

Different lipid classes were shown to contribute to the separation between fracture hematoma of different time points in **Chapter 4**, as described above. The different lipid classes can be related to different signaling pathways, because of their role as signaling molecules. PIs contribute to the Inositol-3-phosphate/diacylglycerol

(IP3/DAG) and the phosphatidylinositol-3-Kinase/protein kinase B (PI3K/AKT) signaling pathways and are involved in the regulation of angiogenesis and calcium mobilization through these pathways.<sup>172,173</sup> Therefore, the higher contribution of PIs on day 19 in comparison to day 2 can be expected. PAs are involved in inflammation regulation and cell differentiation via the mTOR signaling pathway, and angiogenesis via the HIF-1 $\alpha$ -VEGF pathway.<sup>174,175</sup> The role of PAs explains their higher contribution to day 9 compared to day 2, although the inflammatory response is already present on day 2. PEs and PCs are both involved in the production of hydroxyapatite as phosphate donors and glycine and serine metabolism, which is important in the production of collagen.<sup>163,178,180,181</sup> Higher contribution for day 9 compared to day 2 in negative ion mode can be explained by the role of PEs. PCs are the main component of cell membranes, which explains their presence at different time points.<sup>179</sup> The fatty acid chain composition of PCs at different time points is changing, which should be explored further to understand the effect of these changes on the fracture healing process. SMs play a role in bone formation, osteoblast development, and apoptosis as signaling molecules, but also as a precursor of PCs.<sup>164,185</sup> The higher contribution of SMs on day 9 compared to day 2 + 19 could be related to the initiation of osteoblast development. In general, the presence of different lipid classes during fracture healing can be explained using their role in signaling pathways, although the role of some lipid classes as well as the importance of specific lipids are more difficult to explain. The lipid analysis throughout the fracture healing process provides new insights into their contribution, although it should be taken into consideration that certain molecules might be removed during the washing step. The results shown in **Chapter 4** should be confirmed in a study with a larger sample size to validate the assigned roles of different lipids. The addition of more time points is important to get a more complete description of the lipid pathways during fracture healing.

The washing method for the removal of the blood containing heme from the fracture hematoma section is crucial for the acquisition of informative mass spectra. Heme will be a high-intensity peak without blood removal, due to the easy ionization of the heme. This results in ion suppression of other molecules present in the fracture hematoma. Lipid intensity can be enhanced by washing away the blood containing the heme, as shown in **Chapter 4**. Prevention of molecular delocalization of the lipids is important, although some delocalization and potential removal of molecules are always expected to result from a washing step.<sup>36</sup> It is not possible without further optimization of the washing method to acquire the MALDI-MSI data at a single cell resolution, due to the delocalization. Single cell resolution MSI would allow for studying the molecular contributions of, for example, different

inflammation cells in the early phases of the bone healing process. It might be possible to link impaired healing to a specific cell type with this spatial resolution. The limited spatial resolution is a disadvantage of the developed protocol. The washing protocol might serve as a starting point for the analysis of other molecular classes in fracture hematoma, like proteins. Furthermore, this washing protocol for blood removal could be applied to other samples with high blood content.

A point of discussion is the constantly changing environment within the fracture hematoma. The formation of the fracture hematoma starts with the formation of a blood clot due to the inflow of blood into the fracture site.<sup>2,4-6,9</sup> This blood clot is replaced by granulation tissue, soft callus, and hard callus, consecutively.<sup>2,4-6,9</sup> The highest amount of blood is present just after bone fracture and during the different consecutive phases the amount of blood changes resulting in different amounts of heme from hemoglobin. In addition, the structure of the fracture hematoma changes with time, which might affect the removal of blood from it. The amount of remaining blood can vary between fracture hematoma taken at different time points after bone fracture, due to variances in the efficiency of the washing method. Consequently, the amount of ion suppression caused by the heme differs. In addition, the amount of remaining tissue after washing might vary due to the different structures of the fracture hematoma at different time points. Washing of the fracture hematoma sections can result in holes in the tissue where blood used to be present. Therefore, the amount of tissue that can be used for MALDI-MSI differs. The potential differences in remaining blood and acquisition areas of fracture hematoma of different time points are no problem as long as one is aware of these factors and if needed they are corrected for during data analysis.

The intra-variability within a fracture hematoma was smaller than the inter-variability between samples, as shown in **Chapter 4**. This indicated that there was no effect on the molecular profile based on the sample location. This is counterintuitive with the constantly changing environment within the fracture hematoma that will affect the molecular distributions throughout the sample. One of the reasons contributing to small intra-variability between samples is the use of combined molecular profiles per sample location. The different sample locations could show similar molecular profiles while different molecular profiles are present within each sample location because of this approach. These different molecular profiles per sample location will be more difficult to detect, because of the delocalization caused by the washing method. Only one time point was used for this comparison, which might not reflect the structural differences found throughout the fracture healing process. The sampling location might have a bigger

effect on other time points with more defined structural differences within the fracture hematoma. Therefore, these results should be confirmed in future research, in which the molecular distributions within fracture hematoma should be explored as well.

Fracture hematoma have not been studied with MALDI-MSI before and, therefore, the method development and analyses performed in **Chapter 4** were the first on this tissue type. The advantage of MALDI-MSI for fracture hematoma is the potential to understand the molecular changes within the tissue during fracture healing. It might be possible to relate local molecular variations to certain steps in the fracture healing process, although it was shown that the intra-variability between different parts of the fracture hematoma is low. These molecular distributions in the tissue cannot be discovered when the tissue is homogenized as commonly done for different types of molecular analysis. The application of the developed methodology will be limited to clinical research, as fracture hematoma are related to bone fractures. Within the clinical research, analysis of fracture hematoma can be used to study molecular changes in this tissue during normal fracture healing as well as to improve molecular understanding of the causes of impaired healing.

### 7.2 3D imaging with LA-REIMS

The development of an automated setup that allows for 3D acquisition on sample surfaces using LA-REIMS is described in **Chapter 6**. The automated setup, the 3D MS Scanner, creates a topographical scan based on a laser point distance sensor. This scan is used to define a measurement mesh on the sample surface and based on this the sample is moved underneath the laser for MS analysis. A constant distance between the sample surface and laser probe is obtained by automated positioning of the sample. Compensating for these height variations is important, as they can cause laser defocusing and associated intensity variations in the obtained mass spectra.<sup>40,144,260</sup> The higher signal reproducibility between measurement points for the automated acquisition in comparison to manual acquisition shows the importance of keeping the distance between the sample surface and laser probe constant. The 3D MS Scanner enables the possibility to use LA-REIMS for MSI on a sample surface and allows for the 3D visualization of molecular distributions on sample surfaces. This feasibility was shown by the visualization of different molecular distributions on the surfaces of an apple, a marrowbone, and a human femoral head. The demonstrated molecular distributions were related to structural differences in the sample surfaces, but additional distributions that were not related to structures were observed.

The 3D MS Scanner is equipped with a surgical CO<sub>2</sub> laser for the ablation of tissue and generation of smoke rich in molecules. This smoke is aspirated towards the mass spectrometer for ionization and mass analysis. Two important aspects of 3D imaging with LA-REIMS should be taken into consideration and addressed in the future, if possible. Firstly, only one combination of laser settings (mode of operation, laser power, and pulse duration) can be set per 3D imaging acquisition. The settings cannot be changed between measurement points, as the preparation of different laser settings takes longer than the preparation time of the laser. The fixed laser settings can be a problem for complex samples with many different tissue types, as ablation efficiency is affected by differences in structure and mechanical properties between tissues.<sup>51,53,304</sup> Each tissue type will have its own set of optimal laser settings that produces the highest intensity and cleanest mass spectra. The laser settings that work best for all different tissue types have to be selected in case of samples with complex surfaces, despite the resulting intensity variations. Secondly, the diameter of the laser focus might be a limiting factor. The laser spot size was around 1 mm for the acquisitions performed in **Chapter 6**. The spot size of a CO<sub>2</sub> laser is larger than for most other types of lasers, due to its wavelength. The laser spot size will limit the achievable spatial resolution and, therefore, some smaller molecular changes on sample surfaces might not be noticed. The effect of this will be limited for a larger sample, like human femoral heads. The CO<sub>2</sub> laser causes visible damage, due to its large spot size. Depending on the sample, firing a CO<sub>2</sub> laser on the surface result in a clean crater or a carbonized layer in the crater. The amount of damage depends on the combination of sample and laser settings. The limitations in laser settings and spot size are related to the characteristics of the surgical CO<sub>2</sub> laser. A CO<sub>2</sub> laser enables an easier transition to *in vivo* application in the future, but another type of laser might be beneficial for research purposes, especially outside clinical research. An alternative laser ideally should have a smaller spot size and faster adjustment of laser settings, although enough tissue ablation is crucial. Other infrared lasers or even UV lasers can be explored, for example, the IR lasers used in the SpiderMass setup and picosecond infrared laser (PIRL) setup. The Spidermass laser has been shown to be low invasive, has a diameter of 500 μm, and results a smoke rich of in lipid ions.<sup>61,121,273</sup> The use on bone tissue of the SpiderMass system might be complicated by its low water content. The SpiderMass system has been used to analyze sarcomas, including osteosarcomas, and, therefore, can be applied on bone tissues.<sup>121</sup> In addition, SpiderMass has also been used in a 3D imaging approach in which a robotic arm moves the laser probe and MS inlet according to the topography of the sample.<sup>273</sup> The PIRL setup ablates molecules belonging to

different lipid classes and fragments thereof with a spot size of approximately 500  $\mu\text{m}$  and minimal thermal damage.<sup>118,119,123</sup> Sampling for multiple seconds is needed to desorb enough lipids and small molecules.<sup>119</sup> The PIRL has not been used for a 3D imaging approach like the  $\text{CO}_2$  laser and SpiderMass setup. An Er:YAG laser with a wavelength similar to the PIRL, is able to cut through dental enamel.<sup>119,305</sup> The possibility to ablate bone tissue with the PIRL setup seems likely, although this has not been shown yet. The ablation of bone for the wavelengths of SpiderMass and PIRL systems could be explained by the vibrational band of hydroxyapatite in that range.<sup>49,305</sup> Both the SpiderMass and PIRL setup have several advantages over the  $\text{CO}_2$  laser used in **Chapter 6**, but a drawback is that it is not yet surgically approved, which prolongs the implementation into the operating room in the near future.

The molecular distributions shown in **Chapter 6** to demonstrate the feasibility of the 3D imaging capabilities were acquired on a limited surface area. Acquisitions of larger areas should be possible with the 3D MS Scanner. There are a few factors that need to be taken into consideration for these longer acquisitions. Molecular degradation of lipids from the sample at room temperature is expected to be minimal and does not cause a problem for shorter acquisitions. Potential increasing molecular degradation should be taken into account during data analysis and interpretation for longer acquisitions.<sup>282,283</sup> The 3D MS Scanner first performs the topographical scan and subsequently the MS acquisition, which should keep the molecular degradation more consistent throughout the sample. The application of this sequence also contributes to molecular degradation, especially for the acquisitions of large areas. The developed 3D MS Scanner might be too slow at the moment to perform such large area acquisitions without too much molecular degradation. Future developments of the 3D MS Scanner should focus on improving the speed of the topographical scan and MS measurement. In addition, the alignment between the analog laser trigger registration and the total ion current chromatogram will be affected by longer acquisitions. There is a slight misalignment in time between the registration of the analog signal and the mass spectra, which will amplify with time. The misalignment can be fixed during data processing, as the misalignment is constantly increasing.

The direct *in vivo* application of the 3D MS Scanner is not possible, because of the created setup in which the sample moves underneath the laser probe. *In vivo* application was not the goal of the present setup, as the development was focused on the LA-REIMS analysis of uneven sample surfaces to study molecular distributions. The movement of the sample underneath the laser was adopted because of safety considerations of the class IV  $\text{CO}_2$  laser. The *in vivo* application of

a system similar to the 3D MS Scanner can result in more precise and reproducible sampling during operations. This would aid in the model classification of the obtained signal, for example, in outcome prediction. Therefore, the explicit *ex vivo* use of the 3D MS Scanner is a limitation of the developed system at the present.

The developed 3D MS Scanner allows for the acquisition of 3D MSI data from samples with uneven surfaces using LA-REIMS. The use of ambient mass spectrometry techniques for the surface images of 3D samples is a new field of applications. Therefore, any contribution to this developing field is of significance. The 3D MS Scanner as described in **Chapter 6** is the first application of LA-REIMS for 3D MSI. This allows for the analysis of molecular distributions of any surface as long as the sample keeps its shape during analysis and can be ablated by the laser. Clinical applications can explore the molecular distributions on, for example, healthy and osteoarthritic joints or fractured bones. This can contribute to the improved molecular understanding of the different processes in the skeletal system. Besides the clinical application of the 3D MS Scanner, applications in the food industry are possible, as shown in **Chapter 6** by the acquisitions on apple and marrowbone. An additional application could be in the material science field, for example, to study material homogeneity. The sample possibilities of this development are endless as long as ablation and analysis of the sample are possible with LA-REIMS without contamination of the mass spectrometer.

### 7.3 Translation to a (pre)clinical application

The results presented in this thesis are preliminary and need validation studies before implementation in clinical practice. The enhancement of fracture healing by citrulline supplementation shown in **Chapter 5** could be further explored in extended clinical studies. In general, some hurdles still exist for the (pre)clinical application for MALDI-MSI and LA-REIMS, of which a few examples are provided. In general, the reproducibility should be improved, which can be done by further automation of the different workflows. In addition, reproducibility could be addressed by implementation of quality control measurements to assess the instrument and laser status, and sample preparation in case of MALDI-MSI. Furthermore, the preliminary results should be confirmed and validated in large sample size studies and multicenter studies. Quantification for a specific molecule is difficult with MALDI-MSI, but especially with LA-REIMS. The quantification of molecules is complicated by the differences in ionization efficiency between tissue types. Different efforts have been made for molecular quantification with MALDI-MSI, especially in the drug development field. These include the use of calibration curves off or on tissue (spotted or sprayed), the application of spiked homogenates,

and the use of stable isotopes.<sup>306-308</sup> Nevertheless, for LA-REIMS and other REIMS techniques this has not been implemented yet. Molecular quantification for REIMS is more difficult due to the aspiration of smoke and differences in sampling volume, which will affect amount molecules detected by the MS. The different mass spectrometry techniques used in this thesis (MALDI-MSI and LA-REIMS) have potentially clinical applications in the research and patient care of traumas to the skeletal system. The steps, considerations, and research possibilities for the potential translation to (pre)clinical applications are described in section 7.3.1 for MALDI-MSI and 7.3.2 for LA-REIMS.

### 7.3.1 *Ex vivo* application of MALDI-MSI

In a clinical context, MALDI-MSI can only be applied *ex vivo*, due to the nature of the MS technique. The sample preparation protocols developed in **Chapters 3** and **4** for the application of MALDI-MSI on bone tissue and fracture hematoma allow for the expansion of the preclinical utilization of this technique. One of the application fields of these new protocols will be in healthy and impaired fracture healing, i.e. delayed healing and non-union development. MALDI-MSI of bone tissue and fracture hematoma can contribute to an improved molecular understanding of healthy and impaired fracture healing, as a preclinical research tool. Investigating the molecular profiles of healthy and abnormal fracture healing can contribute to new early diagnostic and prediction developments as well as potential new therapies to treat the over- or under-expression of molecules during abnormal fracture healing. Furthermore, MALDI-MSI could be applied to study the effect of therapies on fracture healing. **Chapter 5** provides an example application, as the enhancing effect of citrulline supplementation on fracture healing was studied using MALDI-MSI for lipid analysis. Another application is the discovery of the spots in the tissue that are of the highest molecular importance to distinguish between healthy and impaired healing. These spots can be targeted with *in vivo* applications for diagnosis and prediction, either by an *in vivo* mass spectrometry technique or by reducing biopsy size due to a focused analysis. In this thesis, MALDI-MSI was applied with a focus on lipid analysis, but also other molecular classes could be analyzed, such as metabolites and peptides.

MALDI-MSI is an untargeted technique and can be used to investigate molecular pathways in fracture healing for different molecular classes. Attention should be paid to the reproducibility of different steps in the MALDI-MSI workflow, especially the sample preparation and matrix application in the protocols for bone tissue and fracture hematoma. The sample preparation protocol for bone tissue and fracture hematoma are quite complex. The analysis of bone tissue with MALDI-MSI will

remain mainly a research tool, because of these steps. Nevertheless, potentially MALDI-MSI can provide supporting information besides pathology analyses based on biopsies taken during the operation with further optimization and standardization. MALDI-MSI of fracture hematoma has the potential to become a rapid diagnostic analysis tool, although attention should be paid to the reproducibility of the washing step. One should be wary of the reproducibility of matrix application. The sublimation or spraying of the matrix will affect the extraction of the molecules and acquired mass spectra will depend hereon.<sup>36,254</sup> The reproducibility of the matrix application has greatly improved over the past years with the development of automated sprayers and sublimators.<sup>36</sup> In addition, the matrix application takes time, limiting the potential as a rapid diagnostic tool. In general, spraying is more time-consuming than sublimation, but fast spraying protocols have been developed that take approximately the same time as sublimation.<sup>254,309</sup> In the current state, MALDI-MSI can be applied as an untargeted analytical technique as shown in this thesis, which can be used in research to improve molecular understanding. MALDI-MSI has a potential to provide diagnostic information next to pathological evaluations with further optimization and standardization.

The preliminary results of a small cohort study using human fracture hematoma in **Chapter 4** have shown that the lipids have time-dependent patterns throughout the healthy fracture healing process. Large cohort studies will be necessary to improve the molecular understanding of healthy fracture healing as well as impaired healing. Fracture hematoma can relatively easily be collected from patients in case they have a surgical intervention for their bone fracture. Another option is the use of bone tissue in cases where bone pieces are removed during surgical intervention. It will take time until a large enough cohort is collected for studying molecular changes for fracture hematoma as well as bone samples. A number of confounding factors will be present within the cohort and, therefore, large cohort sizes are needed. For example, the speed of fracture healing is affected by the fracture location and type. Besides, certain diseases can potentially affect the healing process, such as osteoporosis and diabetes mellitus. The number of days between the fracture and surgery will depend on the patient's treatment plan. Sample collection from certain time points will be restricted, for example, during the hard callus formation and bone remodeling phase. An additional complication to studying molecular pathways in fracture healing is the differences in healing rates between patients. Therefore, the time point after the fracture as well as the stage of the fracture healing process should be defined for each sample. Especially, shortly after fracture, the time between the incident and surgery should be noted

as precisely as possible due to the rapidly changing molecular and cellular environment. In addition, patients should be followed-up after surgery to obtain information about the result of the healing process. An option to overcome a few of the sampling issues is to group the samples on the fracture healing phases for initial analyses. This could result in a better definition of the different molecular pathways active during certain fracture healing phases. In addition, this information could be used to understand the importance of different pathways, also related to impaired healing. If molecular differences are found between the groups, it might be possible to predict the outcome of the fracture healing process based on the analysis of removed fracture hematoma after surgery or potentially even during surgery by direct analysis of the fracture hematoma. A surgeon could adapt the treatment based on this prediction to prevent impaired healing and, thereby, improve treatment outcomes.

The methodology for the analysis of undecalcified bone tissue developed in **Chapter 3** shows the possibility to analyze lipids with MALDI-MSI from the bone and bone marrow of samples from mice. This methodology can also be applied to rat bones, as shown in **Chapter 3** and **5**. Furthermore, pig fracture hematoma were used in **Chapter 4** for washing method optimization and analysis of the intra-variability of the fracture hematoma. Bone samples from an animal model was used to study the effect of citrulline supplementation during fracture healing in **Chapter 5**. These examples show the diversity and suitability of samples collected from animal experiments to explore molecular changes. Animal models can be used to study normal and abnormal fracture healing.<sup>310</sup> One of the important considerations herein is the differences between the fracture healing process between humans and animals.<sup>310</sup> For example, the fracture healing in rats is more rapid than in humans, namely, four to five weeks.<sup>310</sup> Rats are the most commonly used animal model due to their high predictability and practicality in performing surgeries and biomechanical testing.<sup>310</sup> Mice are also commonly used, as they allow for genetic manipulation.<sup>310</sup> Larger animals, like dogs, sheep, and goats, have a more similar fracture healing process to human fracture healing than small rodents and biomechanical analysis can easily be performed.<sup>310</sup> These animals are used less in research because of a lack of social acceptance and higher costs.<sup>310</sup> An advantage of animal studies is the higher similarity between animals than between humans, due to breeding and the controlled environment. The higher similarity also extends to the fracture, as it is created in a controlled manner. In addition, it is easier to collect multiple different tissue samples from animal studies than from a patient, which, for example, allows for the collection of the fracture hematoma as well as the bone tissue during the fracture healing process. This possibility allows for more

extensive research options including different tissue types. The overall goal of this research should be to improve molecular understanding of the pathways involved in fracture healing as well as their importance, also with the use of impaired healing and knock-out animal models. The complexity of these studies is the comparability of these impaired healing animal models with the development of impaired healing in human, as whether or not healing will be abnormal is depending on many factors, which are impossible to all cover in animal models. Another application of animal experiments could be studying the effect of different treatments on fracture healing, as presented in **Chapter 5** for citrulline supplementation. Other treatments that could improve or facilitate fracture healing or prevent impaired healing based on the improved understanding of the molecular pathways could also be explored. The translational aspects of the treatment and its effects on fracture healing from animal model to patients should be taken into consideration in these treatment studies. Animal experiments should be limited as much as possible, due to their controversy. In addition, for all animal experiments the 3R principle should be applied, namely replacement, reduction, and refinement.

The developed methodology for the sample preparation of bone tissue from **Chapter 3** could also be used to investigate of cartilage repair. The methodology can be used to section bone with bone marrow, despite their different tissue densities. The addition of cartilage within these sections should be possible, although it will be difficult to transfer all tissues intact to a glass slide due to the different densities. Most of the research performed with MALDI-MSI related to cartilage is applied on the different layers of cartilage and exclude the subchondral bone.<sup>62,106,108</sup> For example, Briggs *et al.* did include subchondral bone, but they used formalin-fixed and paraffin-embedded (FFPE) tissues, of which lipid analysis is more complicated.<sup>109</sup> The inclusion of the subchondral bone in the cartilage repair research is important, as this bone plays a crucial role in the cartilage repair processes.<sup>17,21</sup> The developed methodology can contribute to an improved understanding of the importance and effect of the subchondral bone during cartilage repair.

### 7.3.2 *Ex vivo* and *in vivo* application of LA-REIMS

LA-REIMS can be (pre)clinically applied *ex vivo* as well as *in vivo*, as no sample preparation is needed and the samples can be analyzed directly under ambient conditions. The *ex vivo* application will be mainly research-oriented to improve molecular understanding. Another important aspect of *ex vivo* experiments is the collection of data for diagnostic model building for the *in vivo* application. The goal of *in vivo* application is the near real-time diagnosis of the sampled tissue based on

a built recognition model. LA-REIMS is one of the few ambient mass spectrometry techniques that can generate a molecular signal from bone and cartilage. The analysis of whole bones and joints is possible with LA-REIMS due to the ambient conditions of the technique. Therefore, LA-REIMS could be applied to improve molecular understanding of healthy fracture healing as well as cartilage repair, from fractured bones and joints, as well as impaired skeletal healing. The analyzed molecular classes with LA-REIMS will be mainly lipids and metabolites, due to the nature of the technique. It is expected that the lipid composition will also be affected in cases of impaired healing.

The *ex vivo* analysis of samples with LA-REIMS can be used to improve molecular understanding, as the number of sampling points is not limited, unlike for *in vivo* applications. *Ex vivo* application could, for example, be used to study molecular patterns on joints, like a femoral head. An interesting field to explore here is to study the molecular differences between healthy and damaged cartilage, and the transition area between them. Herein, of special interest is to explore the range of damage and to what extent the surrounding cartilage is already affected after cartilage damage, as the size of the affected area might be related to the development of post-traumatic osteoarthritis (PTOA).<sup>19,29,30</sup> Another example of *ex vivo* research can be exploring the molecular distributions within a bone fracture and the surrounding bone and other tissues. This could be used to study the range of damage to the surrounding bone, but also potentially the contribution of surrounding tissues to the fracture healing process. For example, it is known that mesenchymal stem cells are recruited from the periosteum (bone membrane), bone marrow, and surrounding tissue by different cytokines and growth factors.<sup>6,14</sup> In the case of a non-union, the amount of damage and the vitality of the surrounding bone could be explored. The accurate and reproducible acquisition of mass spectra for each sampling point is important for these examples of research directions. Automated acquisition is necessary to achieve this, as manual acquisition can be too inaccurate and results in high coefficients of variance. Therefore, the 3D MS Scanner was developed, as described in **Chapter 6**. The 3D MS Scanner has increased reproducibility between measurement points and imaging capabilities, and this setup could be applied for further research on bones and joints. Overall, the samples should not be too small, as this would reduce the number of sampling points, due to the laser spot size of approximately 1 mm. The laser spot size also affects the minimal achievable spatial resolution and this might be too large to pick up smaller changes, especially in small samples. *Ex vivo* research can have multiple research fields for different applications. One of these research fields can be the improved molecular understanding of normal and impaired

skeletal healing, although detailed molecular understanding might not be required to distinguish between these groups. Recognition models can be built to identify different molecular profiles between different groups *in vivo*. Large databases that extensively cover all potential conditions need to be acquired to create robust and accurate models. This is still one of the main challenges of moving REIMS-based and other *in vivo* techniques into the operating room for near-real time identification during surgery.<sup>69,111,112</sup> Another application of *ex vivo* research is finding the spots in the tissue that are of the highest molecular importance to identify the tissue, for example, as where to detect healthy or abnormal bone. These optimal spots can be targeted for sampling with the *in vivo* application, reducing the amount of damage caused by sampling with LA-REIMS.

There are a few considerations for the translation from an *ex vivo* to an *in vivo* application, due to the different environmental conditions. The concerns are related to the translatability of the recognition models from *ex vivo* to *in vivo*, as these might affect the molecular profile of the sampling points. Firstly, often the samples used for *ex vivo* are frozen and thawed before data acquisition, although direct analysis also possible due to lack of sample preparation.<sup>311</sup> It is expected that the effect of freezing and thawing is minimal in most cases. However, in the case of multiple thaw and freeze cycles or longer periods of thawed condition, molecular changes and degradation might occur.<sup>283</sup> Secondly, blood circulation could affect the measurement in case of *in vivo* tissue sampling, while this effect is limited in *ex vivo* samples. The effect of the presence of blood on the acquire mass spectra is unclear. On one hand, blood might have a positive effect on the ablation of tissue during sampling, as the presence of liquid (water) can enhance absorption of the laser, due to laser wavelength.<sup>49,51,304</sup> The presence of perfusion might also protect the bone against thermal damage, which has been shown for water.<sup>312,313</sup> On the other hand, the presence of molecules, like heme, and other components from blood might negatively affect the ionization efficiency of the molecules from the tissue and can potentially be detected. Lastly, often saline solution is used for cleaning during surgeries. This solution contains, among others, salts, which might affect the ionization efficiency of the molecules present in the tissue.<sup>36</sup> Due to these different reasons, the resulting molecular profile can be different between the *ex vivo* and *in vivo* measurements and might not be classified correctly by the recognition model. The effect of these different potentially contributing factors should be studied before *in vivo* application based on standard operating procedures. Furthermore, the laser settings used to build the *ex vivo* model should be the same as the *in vivo* settings. Each of the laser settings will affect the obtained mass spectra, as the signal intensity and amount of fragmentation will differ

between modes and settings. Higher laser powers and pulse durations might result in higher intensities in the mass spectra, which can be beneficial for building recognition models. The resulting amount of damage to the tissue is also higher, due to the invasiveness of the CO<sub>2</sub> laser at higher laser fluencies.<sup>51,52,314,315</sup> Therefore, the optimal laser settings are always a trade-off between signal intensity and the amount of tissue damage and clinically suitable laser settings should be used for *ex vivo* model building. Overall, more testing and optimization of the laser settings and acquisitions are necessary before LA-REIMS is clinically applicable. In addition, building robust and accurate models requires large databases. Despite these hurdles and considerations, the *in vivo* application of LA-REIMS has the potential for the recognition and near-real time diagnosis of the healing capacity of bone and the amount of articular cartilage damage. A surgeon could adapt the treatment based on this diagnosis if necessary, which would improve the outcome.

The a main concern related to the *in vivo* application of a surgical CO<sub>2</sub> laser with LA-REIMS is the effect of the tissue damage caused by the invasive nature of the laser. The amount of tissue ablation and damage is depending on the type of tissue, the type of laser, and laser fluence.<sup>49,51-53,304,313,314</sup> The laser spot size of CO<sub>2</sub> lasers is relatively big in comparison to other laser types, which results in larger areas of damage.<sup>49</sup> In low dosages, CO<sub>2</sub> laser irradiations could have potentially a positive effect on bone healing, but those values are below the ablation threshold.<sup>316,317</sup> The tissue damage of higher CO<sub>2</sub> laser dosages for bone is characterized by a carbonization layer (burned discolored layer with charred bone debris), a layer with disturbance of the bone matrix, and a layer of thermal damage including cell death.<sup>49,51,52,315,318-320</sup> The thickness of these layers is affected by the mode of operation (continuous wave or pulsed mode) and laser fluency depending on laser power and pulse duration.<sup>51,52,314,315,319,321</sup> In addition, plasma formation can occur at high laser fluencies, which will affect laser ablation.<sup>51,314</sup> The thermal damage layer and carbonization can be reduced using a layer of water for bone tissue, which also increases the ablation efficiency.<sup>312,313,322</sup> Multiple studies have shown delayed healing of the bone after osteotomy or drilling of holes with a CO<sub>2</sub> laser caused by the thermal damage to the bone tissue, especially the formation of the carbonization layer.<sup>318,320,323-325</sup> Some studies show that the bone healing process will continue with no significant long-term biomechanical effects of the laser osteotomy, although charred bone debris can remain in the healed fracture site and is encapsulated.<sup>315,320,323,324</sup> On the contrary, other studies show continued bone formation with time except for in the ablation affected area and the bone healing does not reach completion.<sup>318,326</sup> Overall, the negative effect of the CO<sub>2</sub> laser on bone healing increases with higher laser energies, due to the larger area of

thermal damage and increasing ablation depths.<sup>49,52,319</sup> Less research has been performed to study the effect of CO<sub>2</sub> laser ablation on cartilage. High dosages of CO<sub>2</sub> laser irradiations result in thermal damage layer, including cell death and the destruction of healing.<sup>327,328</sup> A discolored layer can be seen at the ablation site.<sup>327</sup> In addition, the subchondral bone could potentially be damaged, depending on the cartilage thickness and the laser energy. The cartilage damage created with a CO<sub>2</sub> laser has the same low repair capability as 'normal' cartilage damage, resulting in filling of the defect with fibrous tissue.<sup>328</sup> The damage to articular cartilage did not progress either.<sup>328</sup> Another type of laser than a CO<sub>2</sub> laser might be a better option for *in vivo* application, but different laser types result in tissue damage and a thermal damage zone as well.<sup>49,318,327</sup> Not all lasers result in the formation of a carbonization layer and the thermal damage layer might be thinner.<sup>49</sup> In general, the amount of thermal damage is lower for cartilage than for bone.<sup>327</sup> The ablation efficiency of bone by a CO<sub>2</sub> laser is low due to its relatively low water content, as water has a high absorption coefficient at the CO<sub>2</sub> laser wavelength (10.6 μm).<sup>49,51,304,325,326</sup> Other components of the bone, including hydroxyapatite and minerals, contribute to ablation.<sup>49,313,314,318,319,326</sup> The ablation of cartilage with a CO<sub>2</sub> laser is more efficient, due to the higher water content.<sup>328</sup> The CO<sub>2</sub> laser is a good option for the ablation of bone and cartilage, due to its excellent depth control and efficient vaporization.<sup>315,328</sup> In addition, the CO<sub>2</sub> laser is one of the few lasers that can create mass spectra from bone and cartilage, as shown in **Chapter 6**. Furthermore, Schafer *et al.* (2011) compared a CO<sub>2</sub> laser with a Nd:YAG laser for different tissue types, although they did not include bone or cartilage.<sup>39</sup> The CO<sub>2</sub> laser resulted in a higher reproducibility between the mass spectra, improved coagulative properties, and reduced photochemical process in the tissues compared to the Nd:YAG laser.<sup>39</sup> Unfortunately, these studies are not directly translatable to the potential *in vivo* application of the surgical CO<sub>2</sub> laser coupled to REIMS, due to the differences in tissues, energies and application of the laser, and operational conditions. Therefore, additional research to explore the effects of tissue damage should be performed before *in vivo* application of LA-REIMS. Firstly, the tissue damage of only a few sampling points with a CO<sub>2</sub> laser should be investigated for bone and cartilage. The effect of the presence of blood and/or saline on the tissue damage should be explored, as these might be able to reduce the thermal damage. Besides, other solutions that could potentially reduce the thermal damage should be researched. Secondly, the effect of the tissue damage on bone healing and cartilage repair should be studied. Herein, it is not only important to study the effect of tissue damage from different laser settings, but also to explore this effect for different sampling locations. Overall, it is important

to optimize the laser settings such that tissue damage is minimized both for the carbonization and the thermal damage layer, although these settings will be different for each tissue type. Despite the considerations about the effect of tissue damage, CO<sub>2</sub> lasers are a good option for *in vivo* application as long as the number of sampling points is kept to a minimum to reduce the amount of tissue damage.

#### 7.4 Conclusion and outlook

The application of different mass spectrometry techniques for the analysis of bone, fracture hematoma, and cartilage is shown in this thesis. Different developments were undertaken that enable the analysis of these tissue types using different MSI approaches. The sample preparation of bone and fracture hematoma was optimized to allow for their analysis with MALDI-MSI. The results for MALDI-MSI of bone tissue showed the highest intensity mass spectra using CHCA or DHB as matrix. Time-dependent lipid patterns in fracture healing were revealed by applying MALDI-MSI on fracture hematoma at different time points after bone fracture. Distinct lipid and protein profiles were observed for the citrulline supplement group in comparison to the control group at different time points during fracture healing using MALDI-MSI and LC-MS/MS, respectively. Furthermore, the development of an automated setup for acquisitions with LA-REIMS allowed for the visualization of molecular distributions on different sample types, including a human femoral head. This development contributes to future MS analyses of samples with an uneven surface without any sample preparation.

The different developments presented in this thesis highlight the potential for mass spectrometry to improve molecular understanding of the processes and impaired pathways underlying non-union and PTOA development in comparison to normal bone fracture healing and cartilage repair, respectively. MALDI-MSI can be applied *ex vivo* for research involving bone and fracture hematoma, while LA-REIMS can be applied *ex vivo* as well as potentially *in vivo* on cartilage and bone. The ultimate ambition is to apply LA-REIMS *in vivo* for the outcome prediction during operation. This can help surgeons to earlier adapt treatment to prevent impaired healing if needed, potentially already at the time of the surgery. MALDI-MSI can be used to find important molecular changes in impaired healing, which can be targeted with new treatments. A few examples of future research directions applying the developed methods are given, but the possibilities are more extensive. Firstly, the lipid analysis in bone and bone marrow using MALDI-MSI in a non-union animal model can show the importance and contribution of certain lipids during the healing process. Secondly, a large cohort study on fracture hematoma of normal and impaired healing patients for different time points in the healing process can

show the lipid patterns during fracture healing using MALDI-MSI as well as the molecular differences between patient groups. Thirdly, the 3D MS Scanner connected with LA-REIMS can be used for the analysis of the complete surface of a femoral head from a healthy person and OA patient to demonstrate the difference in molecular distributions in 3D. Lastly, MALDI-MSI can be applied on samples after LA-REIMS analysis of, for example, a femoral head to examine the extent of heat damage caused by the CO<sub>2</sub> laser.



**Chapter 8: Impact paragraph**





## 8.1 Scientific impact

The scientific impact of the work described in this thesis can be divided between the impact of the developments for sample preparation for matrix-assisted laser desorption/ionization mass spectrometry imaging (MALDI-MSI) and the development of a 3D imaging setup using laser-assisted rapid evaporative ionization mass spectrometry (LA-REIMS), which will be discussed separately.

The sample preparation protocols developed in this thesis for MALDI-MSI allow for the analysis of new tissue types, namely bone and fracture hematoma, that were limitedly analyzed with this technique before. In the case of bone tissue, the developed embedding and sectioning protocol allows for the sectioning of undecalcified bone tissue with limited fragmentation. The sectioning of bone tissue is complicated by the different structures present. The optimized sample preparation protocol for mouse, rat, and human bones as well as a targeted forensic and untargeted preclinical application were published in *Analytical and Bioanalytical Chemistry* and was presented as a lecture and as a poster during a 24 hours IMSI (International Mass Spectrometry Imaging) conference. Bone tissue can be analyzed with MALDI-MSI using this protocol allowing for a broad range of potential applications, for example, in preclinical and biomedical research, forensic research, and paleontology. In preclinical research, MALDI-MSI analysis of undecalcified bone tissue can be used to improve molecular understanding of different healing conditions of the skeletal system. One of these topics was the research into the molecular pathways during bone fracture healing and the impaired pathways in non-union development, which was the main protocol development target. The animal study into the effects of citrulline supplementation during fracture healing described in this thesis is an example of an application of the developed MALDI-MSI protocol. Other applications related to bone diseases, like osteoporosis and bone cancer, are now possible as well. In biomedical research, the sample preparation protocol will find innovative applications, for example, in the field of tissue engineering for the analysis of fabricated bone with MALDI-MSI. In forensic research, it can be applied for the detection of drugs and other compounds that might have been related to someone's death, like methadone and its metabolite EDDP. The potential application in the field of paleontology can be to study the different components present in fossils.

In the case of fracture hematoma, the optimized washing method allows for the analysis of the tissue with MALDI-MSI. The washing method is essential to reduce the ion suppression caused by heme presented in the blood of the fracture hematoma. In addition, this was the first time that fracture hematoma was

analyzed with MALDI-MSI. The optimization of the washing methods as well as preliminary results about lipid patterns at different time points after bone fracture were published in *Frontiers in Chemistry* and were presented as a poster during a TERMIS (Tissue Engineering and Regenerative Medicine International Society) conference, an ECTES (European Congress of Trauma and Emergency Surgery) conference, an EFFORT (European Federation of National Associations of Orthopedics and Traumatology) conference, and an IMSC (International Mass Spectrometry Conference) showing the broader impact of this research. The analysis of fracture hematoma with MALDI-MSI will mainly be applied in preclinical and biomedical research, as bone fracture hematoma are specific for bone fractures, although hematoma are formed after injury. The MALDI-MSI analysis of fracture hematoma can be used to improve molecular understanding of bone fracture healing and non-union development. The general results obtained during the optimization of the washing protocol can be extrapolated to other tissues containing substantial amounts of blood. The washing method will need to be tested and optimized per tissue type, due to structural differences between tissues.

The 3D MS Scanner is developed to deploy LA-REIMS for the imaging of uneven sample surfaces. The setup is one of the few techniques that has been developed for 3D imaging of sample surfaces with height differences in terms of millimeters. The setup was not patented, as similar techniques were already developed in parallel by other research groups. This imaging setup is the first one to use a surgical CO<sub>2</sub> laser in combination with REIMS. Furthermore, it is the first ambient mass spectrometry 3D imaging performed on the bone from marrowbone and cartilage from a human femoral head resulting in different molecular distributions on these surfaces. LA-REIMS is one of the few ambient mass spectrometry techniques that can be applied to these tissue types. The 3D MS Scanner and the obtained results with this setup were published in the *Journal of the American Society for Mass Spectrometry* and orally presented at a MSACL (Mass Spectrometry & Advances in the Clinical Lab) conference. The 3D MS Scanner can be used to visualize molecular distributions on sample surfaces with height differences by applying 3D imaging, as indicated. This allows for the extensive analysis of surfaces of a wide range of objects. The fields of application can be (pre)clinical and biomedical research, the food industry, material sciences, and many others. In (pre)clinical and biomedical applications, the surfaces of whole bones and joints could be analyzed to explore the molecular distributions. This can be used to improve molecular understanding of cartilage damage and repair and the impaired pathways in osteoarthritis (OA) and post-traumatic osteoarthritis (PTOA) development. This data can be used to build more accurate recognition models, for example, for the classification of

normal versus impaired healing. These models can be used for *in vivo* recognition with precise *in vivo* sampling using LA-REIMS. This is just one example of a potential (pre)clinical and biomedical application, but many other tissue types could be analyzed with this setup. Furthermore, the 3D MS Scanner could be used in the food industry, for example, to study the distribution of compounds (pesticides, waxes, etc.) on the surfaces of these foods or to explore the effects and spread of parasites, bacteria, and fungi on the surface of the food, such as fruits and vegetables. Another example application of the 3D MS Scanner is its use to analyze the surfaces of developed materials to evaluate their chemical homogeneity in the field of material sciences. In general, almost all objects could be analyzed in the 3D MS Scanner with the application of LA-REIMS as long as they fulfill four requirements: 1) the object has to maintain its shape while it is being moved during the topographical scan and the mass spectrometry acquisition; 2) ablation of the material of the object should be possible with a CO<sub>2</sub> laser; 3) ionization of the ablated molecules should be possible with REIMS; and 4) the resulting ablated smoke and molecules should not contaminate the source or mass spectrometer.

## 8.2 Social impact

In general, the end goal of (pre)clinical research is to apply research in such a way that it can help to improve health care and the patient's quality of life. Possible improvements are a progression in understanding of the disease, formulation of new treatment options, earlier or more accurate diagnosis, or prediction of outcome. Currently, the burden of non-union and PTOA development is high for the patients. This is due to the amount of time between bone fracture or cartilage damage and diagnosis as well as the long and/or intensive treatments and revalidation times, which causes a lower quality of life for the patients during these periods. The results as described in this thesis are preliminary and cannot directly be applied in the clinical environment without further validation through future research and clinical trials. These applications do have the potential to evolve from research to earlier prediction of outcome in the near future. In addition, the citrulline supplementation study showed enhancement of fracture healing in a rat model, which could be further explored in impaired healing and is a potential clinical target. The developed MALDI-MSI methodologies as well as the 3D imaging approach for LA-REIMS can be used to study the impaired molecular pathways involved in the development of non-unions and PTOA. This can improve molecular understanding by defining which pathways are essential for bone fracture healing and cartilage repair. In addition, the different molecular profiles between normal and impaired healing can be explored. These profiles can be used to build recognition models for early diagnosis and prediction of outcome. This early

prediction of the outcome can be done either *in vivo* using LA-REIMS for near-real time diagnosis during operation, or *ex vivo* by applying LA-REIMS or MALDI-MSI on a sample taken during surgery. The earlier prediction of outcome allows a clinician to adapt or start additional treatment before the onset of the symptoms related to non-union and PTOA development and possibly prevents the development of non-union or PTOA resulting in improved quality of life for the patient and reducing the burden of the disease.

This research emphasizes the importance of collaborations between the research institutes and clinical practice. This is specifically the case in (pre)clinical and biomedical research, as the researchers in these fields try to answer clinically relevant questions. The first important and impactful aspect of collaboration is to define an unmet clinical need, which can be either a more fundamental or a more applied question. The fundamental questions answered using mass spectrometry are molecular by nature and can be, for example, to understand the importance of one specific molecule in a certain pathway or disease, or to find a molecular profile that can be used for the classification between healthy and disease as well as different disease types or stages. All these questions are related to the improvement of the molecular understanding of health and disease. Mass spectrometry targets the discovery of molecular profiles that can be used for early diagnosis and prediction of outcome, which would allow for earlier adaption of treatment if necessary. Samples of different disease stages or classes as well as healthy tissue is necessary to answer these questions. Therefore, the second aspect of the collaboration is for the clinic to provide part of the samples necessary for the research if possible. These clinical samples are of importance to finding molecular profiles and test prediction models, as not all research can be based on animal models alone. The last important aspect is the exchange of knowledge between research institutes and the clinic. Often, all the different possibilities and techniques in the research institutes are not well known to the clinicians. It is important to ensure they get familiar with the possibilities and understand how the techniques can be applied. The other way around, the researchers work hand in hand with the clinicians to understand not only their unmet needs, but also to learn from what they already know and what the hurdles are when applying such a technology in “real life”. The collaboration between research institutes and clinical practice is essential to incorporate mass spectrometry techniques like LA-REIMS and potentially MALDI-MSI into patient care.

Besides collaborations between research institutes and the clinic, the collaborations between different research institutes are also of importance.

Sharing knowledge about all the different aspects of research boosts the research performed at the collaborating institutes. This is accomplished via CORE lab (collaborative open research and education) within M4i, which, among others, allows other research groups to use the facilities at M4i. I had the pleasure of experiencing this type of collaboration myself during my month-long visit to Martina Marchetti-Deschmann's research group at the TU Wien (Vienna, Austria). I learned a lot about the sample preparation protocol developed by a research group member (Anastasiya Svirikova) and another guest visitor (Michiel Vandenbosch) during this visit. Without this knowledge, I would not have been able to get the MALDI-MSI results on bone tissue as presented in this thesis. This visit also resulted in a shared publication between the research institutes, namely the research shown in Chapter 3. In terms of personal development, this visit taught me that I can adapt to a different research group and its dynamics. In addition, I developed my experimental and data analysis skills further during this visit. Of course, I also used my time in Vienna to explore many of the cultural sights.

Performing a Ph.D. project and the related research is of course a personal investment as well. The obvious acquired skills are the knowledge I acquired about different sample preparation and mass spectrometry techniques. I learned a lot about data analysis and visualization in general as well as specifically for mass spectrometry data. My instrumental knowledge increased as well, especially because of all the troubleshooting on different instruments that I had to perform over the past years. In addition, I developed numerous soft skills further, for example, scientific writing and presenting. It was confirmed for me that I work in an organized and structured manner throughout my project, although I should be on the lookout to not let this slow me down. Furthermore, I developed my communication skills during the past years. Not only in the form of scientific publications and presentations at international conferences, but also in the communication with different types of people. Specifically, the collaboration between M4i and MUMC+, which is the basis of this research, challenged me to explain my research, for example, to surgeons. This collaboration is important to me, as the potential direct clinical implications and applications of the project drove me. In addition, it made it possible for me to visit the operating room during which I could see the challenges surgeons are facing. All of the things I learned during the past years have turned me into the person I am now and will impact the rest of my carrier.

### 8.3 Economic impact

The future applications of the developments described in this thesis are, in short, the improvement of molecular understanding in the development of non-unions and PTOA as well as the early prediction of outcome based on these different molecular profiles. In addition, the effect of citrulline supplementation on the lipid and protein profiles during fracture healing can be used for improved molecular understanding as well as a potential clinical target. Improved molecular understanding could result in the development of new or more efficient treatments to prevent or cure impaired healing. These developments can be interesting for pharmaceutical companies, as they can research, fabricate, and distribute these new treatment options. In addition, the potential early prediction of outcome might require additional developments that different companies can contribute to, in the mass spectrometry field as well as beyond. Mass spectrometers need to be further developed such that they can be placed in the operating room without being affected by the cleaning processes taking place there and without taking too much space in case of *in vivo* prediction of outcome using LA-REIMS. In addition, companies might contribute to the development of the surgical CO<sub>2</sub> laser. This laser was selected, as it is already clinically approved, but, for example, future improvements could be made to the spot size of the laser to reduce the tissue damage. For the *ex vivo* application of MALDI-MSI, companies could develop sample preparation kits that would allow for quicker and/or easier sample preparation of bone tissue and fracture hematoma. Another possibility for an investment of companies or a spin-off company is offering sample analysis to hospitals. In this case, the distinguishing profiles for normal and impaired healing should have been defined. A company could in that case do the sample preparation and analysis and provide the surgeon with the information. This could be applied to the *ex vivo* application of MALDI-MSI or LA-REIMS. Another option for a spin-off company is to further advance the developed 3D MS Scanner to sell it as an ambient 3D imaging technique. For example, other types of lasers or probes could be explored or the sample types could be broadened with different types of sample holders. These are just a few of the examples in which companies could invest based on the research performed in this thesis.

Besides the potential investment options for companies, the potential development of new treatments and the early prediction of outcome can both contribute to shorter treatment times and, thereby they will reduce health care costs. A specific example of this is the potential fracture healing enhancing effect of citrulline supplementation after bone fracture, as shown in this thesis. Currently, the treatments for non-union and PTOA are long and expensive and, therefore,

these treatment costs are an economical burden. Contributing to the high treatment costs is the long duration until diagnosis. Overall, the research presented in this thesis positively impacts the costs related to non-union and PTOA development in health care.



## Chapter 9: Summaries

9



## 9.1 English summary

Common, injury-related traumas to the skeletal system are bone fractures and articular cartilage damage. Bone fractures are repaired via a well-defined series of overlapping healing phases, which result in constantly changing cellular and molecular environment. Impaired bone fracture healing can cause non-union development, which occurs in 1-10% of the fractures. The articular cartilage and underlying bone attempt to heal the damage after articular cartilage damage. However, the repair capacity of cartilage is limited and, therefore, articular cartilage damage results in post-traumatic osteoarthritis (PTOA) in up to 75% of the cases. The knowledge of the molecular processes that are essential for successful healing after trauma are limited. Mass spectrometry (MS) is an analytical technique that can be applied in an untargeted fashion to a broad range of sample types. The application of mass spectrometry imaging (MSI) techniques for the analysis of skeletal tissue has been limited, although recent developments show an increase in studies on these tissues. In this thesis, the use of different mass spectrometry techniques for the analysis of skeletal tissues was explored with a focus on imaging of skeletal tissues. The following techniques have been applied: 1) matrix-assisted laser desorption/ionization mass spectrometry imaging (MALDI-MSI) for lipid analysis, 2) liquid-chromatography tandem mass spectrometry (LC-MS/MS) for protein analysis, and 3) laser-assisted rapid evaporative ionization mass spectrometry (LA-REIMS) for analysis with minimal sample preparation.

**Chapter 2** reviews the current knowledge of non-union and PTOA development, as well as the use of MSI and different ambient ionization MS techniques for the analysis of skeletal tissue. Risk factors and key molecules that are involved in the normal and impaired healing processes, as well as the current possibilities of diagnosis and outcome prediction, are described for both non-unions and PTOA. At the moment, it is impossible to accurately predict the outcome of the healing process after skeletal trauma, despite the amount of research performed in the past years. Additional molecular knowledge is necessary to obtain further insight into impaired healing, which can be provided by MS. Therefore, the use of secondary ion mass spectrometry (SIMS) imaging as well as MALDI-MSI of bone and cartilage were explored. Both tissue types have been analyzed with both MSI techniques. No research is available in relation to fracture healing and non-union development, while only some research on cartilage with MSI techniques is available in relation to osteoarthritis (OA). In addition, the use of different ambient ionization MS techniques and their potential towards *in vivo* tissue evaluation were discussed, with a focus on the use on skeletal tissue. Different ambient ionization MS techniques have been developed based on electrocautery, laser ablation, and

other molecular extraction methods. The application of these techniques on skeletal tissue is limited and has only been shown for a CO<sub>2</sub> laser coupled to REIMS. These MS techniques have the potential to be used *in vivo* for outcome prediction during surgery, although each of these techniques has their own advantages and limitations.

**Chapter 3** describes the optimization of a sample preparation protocol for MALDI-MSI for the analysis of undecalcified bone tissue for targeted forensic and untargeted (pre)clinical applications. The first optimized sample preparation step was the embedding material used for the bones. A composition of 20% gelatin and 7.5% carboxymethyl cellulose (CMC) showed the best support of the tissue while sectioning. Secondly, the sectioning of the bone tissue was optimized and this step needed to be performed with a tungsten carbide knife while the sections were supported by double-sided tape to maintain their morphology. Methadone and EDDP were detected using DHB in positive ion mode for the targeted forensic application. The limit of detection was estimated at 50 pg/spot on bone tissue and the presence of methadone and EDDP in dosed rat femur and human clavicle were shown. The untargeted (pre)clinical application was focused on the detection of unknown lipids. The desorption and ionization efficiency of lipids was compared for different matrices. CHCA and DHB demonstrate to be the best matrices for detection of lipids in mouse hind legs in positive ion mode based on the number of tissue-specific peaks and signal-to-noise ratios. None of the tested matrices provided the desired results in negative ion mode. The developed sample preparation protocol can be used in future forensic and (pre)clinical research.

**Chapter 4** shows the optimization of a washing protocol for fracture hematoma for lipid analysis with MALDI-MSI. In addition, the intra-variability within a fracture hematoma was studied as well as the changes of lipid patterns throughout the fracture healing process. The fracture hematoma was analyzed because of its relevant role in fracture healing. A washing protocol of 15 seconds twice in ammonium formate provided the best results in terms of removal of heme from the blood present in the fracture hematoma, increase of lipid peak intensity, and minimal delocalization. The intra-variability within a fracture hematoma was smaller than the inter-variability between fracture hematoma indicating that sampling location within a fracture hematoma was of less importance. Different lipid patterns were detected for human fracture hematoma of 2, 9, and 19 days after fracture in both positive and negative ion mode. Days 2 and 19 could be separated in negative ion mode based on higher presence of phosphatidylethanolamines (PEs) on day 2 and phosphatidylinositols (PIs) and

cardiolipins (CLs) on day 19. Days 2 and 9 could be separated in negative ion mode based on the higher presence of CLs on day 2 and phosphatidic acids (PAs), PEs, and phosphatidylserines (PSs) on day 9. Days 2 and 19 were separated in positive ion mode by the higher presence of specific, but different phosphatidylcholines (PCs) at day 2 and 19 and lysophosphatidylcholines (LPCs) on day 2. Day 9 could be separated from days 2 + 19 in positive ion mode based on the higher presence of acyl carnitines (CARs) on days 2 + 19 and a sphingomyelin (SM) and LPC on day 9 as well as specific PCs on days 9 and 2 + 19. These different lipid classes are involved in various processes throughout fracture healing, such as inflammation, angiogenesis, cell differentiation, and extracellular matrix production. Nevertheless, the contribution and importance of the different lipids throughout fracture healing is still unknown.

**Chapter 5** explores the effect of citrulline supplementation on the lipids and proteins during bone fracture healing in a rat model. The effect of citrulline supplementation was studied because of the importance of the citrulline-arginine-nitric oxide metabolism in fracture healing. Lipids were analyzed with MALDI-MSI on bone sections and proteins were analyzed using LC-MS/MS on protein extracts of crushed bone tissue. The lipid profiles that separated the citrulline supplement and the respective control group were distinct for the different stages of fracture healing, as well as for bone and bone marrow. The main lipid classes contributing to the separation between citrulline supplement and control group were PCs and LPCs, but also CARs, triradylglycerols (TGs), and a SM were observed. However, no pattern could be observed in the contribution of the different lipid classes to either one of the groups or throughout the different phases of fracture healing. The more abundant proteins in the citrulline supplement and control group were different throughout the fracture healing phases, indicating a changing effect of the citrulline supplementation. Pathway analyses based on these proteins showed an enhancement of the fracture healing process in the citrulline supplement group in comparison to the control group. This enhancement was based on improved angiogenesis and earlier formation of the soft and hard callus. In addition, different pathways related to the citrulline-arginine-nitric oxide metabolism were more active in the citrulline supplement group. The differences between the citrulline supplement and control group were less pronounced during the bone remodeling phase, which was reflected in the lipid, protein, and pathway analyses.

**Chapter 6** describes the development of an automated setup for LA-REIMS and the application of this setup, the “3D MS Scanner”, for the imaging of sample surfaces in 3D. This automated setup has been developed because conventional MSI

techniques are affected by height variations in samples surfaces. While LA-REIMS can be used on sample surfaces with height variations, but it does not have any imaging capabilities. Different parameters of the 3D MS Scanner were optimized to obtain the highest signal intensities in combination with the lowest coefficients of variation between measurement points. These optimized settings resulted in the completion of a measurement of 300 points within 1 hour. Automated acquisitions with 3D MS Scanner resulted in increased reproducibility between measurement points in comparison to manual acquisitions for different sample types, including human femoral heads. These differences were seen for the total molecular signal as well as for selected  $m/z$  values. In addition, the 3D MS Scanner can be used for 3D imaging of a sample surface, which allows for visualization of molecular distributions on these surfaces. The feasibility of this application was shown on the surfaces of an apple, marrowbone, and human femoral head. These acquisitions showed distinct molecular distributions on the sample surfaces that could be related to structural differences.

In conclusion, different developments necessary for the MSI analysis of skeletal tissue were presented in this thesis. Firstly, sample preparation protocols for undecalcified bone and fracture hematoma were optimized for analysis with MALDI-MSI. Time-dependent changes in the lipid profiles were observed for different time points in human fracture hematoma in positive and negative ion mode. In addition, different lipid profiles were seen between the citrulline supplement and control group as well as for bone and bone marrow at different time points after fracture in a rat model in positive ion mode. Protein and pathway analyses showed an enhancement of fracture healing in the citrulline supplement group in comparison to the control group. An automated setup for LA-REIMS was developed for the analyze of sample surfaces with height variations. This setup allowed for the visualization of molecular distributions for a wide variety of samples, including human femoral heads. The different methodological developments and the applications shown in this thesis can be used for future research in skeletal tissue and its healing processes to improve molecular understanding and outcome prediction.

## 9.2 Nederlandse samenvatting

Botbreuken en gewrichtskaakbeenschade zijn vaak voorkomende trauma's aan het skelet. Botbreuken worden genezen via een reeks van goed gedefinieerde, maar overlappende genezingsfasen. Deze fasen resulteren in een constant veranderende cellulaire en moleculaire omgeving. Een verstoorde fractuurgenezing kan de ontwikkeling van een non-union veroorzaken, wat voorkomt in 1-10% van de botbreuken. Het gewrichtskraakbeen en het onderliggende bot proberen de schade te herstellen na gewrichtskraakbeenschade. Het reparatievermogen van kraakbeen is echter beperkt en daarom leidt gewrichtskraakbeenschade in tot 75% van de gevallen tot posttraumatische osteoartrose (PTOA). De kennis van de essentiële moleculaire processen voor een succesvolle genezing na trauma is beperkt. Massaspectrometrie (MS) is een analytische techniek die op een ongerichte manier kan worden toegepast op veel verschillende soorten weefseltypen. De toepassing van beeldvormende massaspectrometrie (*mass spectrometry imaging*, MSI) technieken voor de analyse van weefsels van het skelet is beperkt. Al laten recente ontwikkelingen wel een toename in onderzoeken naar deze weefsels zien. In dit poefschrift wordt het gebruik van verschillende massaspectrometrie technieken onderzocht voor de analyse van skeletweefsels. Hierin ligt de focus op beeldvorming van skeletweefsels met deze technieken. De volgende MS technieken zijn toegepast: 1) matrix-geassisteerde laser desorptie/ionisatie beeldvormende massaspectrometrie (*matrix-assisted laser desorption/ionization mass spectrometry imaging*, MALDI-MSI) voor lipidenanalyse, 2) vloeistofchromatografie tandem massaspectrometrie (*liquid-chromatography tandem mass spectrometry*, LC-MS/MS) voor eiwitanalyse, en 3) laser-geassisteerde snelle verdampingsionisatie massaspectrometrie (*laser-assisted rapid evaporative ionization mass spectrometry*, LA-REIMS) voor analyse met minimale weefselvoorbereiding.

**Hoofdstuk 2** geeft een overzicht van de huidige kennis over de ontwikkeling van non-union en PTOA. Daarnaast worden in **Hoofdstuk 2** het gebruik van MSI en verschillende ambient ionisatie MS technieken voor de analyse van skeletweefsel beschreven. Risicofactoren, belangrijke moleculen die betrokken zijn bij de normale en verstoorde genezingsprocessen, als ook de huidige mogelijkheden van diagnose en voorspelling van de uitkomst van het genezingsproces worden beschreven voor non-unions en PTOA. Momenteel is het niet mogelijk om de uitkomst van het genezingsproces na trauma aan het skelet accuraat te voorspellen, ondanks de onderzoeken die de afgelopen jaren zijn uitgevoerd. MS kan aanvullende moleculaire kennis bieden, die nodig is om verder inzicht te krijgen in verstoorde genezingsprocessen. Daarom wordt het gebruik van beeldvormende secundaire

ionenmassaspectrometrie (*secondary ion mass spectrometry*, SIMS) en MALDI-MSI op bot en kraakbeen onderzocht. Beide weefseltypes zijn geanalyseerd met beide MSI technieken. Er is nog geen onderzoek beschikbaar met betrekking tot fractuurgenezing en non-union ontwikkeling, terwijl er slechts enkele onderzoeken gedaan zijn op kraakbeen met MSI technieken in relatie tot osteoartrose (OA). Daarnaast worden verschillende ambient ionisatie MS technieken besproken en hun potentie voor het gebruik bij *in vivo* weefsevaluatie, hierbij ligt de focus op het gebruik op skeletweefsel. Er zijn verschillende ambient ionisatie MS technieken ontwikkeld op basis van elektrocauterisatie, laserablatie en andere moleculaire extractiemethoden. De toepassing van deze technieken op skeletweefsel is beperkt en is alleen aangetoond voor een CO<sub>2</sub> laser die wordt gekoppeld aan REIMS. De beschreven MS technieken hebben de potentie om *in vivo* gebruikt te worden voor het voorspellen van de uitkomst tijdens een operatie, hoewel elk van deze technieken zijn eigen voordelen en beperkingen heeft.

**Hoofdstuk 3** beschrijft de optimalisatie van een weefselvoorbereidingsprotocol voor MALDI-MSI voor de analyse van niet-ontkalkt botweefsel voor gerichte forensische en ongerichte (pre)klinische toepassingen. De eerste stap in de optimalisatie van het weefselvoorbereidingsprotocol was het inbeddingsmateriaal dat voor botten wordt gebruikt. De beste steun om het weefsel te snijden werd behaald met een samenstelling van 20% gelatine en 7,5% carboxymethylcellulose (CMC). In de tweede stap werd het snijden van het botweefsel geoptimaliseerd. Het snijden van botweefsel moet uitgevoerd worden met een mes van wolframcarbide terwijl secties ondersteund worden door dubbelzijdige tape voor het behoud van morfologie. Methadon en EDDP werden gedetecteerd met behulp van DHB in positieve ionenmodus voor de gerichte forensische toepassing. De detectielimiet werd geschat op 50 pg/spot op botweefsel. De aanwezigheid van methadon en EDDP in gedoseerde rattendijen en menselijk sleutelbeen werden aangetoond. De ongerichte (pre)klinische toepassing was gericht op de detectie van onbekende lipiden. De desorptie- en ionisatie-efficiëntie van lipiden werden vergeleken voor verschillende matrices. CHCA en DHB waren de beste matrices voor de detectie van lipiden in muizenachterpoten in positieve ionenmodus op basis van het aantal weefsel-specifieke pieken en signaal-ruisverhoudingen. Geen van de geteste matrices gaf het gewenste resultaat in negatieve ionenmodus. Het ontwikkelde weefselvoorbereidingsprotocol kan worden gebruikt in toekomstig forensisch en (pre)klinisch onderzoek.

**Hoofdstuk 4** toont de optimalisatie van een wasprotocol voor fractuurhematomen voor lipidenanalyse met MALDI-MSI. Daarnaast wordt de intra-variabiliteit in een

fractuurhematoom bestudeerd, evenals de veranderingen in lipidenpatronen gedurende het fractuurgenezingsproces. Het fractuurhematoom wordt bestudeerd vanwege zijn relevante rol in fractuurgenezing. Een wasprotocol van tweemaal 15 seconden in ammoniumformiaat leverde de beste resultaten op het gebied van verwijderen van heem als onderdeel van het bloed dat aanwezig is in het fractuurhematoom, toename van piekintensiteit van lipiden en minimale delokalisatie. De intra-variabiliteit in een fractuurhematoom was kleiner dan de inter-variabiliteit tussen fractuurhematomen. Dit geeft aan dat de plaats van de monstername binnen een fractuurhematoom minder van belang is. Verschillende lipidenpatronen werden gedetecteerd voor menselijke fractuurhematomen voor 2, 9 en 19 dagen na een botbreuk in zowel positieve als negatieve ionenmodus. Onderscheid tussen dag 2 en 19 kan worden gemaakt op basis van de hogere aanwezigheid van fosfatidylethanolamines (*phosphatidylethanolamines*, PEs) op dag 2 en fosfatidylinositolen (*phosphatidylinositols*, PIs) en cardiolipines (*cardiolipins*, CLs) op dag 19 in negatieve ionenmodus. Onderscheid tussen dag 2 en 9 kan worden gemaakt op basis van de hogere aanwezigheid van CLs op dag 2 en fosfatidezuren (*phosphatidic acids*, PAs), PEs en fosfatidylserines (*phosphatidylserines*, PSs) op dag 9 in negatieve ionenmodus. Onderscheid tussen dag 2 en 19 kan worden gemaakt op basis van de hogere aanwezigheid van specifieke, maar verschillende fosfatidylcholines (*phosphatidylcholines*, PCs) op dag 2 en 19 en lysofosfatidylcholines (*lysophosphatidylcholines*, LPCs) op dag 2 in positieve ionenmodus. Onderscheid tussen dag 9 en 2 + 19 kan worden gemaakt op basis van hogere aanwezigheid van acylcarnitines (*acyl carnitines*, CARs) op dag 2 + 19 en een sfinogomyeline (*sphingomyelin*, SM) en LPC op dag 9, evenals specifiek PCs voor dag 9 en 2 + 19 in positieve ionenmodus. Deze verschillende lipidenklassen zijn betrokken bij een grote verscheidenheid aan processen tijdens de fractuurgenezing, zoals ontsteking, angiogenese, cel differentiatie en extracellulaire matrixproductie. Desalniettemin zijn de bijdrage en het belang van de verschillende lipiden tijdens de fractuurgenezing nog steeds onbekend.

**Hoofdstuk 5** onderzoekt het effect van citrulline-supplement op de lipiden en eiwitten tijdens fractuurgenezing in een rattenmodel. Het effect van citrulline-supplement werd bestudeerd vanwege het belang van het citrulline-arginine-stikstofmonoxide-metabolisme tijdens de genezing van botbreuken. MALDI-MSI werd gebruikt voor het analyseren van lipiden in botsecties en eiwitten werden geanalyseerd met behulp van LC-MS/MS op eiwitextracties van verbrijzeld botweefsel. De lipidenprofielen die de citrulline-supplement- van de respectievelijke controlegroepen onderscheiden, waren verschillend voor de verschillende stadia van fractuurgenezing en voor bot en beenmerg. De

belangrijkste lipidenklassen die een bijdrage leverden aan de onderscheiding tussen de citrulline-supplement- en controlegroepen waren PCs en LPCs, maar ook CARs, triradylglycerolen (*triradylglycerols*, TGs) en een SM. Er kon echter geen patroon worden waargenomen in de bijdrage die verschillende lipidenklassen aan één van de groepen of in de verschillende fasen van fractuurgenezing leverden. De meer aanwezige eiwitten in de citrulline-supplement- en controlegroepen waren verschillend gedurende de fractuurgenezingsfasen, dit wijst op een veranderend effect van citrulline-supplement. Pathway-analyses op basis van deze eiwitten toonden een verbetering van het fractuurgenezingsproces aan in de citrulline-supplementgroep in vergelijking tot de controlegroep. Deze verbetering was gebaseerd op verbeterde angiogenese en een eerdere vorming van de zachte en harde callus. Bovendien waren er verschillende pathways gerelateerd aan het citrulline-arginine-stikstofmonoxide-metabolisme actiever in de citrulline-supplementgroep. De verschillen tussen de citrulline-supplement- en controlegroep waren minder duidelijk tijdens de bot-remodelleringsfase, wat tot uiting kwam in de lipiden-, eiwit- en pathway-analyses.

**Hoofdstuk 6** beschrijft de ontwikkeling van een geautomatiseerde opstelling voor LA-REIMS en de toepassing van deze opstelling, de “3D MS Scanner”, voor de beeldvorming op weefseloppervlakken in 3D. Deze geautomatiseerde opstelling is ontwikkeld omdat conventionele MSI technieken worden beïnvloed door hoogtevariëaties in weefseloppervlakken. Daarentegen kan LA-REIMS worden gebruikt op weefseloppervlakken met hoogtevariëaties, maar deze techniek heeft echter geen beeldvormingsmogelijkheden. Verschillende parameters van de 3D MS Scanner zijn geoptimaliseerd om de hoogste signaalintensiteiten te verkrijgen met de laagste variatiecoëfficiënten tussen meetpunten. Een meting van 300 punten kan binnen 1 uur worden voltooid met deze geoptimaliseerde instellingen. De geautomatiseerde metingen met de 3D MS Scanner resulteerden in een verhoogde reproduceerbaarheid tussen meetpunten in vergelijking met handmatige metingen voor verschillende soorten weefsels, waaronder menselijke heupkoppen. Deze verschillen waren zowel voor het totale moleculaire signaal als voor geselecteerde *m/z*-waarden te zien. Bovendien kan de 3D MS Scanner worden gebruikt voor 3D-beeldvorming van weefseloppervlakken en hierdoor kunnen moleculaire distributies op deze oppervlakken worden gevisualiseerd. De haalbaarheid van deze toepassing werd aangetoond op het oppervlak van een appel, mergpijp en menselijke heupkop. Deze metingen toonden duidelijke moleculaire distributies op de weefseloppervlakken aan die in verband konden worden gebracht met structurele verschillen.

Concluderend zijn in dit proefschrift verschillende ontwikkelingen gepresenteerd die nodig zijn voor MSI analyses van skeletweefsel. Ten eerste zijn de weefselvoorbereidingsprotocollen voor niet-ontkalkt botweefsel en voor fractuurhematomen geoptimaliseerd voor MALDI-MSI analyses. Tijdsafhankelijke veranderingen in de lipidenprofielen werden waargenomen voor verschillende tijdstippen in menselijke fractuurhematomen in positieve en negatieve ionenmodus. Daarnaast werden verschillende lipidenprofielen waargenomen tussen de citrulline-supplement- en controlegroepen, evenals voor bot en beenmerg op verschillende tijdstippen na een botbreuk in een rattenmodel in positieve ionenmodus. Eiwit- en pathway-analyses toonden een verbetering van de fractuurgenezing in de citrulline-supplementgroep aan in vergelijking met de controlegroep. Voor de analyse van weefseloppervlakken met hoogtevariaties is een geautomatiseerde opstelling voor LA-REIMS ontwikkeld. Deze opstelling maakt de visualisatie van moleculaire distributies mogelijk voor een breed scala aan weefsels, waaronder menselijke heupkoppen. De verschillende methodologische ontwikkelingen en de toepassingen, die in dit proefschrift worden getoond, kunnen worden gebruikt voor toekomstig onderzoek naar skeletweefsel en bijbehorende genezingsprocessen om de moleculaire kennis en de uitkomstvoorspelling te verbeteren.



## Chapter 10: References

# 10



1. Beerekamp MSH, de Muinck Keizer RJO, Schep NWL, Ubbink DT, Panneman MJM, Goslings JC. Epidemiology of extremity fractures in the Netherlands. *Injury*. 2017;48(7):1355-62.
2. den Boer FC, Patka P, Bakker FC, Haarman HJTM. Current Concepts of Fracture Healing, Delayed Unions, and Nonunions. *Osteo trauma care*. 2002;10(01):1-7.
3. Court-Brown CM, Caesar B. Epidemiology of adult fractures: A review. *Injury*. 2006;37(8):691-7.
4. Harwood PJ, Newman JB, Michael ALR. (ii) An update on fracture healing and non-union. *Orthopaedics and Trauma*. 2010;24(1):9-23.
5. Oryan A, Monazzah S, Bigham-Sadegh A. Bone injury and fracture healing biology. *Biomed Environ Sci*. 2015;28(1):57-71.
6. Schindeler A, McDonald MM, Bokko P, Little DG. Bone remodeling during fracture repair: The cellular picture. *Semin Cell Dev Biol*. 2008;19(5):459-66.
7. Dimitriou R, Tsiridis E, Giannoudis PV. Current concepts of molecular aspects of bone healing. *Injury*. 2005;36(12):1392-404.
8. Giannoudis PV, Einhorn TA, Marsh D. Fracture healing: the diamond concept. *Injury*. 2007;38 Suppl 4:S3-6.
9. Hak DJ, Fitzpatrick D, Bishop JA, et al. Delayed union and nonunions: epidemiology, clinical issues, and financial aspects. *Injury*. 2014;45(Suppl 2):S3-7.
10. Tsiridis E, Upadhyay N, Giannoudis P. Molecular aspects of fracture healing: which are the important molecules? *Injury*. 2007;38(Suppl 1):S11-25.
11. (CBS) CBvds. Ziekenhuisopnamen en -patiënten; diagnose-indeling ICD-10 (3-teken niveau). 15-04-2021. Accessed 18-01-2022.
12. Loi F, Cordova LA, Pajarinen J, Lin TH, Yao Z, Goodman SB. Inflammation, fracture and bone repair. *Bone*. 2016;86:119-30.
13. Tosounidis T, Kontakis G, Nikolaou V, Papathanassopoulos A, Giannoudis PV. Fracture healing and bone repair: an update. *Trauma*. 2009;11(3):145-56.
14. Marsell R, Einhorn TA. The biology of fracture healing. *Injury*. 2011;42(6):551-5.
15. Tzioupis C, Giannoudis PV. Prevalence of long-bone non-unions. *Injury*. 2007;38 Suppl 2:S3-9.
16. Kanakaris NK, Giannoudis PV. The health economics of the treatment of long-bone non-unions. *Injury*. 2007;38(Suppl 2):S77-84.
17. Buckwalter JA. Articular cartilage: injuries and potential for healing. *J Orthop Sports Phys Ther*. 1998;28(4):192-202.
18. Buckwalter JA. Articular cartilage injuries. *Clin Orthop Relat Res*. 2002;(402):21-37.
19. Carbone A, Rodeo S. Review of current understanding of post-traumatic osteoarthritis resulting from sports injuries. *J Orthop Res*. 2017;35(3):397-405.
20. Buckwalter JA, Brown TD. Joint injury, repair, and remodeling: roles in post-traumatic osteoarthritis. *Clin Orthop Relat Res*. 2004;(423):7-16.
21. Buckwalter JA. Evaluating methods of restoring cartilaginous articular surfaces. *Clin Orthop Relat Res*. 1999;367(Suppl):S224-38.
22. Anderson DD, Marsh JL, Brown TD. The pathomechanical etiology of post-traumatic osteoarthritis following intraarticular fractures. *Iowa Orthop J*. 2011;31:1-20.

23. Anderson DD, Chubinskaya S, Guilak F, et al. Post-traumatic osteoarthritis: improved understanding and opportunities for early intervention. *J Orthop Res*. 2011;29(6):802-9.
24. Hunziker EB. Articular cartilage repair: basic science and clinical progress. A review of the current status and prospects. *Osteoarthritis Cartilage*. 2002;10(6):432-63.
25. Riordan EA, Little C, Hunter D. Pathogenesis of post-traumatic OA with a view to intervention. *Best Pract Res Clin Rheumatol*. 2014;28(1):17-30.
26. Thomas AC, Hubbard-Turner T, Wikstrom EA, Palmieri-Smith RM. Epidemiology of Posttraumatic Osteoarthritis. *J Athl Train*. 2017;52(6):491-96.
27. Lotz MK, Kraus VB. New developments in osteoarthritis. Posttraumatic osteoarthritis: pathogenesis and pharmacological treatment options. *Arthritis Res Ther*. 2010;12(3):211.
28. Kramer WC, Hendricks KJ, Wang J. Pathogenetic mechanisms of posttraumatic osteoarthritis: opportunities for early intervention. *Int J Clin Exp Med*. 2011;4(4):285-98.
29. Schenker ML, Mauck RL, Ahn J, Mehta S. Pathogenesis and prevention of posttraumatic osteoarthritis after intra-articular fracture. *J Am Acad Orthop Surg*. 2014;22(1):20-8.
30. McKinley TO, Borrelli J, Jr., D'Lima DD, Furman BD, Giannoudis PV. Basic science of intra-articular fractures and posttraumatic osteoarthritis. *J Orthop Trauma*. 2010;24(9):567-70.
31. Brown TD, Johnston RC, Saltzman CL, Marsh JL, Buckwalter JA. Posttraumatic osteoarthritis: a first estimate of incidence, prevalence, and burden of disease. *J Orthop Trauma*. 2006;20(10):739-44.
32. Bodzon-Kulakowska A, Suder P. Imaging mass spectrometry: Instrumentation, applications, and combination with other visualization techniques. *Mass Spectrom Rev*. 2016;35(1):147-69.
33. Chughtai K, Heeren RM. Mass spectrometric imaging for biomedical tissue analysis. *Chem Rev*. 2010;110(5):3237-77.
34. Glish GL, Vachet RW. The basics of mass spectrometry in the twenty-first century. *Nat Rev Drug Discov*. 2003;2(2):140-50.
35. Vaysse PM, Heeren RMA, Porta T, Balluff B. Mass spectrometry imaging for clinical research - latest developments, applications, and current limitations. *Analyst*. 2017;142(15):2690-712.
36. Goodwin RJA. Sample preparation for mass spectrometry imaging: small mistakes can lead to big consequences. *J Proteomics*. 2012;75(16):4893-911.
37. Kaletas BK, van der Wiel IM, Stauber J, et al. Sample preparation issues for tissue imaging by imaging MS. *Proteomics*. 2009;9(10):2622-33.
38. Genangeli M, Heeren RMA, Porta Siegel T. Tissue classification by rapid evaporative ionization mass spectrometry (REIMS): comparison between a diathermic knife and CO<sub>2</sub> laser sampling on classification performance. *Anal Bioanal Chem*. 2019;411(30):7943-55.
39. Schafer KC, Szaniszlo T, Gunther S, et al. In situ, real-time identification of biological tissues by ultraviolet and infrared laser desorption ionization mass spectrometry. *Anal Chem*. 2011;83(5):1632-40.
40. Boesl U. Time-of-flight mass spectrometry: Introduction to the basics. *Mass Spectrom Rev*. 2017;36(1):86-109.

41. Weickhardt C, Moritz F, Grotemeyer J. Time-of-flight mass spectrometry: State-of-the-art in chemical analysis and molecular science. *Mass Spectrom Rev.* 1996;15(3):139-62.
42. Marshall AG, Hendrickson CL, Jackson GS. Fourier transform ion cyclotron resonance mass spectrometry: a primer. *Mass Spectrom Rev.* 1998;17(1):1-35.
43. Makarov A. Electrostatic axially harmonic orbital trapping: a high-performance technique of mass analysis. *Anal Chem.* 2000;72(6):1156-62.
44. Schwartz SA, Reyzer ML, Caprioli RM. Direct tissue analysis using matrix-assisted laser desorption/ionization mass spectrometry: practical aspects of sample preparation. *J Mass Spectrom.* 2003;38(7):699-708.
45. Hankin JA, Barkley RM, Murphy RC. Sublimation as a method of matrix application for mass spectrometric imaging. *J Am Soc Mass Spectrom.* 2007;18(9):1646-52.
46. Balog J, Szaniszlo T, Schaefer KC, et al. Identification of biological tissues by rapid evaporative ionization mass spectrometry. *Anal Chem.* 2010;82(17):7343-50.
47. Jones EA, Simon D, Karancsi T, Balog J, Pringle SD, Takats Z. Matrix Assisted Rapid Evaporative Ionization Mass Spectrometry. *Anal Chem.* 2019;91(15):9784-91.
48. Schaefer KC, Denes J, Albrecht K, et al. In vivo, in situ tissue analysis using rapid evaporative ionization mass spectrometry. *Angew Chem Int Ed Engl.* 2009;48(44):8240-2.
49. Nuss RC, Fabian RL, Sarkar R, Puliafito CA. Infrared laser bone ablation. *Lasers Surg Med.* 1988;8(4):381-91.
50. Venugopalan V, Nishioka NS, Mikic BB. The effect of CO2 laser pulse repetition rate on tissue ablation rate and thermal damage. *IEEE Trans Biomed Eng.* 1991;38(10):1049-52.
51. Walsh JT, Jr., Flotte TJ, Anderson RR, Deutsch TF. Pulsed CO2 laser tissue ablation: effect of tissue type and pulse duration on thermal damage. *Lasers Surg Med.* 1988;8(2):108-18.
52. Rayan GM, Pitha JV, Edwards JS, Everett RB. Effects of CO2 laser beam on cortical bone. *Lasers Surg Med.* 1991;11(1):58-61.
53. Schomacker KT, Walsh JT, Jr., Flotte TJ, Deutsch TF. Thermal damage produced by high-irradiance continuous wave CO2 laser cutting of tissue. *Lasers Surg Med.* 1990;10(1):74-84.
54. Gaston MS, Simpson AH. Inhibition of fracture healing. *J Bone Joint Surg Br.* 2007;89(12):1553-60.
55. Pountos I, Georgouli T, Pneumaticos S, Giannoudis PV. Fracture non-union: Can biomarkers predict outcome? *Injury.* 2013;44(12):1725-32.
56. Lorenz H, Richter W. Osteoarthritis: cellular and molecular changes in degenerating cartilage. *Prog Histochem Cytochem.* 2006;40(3):135-63.
57. Brinker MR, O'Connor DP. Nonunions: Evaluation and Treatment. In: Browner BD, Jupiter JB, Krettek C, Anderson PA, eds. *Skeletal Trauma: Basic Science, Management, and Reconstruction.* Elsevier; 2015:637-718.e8:chap 25.
58. Bishop JA, Palanca AA, Bellino MJ, Lowenberg DW. Assessment of compromised fracture healing. *J Am Acad Orthop Surg.* 2012;20(5):273-82.
59. Miranda MA, Moon MS. Treatment strategy for nonunions and malunions. In: Stannard JP, Schmidt AH, Kregor PJ, eds. *Surgical Treatment of Orthopaedic Trauma.* Thieme; 2007:77-100:chap 5.
60. Copuroglu C, Calori GM, Giannoudis PV. Fracture non-union: who is at risk? *Injury.* 2013;44(11):1379-82.

## Chapter 10

61. Fatou B, Saudemont P, Leblanc E, et al. In vivo Real-Time Mass Spectrometry for Guided Surgery Application. *Sci Rep*. 2016;6:25919.
62. Cillero-Pastor B, Eijkel GB, Kiss A, Blanco FJ, Heeren RM. Matrix-assisted laser desorption ionization-imaging mass spectrometry: a new methodology to study human osteoarthritic cartilage. *Arthritis Rheum*. 2013;65(3):710-20.
63. Rocha B, Cillero-Pastor B, Blanco FJ, Ruiz-Romero C. MALDI mass spectrometry imaging in rheumatic diseases. *Biochim Biophys Acta Proteins Proteom*. 2017;1865(7):784-94.
64. St John ER, Balog J, McKenzie JS, et al. Rapid evaporative ionisation mass spectrometry of electrosurgical vapours for the identification of breast pathology: towards an intelligent knife for breast cancer surgery. *Breast Cancer Res*. 2017;19(1):59.
65. Chughtai S, Chughtai K, Cillero-Pastor B, et al. A multimodal mass spectrometry imaging approach for the study of musculoskeletal tissues. *Int J Mass Spectrom*. 2012;325:150-60.
66. Hanel L, Kwiatkowski M, Heikaus L, Schluter H. Mass spectrometry-based intraoperative tumor diagnostics. *Future Sci OA*. 2019;5(3):FSO373.
67. Hsu CC, Dorrestein PC. Visualizing life with ambient mass spectrometry. *Curr Opin Biotechnol*. 2015;31:24-34.
68. Ifa DR, Eberlin LS. Ambient Ionization Mass Spectrometry for Cancer Diagnosis and Surgical Margin Evaluation. *Clin Chem*. 2016;62(1):111-23.
69. Zhang J, Yu W, Suliburk J, Eberlin LS. Will Ambient Ionization Mass Spectrometry Become an Integral Technology in the Operating Room of the Future? *Clin Chem*. 2016;62(9):1172-74.
70. Hayda RA, Brighton CT, Esterhai JL, Jr. Pathophysiology of delayed healing. *Clin Orthop Relat Res*. 1998;355(Suppl):S31-40.
71. Megas P. Classification of non-union. *Injury*. 2005;36(Suppl 4):S30-7.
72. Weinlein JC. Delayed union and nonunion of fractures. In: Azar FM, Beaty JH, Canale ST, eds. *Campbell's Operative Orthopaedics*. Elsevier; 2017:3081-3116.e8:chap 59.
73. Lynch JR, Taitsman LA, Barei DP, Nork SE. Femoral nonunion: risk factors and treatment options. *J Am Acad Orthop Surg*. 2008;16(2):88-97.
74. Naimark A, Miller K, Segal D, Kossoff J. Nonunion. *Skeletal Radiol*. 1981;6(1):21-5.
75. Gelalis ID, Politis AN, Arnaoutoglou CM, et al. Diagnostic and treatment modalities in nonunions of the femoral shaft: a review. *Injury*. 2012;43(7):980-8.
76. Calori GM, Albisetti W, Agus A, Iori S, Tagliabue L. Risk factors contributing to fracture non-unions. *Injury*. 2007;38(Suppl 2):S11-8.
77. Zimmermann G, Muller U, Wentzensen A. The value of laboratory and imaging studies in the evaluation of long-bone non-unions. *Injury*. 2007;38(Suppl 2):S33-7.
78. Lieberthal J, Sambamurthy N, Scanzello CR. Inflammation in joint injury and post-traumatic osteoarthritis. *Osteoarthritis Cartilage*. 2015;23(11):1825-34.
79. Zhang M, Mani SB, He Y, et al. Induced superficial chondrocyte death reduces catabolic cartilage damage in murine posttraumatic osteoarthritis. *J Clin Invest*. 2016;126(8):2893-902.
80. Harkey MS, Luc BA, Golightly YM, et al. Osteoarthritis-related biomarkers following anterior cruciate ligament injury and reconstruction: a systematic review. *Osteoarthritis Cartilage*. 2015;23(1):1-12.

81. Botter SM, van Osch GJ, Waarsing JH, et al. Quantification of subchondral bone changes in a murine osteoarthritis model using micro-CT. *Biorheology*. 2006;43(3,4):379-88.
82. Burr DB. The importance of subchondral bone in osteoarthritis. *Curr Opin Rheumatol*. 1998;10(3):256-62.
83. Burr DB. The importance of subchondral bone in the progression of osteoarthritis. *J Rheumatol Suppl*. 2004;70:77-80.
84. Hashimoto S, Rai MF, Janiszak KL, Cheverud JM, Sandell LJ. Cartilage and bone changes during development of post-traumatic osteoarthritis in selected LGXSM recombinant inbred mice. *Osteoarthritis Cartilage*. 2012;20(6):562-71.
85. Yu DG, Nie SB, Liu FX, et al. Dynamic Alterations in Microarchitecture, Mineralization and Mechanical Property of Subchondral Bone in Rat Medial Meniscal Tear Model of Osteoarthritis. *Chin Med J (Engl)*. 2015;128(21):2879-86.
86. Olson SA, Guilak F. From articular fracture to posttraumatic arthritis: a black box that needs to be opened. *J Orthop Trauma*. 2006;20(10):661-2.
87. Dare D, Rodeo S. Mechanisms of post-traumatic osteoarthritis after ACL injury. *Curr Rheumatol Rep*. 2014;16(10):448.
88. Lubbeke A, Salvo D, Stern R, Hoffmeyer P, Holzer N, Assal M. Risk factors for post-traumatic osteoarthritis of the ankle: an eighteen year follow-up study. *Int Orthop*. 2012;36(7):1403-10.
89. Borrelli J, Jr., Ricci WM, Steger-May K, Totty WG, Goldfarb C. Postoperative radiographic assessment of acetabular fractures: a comparison of plain radiographs and CT scans. *J Orthop Trauma*. 2005;19(5):299-304.
90. Schaepe K, Bhandari DR, Werner J, et al. Imaging of Lipids in Native Human Bone Sections Using TOF-Secondary Ion Mass Spectrometry, Atmospheric Pressure Scanning Microprobe Matrix-Assisted Laser Desorption/Ionization Orbitrap Mass Spectrometry, and Orbitrap-Secondary Ion Mass Spectrometry. *Anal Chem*. 2018;90(15):8856-64.
91. Henss A, Rohnke M, El Khassawna T, et al. Applicability of ToF-SIMS for monitoring compositional changes in bone in a long-term animal model. *J R Soc Interface*. 2013;10(86):20130332.
92. Henss A, Rohnke M, Knaack S, et al. Quantification of calcium content in bone by using ToF-SIMS--a first approach. *Biointerphases*. 2013;8(1):31.
93. Henss A, Hild A, Rohnke M, Wenisch S, Janek J. Time of flight secondary ion mass spectrometry of bone-Impact of sample preparation and measurement conditions. *Biointerphases*. 2015;11(2):02A302.
94. Kern C, Quade M, Ray S, et al. Investigation of strontium transport and strontium quantification in cortical rat bone by time-of-flight secondary ion mass spectrometry. *J R Soc Interface*. 2019;16(151):20180638.
95. Muller R, Henss A, Kampschulte M, et al. Analysis of microscopic bone properties in an osteoporotic sheep model: a combined biomechanics, FE and ToF-SIMS study. *J R Soc Interface*. 2019;16(151):20180793.
96. Palmquist A, Emanuelsson L, Sjoval P. Chemical and structural analysis of the bone-implant interface by TOF-SIMS, SEM, FIB and TEM: Experimental study in animal. *Appl Surf Sci*. 2012;258(17):6485-94.
97. Fujino Y, Minamizaki T, Yoshioka H, Okada M, Yoshiko Y. Imaging and mapping of mouse bone using MALDI-imaging mass spectrometry. *Bone Rep*. 2016;5:280-5.

## Chapter 10

98. Svirikova A, Turyanskaya A, Pernecky L, Strelci C, Marchetti-Deschmann M. Multimodal imaging of undecalcified tissue sections by MALDI MS and uXRF. *Analyst*. 2018;143(11):2587-95.
99. Nielson CM, Jacobs JM, Orwoll ES. Proteomic studies of bone and skeletal health outcomes. *Bone*. 2019;126:18-26.
100. Grgurevic L, Macek B, Durdevic D, Vukicevic S. Detection of bone and cartilage-related proteins in plasma of patients with a bone fracture using liquid chromatography-mass spectrometry. *Int Orthop*. 2007;31(6):743-51.
101. Malmberg P, Nygren H. Methods for the analysis of the composition of bone tissue, with a focus on imaging mass spectrometry (TOF-SIMS). *Proteomics*. 2008;8(18):3755-62.
102. Eriksson C, Malmberg P, Nygren H. Time-of-flight secondary ion mass spectrometric analysis of the interface between bone and titanium implants. *Rapid Commun Mass Spectrom*. 2008;22(7):943-9.
103. Rohnke M, Henss A, Kokesch-Himmelreich J, et al. Mass spectrometric monitoring of Sr-enriched bone cements-from in vitro to in vivo. *Anal Bioanal Chem*. 2013;405(27):8769-80.
104. Rohnke M, Pfitzenreuter S, Mogwitz B, et al. Strontium release from Sr(2+)-loaded bone cements and dispersion in healthy and osteoporotic rat bone. *J Control Release*. 2017;262:159-69.
105. Thormann U, Ray S, Sommer U, et al. Bone formation induced by strontium modified calcium phosphate cement in critical-size metaphyseal fracture defects in ovariectomized rats. *Biomaterials*. 2013;34(34):8589-98.
106. Barre F, Rocha B, Dewez F, et al. Faster raster matrix-assisted laser desorption/ionization mass spectrometry imaging of lipids at high lateral resolution. *Int J Mass Spectrom*. 2019;437:38-48.
107. Cillero-Pastor B, Eijkel G, Kiss A, Blanco FJ, Heeren RM. Time-of-flight secondary ion mass spectrometry-based molecular distribution distinguishing healthy and osteoarthritic human cartilage. *Anal Chem*. 2012;84(21):8909-16.
108. Peffers MJ, Cillero-Pastor B, Eijkel GB, Clegg PD, Heeren RM. Matrix assisted laser desorption ionization mass spectrometry imaging identifies markers of ageing and osteoarthritic cartilage. *Arthritis Res Ther*. 2014;16(3):R110.
109. Briggs MT, Kuliwaba JS, Muratovic D, et al. MALDI mass spectrometry imaging of N-glycans on tibial cartilage and subchondral bone proteins in knee osteoarthritis. *Proteomics*. 2016;16(11-12):1736-41.
110. Barre FP, Flinders B, Garcia JP, et al. Derivatization Strategies for the Detection of Triamcinolone Acetonide in Cartilage by Using Matrix-Assisted Laser Desorption/Ionization Mass Spectrometry Imaging. *Anal Chem*. 2016;88(24):12051-9.
111. Takats Z, Strittmatter N, McKenzie JS. Ambient Mass Spectrometry in Cancer Research. *Adv Cancer Res*. 2017;134:231-56.
112. St John ER, Rossi M, Pruski P, Darzi A, Takats Z. Intraoperative tissue identification by mass spectrometric technologies. *Trac-Trend Anal Chem*. 2016;85(A):2-9.
113. Phelps DL, Balog J, Gildea LF, et al. The surgical intelligent knife distinguishes normal, borderline and malignant gynaecological tissues using rapid evaporative ionisation mass spectrometry (REIMS). *Br J Cancer*. 2018;118(10):1349-58.

114. Alexander J, Gildea L, Balog J, et al. A novel methodology for in vivo endoscopic phenotyping of colorectal cancer based on real-time analysis of the mucosal lipidome: a prospective observational study of the iKnife. *Surg Endosc.* 2017;31(3):1361-70.
115. Balog J, Sasi-Szabo L, Kinross J, et al. Intraoperative tissue identification using rapid evaporative ionization mass spectrometry. *Sci Transl Med.* 2013;5(194):194ra93.
116. Balog J, Kumar S, Alexander J, et al. In vivo endoscopic tissue identification by rapid evaporative ionization mass spectrometry (REIMS). *Angew Chem Int Ed Engl.* 2015;54(38):11059-62.
117. Schafer KC, Balog J, Szaniszló T, et al. Real time analysis of brain tissue by direct combination of ultrasonic surgical aspiration and sonic spray mass spectrometry. *Anal Chem.* 2011;83(20):7729-35.
118. Woolman M, Gribble A, Bluemke E, et al. Optimized Mass Spectrometry Analysis Workflow with Polarimetric Guidance for ex vivo and in situ Sampling of Biological Tissues. *Sci Rep.* 2017;7(1):468.
119. Woolman M, Ferry I, Kuzan-Fischer CM, et al. Rapid determination of medulloblastoma subgroup affiliation with mass spectrometry using a handheld picosecond infrared laser desorption probe. *Chem Sci.* 2017;8(9):6508-19.
120. Zhang J, Rector J, Lin JQ, et al. Nondestructive tissue analysis for ex vivo and in vivo cancer diagnosis using a handheld mass spectrometry system. *Sci Transl Med.* 2017;9(406):eaan3968.
121. Saudemont P, Quanicco J, Robin YM, et al. Real-Time Molecular Diagnosis of Tumors Using Water-Assisted Laser Desorption/Ionization Mass Spectrometry Technology. *Cancer Cell.* 2018;34(5):840-51.e4.
122. Sans M, Zhang J, Lin JQ, et al. Performance of the MasSpec Pen for Rapid Diagnosis of Ovarian Cancer. *Clin Chem.* 2019;65(5):674-83.
123. Woolman M, Kuzan-Fischer CM, Ferry I, et al. Picosecond Infrared Laser Desorption Mass Spectrometry Identifies Medulloblastoma Subgroups on Intrasurgical Timescales. *Cancer Res.* 2019;79(9):2426-34.
124. Keung EZ, Roland CL. Accurate and Reproducible Diagnosis of Canine Soft Tissue Sarcoma Using Mass Spectrometry: A Step in the Right Direction. *Cancer Cell.* 2018;34(5):697-9.
125. Bodai Z, Cameron S, Bolt F, et al. Effect of Electrode Geometry on the Classification Performance of Rapid Evaporative Ionization Mass Spectrometric (REIMS) Bacterial Identification. *J Am Soc Mass Spectrom.* 2018;29(1):26-33.
126. Karlsson O, Hanrieder J. Imaging mass spectrometry in drug development and toxicology. *Arch Toxicol.* 2017;91(6):2283-94.
127. Swales JG, Dexter A, Hamm G, et al. Quantitation of Endogenous Metabolites in Mouse Tumors Using Mass-Spectrometry Imaging. *Anal Chem.* 2018;90(10):6051-8.
128. Cohen L, Go EP, Siuzdak G. Small-Molecule Desorption/Ionization Mass Analysis. *MALDI MS.* 2007:299-337.
129. Hirano H, Masaki N, Hayasaka T, et al. Matrix-assisted laser desorption/ionization imaging mass spectrometry revealed traces of dental problem associated with dental structure. *Anal Bioanal Chem.* 2014;406(5):1355-63.

130. Khodjanizyazova S, Hanne NJ, Cole JH, Muddiman DC. Mass Spectrometry Imaging (MSI) of Fresh Bones using Infrared Matrix-Assisted Laser Desorption Electrospray Ionization (IR-MALDESI). *Anal Methods*. 2019;11(46):5929-38.
131. Seeley EH, Wilson KJ, Yankeelov TE, et al. Co-registration of multi-modality imaging allows for comprehensive analysis of tumor-induced bone disease. *Bone*. 2014;61:208-16.
132. McIntyre LM, King CV, Boratto M, Drummer OH. Post-mortem drug analyses in bone and bone marrow. *Ther Drug Monit*. 2000;22(1):79-83.
133. Orfanidis A, Gika H, Mastrogianni O, et al. Determination of drugs of abuse and pharmaceuticals in skeletal tissue by UHPLC-MS/MS. *Forensic Sci Int*. 2018;290:137-45.
134. Vandenbosch M, Somers T, Cuypers E. Distribution of clomipramine, citalopram, midazolam, and metabolites in skeletal tissue after chronic dosing in rats. *Drug Test Anal*. 2019;11(7):1083-93.
135. Cartiser N, Bevalot F, Fanton L, Gaillard Y, Guitton J. State-of-the-art of bone marrow analysis in forensic toxicology: a review. *Int J Legal Med*. 2011;125(2):181-98.
136. Nauta SP, Poeze M, Heeren RMA, Porta Siegel T. Clinical use of mass spectrometry (imaging) for hard tissue analysis in abnormal fracture healing. *Clin Chem Lab Med*. 2020;58(6):897-913.
137. During A, Penel G, Hardouin P. Understanding the local actions of lipids in bone physiology. *Prog Lipid Res*. 2015;59:126-46.
138. Vandenbosch M, Somers T, Cuypers E. Distribution of Methadone and Metabolites in Skeletal Tissue. *J Anal Toxicol*. 2018;42(6):400-8.
139. Holzlechner M, Strasser K, Oehler R, Allmaier G, Marchetti-Deschmann M. Improved spatial resolution in MALDI MSI for lipids, peptides and proteins by using highly reproducible matrix sublimation. presented at: OurCon III Imaging Mass Spectrometry Conference; 2015; Pisa, Italy. Session Poster N15.
140. Pauling JK, Hermansson M, Hartler J, et al. Proposal for a common nomenclature for fragment ions in mass spectra of lipids. *PLoS One*. 2017;12(11):e0188394.
141. Sud M, Fahy E, Cotter D, et al. LMSD: LIPID MAPS structure database. *Nucleic Acids Res*. 2007;35(Suppl\_1):D527-32.
142. Vandenbosch M, Rooseleers L, Van Den Bogaert W, Wuestenbergs J, Van de Voorde W, Cuypers E. Skeletal tissue, a viable option in forensic toxicology? A view into post mortem cases. *Forensic Sci Int*. 2020;309:110225.
143. Resetar Maslov D, Svirikova A, Allmaier G, Marchetti-Deschamann M, Kraljevic Pavelic S. Optimization of MALDI-TOF mass spectrometry imaging for the visualization and comparison of peptide distributions in dry-cured ham muscle fibers. *Food Chem*. 2019;283:275-86.
144. Kompauer M, Heiles S, Spengler B. Autofocusing MALDI mass spectrometry imaging of tissue sections and 3D chemical topography of nonflat surfaces. *Nat Methods*. 2017;14(12):1156-8.
145. Fernandez JA, Ochoa B, Fresnedo O, Giralt MT, Rodriguez-Puertas R. Matrix-assisted laser desorption ionization imaging mass spectrometry in lipidomics. *Anal Bioanal Chem*. 2011;401(1):29-51.
146. Goodwin RJA, Nilsson A, Borg D, et al. Conductive carbon tape used for support and mounting of both whole animal and fragile heat-treated tissue sections for MALDI MS imaging and quantitation. *J Proteomics*. 2012;75(16):4912-20.

147. Claes L, Recknagel S, Ignatius A. Fracture healing under healthy and inflammatory conditions. *Nat Rev Rheumatol*. 2012;8(3):133-43.
148. Bastian OW, Koenderman L, Alblas J, Leenen LP, Blokhuis TJ. Neutrophils contribute to fracture healing by synthesizing fibronectin+ extracellular matrix rapidly after injury. *Clin Immunol*. 2016;164:78-84.
149. Volpin G, Shtarker Y. Management of Delayed Union, Non-Union and Mal-union of Long Bone Fractures. presented at: European Surgical Orthopaedics and Traumatology - The EFORT Textbook; 2014; London, United Kingdom.
150. Kolar P, Schmidt-Bleek K, Schell H, et al. The early fracture hematoma and its potential role in fracture healing. *Tissue Eng Part B Rev*. 2010;16(4):427-34.
151. Wang X, Friis T, Glatt V, Crawford R, Xiao Y. Structural properties of fracture haematoma: current status and future clinical implications. *J Tissue Eng Regen Med*. 2017;11(10):2864-75.
152. Park SH, Silva M, Bahk WJ, McKellop H, Lieberman JR. Effect of repeated irrigation and debridement on fracture healing in an animal model. *J Orthop Res*. 2002;20(6):1197-204.
153. Schell H, Duda GN, Peters A, Tsitsilonis S, Johnson KA, Schmidt-Bleek K. The haematoma and its role in bone healing. *J Exp Orthop*. 2017;4(1):5.
154. Bastian OW, Kuijjer A, Koenderman L, et al. Impaired bone healing in multitrauma patients is associated with altered leukocyte kinetics after major trauma. *J Inflamm Res*. 2016;9:69-78.
155. Ghiasi MS, Chen J, Vaziri A, Rodriguez EK, Nazarian A. Bone fracture healing in mechanobiological modeling: A review of principles and methods. *Bone Rep*. 2017;6:87-100.
156. Aichler M, Walch A. MALDI Imaging mass spectrometry: current frontiers and perspectives in pathology research and practice. *Lab Invest*. 2015;95(4):422-31.
157. Murphy RC, Hankin JA, Barkley RM. Imaging of lipid species by MALDI mass spectrometry. *J Lipid Res*. 2009;50(Suppl):S317-22.
158. Norris JL, Caprioli RM. Analysis of tissue specimens by matrix-assisted laser desorption/ionization imaging mass spectrometry in biological and clinical research. *Chem Rev*. 2013;113(4):2309-42.
159. Watrous JD, Alexandrov T, Dorrestein PC. The evolving field of imaging mass spectrometry and its impact on future biological research. *J Mass Spectrom*. 2011;46(2):209-22.
160. Alekos NS, Moorer MC, Riddle RC. Dual Effects of Lipid Metabolism on Osteoblast Function. *Front Endocrinol (Lausanne)*. 2020;11:578194.
161. Chiruchiu V, Leuti A, Maccarrone M. Bioactive Lipids and Chronic Inflammation: Managing the Fire Within. *Front Immunol*. 2018;9:38.
162. Kang JH, Ko HM, Han GD, et al. Dual role of phosphatidylserine and its receptors in osteoclastogenesis. *Cell Death Dis*. 2020;11(7):497.
163. Li Z, Wu G, Sher RB, et al. Choline kinase beta is required for normal endochondral bone formation. *Biochim Biophys Acta*. 2014;1840(7):2112-22.
164. Matsumoto G, Hashizume C, Watanabe K, Taniguchi M, Okazaki T. Deficiency of sphingomyelin synthase 1 but not sphingomyelin synthase 2 reduces bone formation due to impaired osteoblast differentiation. *Mol Med*. 2019;25(1):56.

165. Oyen J, Gjesdal CG, Karlsson T, et al. Dietary Choline Intake Is Directly Associated with Bone Mineral Density in the Hordaland Health Study. *J Nutr.* 2017;147(4):572-578.
166. Schwamborn K, Caprioli RM. Molecular imaging by mass spectrometry--looking beyond classical histology. *Nat Rev Cancer.* 2010;10(9):639-46.
167. Guo W, Blasius FM, Greven J, et al. Hematological and Chemical Profiles in a Porcine Model of Severe Multiple Trauma. *Eur Surg Res.* 2020;61(2-3):83-94.
168. Ellis SR, Paine MRL, Eijkel GB, et al. Automated, parallel mass spectrometry imaging and structural identification of lipids. *Nat Methods.* 2018;15(7):515-8.
169. Tortorella S, Tiberi P, Bowman AP, et al. LipostarMSI: Comprehensive, Vendor-Neutral Software for Visualization, Data Analysis, and Automated Molecular Identification in Mass Spectrometry Imaging. *J Am Soc Mass Spectrom.* 2020;31(1):155-63.
170. Angel PM, Spraggins JM, Baldwin HS, Caprioli R. Enhanced sensitivity for high spatial resolution lipid analysis by negative ion mode matrix assisted laser desorption ionization imaging mass spectrometry. *Anal Chem.* 2012;84(3):1557-64.
171. Seeley EH, Oppenheimer SR, Mi D, Chaurand P, Caprioli RM. Enhancement of protein sensitivity for MALDI imaging mass spectrometry after chemical treatment of tissue sections. *J Am Soc Mass Spectrom.* 2008;19(8):1069-77.
172. Davies EM, Gurung R, Le KQ, Mitchell CA. Effective angiogenesis requires regulation of phosphoinositide signaling. *Adv Biol Regul.* 2019;71:69-78.
173. Antal CE, Newton AC. Spatiotemporal dynamics of phosphorylation in lipid second messenger signaling. *Mol Cell Proteomics.* 2013;12(12):3498-508.
174. Foster DA. Phosphatidic acid and lipid-sensing by mTOR. *Trends Endocrinol Metab.* 2013;24(6):272-8.
175. Han S, Huh J, Kim W, Jeong S, Min do S, Jung Y. Phospholipase D activates HIF-1-VEGF pathway via phosphatidic acid. *Exp Mol Med.* 2014;46:e126.
176. Lee JG, Lee SH, Park DW, et al. Phosphatidic acid as a regulator of matrix metalloproteinase-9 expression via the TNF-alpha signaling pathway. *FEBS Lett.* 2007;581(4):787-93.
177. Lim HK, Choi YA, Park W, et al. Phosphatidic acid regulates systemic inflammatory responses by modulating the Akt-mammalian target of rapamycin-p70 S6 kinase 1 pathway. *J Biol Chem.* 2003;278(46):45117-27.
178. Roberts SJ, Stewart AJ, Sadler PJ, Farquharson C. Human PHOSPHO1 exhibits high specific phosphoethanolamine and phosphocholine phosphatase activities. *Biochem J.* 2004;382(Pt 1):59-65.
179. van der Veen JN, Kennelly JP, Wan S, Vance JE, Vance DE, Jacobs RL. The critical role of phosphatidylcholine and phosphatidylethanolamine metabolism in health and disease. *Biochim Biophys Acta Biomembr.* 2017;1859(9 Pt B):1558-72.
180. Albaugh VL, Mukherjee K, Barbul A. Proline Precursors and Collagen Synthesis: Biochemical Challenges of Nutrient Supplementation and Wound Healing. *J Nutr.* 2017;147(11):2011-17.
181. de Paz-Lugo P, Lupianez JA, Melendez-Hevia E. High glycine concentration increases collagen synthesis by articular chondrocytes in vitro: acute glycine deficiency could be an important cause of osteoarthritis. *Amino Acids.* 2018;50(10):1357-65.

182. Bouchareb R, Mahmut A, Nsaibia MJ, et al. Autotaxin Derived From Lipoprotein(a) and Valve Interstitial Cells Promotes Inflammation and Mineralization of the Aortic Valve. *Circulation*. 2015;132(8):677-90.
183. Mebarek S, Abousalham A, Magne D, et al. Phospholipases of mineralization competent cells and matrix vesicles: roles in physiological and pathological mineralizations. *Int J Mol Sci*. 2013;14(3):5036-129.
184. Wiltz DC, Han RI, Wilson RL, Kumar A, Morrisett JD, Grande-Allen KJ. Differential Aortic and Mitral Valve Interstitial Cell Mineralization and the Induction of Mineralization by Lysophosphatidylcholine In Vitro. *Cardiovasc Eng Technol*. 2014;5(4):371-83.
185. Khavandgar Z, Murshed M. Sphingolipid metabolism and its role in the skeletal tissues. *Cell Mol Life Sci*. 2015;72(5):959-69.
186. Bahney CS, Zondervan RL, Allison P, et al. Cellular biology of fracture healing. *J Orthop Res*. 2019;37(1):35-50.
187. Bigham-Sadegh A, Oryan A. Basic concepts regarding fracture healing and the current options and future directions in managing bone fractures. *Int Wound J*. 2015;12(3):238-47.
188. Einhorn TA, Gerstenfeld LC. Fracture healing: mechanisms and interventions. *Nat Rev Rheumatol*. 2015;11(1):45-54.
189. Meesters DM, Neubert S, Wijnands KAP, et al. Deficiency of inducible and endothelial nitric oxide synthase results in diminished bone formation and delayed union and nonunion development. *Bone*. 2016;83:111-18.
190. Meesters DM, Wijnands KAP, Brink PRG, Poeze M. Malnutrition and Fracture Healing: Are Specific Deficiencies in Amino Acids Important in Nonunion Development? *Nutrients*. 2018;10(11):1597.
191. Diwan AD, Wang MX, Jang D, Zhu W, Murrell GA. Nitric oxide modulates fracture healing. *J Bone Miner Res*. 2000;15(2):342-51.
192. Meesters DM, Hannemann PF, van Eijk HM, et al. Enhancement of fracture healing after citrulline supplementation in mice. *Eur Cell Mater*. 2020;39:183-92.
193. Wijnands KA, Brink PR, Weijers PH, Dejong CH, Poeze M. Impaired fracture healing associated with amino acid disturbances. *Am J Clin Nutr*. 2012;95(5):1270-7.
194. Lin HN, Cottrell J, O'Connor JP. Variation in lipid mediator and cytokine levels during mouse femur fracture healing. *J Orthop Res*. 2016;34(11):1883-93.
195. Allori AC, Sailon AM, Warren SM. Biological basis of bone formation, remodeling, and repair-part II: extracellular matrix. *Tissue Eng Part B Rev*. 2008;14(3):275-83.
196. Boskey AL, Robey PG. The Composition of Bone. *Primer on the Metabolic Bone Diseases and Disorders of Mineral Metabolism*. 2018:84-92.
197. O'Connor JP, Manigrasso MB, Kim BD, Subramanian S. Fracture healing and lipid mediators. *Bonekey Rep*. 2014;3:517.
198. Baldik Y, Talu U, Altinel L, Bilge H, Demiryont M, Aykac-Toker G. Bone healing regulated by nitric oxide: an experimental study in rats. *Clin Orthop Relat Res*. 2002;(404):343-52.
199. Corbett SA, Hukkanen M, Batten J, McCarthy ID, Polak JM, Hughes SP. Nitric oxide in fracture repair. Differential localisation, expression and activity of nitric oxide synthases. *J Bone Joint Surg Br*. 1999;81(3):531-7.

200. Zhu W, Diwan AD, Lin JH, Murrell GA. Nitric oxide synthase isoforms during fracture healing. *J Bone Miner Res.* 2001;16(3):535-40.
201. Zhu W, Murrell GA, Lin J, Gardiner EM, Diwan AD. Localization of nitric oxide synthases during fracture healing. *J Bone Miner Res.* 2002;17(8):1470-7.
202. Rajfer RA, Kilic A, Neviasser AS, et al. Enhancement of fracture healing in the rat, modulated by compounds that stimulate inducible nitric oxide synthase: Acceleration of fracture healing via inducible nitric oxide synthase. *Bone Joint Res.* 2017;6(2):90-7.
203. Good CJ, Neumann EK, Butrico CE, Cassat JE; Caprioli RM, Spraggins JM. High Spatial Resolution MALDI Imaging Mass Spectrometry of Fresh-Frozen Bone. *Anal Chem.* 2022;94(7):3165-72.
204. Vandenbosch M, Nauta SP, Svirikova A, et al. Sample preparation of bone tissue for MALDI-MSI for forensic and (pre)clinical applications. *Anal Bioanal Chem.* 2021;413(10):2683-94.
205. Cleland TP, Schroeter ER. A Comparison of Common Mass Spectrometry Approaches for Paleoproteomics. *J Proteome Res.* 2018;17(3):936-45.
206. Kostyukevich Y, Bugrova A, Chagovets V, et al. Proteomic and lipidomic analysis of mammoth bone by high-resolution tandem mass spectrometry coupled with liquid chromatography. *European Journal of Mass Spectrometry.* 2018;24(6):411-9.
207. Lee JH, Cho JY. Proteomics approaches for the studies of bone metabolism. *BMB Rep.* 2014;47(3):141-8.
208. Bonnarens F, Einhorn TA. Production of a standard closed fracture in laboratory animal bone. *J Orthop Res.* 1984;2(1):97-101.
209. Bankhead P, Loughrey MB, Fernandez JA, et al. QuPath: Open source software for digital pathology image analysis. *Sci Rep.* 2017;7(1):16878.
210. Strohalm M, Hassman M, Kosata B, Kodicek M. mMass data miner: an open source alternative for mass spectrometric data analysis. *Rapid Commun Mass Spectrom.* 2008;22(6):905-8.
211. Fabregat A, Sidiropoulos K, Viteri G, et al. Reactome pathway analysis: a high-performance in-memory approach. *BMC bioinformatics.* 2017;18(1):142.
212. Groven RVM, Nauta SP, Gruisen J, et al. Lipid Analysis of Fracture Hematoma With MALDI-MSI: Specific Lipids are Associated to Bone Fracture Healing Over Time. *Front Chem.* 2021;9:780626.
213. Boskey AL, Timchak DM, Lane JM, Posner AS. Phospholipid changes during fracture healing. *Proc Soc Exp Biol Med.* 1980;165(2):368-73.
214. Goto-Inoue N, Hayasaka T, Zaima N, Setou M. Imaging mass spectrometry for lipidomics. *Biochim Biophys Acta.* 2011;1811(11):961-9.
215. Li Z, Wu G, van der Veen JN, Hermansson M, Vance DE. Phosphatidylcholine metabolism and choline kinase in human osteoblasts. *Biochim Biophys Acta.* 2014;1841(6):859-67.
216. Mao L, Wang ML, Li YY, Liu YX, Wang JF, Xue CH. Eicosapentaenoic acid-containing phosphatidylcholine promotes osteogenesis: mechanism of up-regulating Runx2 and ERK-mediated phosphorylation of PPAR gamma at serine 112. *Journal of Functional Foods.* 2019;52:73-80.
217. Lin X, Patil S, Gao YG, Qian A. The Bone Extracellular Matrix in Bone Formation and Regeneration. *Front Pharmacol.* 2020;11:757.

218. Genetos DC, Wong A, Weber TJ, Karin NJ, Yellowley CE. Impaired osteoblast differentiation in annexin A2- and -A5-deficient cells. *PLoS One*. 2014;9(9):e107482.
219. Lee BS. Myosins in Osteoclast Formation and Function. *Biomolecules*. 2018;8(4):157.
220. Veschi EA, Bolean M, Strzelecka-Kiliszek A, et al. Localization of Annexin A6 in Matrix Vesicles During Physiological Mineralization. *Int J Mol Sci*. 2020;21(4):1367.
221. Jiang L, Sun J, Huang D. Role of Slit/Robo Signaling pathway in Bone Metabolism. *Int J Biol Sci*. 2022;18(3):1303-12.
222. Tong M, Jun T, Nie Y, Hao J, Fan D. The Role of the Slit/Robo Signaling Pathway. *J Cancer*. 2019;10(12):2694-705.
223. Shiu HT, Leung PC, Ko CH. The roles of cellular and molecular components of a hematoma at early stage of bone healing. *J Tissue Eng Regen Med*. 2018;12(4):e1911-25.
224. Paiva KB, Granjeiro JM. Bone tissue remodeling and development: focus on matrix metalloproteinase functions. *Arch Biochem Biophys*. 2014;561:74-87.
225. Chandel NS. Carbohydrate Metabolism. *Cold Spring Harb Perspect Biol*. 2021;13(1):a040568.
226. Kovtun A, Messerer DAC, Scharffetter-Kochanek K, Huber-Lang M, Ignatius A. Neutrophils in Tissue Trauma of the Skin, Bone, and Lung: Two Sides of the Same Coin. *J Immunol Res*. 2018;2018:8173983.
227. Mangoni ML, McDermott AM, Zasloff M. Antimicrobial peptides and wound healing: biological and therapeutic considerations. *Exp Dermatol*. 2016;25(3):167-73.
228. Canalis E. Notch in skeletal physiology and disease. *Osteoporos Int*. 2018;29(12):2611-21.
229. Ballhause TM, Jiang S, Baranowsky A, et al. Relevance of Notch Signaling for Bone Metabolism and Regeneration. *Int J Mol Sci*. 2021;22(3):1325.
230. Zieba JT, Chen YT, Lee BH, Bae Y. Notch Signaling in Skeletal Development, Homeostasis and Pathogenesis. *Biomolecules*. 2020;10(2):332.
231. Cordat E, Casey JR. Bicarbonate transport in cell physiology and disease. *Biochem J*. 2009;417(2):423-39.
232. Mo C, Ke J, Zhao D, Zhang B. Role of the renin-angiotensin-aldosterone system in bone metabolism. *J Bone Miner Metab*. 2020;38(6):772-9.
233. Garcia P, Schwenzer S, Slotta JE, et al. Inhibition of angiotensin-converting enzyme stimulates fracture healing and periosteal callus formation - role of a local renin-angiotensin system. *Br J Pharmacol*. 2010;159(8):1672-80.
234. Chim SM, Tickner J, Chow ST, et al. Angiogenic factors in bone local environment. *Cytokine Growth Factor Rev*. 2013;24(3):297-310.
235. Su YW, Zhou XF, Foster BK, Grills BL, Xu J, Xian CJ. Roles of neurotrophins in skeletal tissue formation and healing. *J Cell Physiol*. 2018;233(3):2133-45.
236. Plotkin LI, Essex AL, Davis HM. RAGE Signaling in Skeletal Biology. *Curr Osteoporos Rep*. 2019;17(1):16-25.
237. Abu-Amer Y. NF-kappaB signaling and bone resorption. *Osteoporos Int*. 2013;24(9):2377-86.
238. Thouverey C, Caverzasio J. Focus on the p38 MAPK signaling pathway in bone development and maintenance. *Bonekey Rep*. 2015;4:711.

239. Chae HJ, Park RK, Chung HT, et al. Nitric oxide is a regulator of bone remodelling. *J Pharm Pharmacol.* 1997;49(9):897-902.
240. Tejero J, Stuehr D. Tetrahydrobiopterin in nitric oxide synthase. *IUBMB Life.* 2013;65(4):358-65.
241. Guo YC, Zhang SW, Yuan Q. Deubiquitinating Enzymes and Bone Remodeling. *Stem Cells Int.* 2018;2018:3712083.
242. Hou CH, Lin J, Huang SC, Hou SM, Tang CH. Ultrasound stimulates NF-kappaB activation and iNOS expression via the Ras/Raf/MEK/ERK signaling pathway in cultured preosteoblasts. *J Cell Physiol.* 2009;220(1):196-203.
243. Kubo Y, Wruck CJ, Fragoulis A, et al. Role of Nrf2 in Fracture Healing: Clinical Aspects of Oxidative Stress. *Calcif Tissue Int.* 2019;105(4):341-52.
244. Chen Y, Alman BA. Wnt pathway, an essential role in bone regeneration. *J Cell Biochem.* 2009;106(3):353-62.
245. Houschyar KS, Tapking C, Borrelli MR, et al. Wnt Pathway in Bone Repair and Regeneration - What Do We Know So Far. *Front Cell Dev Biol.* 2018;6:170.
246. Noel LS, Champion BR, Holley CL, et al. RoBo-1, a novel member of the urokinase plasminogen activator receptor/CD59/Ly-6/snake toxin family selectively expressed in rat bone and growth plate cartilage. *J Biol Chem.* 1998;273(7):3878-83.
247. Kajiya H. Calcium Signaling in Osteoclast Differentiation and Bone Resorption. In: Islam MS, ed. *Calcium Signaling.* Springer Netherlands; 2012:917-32.
248. Zayzafoon M. Calcium/calmodulin signaling controls osteoblast growth and differentiation. *J Cell Biochem.* 2006;97(1):56-70.
249. Strzelecka-Kiliszek A, Mebarek S, Roszkowska M, Buchet R, Magne D, Pikula S. Functions of Rho family of small GTPases and Rho-associated coiled-coil kinases in bone cells during differentiation and mineralization. *Biochim Biophys Acta Gen Subj.* 2017;1861(5 Pt A):1009-23.
250. Schroder K. NADPH oxidases in bone homeostasis and osteoporosis. *Free Radic Biol Med.* 2019;132:67-72.
251. Ducy P. Bone Regulation of Insulin Secretion and Glucose Homeostasis. *Endocrinology.* 2020;161(10): bqaa149.
252. Fulzele K, Clemens TL. Novel functions for insulin in bone. *Bone.* 2012;50(2):452-6.
253. Agrawal A, Jorgensen NR. Extracellular purines and bone homeostasis. *Biochem Pharmacol.* 2021;187:114425.
254. Velickovic D, Zhang G, Bezbradica D, et al. Response Surface Methodology As a New Approach for Finding Optimal MALDI Matrix Spraying Parameters for Mass Spectrometry Imaging. *J Am Soc Mass Spectrom.* 2020;31(3):508-16.
255. Fuchs B, Schiller J. Application of MALDI-TOF mass spectrometry in lipidomics. *Eur J Lipid Sci Tech.* 2009;111(1):83-98.
256. Harshfield EL, Koulman A, Ziemek D, et al. An Unbiased Lipid Phenotyping Approach To Study the Genetic Determinants of Lipids and Their Association with Coronary Heart Disease Risk Factors. *J Proteome Res.* 2019;18(6):2397-410.
257. Wang C, Wang M, Han X. Applications of mass spectrometry for cellular lipid analysis. *Mol Biosyst.* 2015;11(3):698-713.

258. Coutu DL, Kokkaliaris KD, Kunz L, Schroeder T. Three-dimensional map of nonhematopoietic bone and bone-marrow cells and molecules. *Nat Biotechnol.* 2017;35(12):1202-10.
259. Angel PM, Comte-Walters S, Ball LE, et al. Mapping Extracellular Matrix Proteins in Formalin-Fixed, Paraffin-Embedded Tissues by MALDI Imaging Mass Spectrometry. *J Proteome Res.* 2018;17(1):635-46.
260. Bartels B, Kulkarni P, Danz N, Bocker S, Saluz HP, Svatos A. Mapping metabolites from rough terrain: laser ablation electrospray ionization on non-flat samples. *Rsc Adv.* 2017;7(15):9045-50.
261. Bennett RV, Morzan EM, Huckaby JO, Monge ME, Christensen HI, Fernandez FM. Robotic plasma probe ionization mass spectrometry (RoPPI-MS) of non-planar surfaces. *Analyst.* 2014;139(11):2658-62.
262. Li A, Paine MRL, Zambrzycki S, et al. Robotic Surface Analysis Mass Spectrometry (RoSA-MS) of Three-Dimensional Objects. *Anal Chem.* 2018;90(6):3981-6.
263. Kertesz V, Ford MJ, Van Berkel GJ. Automation of a surface sampling probe/electrospray mass spectrometry system. *Anal Chem.* 2005;77(22):7183-9.
264. Lanekoff I, Heath BS, Liyu A, Thomas M, Carson JP, Laskin J. Automated platform for high-resolution tissue imaging using nanospray desorption electrospray ionization mass spectrometry. *Anal Chem.* 2012;84(19):8351-6.
265. Bradshaw JA, Ovchinnikova OS, Meyer KA, Goeringer DE. Combined chemical and topographic imaging at atmospheric pressure via microprobe laser desorption/ionization mass spectrometry-atomic force microscopy. *Rapid Commun Mass Spectrom.* 2009;23(23):3781-6.
266. Ovchinnikova OS, Nikiforov MP, Bradshaw JA, Jesse S, Van Berkel GJ. Combined atomic force microscope-based topographical imaging and nanometer-scale resolved proximal probe thermal desorption/electrospray ionization-mass spectrometry. *ACS Nano.* 2011;5(7):5526-31.
267. Ovchinnikova OS, Kjoller K, Hurst GB, Pelletier DA, Van Berkel GJ. Atomic force microscope controlled topographical imaging and proximal probe thermal desorption/ionization mass spectrometry imaging. *Anal Chem.* 2014;86(2):1083-90.
268. Ovchinnikova OS, Tai T, Bocharova V, et al. Co-registered Topographical, Band Excitation Nanomechanical, and Mass Spectral Imaging Using a Combined Atomic Force Microscopy/Mass Spectrometry Platform. *ACS Nano.* 2015;9(4):4260-9.
269. Nguyen SN, Liyu AV, Chu RK, Anderton CR, Laskin J. Constant-Distance Mode Nanospray Desorption Electrospray Ionization Mass Spectrometry Imaging of Biological Samples with Complex Topography. *Anal Chem.* 2017;89(2):1131-7.
270. Nudnova MM, Sigg J, Wallimann P, Zenobi R. Plasma ionization source for atmospheric pressure mass spectrometry imaging using near-field optical laser ablation. *Anal Chem.* 2015;87(2):1323-9.
271. Schmitz TA, Gamez G, Setz PD, Zhu L, Zenobi R. Towards nanoscale molecular analysis at atmospheric pressure by a near-field laser ablation ion trap/time-of-flight mass spectrometer. *Anal Chem.* 2008;80(17):6537-44.
272. Rejsek J, Vrkoslav V, Pokorny V, Pribyl V, Cvacka J. Ion Source with Laser Triangulation for Ambient Mass Spectrometry of Nonplanar Samples. *Anal Chem.* 2017;89(21):11452-9.

273. Ogrinc N, Kruszewski A, Chaillou P, et al. Robot-Assisted SpiderMass for In Vivo Real-Time Topography Mass Spectrometry Imaging. *Anal Chem*. 2021;93(43):14383-91.
274. Van Meulebroek L, Cameron S, Plekhova V, et al. Rapid LA-REIMS and comprehensive UHPLC-HRMS for metabolic phenotyping of feces. *Talanta*. 2020;217:121043.
275. Cameron SJS, Bodai Z, Temelkuran B, et al. Utilisation of Ambient Laser Desorption Ionisation Mass Spectrometry (ALDI-MS) Improves Lipid-Based Microbial Species Level Identification. *Sci Rep*. 2019;9(1):3006.
276. Cameron SJS, Perdones-Montero A, Van Meulebroek L, et al. Sample Preparation Free Mass Spectrometry Using Laser-Assisted Rapid Evaporative Ionization Mass Spectrometry: Applications to Microbiology, Metabolic Biofluid Phenotyping, and Food Authenticity. *J Am Soc Mass Spectrom*. 2021;32(6):1393-401.
277. Gowers GF, Cameron SJS, Perdones-Montero A, et al. Off-Colony Screening of Biosynthetic Libraries by Rapid Laser-Enabled Mass Spectrometry. *ACS Synth Biol*. 2019;8(11):2566-75.
278. Paraskevaïdi M, Cameron SJS, Whelan E, et al. Laser-assisted rapid evaporative ionisation mass spectrometry (LA-REIMS) as a metabolomics platform in cervical cancer screening. *EBioMedicine*. 2020;60:103017.
279. Wijnant K, Van Meulebroek L, Pomian B, et al. Validated Ultra-High-Performance Liquid Chromatography Hybrid High-Resolution Mass Spectrometry and Laser-Assisted Rapid Evaporative Ionization Mass Spectrometry for Salivary Metabolomics. *Anal Chem*. 2020;92(7):5116-24.
280. Kaya F, Zimmerman MD, Antilus-Sainte R, Gengenbacher M, Carter CL, Dartois V. Spatial quantitation of antibiotics in bone tissue compartments by laser-capture microdissection coupled with UHPLC-tandem mass spectrometry. *Anal Bioanal Chem*. 2022;414(23):6919-27.
281. Anton G, Wilson R, Yu ZH, et al. Pre-analytical sample quality: metabolite ratios as an intrinsic marker for prolonged room temperature exposure of serum samples. *PLoS One*. 2015;10(3):e0121495.
282. Patterson NH, Thomas A, Chaurand P. Monitoring time-dependent degradation of phospholipids in sectioned tissues by MALDI imaging mass spectrometry. *J Mass Spectrom*. 2014;49(7):622-7.
283. Ulmer CZ, Koelmel JP, Jones CM, et al. A Review of Efforts to Improve Lipid Stability during Sample Preparation and Standardization Efforts to Ensure Accuracy in the Reporting of Lipid Measurements. *Lipids*. 2021;56(1):3-16.
284. Nelson KA, Daniels GJ, Fournie JW, Hemmer MJ. Optimization of whole-body zebrafish sectioning methods for mass spectrometry imaging. *J Biomol Tech*. 2013;24(3):119-27.
285. Helgason B, Perilli E, Schileo E, Taddei F, Brynjolfsson S, Viceconti M. Mathematical relationships between bone density and mechanical properties: a literature review. *Clin Biomech (Bristol, Avon)*. 2008;23(2):135-46.
286. Symmons R. Digital photodensitometry: a reliable and accessible method for measuring bone density. *Journal of Archaeological Science*. 2004;31(6):711-9.
287. Roschger P, Paschalis EP, Fratzl P, Klaushofer K. Bone mineralization density distribution in health and disease. *Bone*. 2008;42(3):456-66.

288. Barre FPY, Claes BSR, Dewez F, et al. Specific Lipid and Metabolic Profiles of R-CHOP-Resistant Diffuse Large B-Cell Lymphoma Elucidated by Matrix-Assisted Laser Desorption Ionization Mass Spectrometry Imaging and in Vivo Imaging. *Anal Chem*. 2018;90(24):14198-206.
289. Ellis SR, Soltwisch J, Paine MRL, Dreisewerd K, Heeren RMA. Laser post-ionisation combined with a high resolving power orbitrap mass spectrometer for enhanced MALDI-MS imaging of lipids. *Chem Commun (Camb)*. 2017;53(53):7246-9.
290. Li Z, Guan M, Lin Y, et al. Aberrant Lipid Metabolism in Hepatocellular Carcinoma Revealed by Liver Lipidomics. *Int J Mol Sci*. 2017;18(12):2550.
291. McMillen JC, Fincher JA, Klein DR, Spraggins JM, Caprioli RM. Effect of MALDI matrices on lipid analyses of biological tissues using MALDI-2 postionization mass spectrometry. *J Mass Spectrom*. 2020;55(12):e4663.
292. Muller L, Kailas A, Jackson SN, et al. Lipid imaging within the normal rat kidney using silver nanoparticles by matrix-assisted laser desorption/ionization mass spectrometry. *Kidney Int*. 2015;88(1):186-92.
293. Wang Z, Cai Y, Wang Y, Zhou X, Zhang Y, Lu H. Improved MALDI imaging MS analysis of phospholipids using graphene oxide as new matrix. *Sci Rep*. 2017;7:44466.
294. Zhou D, Guo S, Zhang M, Liu Y, Chen T, Li Z. Mass spectrometry imaging of small molecules in biological tissues using graphene oxide as a matrix. *Anal Chim Acta*. 2017;962:52-9.
295. Hasin Y, Seldin M, Lusic A. Multi-omics approaches to disease. *Genome Biol*. 2017;18(1):83.
296. Reel PS, Reel S, Pearson E, Trucco E, Jefferson E. Using machine learning approaches for multi-omics data analysis: A review. *Biotechnol Adv*. 2021;49:107739.
297. Dewez F, Oejten J, Henkel C, et al. MS Imaging-Guided Microproteomics for Spatial Omics on a Single Instrument. *Proteomics*. 2020;20(23):e1900369.
298. Dilillo M, Pellegrini D, Ait-Belkacem R, de Graaf EL, Caleo M, McDonnell LA. Mass Spectrometry Imaging, Laser Capture Microdissection, and LC-MS/MS of the Same Tissue Section. *J Proteome Res*. 2017;16(8):2993-3001.
299. Mezger STP, Mingels AMA, Bekers O, Heeren RMA, Cillero-Pastor B. Mass Spectrometry Spatial-Omics on a Single Conductive Slide. *Anal Chem*. 2021;93(4):2527-33.
300. Miquelestorena-Standley E, Jourdan ML, Collin C, et al. Effect of decalcification protocols on immunohistochemistry and molecular analyses of bone samples. *Mod Pathol*. 2020;33(8):1505-17.
301. Fedchenko N, Reifenrath J. Different approaches for interpretation and reporting of immunohistochemistry analysis results in the bone tissue - a review. *Diagn Pathol*. 2014;9:221.
302. Wittenburg G, Volkel C, Mai R, Lauer G. Immunohistochemical comparison of differentiation markers on paraffin and plastic embedded human bone samples. *J Physiol Pharmacol*. 2009;60(Suppl 8):43-9.
303. Di Carlo S, De Angelis F, Brauner E, et al. Histological and immunohistochemical evaluation of mandibular bone tissue regeneration. *Int J Immunopathol Pharmacol*. 2018;32:2058738418798249.
304. Walsh JT, Jr., Deutsch TF. Pulsed CO<sub>2</sub> laser ablation of tissue: effect of mechanical properties. *IEEE Trans Biomed Eng*. 1989;36(12):1195-201.

305. Franjic K, Cowan ML, Kraemer D, Miller RJ. Laser selective cutting of biological tissues by impulsive heat deposition through ultrafast vibrational excitations. *Opt Express*. 2009;17(25):22937-59.
306. Huizing LRS, McDuffie J, Cuyckens F, et al. Quantitative Mass Spectrometry Imaging to Study Drug Distribution in the Intestine Following Oral Dosing. *Anal Chem*. 2021;93(4):2144-51.
307. Porta T, Lesur A, Varesio E, Hopfgartner G. Quantification in MALDI-MS imaging: what can we learn from MALDI-selected reaction monitoring and what can we expect for imaging? *Anal Bioanal Chem*. 2015;407(8):2177-87.
308. Schulz S, Becker M, Groseclose MR, Schadt S, Hopf C. Advanced MALDI mass spectrometry imaging in pharmaceutical research and drug development. *Curr Opin Biotechnol*. 2019;55:51-9.
309. Huizing LRS, Ellis SR, Beulen B, et al. Development and evaluation of matrix application techniques for high throughput mass spectrometry imaging of tissues in the clinic. *Clin Mass Spectrom*. 2019;12:7-15.
310. O'Loughlin PF, Morr S, Bogunovic L, Kim AD, Park B, Lane JM. Selection and development of preclinical models in fracture-healing research. *J Bone Joint Surg Am*. 2008;90 Suppl 1:79-84.
311. Vaysse PM, Grabsch HI, van den Hout M, et al. Real-time lipid patterns to classify viable and necrotic liver tumors. *Lab Invest*. 2021;101(3):381-95.
312. Li XW, Chen CG, Zhang XZ, Zhan ZL, Xie SS. Visualization of liquid-assisted hard tissue ablation with a pulsed CO<sub>2</sub> laser. *Laser Phys Lett*. 2015;12(1)
313. Zhang X, Zhan Z, Liu H, Zhao H, Xie S, Ye Q. Influence of water layer thickness on hard tissue ablation with pulsed CO<sub>2</sub> laser. *J Biomed Opt*. 2012;17(3):038003.
314. Forrer M, Frenz M, Romano V, et al. Bone-Ablation Mechanism Using CO<sub>2</sub>-Lasers of Different Pulse Duration and Wavelength. *Applied Physics B-Photophysics and Laser Chemistry*. 1993;56(2):104-12.
315. Rayan GM, Stanfield DT, Cahill S, Kosanke SD, Kopta JA. Effects of rapid pulsed CO<sub>2</sub> laser beam on cortical bone in vivo. *Lasers Surg Med*. 1992;12(6):615-20.
316. Bashardoust Tajali S, Macdermid JC, Houghton P, Grewal R. Effects of low power laser irradiation on bone healing in animals: a meta-analysis. *J Orthop Surg Res*. 2010;5:1.
317. Tang XM, Chai BP. Effect of CO<sub>2</sub> laser irradiation on experimental fracture healing: a transmission electron microscopic study. *Lasers Surg Med*. 1986;6(3):346-52.
318. Friesen LR, Cobb CM, Rapley JW, Forgas-Brockman L, Spencer P. Laser irradiation of bone: II. Healing response following treatment by CO<sub>2</sub> and Nd:YAG lasers. *J Periodontol*. 1999;70(1):75-83.
319. Krause LS, Cobb CM, Rapley JW, Killoy WJ, Spencer P. Laser irradiation of bone. I. An in vitro study concerning the effects of the CO<sub>2</sub> laser on oral mucosa and subjacent bone. *J Periodontol*. 1997;68(9):872-80.
320. Tauber C, Farine I, Horoszowski H, Gassner S. Fracture healing in rabbits after osteotomy using the CO<sub>2</sub> laser. *Acta Orthop Scand*. 1979;50(4):385-90.
321. Lanzafame RJ, Naim JO, Rogers DW, Hinshaw JR. Comparison of continuous-wave, chop-wave, and super pulse laser wounds. *Lasers Surg Med*. 1988;8(2):119-24.
322. Ivanenko MM, Hering P. Wet bone ablation with mechanically Q-switched high-repetition-rate CO<sub>2</sub> laser. *Applied Physics B-Lasers and Optics*. 1998;67(3):395-7.

323. Callahan DJ. Osseous healing after CO<sub>2</sub> laser osteotomy. *Foot Ankle*. 1990;11(3):146-51.
324. Gertzbein SD, deDemeter D, Cruickshank B, Kapasouri A. The effect of laser osteotomy on bone healing. *Lasers Surg Med*. 1981;1(4):361-73.
325. James HE, Wiley CA, Schneider S. The effect of carbon dioxide laser irradiation on cranial bone healing. An experimental study. *Childs Nerv Syst*. 1986;2(5):248-51.
326. McDavid VG, Cobb CM, Rapley JW, Glaros AG, Spencer P. Laser irradiation of bone: III. Long-term healing following treatment by CO<sub>2</sub> and Nd:YAG lasers. *J Periodontol*. 2001;72(2):174-82.
327. Gonzalez C, Vandemerwe WP, Smith M, Reinisch L. Comparison of the Erbium-Yttrium-Aluminum-Garnet and Carbon-Dioxide Lasers for Invitro Bone and Cartilage Ablation. *Laryngoscope*. 1990;100(1):14-7.
328. Vangsness CT, Jr., Smith CF, Marshall GJ, Sweeney JR, Johansen E. The biological effects of carbon dioxide laser surgery on rabbit articular cartilage. *Clin Orthop Relat Res*. 1995;(310):48-51.



## Chapter 11: Appendices

1

1



## 11.1 List of abbreviations

ABC	Ammonium bicarbonate
ACL	Anterior cruciate ligament
ACN	Acetonitrile
ADAMTS	ADAM metalloproteinase with thrombospondin type 1
APS-MALDI	Atmospheric-pressure scanning microprobe MALDI
Arg1	Arginase 1
ASL	Argininosuccinate lyase
ASS	Argininosuccinate synthetase
BAMBI	Bone morphogenetic protein and activin membrane-bound inhibitor
BH4	Tetrahydrobiopterin
BMP	Bone morphogenetic proteins
CAR	Acyl carnitine
CBC	Complete blood count
CCL	C-C chemokine ligand
CCR	C-C chemokine receptor
CE	Collision energy
CerP	Ceramide phosphate
CerPE	Glycerophosphoethanolamine ceramide
CHCA	$\alpha$ -cyano-4-hydroxycinnamic acid
CID	Collision-induced dissociation
CL	Cardiolipin
CMC	Carboxymethyl cellulose
COX	Cyclooxygenase
CT	Computed tomography
CUSA	Cavitron ultrasonic surgical aspirator
CV	Coefficient of variance
CW	Continuous wave
D	Laser pulse duration
DAG/DG	Diacyl/alkylglycerides (diglycerides)
DAN	1',5'-diaminonaphthalene
DART	Direct analysis in real time
DDA	Data-dependent acquisition
DESI	Desorption electrospray ionization
DF	Discriminant function
DHA	2',6'-dihydroxyacetophenone
DHB	2,5-dihydroxybenzoic acid
DPO	Days post-operative
DTT	Dithiothreitol
DUB	Deubiquitinase

## Chapter 11

E	Sampling energy
ECM	Extracellular matrix
EDDP	2-ethylidene-1,5-dimethyl-3,3-diphenylpyrrolidine
EDTA	Ethylenediaminetetraacetic acid
EGFR	Epidermal growth factor receptor
EIC	Extracted ion chromatogram
EPC	Ethanolaminephosphorylceramides
ESI	Electrospray ionization
ESR	Erythrocyte sedimentation rate
FA	Fatty acids
FA	Formic acid
FDR	False discovery rate
FFPE	Formalin-fixed and paraffin-embedded
FGF	Fibroblast growth factor
FT-ICR	Fourier transform ion cyclotron resonance
fwhm	Full width at half-maximum
Fxh	Fracture hematoma
GDF	Growth differentiation factor
H&E	Hematoxylin and eosin
HexCer	Hexosylceramide
HIF-1 $\alpha$	Hypoxia-inducible factor 1 $\alpha$
IAM	Iodoacetamide
IFN- $\gamma$	Interferon- $\gamma$
IGF	Insulin-like growth factor
IGFBP	IGF-binding protein
IHC	Immunohistochemistry
IL	Interleukin
IP3/DAG	Inositol-3-phosphate/diacylglycerol
IR-MALDESI	Infrared matrix assisted laser desorption electrospray ionization
ITO	Indium tin oxide coated
LA-REIMS	Laser-assisted rapid evaporative ionization mass spectrometry
LC-MS/MS	Liquid-chromatography tandem mass spectrometry
LDA	Linear discriminant analysis
LDI-MS	Laser desorption/ionization mass spectrometry
Leu-Enk	Leucine-enkephalin
LFQ	Label free quantification
LIPC	Lyso-inositolphosphorylceramides
LMD	Laser capture microdissection
LOD	Limit of detection
LPA	Lysophosphatidic acid
LPC	Lysophosphatidylcholines

LPI	Lysophosphatidylinositol
LSM	Lysosphingomyelin
M	Operation mode
<i>m/z</i>	Mass-to-charge ratio
MALDI	Matrix-assisted laser desorption/ionization
MAP	Mitogen-activated protein
MGDG	Monogalactosyldiacylglycerol
MGMG	Monogalactosylmonoacylglycerol
MMP	Matrix metalloproteinase
MRI	Magnetic resonance imaging
MS	Mass spectrometry
MS/MS	Tandem mass spectrometry
MSC	Mesenchymal stem cell
MSI	Mass spectrometry imaging
mTOR	Mammalian target of rapamycin
NAE	N-acyl ethanolamine
NEDC	N-(1-naphthyl)ethylenediamine dihydrochloride
NFE2L	Nuclear factor erythroid 2-related factor
NF-κB	Nuclear factor kappa B
NGF	Nerve growth factor
NOS	Nitric oxide synthase
NOTCH	Neurogenic locus notch homolog
NSAID	Nonsteroidal anti-inflammatory drug
NTRK	Neurotrophic receptor tyrosine kinase
OA	Osteoarthritis
OC	Osteocalcin
OCT	Ornithine transcarbamylase
ODC	Ornithine decarboxylase
OPN	Osteopontin
OPSI	Open port sampling interface
oTOF	Orthogonal time-of-flight
P	Laser power
PA	Phosphatidic acid
PAA	Glycerophospholipid class
PBS	Phosphate buffered saline
PC	Phosphatidylcholine
PCA	Principal component analysis
PCA-LDA	Principle component analysis-linear discriminant analysis
PDGF	Platelet-derived growth factor
PE	Phosphatidylethanolamine
PEMF	Pulsed electromagnetic field

## Chapter 11

PFA	Paraformaldehyde
PG	Phosphatidylglycerol
PGE2	Prostaglandin E2
PHOSPHO1	Phosphoethanolamine/phosphocholine phosphatase
PI	Phosphatidylinositol
PI3K/AKT	Phosphatidylinositol-3-Kinase/protein kinase B
PIRL	Picosecond infrared laser
PS	Phosphatidylserine
PTOA	Post-traumatic osteoarthritis
PW	Pulsed wave
qTOF	Quadrupole time-of-flight
RA	Rheumatoid arthritis
RAAS	Renin-angiotensin-aldosterone system
RAGE	Receptor for advanced glycation end-products
REIMS	Rapid evaporative ionization mass spectrometry
RHO GTPase	RAS homolog family member of nucleotide guanosine triphosphate-ase
RIR-LA	Resonant infrared laser ablation
ROI	Region of interest
ROS	Reactive oxygen species
RUNX	Runt-related transcription factor
S/N	Signal-to-noise ratio
SA	Sinapic acid
SD	Standard deviation
SIMS	Secondary ion mass spectrometry
SM	Sphingomyelin
SMS	Sphingomyelin synthase
SPB	Sphingoid base
SPW	Super pulsed wave
SQMG	Sulfoquinovosylmonoacylglycerol
SSA	Sulfosalicylic acid
ST	Sterol
TAA	Triamcinolone acetonide
TAG/TG	Triacyl/alkylglycerides (triglycerides)
TCA	Trichloroacetic acid
TFA	Trifluoroacetic acid
TGF- $\beta$	Transforming growth factor- $\beta$
THAP	2,4,6-trihydroxyacetophenone hydrate
TIC	Total ion current
TIMP	Tissue inhibitors of matrix metalloproteinase
TLR	Toll-like receptor

TnC	Tenascin-C
TNF- $\alpha$	Tumor necrosis factor- $\alpha$
TOF	Time-of-flight
TRAF	TNF receptor associated factor
VEGF	Vascular endothelial growth factor
$\mu$ XRF	Micro X-ray fluorescence

## 11.2 List of publications

### 11.2.1 Publications

- **Nauta SP**, Poeze M, Heeren RMA, Porta Siegel T. *Clinical use of mass spectrometry (imaging) for hard tissue analysis in abnormal fracture healing*. *Clinical Chemistry and Laboratory Medicine (CCLM)*. 2020; 58(6):897-913. <https://doi.org/10.1515/cclm-2019-0857>
- Vandenbosch M, **Nauta SP**, Svirikova A, Poeze M, Heeren RMA, Porta Siegel T, Cuypers E, Marchetti-Deschmann M. *Sample preparation of bone tissue for MALDI-MSI for forensic and (pre)clinical applications*. *Analytical and Bioanalytical Chemistry*. 2021; 413:2683-2694. <https://doi.org/10.1007/s00216-020-02920-1>  
Vandenbosch M and **Nauta SP** contributed equally to this work.
- **Nauta SP**, Huysmans P, Tuijthof GJM, Eijkel GB, Poeze M, Porta Siegel T, Heeren RMA. *Automated 3D Sampling and Imaging of Uneven Sample Surfaces with LA-REIMS*. *Journal of the American Society for Mass Spectrometry (JASMS)*. 2022; 33(1):111-122. <https://doi.org/10.1021/jasms.1c00290>
- Groven RVM, **Nauta SP**, Gruisen J, Claes BSR, Greven J, van Griensven M, Poeze M, Heeren RMA, Porta Siegel T, Cillero-Pastor B, Blokhuis TJ. *Lipid Analysis of Fracture Hematoma With MALDI-MSI: Specific Lipids are Associated to Bone Fracture Healing Over Time*. *Frontiers in Chemistry*. 2022; 9:780626. <https://doi.org/10.3389/fchem.2021.780626>  
Groven RVM and **Nauta SP** contributed equally to this work.
- **Nauta SP**, Hofman M, Greven J, Hildebrand F, Mohren RJC, Porta Siegel T, Cuypers E, Heeren RMA, Poeze M. *Effects of citrulline supplement on lipid and protein profiles during bone fracture healing in a rat model*. In preparation.

### 11.2.2 Conference contributions

- **Nauta SP** and Vandenbosch M, Svirikova A, Poeze M, Heeren RMA, Porta Siegel T, Cuypers E, Marchetti-Deschmann M. *Sample preparation of bone tissue for MALDI-MSI for forensic and (pre)clinical applications*. Oral presentation. International Mass Spectrometry Imaging (24h IMSI). 2020, online.
- **Nauta SP** and Vandenbosch M, Svirikova A, Poeze M, Heeren RMA, Porta Siegel T, Cuypers E, Marchetti-Deschmann M. *Sample preparation of bone tissue for MALDI-MSI for forensic and (pre)clinical applications*. Poster presentation. International Mass Spectrometry Imaging Poster Gala. 2020, online.
- **Nauta SP**, Huysmans P, Tuijthof GJM, Eijkel GB, Poeze M, Porta Siegel T, Heeren RMA. *Automated 3D sampling and imaging of uneven sample surfaces with LA-*

- REIMS*. Oral presentation. Mass Spectrometry & Advances in the Clinical Lab (MSACL). 2021, online.
- **Nauta SP** and Groven RVM, Gruisen J, Eveque-Mouroux M, Poeze M, van Griensven M, Porta Siegel T, Cillero-Pastor B, Blokhuis TJ. *Lipid Analysis of Fracture Hematoma with MALDI-MSI*. Poster presentation. International Mass Spectrometry Conference (IMSC). 2022. Maastricht, the Netherlands.
  - Groven RVM and **Nauta SP**, Gruisen J, Eveque-Mouroux M, Poeze M, van Griensven M, Porta Siegel T, Cillero-Pastor B, Blokhuis TJ. *Specific lipids are associated to bone fracture healing over time: lipid analysis of fracture hematoma with MALDI-MSI*. Poster presentation. Tissue Engineering and Regenerative Medicine International Society (TERMIS). 2021, online.
  - Groven RVM and **Nauta SP**, Gruisen J, Eveque-Mouroux M, Poeze M, van Griensven M, Porta Siegel T, Cillero-Pastor B, Blokhuis TJ. *Specific lipids are associated to bone fracture healing over time: lipid analysis of fracture hematoma with MALDI-MSI*. Poster presentation. European Congress of Trauma and Emergency Surgery (ECTES). 2022, Oslo, Norway.
  - Groven RVM and **Nauta SP**, Gruisen J, Eveque-Mouroux M, Poeze M, van Griensven M, Porta Siegel T, Cillero-Pastor B, Blokhuis TJ. *Specific lipids are associated to bone fracture healing over time: lipid analysis of fracture hematoma with MALDI-MSI*. Poster presentation. European Federation of National Associations of Orthopaedics and Traumatology (EFFORT) Annual Congress. 2022, Lisbon, Portugal.
  - Vats M, **Nauta SP**, Cillero-Pastor B, Cuypers E., Heeren RMA. *Development of sample preparation method to analyze the distribution of flavor compounds in mushrooms*. Poster presentation. International Mass Spectrometry Conference (IMSC). 2022. Maastricht, the Netherlands.
  - Haartsman MJJ, Emanuel KS, **Nauta SP**, Tuijthof GJM, Heeren RMA, Emans PJ, Cillero-Pastor B. *Rapid Evaporative Ionization Mass Spectrometry (REIMS) with diathermic knife as a potential diagnostic tool in cartilage defect and osteoarthritis patients*. Poster presentation. European Society of Tissue Regeneration in Orthopedics and Traumatology (ESTROT). 2022. Maastricht, the Netherlands.

### 11.3 Acknowledgements

Doing a PhD is a lot of work with performing experiments, doing data analysis, writing papers, troubleshooting instruments, performing educational tasks, and all the other tasks that come along. Making it to the finish line has been a team effort together with my supervisors, all the team members of M4i, and all other colleagues. Therefore, let me start with thanking everyone for their help and support throughout the past years and to help me grow into the person I am today.

Beste Ron, Bedankt dat je mij de mogelijkheid voor dit promotieonderzoek gegeven hebt. Jouw kennis, bevlogenheid en motivatie zijn zeer inspirerend en hebben mij veel geleerd en gedreven om mijn projecten tot een zo goed mogelijk einde te brengen. Besprekingen van resultaten leverde vaak een levendige discussie op over hun betekenis en meestal ook een heleboel opties voor vervolg experimenten of dingen om te testen. Ik heb het altijd zeer gewaardeerd dat je open staat voor een goede discussie en luisterde naar mijn argumenten, maar vooral ook dat je bijstuurde indien nodig. Daarnaast was je altijd beschikbaar en ging je indien nodig meteen over tot actie, ondanks je drukke agenda. Nogmaals bedankt voor de supervisie en support van de afgelopen jaren.

Beste Martijn, Bedankt dat je mij de mogelijkheid hebt gegeven voor dit promotieonderzoek. Jouw enthousiasme voor de verschillende projecten en jouw interesse in de toekomstige mogelijkheden zijn altijd een goede drijfveer geweest. Zelfs in zulke mate dat ik zo nu en dan vergat om bepaalde dingen uit te leggen die voor mij heel logisch waren. Door de verschillende projecten en jaren heen heb jij altijd de klinische kant benadrukt en gevraagd wat een arts er aan heeft. Die vragen zijn zeer belangrijk geweest voor mij, aangezien het klinische aspect binnen het project mij altijd erg geïnteresseerd en gemotiveerd heeft. Ik wil je ook bedanken dat je mij de mogelijkheid gegeven hebt om een aantal keer mee te gaan naar de operatiekamer, dit heeft mij veel geleerd en was een mooie ervaring. Nogmaals bedankt voor de supervisie en support van de afgelopen jaren.

Dear Tiffany, I think I have to thank you most of all for giving me this opportunity. I still remember you telling me that you might have another project for me if the project I was having an interview for would not working out. That project was indeed the right opportunity for me with a combination of technical and biological challenges for a clinical question. I had a lot to learn when I started at M4i, but you were always patient and help me figure everything out. Besides, your door was always open for questions as well as personal matters. I enjoyed spending time with you in the lab when you were teaching me a new instrument or when we were

troubleshooting together. I noticed how much you liked it and looking back it, it was a sign. I still remember the day that you told me you were leaving to Germany. It was quite a shock and I was sad to see you leave, but eventually it all worked out. I might even say that it was good for me, as I forced me to figure everything out more on my own. Nevertheless, your support and help were still there and important for me. Besides, I saw how happy and enthusiastic you are at your new job. So, thank you for all your supervision and the nice times we had. But most of all, thank you for always supporting and believing in me.

Beste Eva, Bedankt voor al je hulp en supervisie in de laatste fase van mijn promotieonderzoek. Ik leerde je kennen als copromotor van Michiel toen we samenwerkten aan een publicatie. Toen Tiffany vertrok, werd jij al snel mijn dagelijkse supervisor, aangezien je ondertussen bij M4i werkte. In die rol heb je mij erg geholpen in de afrondende fase van mijn projecten. Daarom ben ik ook erg blij dat het gelukt is om jou als tweede copromotor aan mijn supervisieteam toe te voegen. Jouw frisse en kritische blik op de lopende projecten heeft erg veel geholpen om te focussen en de projecten af te ronden. Daarnaast kon ik altijd even binnenlopen met vragen en problemen, want je zat tenslotte in het aangrenzende kantoor. Nogmaals bedankt voor het inspringen in de supervisie en alle gezellige momenten.

I want to thank Prof. dr. Daisy Jonkers, Prof. dr. Kristine Glunde, Prof. dr. Steven Olde Damink, Prof. dr. Tim Welting, and Dr. Nina Ogrinc for being part of the assessment committee and taking the time to review my thesis.

Lieve Mirella, Wat was het leuk en gezellig toen jij op het kantoor erbij kwam. We hebben vaak kunnen sparren over onze projecten door alle raakvlakken daarin, maar konden ook over vele andere onderwerpen praten. Daarnaast hebben we uren samen in het lab doorgebracht met de iKnife, want wat is dat een uitdaging op Hoffa's fat pad. In jouw ander projecten zat het ook lang niet altijd mee, maar hopelijk heb je toch wat gehad aan onze discussies en/of gewoon even lekker klagen. Voor gezellige wandelingen en etentjes kon ik bij jou terecht en ook dan raakten we nooit uitgepraat. Dank voor alle gezellige momenten en je steun. Heel veel succes met het afronden van je thesis. En natuurlijk heel erg bedankt dat je mijn paranimef wil zijn.

Dear Anjusha, When you decided to move to our office, you were really happy to join us. One thing is for sure, you enjoy chatting in the office or came back from the lab just to have a chat over a coffee in your case and tea in my case. So, sorry for ignoring you sometimes, but I needed to focus on work as well. Nevertheless, I

## Chapter 11

loved all our chats about work, live, culture, and what not. Also during our dinners and a special thanks for letting me experience real Indian food. Despite me trying really hard, I still do not completely understand your projects, but hopefully our discussion about them were still useful. I know you will finalize them, although writing papers is not your favorite thing to do, as you prefer spending your time in the lab. Thank you for all the fun we had, your support and believing in me. Good luck with finishing your thesis.

In my opinion and experience, having fun office mates that you can chat with about work and life is really important. They support you during the hard times, but also celebrate all achievements with you, making the whole process better. Therefore, besides Mirella and Anjusha, I want to mention my office mates here and thank them for their support. So, thank you, Joel, Romy, Kees (although it was short), Lars, Chiara, and all other guests that stayed in the office for some time. Lieve Romy, Jij zat al op kantoor toen ik daar terecht kwam. Zeker in het begin heb je veel geholpen met wegwijs worden in alle systemen van de universiteit en de afdelingen. Daarnaast kon ik altijd bij je terecht met vragen en verhalen, hopelijk voelde dat andersom ook zo. Je wist altijd een balans te vinden tussen al het werk voor jouw PhD en jouw gezin en dat was mooi om te zien. Lieve Lars, Je begon als student bij Romy, maar je hebt je helemaal ontpopt toen je PhD werd en bij ons op kantoor terecht kwam. Je hebt een hoop gezelligheid op kantoor gebracht, maar we hebben ook een heleboel serieuze gesprekken gehad. En je houdt je maar toch mooi staande tussen al die vrouwen op kantoor. Ik vind het een hele prestatie dat het je lukt om alles voor jouw PhD te doen en daarnaast ook nog bij de huisarts te werken. Romy en Lars, door jullie weet ik nu hoe moeilijk klinisch onderzoek soms kan zijn met al jullie struggles met METC, patiënten, etc. Hopelijk hebben jullie toch wat gehad aan mijn steun tijdens deze periodes. Daarnaast heb ik al jullie studenten en telefoontjes met patiënten en collega's toch maar mooi overleefd. Nogmaals dank voor alle gezellige en serieuze momenten en jullie steun.

Lieve Britt, We zijn op dezelfde dag begonnen aan onze PhD, maar ja, jij had je stage al gedaan bij M4i. Om die reden, heb je me veel geholpen met wegwijs worden bij M4i. Ook daarna is jouw kennis van lipiden en instrumenten altijd een grote hulp geweest. Daarnaast kon ik altijd bij je terecht met problemen en hebben we regelmatig samen zitten klagen over alles waar we tegenaan liepen en wat niet. Maar we hebben ook veel gezellige gesprekken gevoerd, gezamenlijke gegeten, etc. Echter heb ik je ook veel zien strugglen met je projecten en je focus. Niet zo gek, want als iemand veel tegenslagen (die niet verder benoemd mogen worden) heeft gehad in zijn PhD, dan ben jij het. Ik ben blij te zien dat het beter gaat en je je

grenzen beter aangeeft. Nog even doorzetten, je bent er bijna en het gaat je lukken. Dank voor alle gezellige momenten en jouw hulp. Heel veel succes met het afronden van je thesis.

Dear Darya, You were always up for a nice chat, but also were not afraid to kick me out of your office if you did not have time. You were my go-to-girl when I had questions about getting ESI sources working on Waters instruments during troubleshooting, which was more often than anyone likes. Besides, you helped me a lot in the last project by quickly teaching me how to operate the Solarix, helping me find the best settings, and troubleshooting it when something came up, no matter the day or time. So, thank you so much for all of that. You have always been very active besides your projects and I really admire that about you. Thank you for all your help and the nice times we had. Good luck with finishing your thesis.

Dear Jian-Hua, We really got to know each other while we were sharing a room during the summer school in Dubrovnik. We had a lot of fun and I still remember your surprise that I could sleep while you were still finishing the assignments, taking a shower, etc. You are really an outgoing person (despite you saying you are shy) and always up for a chat and food. Thank you for all the fun times and chats and for always believing in me. I wish you all the best with your future career.

Lieve Stephanie, Ondanks dat je je tijd moest verdelen tussen verschillende afdelingen, was het altijd gezellig als je bij M4i was. We hebben veel besproken tijdens onze babbels op het lab en kantoor, maar ik kon ook altijd bij je terecht voor hulp. Je hebt me ook van veel hulp en advies voorzien over banen, vacatures, etc, aangezien ik graag dezelfde of vergelijkbare richting op wil als die jij op bent gegaan. Dus bedankt voor al je hulp en advies, maar ook voor de gezellig gesprekken. Veel succes met de rest van je carrière.

Frans, Gert en Ronny, Jullie zijn de vaste krachten waar M4i op leunt en zorgen dat alles draaiend blijft. Frans, bedankt voor het maken van de lasergordijnen. Ik heb ze vaak mogen gebruiken en dat was zo veel makkelijker dan de gordijnen van IDEE. Gert, bedankt voor alle hulp bij data analyse en visualisatie in verschillende projecten. Het was altijd leuk te zien hoe ik met ideeën of aanpassingen voor software naar je toe kwam en jij meteen al oplossingen zat te bedenken en soms zelfs nog verder ging. Ronny, bedankt voor alle hulp in het lab en dan vooral met de proteomics experimenten voor mijn laatste project.

Michiel, we hebben elkaar leren kennen in Wenen toen we allebei daar te gast waren bij Martina's onderzoeksgroep. Daar heb je mij alle tips en tricks geleerd van het snijden van botweefsel. Zonder deze kennis was ik nooit zo ver gekomen in mijn

## Chapter 11

onderzoeksprojecten. Ik vind het dan ook erg leuk dat we het sample preparation protocol voor botweefsel gezamenlijk hebben afgemaakt op het lab in M4i en gepubliceerd. Ook daarna heb ik altijd gebruik kunnen maken van jouw kennis van onder andere botweefsel. Nogmaals bedankt dat je me geleerd hebt om botweefsel te snijden en alle hulp daarna in verschillende projecten.

Besides these people, I would also like to thank the rest of M4i for their help and support as well as for all the fun times, coffee corner chats, etc. All these people and the moments that we had together have helped to make my time at M4i fun. So, a thank you to all the former and current members of M4i: Aljoscha, Ana, Andrej, Andrew, Anne, Bea, Ben, Benjamin (Thank you for your help with SCiLS), Berta (Thank you for all the help and supervision in the fracture hematoma project), Bo, Brenda, Bryn, Charles, Christel, Erik, Fabian, Florian, Fred (Thank you for all your help with the Synapt), Ian, Isabeau (Bedankt voor je hulp with the proteomics data analyse), Kapser, Kasper, Kim, Klara, Laura, Layla, Lennart, Lieke (Bedankt voor alle hulp met de XEVO), Lidia, Lucia, Maarten, Maria, Marta, Maxime, Michele (Thank you for your help with the CO<sub>2</sub> laser), Mudita, Naomi, Nina, Peiliang, Philippe, Pieter (Bedankt voor je hulp met de eSAT/IN box), P-Max (Thank you for all your help with the REIMS and iKnife), Rob, Roel, Sebastiaan, Shane, Tialfi, Tim, Yuandi, and all the other guests and students.

Daarnaast wil ik ook de chirurgie afdeling bedanken voor al hun gezellige praatjes en momenten. Anne, Annemarie, Annet, Evie, Janine, Nicole, Roxanne, Sabine en alle andere collega's, bedankt. En nog een extra dankjewel voor Annet voor het redden van mijn word document zodat ik niet dagen werk kwijt was (zoals beloofd).

Evelien, Bedankt voor alle praatjes en klaagmomenten tijdens de afgelopen jaren. Ondanks dat we op hele andere afdelingen werkten, hebben we het altijd gezellig gehad. Heel veel succes met het afronden van je thesis.

Helen, Carla en Manuela bedankt voor het regelen van alle overleggen met Ron en Martijn. Het was soms een uitdaging om een moment te vinden waarop ze allebei beschikbaar waren, maar jullie kregen het toch altijd weer voor elkaar.

Furthermore, I would like to thank all the team members of the Institute of Chemical Technologies and Analytics at the TU Wien for welcoming me with open arms during my stay. A special thanks for Martina for providing me with the opportunity to join her research group for some time and her support during that time. I would also like to thank Samuel for his help on the Synapt during my stay. In addition, a thank you to ZonMW from NWO for providing me with a travel grant that made it possible for me to visit the TU Wien.

Tijdens verschillende projecten had ik regelmatig samples nodig voor testen en experimenten. Daarom wil ik iedereen bedanken die mij door de jaren heen samples heeft verstrekt. Dennis en Pascal bedankt voor de muizen achterpoten en Dennis ook bedankt voor je hulp met de sample preparation. Pieter, Tim en Andy bedankt voor alle heupkoppen, ik hoefde nooit lang te wachten tot ik ze kon ophalen. Anne, bedankt voor de ratten achterpoten en het extra werk dat je voor mij verricht hebt om die aan mij te geven.

Het fractuur hematoma project begon als Jane's studentenproject en door de raakvlakken met mijn project werd ik er al snel bij betrokken. Jane, bedankt voor al het werk dat je binnen dit project verzet hebt, maar ook bedankt voor al gezellige momenten. Rald, we hebben samen veel tijd doorgebracht in het lab om dit project af te ronden en tijdens die experimenten heb ik geprobeerd je wegwijs te maken in de massaspectrometrie. Maar we hebben ook over een heleboel andere dingen regelmatig zitten praten. Bedankt voor alle gezellige en serieuze momenten en voor al je werk in onze gezamenlijke publicatie. Jane en Rald, heel veel succes met het afronden van jullie eigen thesis. Ik wil daarnaast ook Taco bedanken voor al zijn feedback en support in dit project.

I would like to thank Martijn Hofman, Johannes Greven, and Frank Hildebrand for providing with the samples for the citrulline supplementation study and for being patient while I figured out the best way to analyze them. I am looking forward to publishing the collaborative paper about this study.

Bij het ontwikkelen van de 3D MS Scanner zijn vele mensen betrokken geweest, die ik allen wil bedanken voor hun hulp en bijdrage. Bovenal wil ik het hele team van IDEE dat betrokken is geweest bij dit project bedanken en in het bijzonder Paul, Pascal, Vincent, Sander en Gabrielle. Pascal en Vincent, we hebben veel tijd samen doorgebracht onder andere in het lab achter de lasergordijnen om elke keer een nieuwe versie of toevoeging te testen. Ik wil jullie en de rest van IDEE bedanken voor jullie medewerking aan de constante stroom van verbeteringen en uitbreidingen binnen dit project. Daarnaast wil ik Chris en Remco bedanken voor hun inzichten en hulp bij het ontwikkelen van geschikte methodes voor het plaatsen van heupkoppen in het systeem.

Last, but definitely not least, mijn familie, zonder jullie had ik het niet gered. Lieve pap en mam, bedankt dat jullie altijd voor me klaar stonden en me gesteund hebben door alle ups en downs. Als ik thuis kwam, dan kon ik echt even met andere dingen bezig zijn en weer opladen. Lieve Laura, mijn kleine zusje (dat kon ik niet laten), ook jij bedankt dat je altijd voor me klaar stond en naar al mijn verhalen

## Chapter 11

luisterde. Onze vakanties samen heb ik altijd heel gezellig gevonden en gewaardeerd, want even alle stress van de verschillende projecten achter me laten en met jou de wereld ontdekken heeft me veel geholpen. Hopelijk gaan we daar nog lang mee door. Daarnaast natuurlijk heel erg bedankt dat je mijn paranimf wil zijn, ook al vind je het best een beetje spannend. Lieve oma Annet, bedankt dat je altijd je best gedaan hebt om al mijn verhalen te begrijpen en me gesteund hebt. Ik vond het ook altijd heel leuk om te horen hoe mijn verhalen je herinnerde aan de tijd dat Gerrit bezig was met zijn promotie en gerelateerd onderzoek. Blijkbaar veranderen bepaalde dingen nooit, ook al zit er vijftig jaar tussen. Lieve opa Jaap, bedankt voor al je steun ook al waren mijn verhalen vast vaak niet helemaal te volgen voor jou. Lieve opa Rob en oma Jenny, ik vind het ontzettend jammer dat jullie er niet bij kunnen zijn tijdens de officiële defense, maar ik weet dat jullie trots op mij zijn. Ik wil ook alle ooms, tantes, neefjes, nichtjes en andere familie bedanken voor hun steun en interesse. Ik heb jullie vast verveeld met mijn verhalen en onbegrijpelijke uitleg, maar jullie zijn altijd geïnteresseerd geweest.

## 11.4 Curriculum Vitae

Sylvia Paulien Nauta was born on the 31<sup>st</sup> of August, 1993 in Almere (the Netherlands). She completed her pre-university education in 2011 at the Lindenberg in Leek. She studied at the University of Groningen from 2011 to 2014 to obtain a Bachelor degree in Life, Science, and Technology with a major in Biomedical Engineering. This study allowed her to combine her interests in science and technology with the additions of biological and medical aspects.



She continued her education at the University of Groningen from 2014 to 2016 to obtain a Master degree with honors in Biomedical Engineering with a sub-specialization in Prothesis & Implant design. During her internship at Center for Congenital Heart Diseases at UMCG, she developed a computational model to evaluate the stiffness of pulmonary arteries in pulmonary arterial hypertension. She completed her master thesis at SPRINT@Work at UMCG and started with the validation of a measuring device using IMUs and sEMG for studying the mechanical workload in physical active employees.

In March 2018, she started her PhD research under supervision of Prof. Dr. R.M.A. Heeren, Prof. Dr. M. Poeze, Dr. T. Porta Siegel, and later Dr. E. Cuyppers in a collaboration between the Maastricht MultiModal Molecular Imaging (M4i) institute at Maastricht University and the Traumasurgery department of MUMC+. Her research was focused on the use of different mass spectrometry imaging techniques to study bone and cartilage in relation to skeletal healing. During this research she collaborated with different research group and visited the TU Wien for a month as guest researcher. The results of these collaborations and the performed research are presented in this thesis.

In March 2023, she started as a postdoctoral researcher in the Specturi project at Radboudumc joining the neonatology department under supervision of Dr. P. van Setten in collaboration with the molecular kidney physiology group of Prof. Dr. J. Hoenderop.



